NEW TRENDS IN HIGH-ENERGY PHYSICS

Budva, Becici, Montenegro
24–30 September 2018

Proceedings of the Conference

JOINT INSTITUTE FOR NUCLEAR RESEARCH

NEW TRENDS IN HIGH-ENERGY PHYSICS

Budva, Becici, Montenegro
24–30 September 2018

Proceedings of the Conference

Dubna 2019

УДК 539.1(063)
ББК 22.3я431
N52

The contributions are reproduced directly from the originals.

New Trends in High-Energy Physics: Proceedings of the Conference
N52 (Budva, Becici, Montenegro, 24–30 September 2018). — Dubna: JINR, 2019. — 287 p.

ISBN 978-5-9530-0509-8

The Conference on New Trends in High-Energy Physics organized by the Joint Institute for Nuclear Research, Dubna, and Bogolyubov Institute for Theoretical Physics, National Academy of Sciences of Ukraine, was held at the Hotel Splendid, Conference Hall, Budva, Becici, Montenegro, on 24–30 September 2018.

The present Proceedings contain direct reproductions of authors' originals (reviews and short communications) that arrived at the Organizing Committee and are grouped somewhat loosely. We have united a number of sections. The contributions within each section are ordered according to the conference program. The Organizing Committee thanks all participants for their contributions. More conference information and pictures can be found on our site: http://indico-new.jinr.ru/event/ntihep2018.

Новые тенденции в физике высоких энергий: Труды конференции (Будва, Бечичи, Черногория, 24–30 сентября 2018 г.). — Дубна: ОИЯИ, 2019. — 287 с.

ISBN 978-5-9530-0509-8

Конференция «Новые тенденции в физике высоких энергий», организованная Объединенным институтом ядерных исследований (Дубна) и Институтом теоретической физики им. Н. Н. Боголюбова НАН Украины (Киев), проходила в конференц-зале гостиницы «Splendid» (Будва, Бечичи, Черногория) 24–30 сентября 2018 г.

Данный сборник содержит материалы (обзоры и короткие сообщения), присланные авторами в оргкомитет, сгруппированные в свободном порядке, ряд разделов объединен. Статьи в каждом разделе упорядочены в соответствии с программой конференции. Оргкомитет благодарит за сотрудничество всех участников. Более подробную информацию о конференции, а также фотографии можно найти на сайте: http://indico-new. jinr.ru/event/ntihep2018.

УДК 539.1(063)
ББК 22.3я431

ISBN 978-5-9530-0509-8

CONTENTS

CONFERENCE PROGRAM

25 September 2018

09:00 - 09:30 **OPENING**

M. Itkis. **International large research infrastructure of JINR**

09:30-10:30 **SECTION "STANDARD MODEL AND BEYOND"**

Chair: R. Lednický

09:30 T. Davidek. **Study of the properties of the Higgs boson**

10:00 G. Gaudio. **The ATLAS experiment. Status and prospects**

10:30-10:50 **Coffee break**

10:50-12:30 **SECTION "NEUTRINO AND ASTROPARTICLE PHYSICS"**

Chair: M. Itkis

10:50 A. Kozlov. **Search for the neutrinoless double beta decay of Xenon-136 and dark matter at KamLAN**

11:20 V. D'Andrea. **Neutrinoless double beta decay search with GERDA Phase II**

11:50 S. Mertens. **First data of the KATRIN experiment**

12:30-14:30 **Lunch time**

14:30-16:00 **SECTION "NEUTRINO AND ASTROPARTICLE PHYSICS"**

Chair: V. Bednyakov

14:30 Yu. Efremenko. **Study of CEvNS by the COHERENT collaboration**

15:00 T. Wachala. **The latest results from the long-baseline neutrino experiment T2K**

15:30 V. Belov. **Actual status of "DANSS" project**

16:00-16:20 **Coffee break**

16:20-18:05 **SECTION "NEW FACILITIES, DETECTORS, COMPUTING AND DATA ANALYSES TECHNIQUES"**

Chair: Yu. Usov

16:20 Yu. Davydov. **Tests of 3x3 undoped CsI matrix with an extremely low intensity electron beam**

16:45 Yu. Kharzheev. **Radiation hardness of scintillation detectors based on organic plastic scintillators and optical fibers**

17:10 M. Lyablin. **The Professional Precision Laser inclinometer: the noise origins and data processing**

17:35 I. Bednyakov. **The Precision Laser Inclinometer, method of data processing and data storage**

20:00 **WELCOME PARTY**

26 September 2018

09:00 - 10:30 **SECTION "STANDARD MODEL AND BEYOND"**

Chair: V. Glagolev

09:00 B. Melado. **New physics at the EW scale and the production of multiple leptons at the LHC**

09:30 P. Krokovny. **Search for new physics with LHCb**

10:00 M. Bombara. **Recent results with ALICE experiment**

10:30-10:50 **Coffee break**

10:50 - 12:30 **SECTION "ADVANCES IN THEORETICAL PHYSICS"**

Chair: R. Lednický

10:50 D. Kazakov. **What makes us think that physics beyond the SM exists**

11:15 L. Jenkovszky. **The odderon: myths and reality**

11:40 O. Solovtsova. **High-precision numerical estimates of Mellin-Barnes integrals for Mellin moments of the structure functions using a stationary phase contour**

12:05 I. Yeletskikh. **Pentaquark states: current status from theory and experiment**

12:30-14:30 **Lunch time**

14:30-16:00 **SECTION "NEUTRINO AND ASTROPARTICLE PHYSICS"**

Chair: M. Itkis

14:30 R. Dvornicky. **Baikal GVD experiment: present status and perspectives**

15:00 L. Tkatchev. **The NUCLEON and TUS space experiments status**

15:25 A. Borodin. **Tunka Advanced Instrument for cosmic rays and Gamma Astronomy (TAIGA): status, results and perspectives**

16:00-16:20 **Coffee break**

16:20-18:25 **SECTION "NEW FACILITIES, DETECTORS, COMPUTING AND DATA ANALYSES TECHNIQUES"**

Chair: D. Peshekhonov

16:20 A. Thomas. **First use of an active polarized Frozen Spin Target in a 4 π detector - detection of particles under cryogenic conditions below 1 Kelvin**

16:45 I. Gorodnov. **New cryostat for Bonn electron accelerator "ELSA"**

17:10 V. Kashevarov. **Polarization experiments at MAMI and ELSA with Dubna-Mainz frozen spin target**

17:35 J. Vlasek. **Data acquisition system for the SCube detector**

18:00 A. Opichal. **Control system for experimental setups of MASHA at cyclotron DC280**

27 September 2018

09:00 - 10:30 **SECTION "NEW COLLIDERS FOR BARYONIC MATTER STUDY"**

Chair: B. Melado

09:00 T. Lesiak **Future e^+e^- colliders at the energy frontier**
09:30 E. Brondolin. **News on physics and detectors at CLIC**
10:00 D. Cervenkov. **The Belle II experiment**

10:30-10:50 **Coffee break**

10:50 - 12:30 **SECTION "STANDARD MODEL AND BEYOND"**

Chair: Yu. Efremenko

10:50 R. Chislett. **The muon g-2 experiment at Fermilab**
11:30 C. Voena. **Status and prospects of charged lepton flavor violation searches with the MEG-II experiment**
12:00 C. Giacomo. **Gravitational wave astronomy with Virgo and the GW detectors network**

12:30-14:30 **Lunch time**

14:00 **EXCURSION**

28 September 2018

09:00 - 10:30 **SECTION "STANDARD MODEL AND BEYOND"**

Chair: Yu. Davydov

09:00 H. Yoshida. **COMET experiment: search for muon to electron conversion**

09:30 S. Nishimura. **Precision measurement of muonium hyperfine structure at J-PARC**

10:00 A. Issadykov. **Hadronic and semileptonic decays of Bc meson**

10:30-10:50 **Coffee break**

10:50 - 12:30 **SECTION "STANDARD MODEL AND BEYOND"**

Chair: R. Lednický

10:50 A. Butenko. **Status of the NICA project at JINR**

11:15 G. Golovanov. **Muon system for spin physics detector at NICA**

11:40 G. Pokatashkin. **BM@N experiment at Nuclotron: status and first results**

12:05 O. Rogachevskiy. **Fractal properties of the multiparticle events in heavy ion collisions**

12:30-14:30 **Lunch time**

14:30-16:00 **SECTION "NEUTRINO AND ASTROPARTICLE PHYSICS"**

Chair: F. Varanini

14:30 J.K. Hwang. **Charged dark matters, cosmic rays and extended standard model**

15:00 E. Yakushev. **Modern approaches in ultra-low background experiments at the LSM underground laboratory**

15:30 S. Rozov. **Direct low-mass WIMP searches with HPGe semiconductor bolometers**

16:00-16:20 **Coffee break**

16:20-18:05 **SECTION "NEUTRINO AND ASTROPARTICLE PHYSICS"**

Chair: E. Yakushev

16:20 F. Varanini. **Sterile neutrino searches with the ICARUS detector**

16:45 M. Gonchar. **New results from the Daya Bay experiment**

17:10 C. Genster. **Status of Jiangmen Underground Neutrino Observatory**

17:35 T. Nosek. **NOvA recent results with neutrino-antineutrino data**

29 September 2018

09:00 - 10:30 **SECTION "STANDARD MODEL AND BEYOND"**

Chair: S. Nishimura

09:00 A. Szczurek. **From D meson asymmetries at the LHC to neutrino production at IceCube**

09:30 G. Lykasov. **Constraints on the intrinsic charm content of the proton from recent ATLAS data**

09:55 Yu. Kulchitsky. **Probing QCD at high energy**

10:30-10:50 **Coffee break**

10:50 - 12:30 **SECTION "NEW FACILITIES, DETECTORS, COMPUTING AND DATA ANALYSES TECHNIQUES"**

Chair: A. Butenko

10:50 S. Kotov. **Machine learning methods for cluster identification in pixel detectors**

11:15 N. Atanov. **The front-end electronics of the Mu2e electromagnetic calorimeter**

11:40 P. Zarubin. **Overview of nuclear clustering studies in dissociation of relativistic light nuclei**

12:05 I. Zarubina. **Imaging of few-body nuclear systems in nuclear track emulsion**

12:30-14:30 **Lunch time**

14:30-16:00 **SECTION "STANDARD MODEL AND BEYOND"**

Chair: A. Szczurek

14:30 M. Sahinsoy. **Search for manifestations of new physics**

15:00 W. Schaefer. **Incoherent and coherent diffractive production of J/ψ and Y on heavy nuclei**

15:25 D. Demin. **Experimental search of nuclear fusion reactions in a ptμ system**

16:00-16:20 **Coffee break**

16:20-17:10 **SECTION "STANDARD MODEL AND BEYOND"**

Chair: L. Jenkovsky

16:20 I. Lavrukhin. **MUSE and the proton radius puzzle**

16:45 N. Pukhaeva. **Future e+e- colliders and CR effects study**

17:10 **CLOSING**

I “NEUTRINO AND ASTROPARTICLE PHYSICS”


MPD building
Collider
Eastern half-ring
SPD building


NEW TRENDS
IN HIGH-ENERGY PHYSICS
24 - 30 September 2018
Montenegro, Budva, Becici
Hotel Splendid Conference & Spa Resort
SPLENDID


HIGH-ENERGY PHYSICS
SPLENDID


of the properties
of the Higgs boson
ATLAS
EXPERIMENT


DANSS
Detector of the reactor AntiNeutrino
based on Solid-state Scintillator
SPLENDID


TRENDS
NERGY PHYSICS
September 2018
Jadran
The 2HDM+S model
Di-lepton or multilepton
Outlook and Conclusions
SPLENDID


TRENDS
NERGY PHYSICS
Jadran
JINR
Overview:
• The Precision Laser Inclinometer(PLI) as data sour
• The Raw type of data from PLI
• Raw data conversion
• CERN Accelerator Logging Service(CALS)
• TimBER User Interface for CALS
• pyTimber as python library
• Data Transfer and storage Method
SPLENDID


NEW TRENDS
IN HIGH-ENERGY PHYSICS
SPLENDID


Collaboration: 9 institutions
1. Institute for Nuclear Research, Moscow, Russia.
2. Joint Institute for Nuclear Research, Dubna, Russia.
3. Irkutsk State University, Irkutsk, Russia.
4. Skobeltsyn Institute of Nuclear Physics MSU, Moscow, Russia.
5. Nizhny Novgorod State Technical University, Russia.
6. St.Petersburg State Marine University, Russia.
7. Ruhrgas Gmbh., Berlin, Germany.
8. Institute of Experimental and Applied Physics, Czech Technical University, Prague, Czech Republic
9. Comenius University, Bratislava, Slovakia.


Jadran
HOTEL
SPLENDID
CONFERENCE & SPA RESORT


NEW TRENDS
IN HIGH-ENERGY PHYSICS
SPLENDID


NEW TRENDS
IN HIGH-ENERGY PHYSICS
HOTEL
SPLENDID

Neutrinoless double beta decay search with GERDA Phase II

V. D'Andrea* on behalf of the GERDA Collaboration

Università degli Studi dell'Aquila & INFN Laboratori Nazionali del Gran Sasso, L'Aquila, Italy

Abstract

The GErmanium Detector Array (GERDA) experiment, located at the Laboratori Nazionali del Gran Sasso (LNGS), searches for the neutrinoless double beta ($0\nu\beta\beta$) decay of the isotope ^{76}Ge. High-purity germanium crystals enriched in ^{76}Ge, simultaneously used as source and detector, are directly deployed into ultra-pure, cryogenic liquid argon, acting both as cooling medium and shield against the external radiation. The second phase of the experiment is taking data since end of 2015 with a total enriched Ge mass of 35.6 kg, with newly developed BEGe type Germanium detectors. Moreover, the instrumentation of the cryogenic liquid volume surrounding the germanium detectors, acts as additional active veto and assures a further background suppression. Initial results from Phase II, with about 10 kg·yr exposure indicate that the target background of 10^{-3} counts/(keV·kg·yr) is achieved, thus making GERDA the first experiment in the field which will be "background-free" up to the design exposure of 100 kg·yr. The last data release of June 2018, presented in this paper, with a total exposure of 82.4 kg·yr of ^{76}Ge allowed to further improve the limit on the half-life to $T^{0\nu}_{1/2} > 0.9 \cdot 10^{26}$ yr (90% C.L.).

1 Introduction

The dominance of the matter over the antimatter in our universe is one of the most interesting aspects of cosmology. One of the favored model to explain this dominance is the leptogenesis [1], that is based on the violation of the lepton number. In many extensions of the Standard Model [2], neutrinos are assumed to be their own antiparticles (Majorana particles), explaining the origin of the low neutrino

*e-mail:valerio.dandrea@lngs.infn.it

mass and leading to lepton number violating processes. At present, the only feasible experiments having the potential of establishing that the massive neutrinos are Majorana particles are the ones searching for the neutrinoless double beta ($0\nu\beta\beta$) decay.

2 Search for $0\nu\beta\beta$ decay

The double beta ($\beta\beta$) decay is a second order weak nuclear decay process with extremely long half-life, consisting of the transformation of a pair of neutrons into two protons as a single process with the emission of two electrons. The standard model predicts the $\beta\beta$ decay with two neutrinos ($2\nu\beta\beta$):

$$(Z, A) \rightarrow (Z + 2, A) + 2e + 2\bar{\nu}_e \, . \tag{1}$$

This decay has been observed in a few isotopes. The neutrinoless mode of this decay is not predicted by the Standard Model and consists in the emission of only two electrons:

$$(Z, A) \rightarrow (Z + 2, A) + 2e \tag{2}$$

this decays violates the lepton number conservation by two units and has never been observed up to now.

The search for a $0\nu\beta\beta$ decay signal consists in the detection of the two emitted electrons. The rate of the $0\nu\beta\beta$ decay is usually factorized into three terms [3]:

$$\left(T^{0\nu}_{1/2}\right)^{-1} = G_{0\nu}|M_{0\nu}|^2 \left(\frac{m_{\beta\beta}}{m_e}\right)^2 \tag{3}$$

where $T^{0\nu}_{1/2}$ is the half-life of the $0\nu\beta\beta$ process, $G_{0\nu}$ is the phase space factor (PSF) and $M_{0\nu}$ is the nuclear matrix element (NME) [4]. In the expression of Eq. (3) a fundamental quantity appears, the effective Majorana mass $m_{\beta\beta}$ defined by:

$$m_{\beta\beta} = \left| \sum_{i=1}^{3} U^2_{ei} m_i \right| \tag{4}$$

where U is the PMNS mixing matrix [5] and m_i are the neutrino mass eigenvalues. This quantity appears in the Eq. (3) because the Majorana neutrino propagator enters in the amplitude calculation. It follows that the decay rate is proportional to $m^2_{\beta\beta}$. The key idea of the experiments is that, by studying the $0\nu\beta\beta$ decay, it is possible to measure its half-life and then estimate $m_{\beta\beta}$.

The sensitivity of a given experiment is expressed by a "detection factor of merit" $S^{0\nu}$, defined as the process half-life corresponding to the maximum signal

isotope	$T^{0\nu}_{1/2}$ [10^{25} yr]	$S^{0\nu}$ [10^{25} yr]	$m_{\beta\beta}$ [eV]	experiment
^{76}Ge	9	11	0.11–0.26	GERDA [6, 7]
^{76}Ge	2.7	4.8	0.24–0.52	Majorana [8]
^{130}Te	1.5	0.7	0.11–0.52	CUORE [9]
^{136}Xe	1.8	3.7	0.15–0.40	EXO-200 [10]
^{136}Xe	10.7	5.6	0.061–0.165	KamLAND-Zen [11]

Table 1: Comparison of results from different $0\nu\beta\beta$ decay experiments reporting lower half-life limits $T^{0\nu}_{1/2}$, sensitivities $S^{0\nu}$ (both at 90% C.L.) and corresponding upper Majorana neutrino mass $m_{\beta\beta}$ limits.

that could be hidden by the background fluctuations and is given by:

$$S^{0\nu} = \frac{\ln 2 \cdot N_A \cdot \epsilon \cdot f_{ab}}{m_A} \cdot \frac{1}{n_\sigma} \cdot \sqrt{\frac{M \cdot T}{\mathrm{BI} \cdot \Delta E}} \,. \tag{5}$$

This formula emphasizes the role of the experimental parameters needed in the search of the decay: the detection efficiency ϵ, the isotopic abundance f_{ab} of the double β emitter, the target mass M, the experimental live-time T, the background index BI and the energy resolution ΔE.

Of particular interest is the case in which BI is so low that the expected number of background events is less than one count within the energy region of interest and a given exposure: this is called "background-free" condition. Next generation experiments aim for having this condition. The first Phase II data [12] showed that GERDA is the first background-free experiment in the field, since it will remain in this condition up to its design exposure. The advantage of this condition is that the sensitivity $S^{0\nu}$ grows linearly with the experimental mass and time, instead of by square root like in Eq. (5).

The most recent results on $0\nu\beta\beta$ decay, including half-life lower limits, sensitivities and upper limit ranges on the effective Majorana neutrino mass $m_{\beta\beta}$ (evaluated with the commonly used PSF and NME calculations) are listed in Tab. 1.

This paper presents the results of the GERDA last data release of June 2018 [6, 7]. With these results GERDA exceeded $0\nu\beta\beta$ decay half-life sensitivity of 10^{26} yr (90% C.L.), as shown in Tab. 1.

3 The GERDA experiment

The GERDA experiment [13] is located at the underground Laboratori Nazionali del Gran Sasso (LNGS) of INFN in Italy. A rock overburden of about 3500 m water equivalent removes the hadronic components of cosmic ray showers and reduces the muon flux at the experiment.

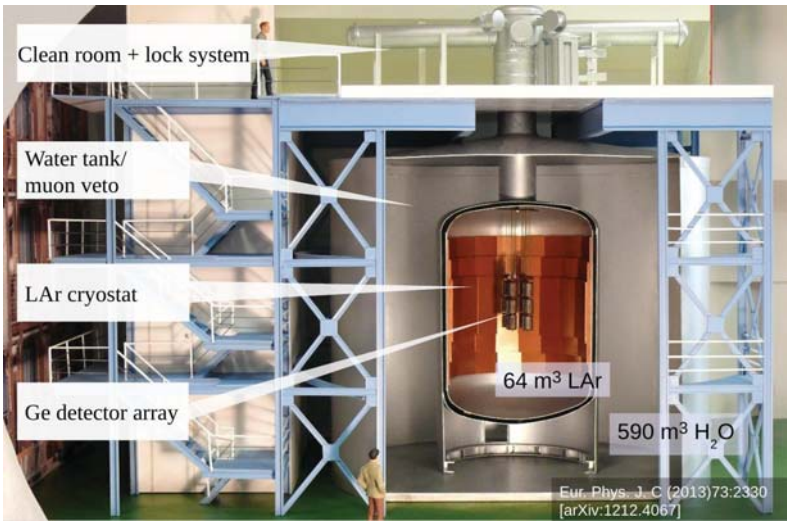

Figure 1: View of the GERDA experiment [13]. The germanium detector array is inserted in the LAr cryostat with an internal copper shield, all is surrounded by a water tank housing the Cherenkov muon veto.

The GERDA setup, illustrated in Fig. 1, has been designed to minimize the main background sources which affected the previous generation experiments. The shielding concept follows a multi-layer approach. High Purity Germanium (HPGe) detectors enriched to about 87% in the double beta emitter ^{76}Ge are operated bare in liquid argon (LAr), being both source and detector of $0\nu\beta\beta$ decay. The argon cryostat is complemented by a water tank with 10 m diameter which further shields from neutron and γ backgrounds and also works as muon veto.

A first physics data taking campaign (Phase I) was carried out from November 2011 to June 2013 and the data showed no indication of a $0\nu\beta\beta$ decay signal [14]. The background index achieved at the Q-value of the ^{76}Ge $0\nu\beta\beta$ decay ($Q_{\beta\beta} = 2039$ keV) was 10^{-2} counts/(keV·kg·yr) with an exposure of 21.8 keV·yr.

4 Upgrade to Phase II

After the completion of Phase I, the GERDA setup has been upgraded to perform its next step (Phase II) [15]: the goal was the tenfold reduction of the background with simultaneous increase of the enriched Ge detector mass.

Thirty Broad Energy Germanium (BEGe) detectors from Canberra [16] were produced for Phase II. The two main advantages of these detectors are their op-

timal energy resolution, due to the very low input capacitance ($\sim$ pF), and the powerful pulse shape discrimination (PSD). This is thanks to the particular shape and configuration of the p^+ and n^+ contacts that produce a highly non-uniform electrical field.

In addition, an active suppression of the background by detecting the LAr scintillation light has been introduced [17]. The LAr veto consists of PMTs and wavelength shifting fibers coupled to SiPMs. 16 PMTs (placed above and below the Ge detector array) collect the light from a LAr volume of 220 cm height and 49 cm diameter surrounding the Ge detectors. The curtain of wavelength shifting fibers encloses the middle 100 cm length of this volume and can collect light also outside the diameter of the cylinder. An event is vetoed if a scintillation signal with amplitude above threshold is found in a narrow time window around the Ge pulse. The threshold and time window is optimized channel-by-channel. Accidental coincidences between the LAr veto system and the detectors create a dead time of $(2.3 \pm 0.1)\%$.

In Fig. 2 the core of the Phase II setup is shown: the Ge detector array is at the center of the instrumented LAr volume. The design allows to assemble both the detector array and the surrounding LAr veto system under dry nitrogen atmosphere and to lower both systems together into the cryostat.

Also the detectors holders, contacts and front-end electronics [18] have been redesigned for Phase II to minimize the mass and improve the radio-purity of the materials close to the detector array.

The Phase II detector array consists of 40 HPGe detectors, arranged in 7 strings: 7 enriched coaxial detectors with a total mass of 15.6 kg, 3 coaxial detectors of natural isotopic abundance from Phase I and 30 enriched BEGe detectors with a mass of 20 kg. The total enriched Ge mass available for the $0\nu\beta\beta$ decay analysis in Phase II is 35.6 kg (enriched coaxial and BEGe detectors).

On December 20th, 2015 the Phase II data taking started with all the detectors.

5 Data taking and performance

The signals from the Ge detectors are amplified by low radioactivity charge-sensitive preamplifiers [18] operated 35 cm above the top of the detector array in the LAr. The signals are led via 10 m long coaxial cables to the outside of the lock where they are digitized. The digital signal processing of the traces is performed within a dedicated software framework [20] and the energy deposited in the Ge detectors is reconstructed using a run-by-run optimized cusp-like filter [21, 22].

The calibration of the energy scale and the evaluation of the detector resolution is performed by lowering three ^{228}Th sources of low neutron emission with an activity on the order of 10 kBq into the cryostat. The stability of the energy scale is monitored using the test pulses injected every 20 s in the detector preamplifiers

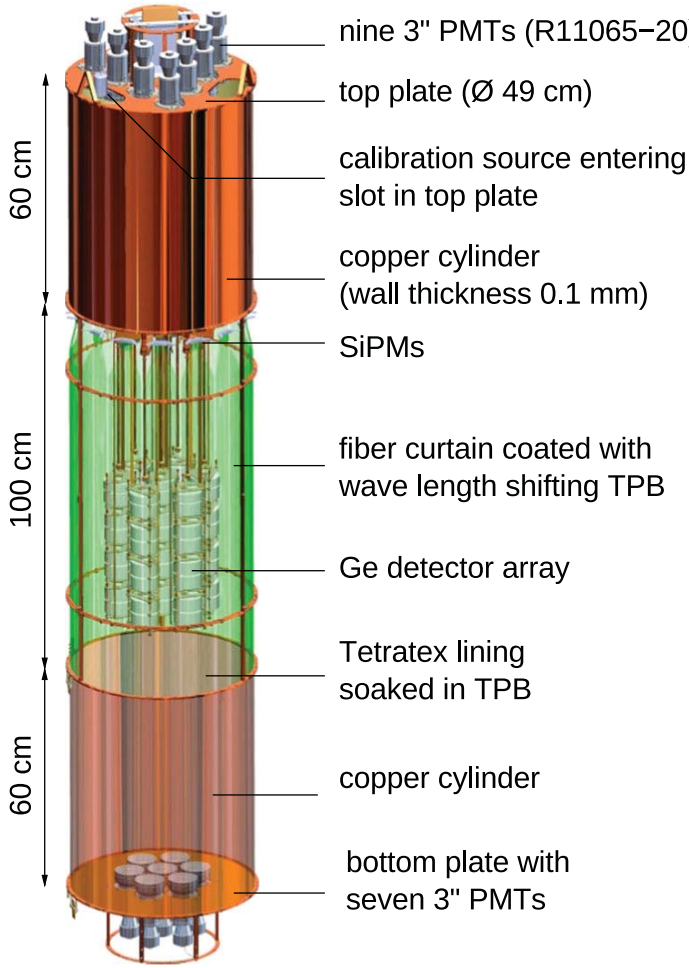

Figure 2: GERDA Phase II assembly of detector array and LAr veto system [15].

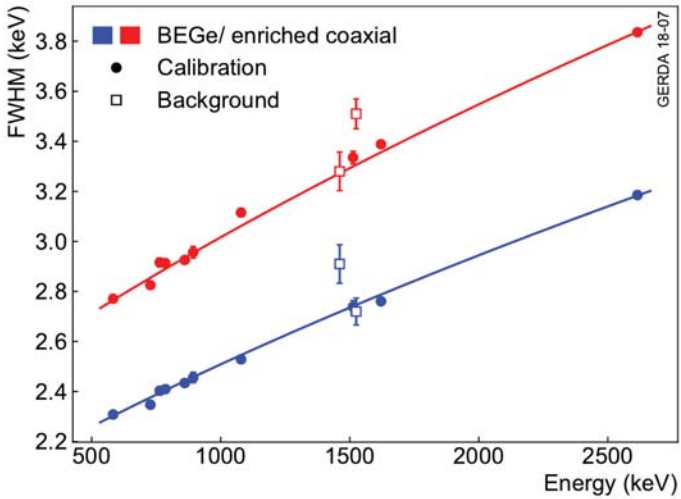

Figure 3: Phase II energy resolution for all BEGe (in blue) and coaxial (in red) detectors as a function of energy from calibration and background data [7].

between successive calibrations. During stable periods, shifts are typically smaller than 1 keV.

During Phase II the average duty cycle is 92.9%, mostly due to calibrations and hardware adjustments. Only data recorded in stable conditions are used for physics analysis, corresponding to 80.4% of the total data. In addition a set of quality cuts provide the rejection of the signals originating from electrical discharges in the high voltage line or bursts of noise.

The energy resolution at $Q_{\beta\beta}$ is extracted from the summed spectrum of all calibrations for individual detectors, then combined according to the exposure contribution in the final physics data s et. The resolution evaluated from calibrations is compared with the average resolutions of the strongest γ-lines in physics data from ^{40}K (at 1461 keV) and ^{42}K (at 1525 keV). The energy resolutions obtained for BEGe and coaxial detectors are shown in Fig. 3. The estimated effective resolution at $Q_{\beta\beta}$ in terms of FWHM is 3.0(1) keV for the BEGe data set and 3.6(1) keV for the coaxial data set.

6 Background and LAr veto

In Fig. 4 the Phase II energy spectra for BEGe and coaxial detectors are shown. Prior to the application of the LAr veto and the pulse shape discrimination (white

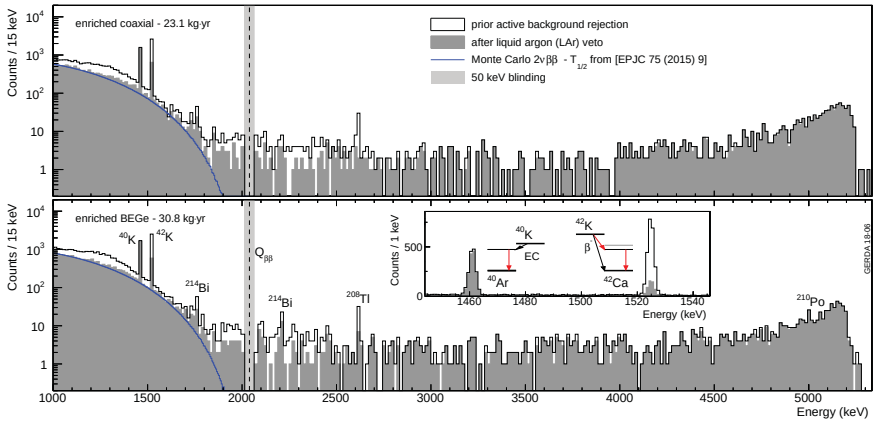

Figure 4: GERDA Phase II energy spectra for enriched coaxial (top panel) and BEGe (bottom panel) detectors with and without the application of the LAr veto. Main contributions to the spectra are labeled. The inset displays the action of the LAr veto cut for the γ-lines from ^{40}K and ^{42}K. In blue the predicted $2\nu\beta\beta$ decay spectrum [23] is shown. The energy region of 50 keV around $Q_{\beta\beta}$ is blinded.

spectra in Fig. 4), the events are rejected if a muon trigger occurs within 10 μs or signals are detected simultaneously in multiple detectors.

In the energy region up to 1700 keV of the background spectra, the events are mostly coming from the spectrum of the $2\nu\beta\beta$ decay. The high energy region ($>$ 3000 keV) shows events coming from ^{210}Po α contamination. At 1461 keV and 1525 keV the γ-lines from ^{40}K and ^{42}K respectively are visible, they are the most intense lines of the spectrum. Minor γ-lines from ^{214}Bi and ^{208}Tl are also visible. The predicted $2\nu\beta\beta$ decay spectrum of the ^{76}Ge using the Phase I result with an half-life of $(1.926 \pm 0.094) \cdot 10^{21}$ yr [23] is also shown Fig. 4.

The LAr veto, as shown in the inset of Fig. 4, suppresses by a factor $\sim$ 5 the ^{42}K line at 1525 keV, due to the β particle depositing energy in the LAr. The Compton continuum below the ^{40}K line is efficiently rejected by the LAr veto, indeed the spectrum up to 1700 keV is an almost pure $2\nu\beta\beta$ decay spectrum as indicated by the overlay with the predicted $2\nu\beta\beta$ decay spectrum.

7 Pulse shape discrimination

The GERDA background is further reduced by applying the pulse shape discrimination (PSD) cut, based on techniques adopted in Phase I [24] with improvements. Due to the different geometry and electric field configuration, BEGe and coaxial

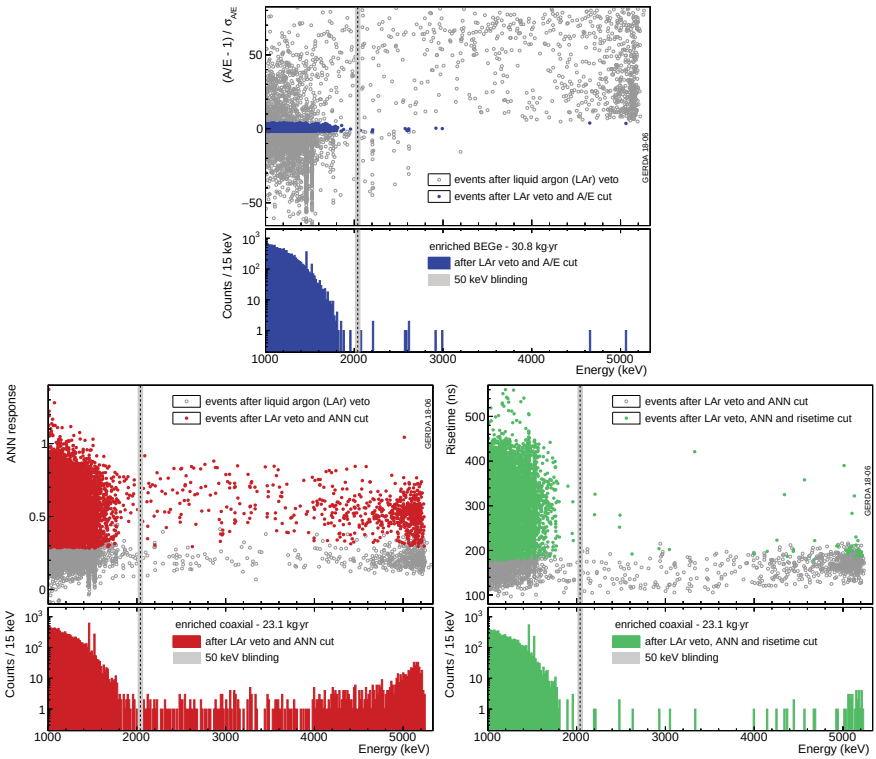

Figure 5: PSD cuts as a function of energy after LAr veto from the three different techniques: in blue (top panel) the events from BEGe detectors surviving the A/E cut, in red (bottom left) the events from the coaxial detectors surviving the neural network cut and in green (bottom right) the events from the coaxial detectors surviving both the neural network and the risetime cuts.

detectors need distinct PSD techniques.

For BEGe detectors the discrimination is based on the ratio between the peak amplitude of the current signal A and the total energy E (A/E parameter). Low values of A/E are typical for multi-site events due to γ-rays and β decays on the detector n^+ contacts, high A/E values are from surface events due to α on p^+ contacts. The results of the PSD in the BEGe data set are reported in Fig. 5 (top panel): the events survived the A/E cut are indicated in blue. The average survival probability of a $0\nu\beta\beta$ decay event is $(87.6 \pm 2.5)\%$, estimated from ^{208}Tl double escape peak events.

For the coaxial detectors the discrimination between single-site and multi-site events is based on an artificial neural network (ANN) [24]. The survival fraction of a $0\nu\beta\beta$ decay event is in this case $(84 \pm 5)\%$, estimated using pulse shape simulations and $2\nu\beta\beta$ decay events. Additionally, a new cut is applied on the risetime of the pulses to reject fast signals from surface events due α decays near the p^+ electrode and in the groove. In this case the survival probability of a $0\nu\beta\beta$ decay event is $(84.7 \pm 1.4)\%$. The combined PSD efficiency for coaxial detectors is $(71.2 \pm 4.3)\%$. The events surviving the neural network cut and the events surviving both the neural network and the risetime cuts are shown in the bottom panels of Fig. 5 in red and green respectively.

8 $0\nu\beta\beta$ decay analysis

Since the beginning of Phase I, GERDA has adopted a blind analysis strategy to ensure an unbiased search for $0\nu\beta\beta$ decay. An energy region of 50 keV around $Q_{\beta\beta}$ is removed from the data stream until all the analysis parameters are finalized.

The relevant parameters for the data sets used in the new analysis are listed in Tab. 2. Data from Phase I and from the first part of Phase II have been already reported in previous data releases [14, 12, 19]. Coaxial detector data from Phase II are split into two data sets because the new PSD method provides a significantly lower background level. The new analysis includes addional 23.1 kg·yr of coaxial detector data (”PhaseII Coax2”) and 18.2 kgyr of BEGe detector data (part of ”PhaseII BEGe”). The total available enriched Ge exposure is 82.4 kg·yr.

The analysis window is from 1930 keV to 2190 keV without the intervals (2104 ± 5) keV and (2119 ± 5) keV of known γ-lines. The final spectra in the analysis region are shown in Fig. 6: the top panel shows the new coaxial detector data (23.1 kg·yr) and the bottom panel shows the Phase II BEGe detector data (30.8 kg·yr).

For the coaxial detectors only three events survived all the cuts while in the BEGe data set five events remain. The background index achieved is $5.7^{+4.1}_{-2.6} \cdot 10^{-4}$ cts/(keV·kg·yr) for coaxial and $5.6^{+3.4}_{-2.4} \cdot 10^{-4}$ cts/(keV·kg·yr) for BEGe de-

Table 2: List of datasets used in the new $0\nu\beta\beta$ decay analysis [12]: exposures (for total mass), energy resolutions in FWHM, efficiencies (including enrichment, active mass, reconstruction efficiencies and dead times) and background indices (BI) in the analysis window.

data sets	esposure [kg·yr]	FWHM [keV]	efficiency	background [cts/(keV·kg·yr)]
Phase I golden	17.9	4.3 (1)	0.58 (4)	$11 \pm 2 \cdot 10^{-3}$
Phase I silver	1.3	4.3 (1)	0.58 (4)	$30 \pm 10 \cdot 10^{-3}$
Phase I BEGe	2.4	2.7 (2)	0.66 (2)	$5^{+4}_{-3} \cdot 10^{-3}$
Phase I extra	1.9	4.2 (2)	0.57 (3)	$5^{+4}_{-3} \cdot 10^{-3}$
Phase II Coax-1	5.0	3.6 (1)	0.52 (4)	$3.5^{+2.1}_{-1.5} \cdot 10^{-3}$
Phase II Coax-2	23.1	3.6 (1)	0.48 (4)	$0.6^{+0.4}_{-0.3} \cdot 10^{-3}$
Phase II BEGe	30.8	3.0 (1)	0.60 (2)	$0.6^{+0.4}_{-0.2} \cdot 10^{-3}$

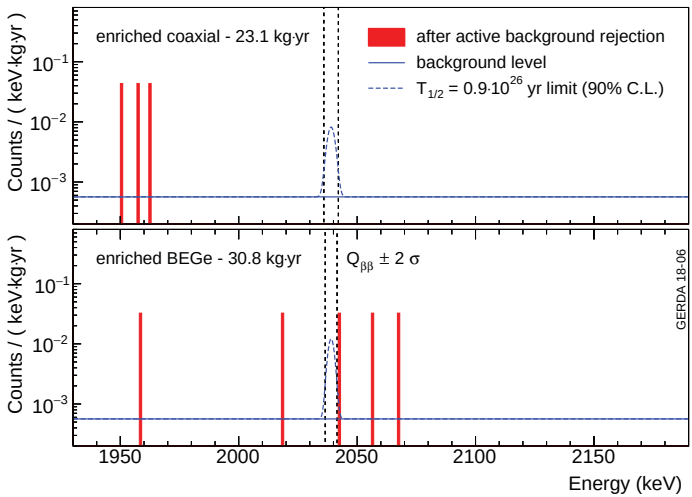

Figure 6: Events observed in the analysis window for coaxial (top) and BEGe (bottom) detectors. The blue lines show fitted background level and the 90% C.L. limit on $0\nu\beta\beta$ decay of $0.9 \cdot 10^{26}$ yr from the likelihood analysis of all GERDA data sets.

tectors. With this result GERDA reaches the lowest background ever achieved in the field, taking into account the energy resolution, and will remain in the background-free condition for all Phase II.

Both a Frequentist and a Bayesian analysis [12] based on an unbinned extended likelihood function were performed combining Phase I and Phase II data. The fit function for every data set corresponds to a flat distribution for the background (one free parameter per set) and a Gaussian centered at $Q_{\beta\beta}$ for a possible signal having width corresponding to the resolutions listed in Tab. 2.

In the Frequentist analysis the best fit yielded no $0\nu\beta\beta$ decay signal, setting a 90% C.L. limit on the ^{76}Ge $0\nu\beta\beta$ decay half-life of:

$$T_{1/2}^{0\nu} > 0.9 \cdot 10^{26} \text{ yr} \tag{6}$$

with a median sensitivity of $1.1 \cdot 10^{26}$ yr (90% C.L.), thus making GERDA the first experiment to surpass 10^{26} yr sensitivity. The probability to obtain a limit stronger than the actual one in an ensemble of repeated experiments with null signal is 63%.

The Bayesian fit for a prior flat in $1/T$ yields a limit of $T_{1/2}^{0\nu} > 0.8 \cdot 10^{26}$ yr (90% C.I.) with a sensitivity assuming no signal of $0.8 \cdot 10^{26}$ yr (90% C.I.). In the Bayesian framework the probability to obtain a stronger limit is 59%.

The fact that the actual $T_{1/2}^{0\nu}$ limit is weaker than the median sensitivity is due to the presence of an event close to $Q_{\beta\beta}$ in the Phase II BEGe data set (Fig. 6 bottom) with energy of 2042.1 keV 2.4 σ away from the $Q_{\beta\beta}$.

9 Conclusions

The new data from Phase II confirmed the high quality of the GERDA design and the effectiveness of background suppression techniques, consisting of the powerful pulse shape discrimination and the detection of the argon scintillation light. GERDA is a background-free experiment and, with an exposure of 82.4 kg·yr, reports a background index of $6 \cdot 10^{-4}$ cts/(keV·kg·yr).

GERDA continues to collect data and is projected to reach a sensitivity on the half-life beyond 10^{26} yr with the design exposure of 100 kg·yr.

Based on the success of GERDA and MAJORANA [8] experiments, the search for $0\nu\beta\beta$ decay in ^{76}Ge will be continued in the next years by the LEGEND-200 experiment [25], that aims to reach a sensitivity up to 10^{27} yr using 200 kg of enriched HPGe detectors. The preparation of this experiment, that will take place at LNGS on the GERDA site, already started.

References

[1] Davidson S., Nardi E., Nir Y., Leptogenesis, Phys. Rep. 466, 105177 (2008)

[2] Mohapatra R. N., Smirnov A. Y., Neutrino mass and new physics, Annu. Rev. Nucl. Part. Sci. 56, 569628 (2006)

[3] Doi M. et al., Neutrino Mass, the Right-Handed Interaction and the Double Beta Decay I, Progr. Theor. Phys. 66(5) 1739-64 (1981)

[4] Barea J. et al., Nuclear matrix elements for double beta decay, Phys. Rev. C 87 014315 (2013)

[5] Pontecorvo B., Zh.Eks Teor.Fiz., 33, 549 (1957)

[6] Zsigmond A.J. (for the GERDA Collaboration), New results from GERDA Phase II, Neutrino 2018, Heidelberg (Germany)

[7] GERDA Collaboration, Probing degenerate Majorana neutrino masses (to be published)

[8] Guiseppe V. (for the MAJORANA Collaboration), New Results from the MAJORANA Demonstrator Experiment, Neutrino 2018, Heidelberg (Germany)

[9] CUORE Collaboration, First Results from CUORE: A Search for Lepton Number Violation via $0\nu\beta\beta$ Decay of ^{130}Te, Phys. Rev. Lett. 120 132501 (2018)

[10] Albert J.B. et al., Search for Neutrinoless Double-Beta Decay with the Upgraded EXO-200 Detector, Phys. Rev. Lett. 120, 072701 (2018)

[11] KamLAND-Zen Collaboration, Search for Majorana Neutrinos near the Inverted Mass Hierarchy Region with KamLAND-Zen, Phys. Rev. Lett. 117 082503 (2016)

[12] GERDA Collaboration, Background-free search for neutrinoless double-β decay of ^{76}Ge with GERDA, Nature 544 7648 (2017)

[13] GERDA Collaboration, The GERDA experiment for the search of $0\nu\beta\beta$ decay in ^{76}Ge, Eur. Phys. J. C 73 2330 (2013)

[14] GERDA Collaboration, Results on neutrinoless double beta decay of ^{76}Ge from GERDA Phase I, Phys. Rev. Lett. 111, 122503 (2013)

[15] GERDA Collaboration, Upgrade for Phase II of the GERDA experiment, Eur. Phys. J 78 388 (2018)

[16] GERDA Collaboration, Production, characterization and operation of ^{76}Ge enriched BEGe detectors in GERDA, Eur. Phys. J. C 75 39 (2015)

[17] Agostini M. et al., LArGe - Active background suppression using argon scintillation for the GERDA $0\nu\beta\beta$-experiment, Eur. Phys. J. C 75 506 (2015)

[18] Riboldi S. et al., Cryogenic readout techniques for Germanium detectors, ANIMMA 2015, Lisbon (Portugal), pp. 1-6

[19] GERDA Collaboration, Improved limit on neutrinoless double-β decay of ^{76}Ge from GERDA Phase II, Phys. Rev. Lett. 120 132503 (2018)

[20] Agostini M. et al., GELATIO: a general framework for modular digital analysis of high-purity Ge detector signals, JINST 6 P08013 (2011)

[21] GERDA Collaboration, Improvement of the Energy Resolution via an Optimized Digital Signal Processing in GERDA Phase I, Eur. Phys. J. C 75 255 (2015)

[22] D'Andrea V., Improvement of performances and background studies in GERDA Phase II, PhD Thesis (2017)

[23] GERDA Collaboration, Results on $\beta\beta$ decay with emission of two neutrinos or Majorons in ^{76}Ge from GERDA Phase I, Eur. Phys. J. C 75 416 (2015)

[24] GERDA Collaboration, Pulse shape discrimination for GERDA Phase I data, Eur. Phys. J. C 73 2583 (2013)

[25] LEGEND Collaboration, The large enriched germanium experiment for neutrinoless double beta decay (LEGEND), AIP Conf. Proc. 1894, 020027 (2017)

COHERENT Experiment at the Spallation Neutrino Source

Yuri Efremenko, on behalf of the COHERENT collaboration

1 Introduction

Coherent elastic neutrino-nucleus scattering (CEvNS) was predicted in 1974 as a consequence of the neutral weak current [1, 2]. Although the cross section is large compared to other neutrino-matter interactions in the $\lesssim 100\,\mathrm{MeV}$ energy range, this standard model (SM) process took a long time to be observed due to the daunting technical requirements: very low nuclear recoil energy thresholds, intense sources/large target masses, and low backgrounds [3]. Employing state-of-the-art low-energy-threshold detector technology coupled with the intense stopped-pion neutrino source [4] available at the Spallation Neutron Source (SNS) at Oak Ridge National Laboratory (ORNL), the COHERENT Collaboration made the first measurement of CEvNS [5] in 2017. This first measurement, which used a 14.6 kg CsI detector, tested the SM with a precision of ~30 %. Even this rather large uncertainty was sufficient to produce consequential constraints on new physics [5–9].

Forthcoming CEvNS measurements on multiple targets and with increased precision is motivated by physics of interest to a diverse community. A first goal is a test of the SM prediction of proportionality of the CEvNS cross section to neutron number squared, N^2. A precision cross section measurement on multiple targets will test for non-standard neutrino interactions (NSI), for which the interaction depends on the quark makeup of the nucleus [4, 10, 11]. Additional beyond-the-standard-model tests are possible. First constraints have already been made with the CsI[Na] measurement [5–9] and future possibilities are described as well in reference [11]. We can also perform systematic characterizations of low-threshold recoil detectors with neutrinos to validate experimental background and detector-response models, given that CEvNS of solar and atmospheric neutrinos is an irreducible background for dark matter WIMP (Weakly Interacting Massive Particle) searches [12]. In the long term, low-energy neutrino-scattering-based measurements of nuclear neutron distributions will be competitive with other methods.

The COHERENT collaboration plans CEvNS measurements in three additional targets spanning a range of N values in the next few years: a 610 kg single-phase liquid argon detector, a 3 t NaI array, and 14.4 kg of Ge crystals. Prototypes of two of these are already deployed at the SNS – a 22 kg liquid argon detector, and a 185 kg NaI detector. First results from the argon detector are expected soon.

In order to move to an era of precision CEvNS studies, we need to reduce experimental uncertainties on several fronts. In part, we aim to reduce the global 10 % uncertainty on the stopped-pion neutrino flux normalization at the SNS by deploying a tonne-scale heavy water detector to measure $\nu_e - d$ interactions. The cross section for this interaction is the only one of reasonable magnitude in this energy range known to the few-% level (besides inverse beta decay, which cannot be used due to lack of $\bar{\nu}_e$ at the SNS).

Furthermore, the CEvNS process has one of the largest cross sections relevant for supernova dynamics and plays a significant role in core-collapse processes [13–15]; measurements will therefore validate models of core-collapse supernovae. Dark-matter detectors will also be able to detect CEvNS interactions in the event of a nearby core-collapse supernova burst [16, 17], which will be sensitive to the full flavor content of the supernova signal.

In addition, non-CEvNS interaction measurements including inelastic neutrino interactions on Ar, NaI, and ^{16}O, as well as neutrino-induced-neutron production cross sections in shielding materials, will also have important scientific impact, due to their relevance for supernova neutrinos. In particular, neutrino-argon cross sections have never been measured in this energy range, and have direct relevance for the supernova neutrino sensitivity of the Deep Underground Neutrino Experiment (DUNE). These measurements also have the potential to test weak interaction physics.

2 The Spallation Neutron Source

The Spallation Neutron Source (SNS) located at the Oak Ridge National Laboratory (ORNL) is the world's premier facility for neutron-scattering research, producing pulsed neutron beams with intensities an order

of magnitude larger than any currently-operating facility. At full beam power, approximately 1.5×10^{14} 1.0 GeV protons bombard the liquid mercury target in short 600 ns wide bursts with a rate of 60 Hz. Neutrons produced in spallation reactions with the mercury target thermalize in cryogenic moderators surrounding the target and are delivered to neutron-scattering instruments in the SNS experiment hall. The SNS is a user facility and operates approximately 2/3 of the year.

As a byproduct, the SNS also provides the world's most intense pulsed source of neutrinos in an energy region of specific interest for particle and nuclear astrophysics. Interactions of the proton beam in the mercury target produce π^+ and π^- in addition to neutrons. These pions quickly stop inside the dense mercury target. Most of π^- are absorbed. Contrary π^+ in the subsequent decay chain produces neutrinos of 3 flavors as shown in Fig. 1. The production of electron anti neutrinos, which is a result of π^- decays in flight, is suppressed by four orders of magnitude relative to other species.

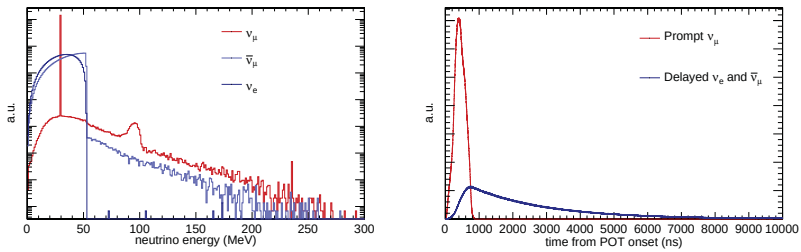

(a) (b)

Figure 1: (a) The expected ν spectrum for 1.0 GeV protons at the SNS, showing the very low level of decay-in-flight flux and ν from μ-capture, in arbitrary units. The total neutrino flux is $4.2 \times 10^7\ \nu/\mathrm{cm}^2/\mathrm{s}$ at 20 m. (b) The distinct time structure for prompt and delayed neutrinos is due to the short 600 ns proton beam spills. "Prompt" neutrinos arise from pion decay, and "delayed" neutrinos arise from muon decay.

The sharp SNS beam timing structure is highly beneficial for background rejection and precise characterization of those backgrounds not associated with the beam [18]. Looking for neutrino signals only in the 10 µs window after a beam spill imposes a factor-of-2000 reduction in the steady-state background.

An SNS neutrino flux simulation has been developed using Geant4.10.1 [19]. Using this code, a beam of protons, with tunable energy, impinges upon a liquid mercury target. For the baseline simulation, a simplified version of the SNS target geometry was implemented, which does not affect simulation results. The resulting energy spectrum (Fig. 1) clearly shows three neutrino flavors ultimately originating from π^+ decays at rest (below 53 MeV), as well as a long, high-energy tail originating from π^+ decays in flight. The exact shape of this tail depends on the detector orientation relative to the incoming proton beam. The timing plot shows a clear differentiation of prompt neutrinos created in π^+ decay from delayed neutrinos created in μ^+ decay with a characteristic lifetime of 2.2 µs.

The simulated neutrino spectra and time distributions for different Geant4 physics lists were compared; good agreement was found between the "QGSP_BERT" and "QGSP_INCLXX" physics lists. The flux prediction corresponding to QGSP_BERT is used for the signal predictions shown here. See the supplemental materials of Ref. [5] for more details.

The results of the simulations show that the contributions to the neutrino spectrum from decay-in-flight π^+ and μ-capture are expected to be very small (Fig. 1). The contribution to the CEvNS signal from these high-energy neutrinos ($E > 50$ MeV) is $< 1\,\%$.

Our present knowledge of the neutrino flux at the SNS is based solely on simulations. Comparison between different models gives an overall neutrino-flux uncertainty estimate of 10 % [5], arising from uncertainties on the charged-pion production rate and pion interactions cross section with mercury. Our present knowledge of neutrino flux at the SNS is a limiting factor on systematics for studies of CEvNS and charged-current interactions. Improvements to our neutrino-flux knowledge are required for accurate studies of CEvNS and

supernova-related neutrino reactions at the SNS.

A stopped-pion beam has several advantages for CEvNS detection relative to reactor-based experiments. First, the relatively high energies enhance the cross section ($\propto E^2$) while still benefiting from coherence; cross sections at stopped-pion energies (up to 50 MeV) are about two orders of magnitude higher than at reactor energies (~3 MeV). Second, recoil energies (few to tens of keV) bring detection of CEvNS within easy reach of the current low-threshold detectors. The pulsed beam structure leads to significant suppression of steady-state backgrounds and the ability to measure signal and backgrounds at almost the same time, without shutting down the facility.

3 Neutrino Alley at the SNS

The COHERENT Collaboration is planing to deploy four detector subsystems for accurate studyes of CEvNS, each containing different target nuclei, spanning a range of neutron number, N. The current deployments are summarized in Tab. 1, and the anticipated upgraded future detectors are described in Tab. 2. The timing resolution of all four detector subsystems is sufficient to allow the observation of the characteristic 2.2 µs lifetime of muon-decay neutrinos, a further cross-check that any interactions are due to neutrinos from the SNS. The technologies are mature and all are presently used for direct dark-matter detection or other low-threshold experiments.

Nuclear target	Technology	Mass (kg)	Distance from source (m)	Recoil threshold (keVnr)
CsI[Na]	Scintillating crystal	14.6	19.3	9
LAr	Single-phase	22	27.5	20
NaI[Tl]	Scintillating crystal	185	21	13

Table 1: Parameters for the currently-deployed COHERENT CEvNS detector subsystems.

Nuclear target	Technology	Mass (kg)	Distance from source (m)	Recoil threshold (keVnr)
Ge	HPGe PPC	14.4	21	2.5
LAr	Single-phase	612	27.5	20
NaI[Tl]	Scintillating crystal	3388	22	13

Table 2: Parameters for the anticipated COHERENT CEvNS detector subsystems.

Fig. 2 shows the configuration of proposed COHERENT detector systems in Neutrino Alley expected to be deployed starting from 2020. The alley is ideally located 20 m from the target with contiguous intervening shielding materials and overburden eliminating almost all free-streaming pathways for fast neutrons which dominate beam related backgrounds. With significant internal funding at ORNL, the basement utility corridor is now a fully equipped and operating neutrino laboratory including dedicated electrical power and ready access to necessary utilities such as chilled water for cryogenic compressors, plant air for system actuators, facility ventilation for cryogenic boil-off, etc. In addition, ORNL has installed an oxygen monitoring and area alarm system for the safe operation of multiple cryogenic detectors along Neutrino Alley including the CENNS-10 liquid argon detector that has operated almost continuously since November 2016.

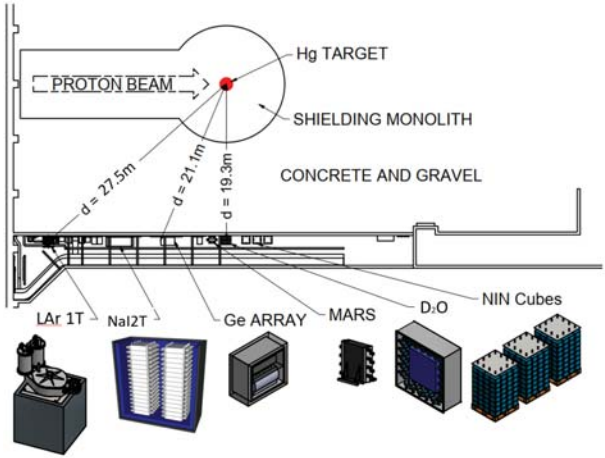

Figure 2: Siting of planned detector systems in Neutrino Alley proposed in this paper and presented in Table 2. The MARS neutron background detector and the Neutrino Induced Neutron (NIN) detectors are also shown.

4 COHERENT Physics

The immediate experimental impacts of the measurements envisioned by COHERENT collaboration include multiple physics topics, related to both CEvNS measurements and to measurements of inelastic charged-current (CC) neutrino interactions. Let us illustrate a few examples.

4.1 Coherent Elastic Neutrino-Nucleus Scattering Physics

The coherence of the CEvNS process results in an enhanced neutrino-nucleus cross section that is approximately proportional to N^2, due to the small weak charge of the proton. The coherence condition, in which the neutrino scatters off all nucleons in a nucleus in phase with each other, requires that the wavelength of the momentum transfer be larger than the size of the target nucleus. The standard-model cross section for CEvNS can be written as [20]:

$$\frac{d\sigma}{dT}_{coh} = \frac{G_F^2 M}{2\pi}\left[(G_V+G_A)^2+(G_V-G_A)^2\left(1-\frac{T}{E_\nu}\right)^2-(G_V^2-G_A^2)\frac{MT}{E_\nu^2}\right] \quad (1)$$

where G_F is the Fermi constant, M is the nuclear mass, T is the recoil energy, E_ν is the neutrino energy. $G_V = (g_V^p Z + g_V^n N)F_{\rm nucl}^V(Q^2)$, $G_A = (g_A^p(Z_+ - Z_-) + g_A^n(N_+ - N_-))F_{\rm nucl}^A(Q^2)$. $g_V^{n,p}$ and $g_A^{n,p}$ are vector and axial-vector coupling factors, respectively, for protons and neutrons, Z and N are the proton and neutron numbers, $Z_\pm$ and $N_\pm$ refer to the number of up or down nucleons, and Q is the momentum transfer [20]. The maximum recoil energy for a given target species and neutrino energy is $T_{\rm max} = \frac{2E_\nu^2}{M+2E_\nu}$. The form factors $F_{\rm nucl}^{A,V}(Q^2)$ are point-like ($F(Q^2)=1$) for interactions of low-energy neutrinos < 10 MeV, but suppress the interaction rate as the wavelength of the momentum transfer becomes comparable to the size of the target nucleus.

Fig. 3 shows the expected CEvNS cross section weighted by stopped-pion neutrino flux as a function of N, with and without form-factor suppression.

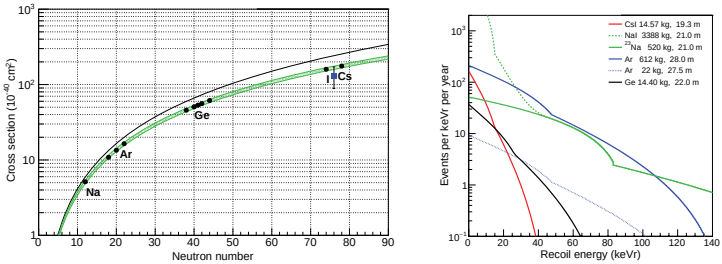

Figure 3: Left: illustration of the $\propto N^2$ proportionality of the stopped-pion-neutrino flux-averaged CEvNS cross section versus neutron number, N. The black line assumes a unity form factor. The green band shows the effect of an assumed form factor. The points show the prediction for proposed COHERENT target materials. The blue square shows cross section inferred from the measurement reported in Ref. [5]. Right: differential recoil rates for the COHERENT suite of detectors at SNS.

COHERENT has made one measurement so far, and measurements with additional targets will result in a clear observation of the N^2 nature of the cross section. The expected precision of the cross section measurements will quickly become dominated by the systematic uncertainty of the knowledge of the nuclear recoil detector thresholds and neutrino flux uncertainties. The expected recoil spectra before detection-efficiency corrections are shown in Fig. 3, right panel. Precision tests of N^2 dependence can unlock access to tests of many BSM phenomena such as non-standard neutrino interactions (NSI), accelerator produced dark matter, measurement of the electroweak angle at low momentum transfer, and search for an anomalous neutrino magnetic moment.

4.1.1 Beyond-the-Standard-Model Physics Searches: NSI

Because the CEvNS cross section is cleanly predicted in the SM, deviations can indicate new physics (e.g., [10, 20–23]). As one example, we consider a new vector coupling in the CEvNS cross section. Possible NSI neutral currents mediated by heavy particles can be parameterized by new flavor-dependent ε couplings. Following [4, 20], under the reasonable assumption that spin-dependent axial contributions are small, the vector couplings $\varepsilon^{qV}_{\alpha\beta} = \varepsilon^{qL}_{\alpha\beta} + \varepsilon^{qR}_{\alpha\beta}$, dominate. The differential cross-section for CEvNS with NSI of neutrinos of flavor α off a nucleus is given by

$$\left(\frac{d\sigma}{dT}\right)_{\nu_\alpha A} = \frac{G_F^2 M}{\pi} F^2(2MT)\left[1 - \frac{MT}{2E_\nu^2}\right] \times \tag{2}$$
$$\{[Z(g_V^p + 2\varepsilon^{uV}_{\alpha\alpha} + \varepsilon^{dV}_{\alpha\alpha}) \quad + N(g_V^n + \varepsilon^{uV}_{\alpha\alpha} + 2\varepsilon^{dV}_{\alpha\alpha})]^2 + \sum_{\alpha\neq\beta} [Z(2\varepsilon^{uV}_{\alpha\beta} + \varepsilon^{dV}_{\alpha\beta}) + N(\varepsilon^{uV}_{\alpha\beta} + 2\varepsilon^{dV}_{\alpha\beta})]^2\},$$

where $g_V^p \sim (\frac{1}{2} - 2\sin^2\theta_W)$, $g_V^n \sim -\frac{1}{2}$ are the SM weak constants (modulo well-understood radiative corrections). The effect of NSI for this type of heavy-mediator model is an *overall scaling* of the CEvNS rate, which can be either a suppression or an enhancement. The ϵ values may be positive or negative, and can conspire to result in the SM rate for given Z, N values.

To provide a concrete example of NSI sensitivity, lets focus on the ε^{uV}_{ee}, ε^{dV}_{ee} parameters. If their values are non-zero, the SM couplings are modified as $G_V = ((g_V^p + 2\varepsilon^{uV}_{ee} + \varepsilon^{dV}_{ee})\, Z + (g_V^n + \varepsilon^{uV}_{ee} + 2\varepsilon^{dV}_{ee})N)\, F^V_{\rm nucl}(Q^2)$. Neutrino-scattering constraints on the magnitude of non-zero values for ε^{qV}_{ee} from CHARM [24] are of order unity. They are shown in Fig. 4, left panel as the shaded grey region[1]. The initial NSI result from COHER-

[1]Note that these constraints are valid only for heavy mediators [11].

ENT [5] for these two parameters, ε_{ee}^{uV} and ε_{ee}^{dV} (assuming all other ε parameters are zero) is shown in Fig. 4 left panel, as a blue band. Reference [6] shows that the first data-set already constrains the "LMA-Dark" degeneracy, which can confound mass ordering measurements at long-baseline experiments. Sensitivity to NSI parameters can be improved with simultaneous measurements of the CEvNS cross section on different nuclei. The angles of the diagonal-band allowed regions vary slightly between the different isotopes due to different $N : Z$ ratios. With realistic efficiency and background for future COHERENT detectors the expected constraints from a null search for a combination of CsI[Na], Ge, Ar, are shown in Fig. 4 right panel, as superimposed diagonal bands.

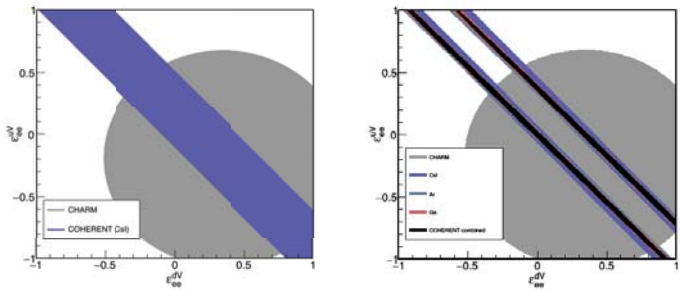

Figure 4: Left panel, result from [5] with initial constraints on two of the NSI ε parameters, showing also the constraint from the CHARM experiment [24]. Right panel, futures sensitivity which can be obtained with the array of COHERENT detectors.

4.1.2 Relevance for Direct Dark Matter Detection Experiments

The CEvNS of solar and atmospheric neutrinos, which produce single-scatter recoils identical to those expected from WIMPs, is recognized as an irreducible background for dark-matter WIMP searches for next-generation dark-matter experiments (neutrino floor) [12, 25–29]. COHERENT can provide detector-specific response information for CEvNS interactions.

4.2 Non-CEvNS Neutrino Interactions

Inelastic charged-current (CC) and neutral-current (NC) interactions in the few tens of MeV regime have never been measured on argon or oxygen. They are relevant especially for supernova neutrino detection. The $^{40}\mathrm{Ar}(\nu_e, e^-)^{40}\mathrm{K}$ cross section is of direct relevance for supernova neutrino detection in DUNE. The future D_2O detector will be sensitive to CC $^{16}\mathrm{O}(\nu_e, e^-)^{16}\mathrm{F}$ on oxygen, from both light-water and heavy-water components (see Sec. 5.1), relevant for Super-K and Hyper-K. We will have those measurements as a by-product of CEvNS studies.

5 Future initiatives

5.1 Heavy Water Detector

The ~10 % uncertainty on the SNS neutrino flux is already one of the dominant systematics for precision studies of CEvNS. The future plan is to address this with a heavy water detector, taking advantage of the fact that the theoretical uncertainty for the charged-current $\nu_e + d \to p + p + e^-$ reaction is on the order of (2-3) % [30–32]. The SNS produces primarily pion decay-at-rest neutrinos, and the three neutrino flavors

from decay of positive pions and muons are produced in equal quantities. Therefor calibration of the ν_e flux is enough to measure the total neutrino flux. A small admixture of decay-in-flight neutrinos is present at the 1 % level, but these are mostly forward-peaked, away from the Neutrino Alley. COHERENT is going to propose to deploy a 1-ton D_2O flux-calibration detector. The improvement in flux uncertainty will improve the precision of all COHERENT analyses. In addition to flux normalization, such a detector can also measure CC interactions on ^{16}O, of relevance to supernova neutrinos for Super-K and Hyper-K [33].

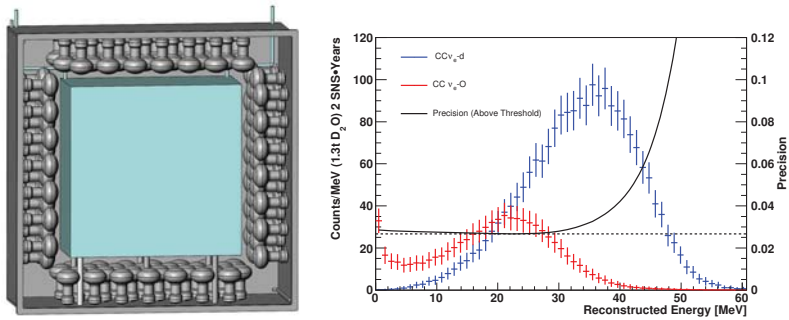

Figure 5: Left, heavy water detector concept for neutrino alley. Right, performance summary of the heavy water detector for two SNS-years for a detector located 20 m from the neutrino source. The statistical precision of the background subtracted measurement integrated above threshold is shown in the black curve. For flux normalization we will use events with energy deposition above 35 MeV where contribution from interaction on oxygen is negligible.

The possible detector concept is shown in the left panel of Fig. 5. Space constraints have driven the design to be asymmetric. A highly transparent acrylic vessel placed inside a steel tank of light water creates a well-defined fiducial mass of heavy water. Cherenkov light emitted by the produced electrons will be collected by photomultiplier tubes arranged on four sides of the outer vessel and within the light water. The 10 cm gap of regular water and acrylic vessel walls will serve as a "tail catcher" and allow complete integration of energy for electrons escaping from the heavy water volume. Teflon reflector panels will cover the remaining two sides.

An initial Geant4 simulation has been implemented to prove the detector concept. The model includes light attenuation and scattering by the acrylic inner vessel with a 1 inch thickness. The proposed design will provide 18 % energy resolution at 50 MeV over the entire fiducial volume. The reconstructed energy distribution of electrons from the charged-current ν_e-d interactions is shown in the right panel of Fig. 5, yielding 2100 counts in two SNS-years. The dominant interaction producing electrons of comparable energy is the charged-current interaction on oxygen which occurs in both the heavy water inner tank and the light water outer tank. Cherenkov light from these interactions has also been modeled Fig. 5, right panel. We find that a statistical precision of 2.6 % can be reached in two years, considering the dominant competing CC ν_e-O interaction in a simple counting analysis. The SNS time structure will significantly suppress all steady state backgrounds. For energy calibration we will use Michel electrons from the decay of stopped cosmic muons which are easily identified.

5.2 Tonne-Scale Argon

The design of the proposed tonne-scale detector and associated shielding will be guided by our ongoing measurements of CENNS-10 performance and backgrounds. The preliminary design, shown in Fig. 6, has been designed to fit into Neutrino Alley with Pb/H_2O shielding at the location of the existing CENNS-10 detector, 27.5 m from the SNS target providing ~3000 CEvNS events year.

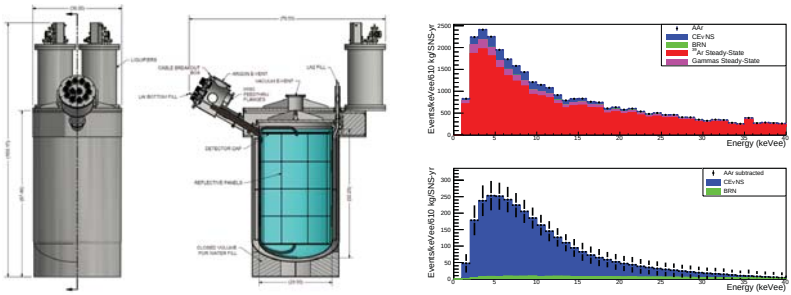

Figure 6: Left, detector layout. Two pulse-tube cryocoolers rest on top of the main liquid volume, and an instrumentation feedthrough protrudes from the side of the main volume. Right, expected detector performance. Top: Total event rate versus energy. The steady-state background is dominated by the ^{39}Ar (red). Bottom: Expected rates after subtraction of the steady-state backgrounds. The remaining background after performing the subtraction is the beam-related neutrons (BRN).

The 750 kg LAr volume will be contained in a cryostat. A TPB-coated teflon cylindrical part converts the short-wavelength primary scintillation light to visible light. This provides a reliable means of light transport, as already demonstrated by the success of CENNS-10.

The expected CEvNS signal and sources of background for the tonne-scale LAr detector are informed by CENNS-10 data. The steady-state backgrounds can be very precisely measured and subtracted from the beam-related CEvNS signal. The dominant steady rate background is from the $1\,\mathrm{Bq\,kg^{-1}}$ of ^{39}Ar with a β-decay that overlaps substantially with the CEvNS recoil spectrum. The expected signal and background rates for the tonne-scale detector including a reduction in background from PSD are shown in Figure 6 right. The CEvNS signal is extracted by selecting the beam-on CEvNS candidate events, then subtracting the well-measured steady state background.

5.3 NaI Detector

NaI[Tl] scintillating crystals are another detector material with the capacity for low-threshold recoil detection. The sole stable sodium isotope, ^{23}Na, with 12 neutrons, has the lowest N value of COHERENT's target materials, and hence will result in the highest-energy recoils so far. A small-N nuclear target in combination with measurements on heavier nuclides reduces the impact of the flux uncertainty and improves the physics reach. Furthermore, a few-percent effect from axial contributions is expected at high recoil energy, and could be of interest to measure with a near-future lower-background, precision effort.

On the order of 4 t of recycled NaI[Tl] detectors are immediately available to the COHERENT collaboration, with potentially more available in the future. The NaI[Tl] detectors are available in the form of 7.7 kg NaI[Tl] modules sealed in aluminum and packaged with Burle S83013 (or equivalent) photomultiplier tubes. These rectangular detectors are suitable for deployment in a compact array, as can be seen in the deployment of the prototype array in Fig. 7. Their intrinsic backgrounds are high, as they were not designed with low-radioactivity operation in mind. However, CEvNS backgrounds can be reduced by rejecting coincident events between multiple detectors. The immediate focus of this CEvNS measurement is on the ^{23}Na recoils, which extend to higher energies than those of ^{127}I. Studies of these crystals with different bases have demonstrated a 3 keVee threshold, which allows the near complete separation of these two recoiling species.

5.4 PPC Germanium Detectors

P-type point contact (PPC) germanium detectors display a set of unique properties in a large-mass (up to few kg) radiation detector: excellent energy resolution, sensitivity to energy depositions well below

(a) (b)

Figure 7: (a) installation of the prototype 185 kg NaI array in Neutrino Alley. (b) 3.388 t array visualization.

1 keVee, and the intrinsic radiopurity that characterizes detector-grade (HPGe) germanium crystals. Following their description in [34, 35], PPCs have been adopted by a number of searches in dark matter and neutrino physics: CoGeNT (Coherent Germanium Neutrino Technology) [36–39], the MAJORANA DEMONSTRATOR [40], GERDA [41], CDEX [42], TEXONO [43], and most recently CONUS [44, 45]. Continuous development over the course of the past decade has enabled kg-scale detectors with energy thresholds below of ~500 eVee to become standard offerings of detector vendors. Taking into consideration the measured quenching factor for nuclear recoils in germanium, this allows for detection of recoils with energy below 2.5 keVnr with off-the-shelf units. Additionally, the SNS neutrinos are preceded by a distributed timing signal which can be used to trigger waveform acquisition; this may allow detection threshold energies to be further reduced. In addition to extremely low energy thresholds, the low noise and 3 eV band-gap energy gives these detectors an excellent energy resolution near threshold. As a result, the measured (background-subtracted) energy-deposition spectrum closely follows the true recoil spectrum, allowing for straightforward searches for deviations of the recoil spectrum due to nuclear form factors or new physics.

The COHERENT Collaboration aims to deploy an array of low-background, low-threshold PPC germanium detectors at the SNS, with the aim of sensitively measuring the CEvNS spectrum. A set of detectors comprising an estimated 14.4 kg will be procured in low-background vendor-supplied cryostats, and deployed in a 160-liter, multi-port dewar.

It has been determined that an 18-detector array (the capacity of the existing dewar) of 0.8-kg detectors is a cost-effective approach appropriate for that funding solicitation; this will yield a total detector mass of 14.4 kg. A compact copper, polyethylene and lead radiological shield will encompass the array, and a 4π plastic scintillator muon veto will be used to constrain backgrounds from cosmic-ray induced neutrons generated in the shielding materials (See Figure 8). The shielding package has a footprint of 66"$\times$40" and stands 54" tall, designed to fit within the constraints of a neutrino alley deployment. With even modest shielding, the environmental and beam-related backgrounds can be reduced to below the level of backgrounds due to the detector cryostat materials. We are currently in the process of simulating environmental backgrounds to determine if a more modest lead shield can be used, which would further reduce NIN and cosmic-ray related backgrounds. A VME-based data acquisition system will be used to acquire waveforms from the germanium detectors and amplitudes from the muon veto PMTs, triggered by the SNS timing signal.

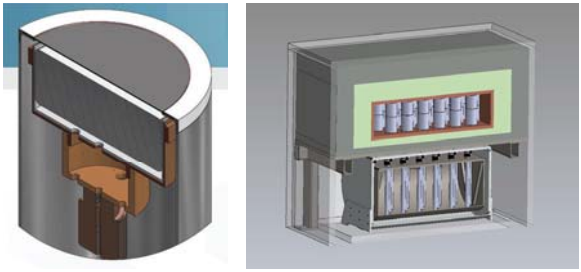

(a) (b)

Figure 8: (a) Schematic view of a Canberra Industries large-mass PPC detector procured for deployment at the SNS. (b) An array of 18 PPC germanium detectors deployed in a baseline design compact radiological shield. From inside to outside: 1 in layer of copper to absorb bremsstrahlung from external shielding materials; 6 in polyethylene neutron absorber to attenuate NINs from the lead shielding; 6 in lead gamma ray shielding; and 2 in plastic scintillator muon veto panels.

6 Neutrino-Induced Neutron Backgrounds

The high-energy neutrinos from pion decay at rest have energies above the neutron separation threshold in ^{208}Pb, a ubiquitous material in detector radiological shields. The CC interaction $^{208}\mathrm{Pb}(\nu_e, e^-)^{208}\mathrm{Bi}$, with subsequent prompt neutron emission, may produce significant numbers of *background-producing* neutrons in the Pb shields, pulsed in time with the beam and sharing the 2.2 µs characteristic time-structure of the ν_e due to the muon lifetime. Other isotopes of Pb should have similarly large neutron-ejection cross sections, and other elements commonly used for shielding (Fe, Cu) may also produce neutrino-induced neutrons (NINs) in CC and NC reactions.

As described in Secs. **??** and **??**, the NIN cross section is relevant as an interesting result in itself and as information needed to evaluate beam-related backgrounds for CEvNS measurements. The NIN cross section is estimated theoretically within a factor of ~3 [46–48]; the single measurement for these targets in this energy range is an inclusive CC $^{56}\mathrm{Fe}(\nu_e, e^-)^{56}\mathrm{Co}$ measurement [49].

The COHERENT liquid-scintillator-cell measurement inside the CsI shielding favors a non-zero NIN signal at 2.9σ [5], although it also suggests a smaller cross section than from theoretical expectation. Dedicated apparatuses for NIN measurements containing liquid-scintillator detectors surrounded by lead or other target materials and further surrounded by a muon veto and neutron moderator were designed and deployed to the SNS basement in September 2015 (see Figure 9). These detector systems, currently running with lead and iron, are expected to continue operation for years to come. Presently we are in the process of updating liquid-scintillator detectors to boron-loaded scintillator to enhance neutron detection capabilities. COHERENT will use these apparatuses to measure the production cross sections of NINs in lead, iron, and copper at the SNS, both to evaluate the NIN background for CEvNS and as independent physics measurements.

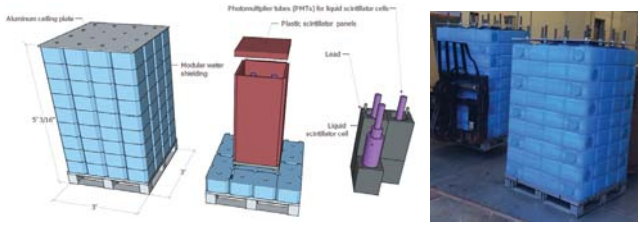

(a) (b)

Figure 9: (a) Schematic drawing of the detectors to measure the neutrino-induced neutron cross section on Pb, Fe, and Cu. (b) The imperfectly-named "Neutrino Cubes," or "NIN Cubes," modular neutrino-induced neutron experiments.

7 Summary

Following its first observation of CEvNS at the SNS, the COHERENT collaboration plans to unfold a broad program of precision tests of the SM. We expect to deliver stringent constraints on neutrino non-standard interactions, which will be significant for exclusion of the "LMA-Dark" sector for neutrino oscillation studies. Other near-term physics reach includes sensitivity to accelerator-produced dark matter. Farther future physics programs include limits on neutrino magnetic moments and neutrino effective charge radius. A future sterile neutrino oscillation program is also possible, exploiting the CEvNS channel as a unique tool for unambiguous measurements of active neutrino disappearance. Measurements of the neutron RMS radius and neutron skin for various nuclei, and study of nuclear axial structure are also of interest. In parallel to the low-threshold CEvNS measurements, we are also planning a set of inelastic CC and NC neutrino cross section measurements to support supernova neutrino physics at underground detectors including Super-K, Hyper-K, DUNE, and HALO, and to potentially probe the nature of the weak interaction.

In the near term, the COHERENT collaboration is planning to deploy the following detectors in Neutrino Alley:

One-tonne-scale heavy water detector: This detector will provide accurate normalization of the SNS neutrino flux which is important for all COHERENT detectors. In addition, it will provide measurement of CC neutrino interactions on oxygen in an energy range relevant to supernova physics.

One-tonne-scale single-phase liquid argon detector: This detector will provide precise measurements of CEvNS on a light nucleus, and will measure CC neutrino interactions on argon in the energy range relevant to supernova physics. Measurements in this argon detector will significantly improve the limits on accelerator produced dark matter.

Three tonnes of NaI[Tl] detectors: The second phase of the NaI[Tl] will build on the NaIvE-185 prototype deployment to produce a significant measurement of CEvNS on the lightest nucleus currently in COHERENT's arsenal, providing a strong lever-arm to study the N^2 nature of the cross-section. This NaI system will also measure CC neutrino interactions on iodine with relevance for g_a quenching studies.

Fourteen kilograms of PPC germanium detectors: The aim of this initial phase of CEvNS measurement in germanium is to measure the CEvNS spectrum in a target with the lowest systematic uncertainties in detectors with an energy resolution capable of faithfully reproducing the nuclear recoil spectrum and a threshold low enough to be sensitive to electromagnetic properties of neutrinos. The germanium target also adds an intermediate N value necessary for mapping the curvature of the cross section's N^2 dependence.

References

[1] D.Z. Freedman. "Coherent effects of a weak neutral current." *Phys. Rev.* **D9**, 1389 (1974).

[2] V. B. Kopeliovich and L. L. Frankfurt. "Isotopic and chiral structure of neutral current." *JETP Lett.* **19**, 145–147 (1974). [Pisma Zh. Eksp. Teor. Fiz.19,236(1974)].

[3] A. Drukier and L. Stodolsky. "Principles and applications of a neutral current detector for neutrino physics and astronomy." *Phys. Rev.* **D30**, 2295 (1984).

[4] K. Scholberg. "Prospects for measuring coherent neutrino nucleus elastic scattering at a stopped-pion neutrino source." *Phys. Rev.* **D73**, 033005 (2006). `hep-ex/0511042`.

[5] D. Akimov *et al.* (COHERENT). "Observation of Coherent Elastic Neutrino-Nucleus Scattering." *Science* (2017). `1708.01294`.

[6] P. Coloma, M. C. Gonzalez-Garcia, M. Maltoni, and T. Schwetz. "A COHERENT enlightenment of the neutrino Dark Side." (2017). `1708.02899`.

[7] J. Liao and D. Marfatia. "COHERENT constraints on nonstandard neutrino interactions." *Phys. Lett.* **B775**, 54–57 (2017). `1708.04255`.

[8] J.B. Dent, B. Dutta, S. Liao, J.L. Newstead, L.E. Strigari, and J.W. Walker. "Accelerator and reactor complementarity in coherent neutrino scattering." (2017). `1711.03521`.

[9] T. S. Kosmas and D. K. Papoulias. "COHERENT constraints to conventional and exotic neutrino physics." (2017). `1711.09773`.

[10] J. Barranco, O.G. Miranda, and T.I. Rashba. "Low energy neutrino experiments sensitivity to physics beyond the standard model." *Phys. Rev.* **D76**, 073008 (2007). `hep-ph/0702175`.

[11] P. Coloma, P. B. Denton, M. C. Gonzalez-Garcia, M. Maltoni, and T. Schwetz. "Curtailing the Dark Side in Non-Standard Neutrino Interactions." *JHEP* **04**, 116 (2017). `1701.04828`.

[12] J. Billard, E. Figueroa-Feliciano, and L. Strigari. "Implication of neutrino backgrounds on the reach of next generation dark matter direct detection experiments." *Phys. Rev.* **D89**, 023524 (2014).

[13] J.R. Wilson. "Coherent Neutrino Scattering and Stellar Collapse." *Phys. Rev. Lett.* **32**, 849 (1974).

[14] K. Sato. "Supernova Explosion and Neutral Currents of Weak Interaction." *Progress of Theoretical Physics* **54**, 1325–1338 (1975).

[15] C.J. Horowitz, M.A. Perez-Garcia, J. Carriere, D.K. Berry, and J. Piekarewicz. "Nonuniform neutron-rich matter and coherent neutrino scattering." *Phys. Rev.* **C70**, 065806 (2004). `astro-ph/0409296`.

[16] C.J. Horowitz, K.J. Coakley, and D.N. McKinsey. "Supernova observation via neutrino nucleus elastic scattering in the CLEAN detector." *Phys. Rev.* **D68**, 023005 (2003). `astro-ph/0302071`.

[17] S. Chakraborty, P. Bhattacharjee, and K. Kar. "Observing supernova neutrino light curve in future dark matter detectors." *Phys. Rev.* **D89**, 013011 (2014). `1309.4492`.

[18] A. Bolozdynya, F. Cavanna, Y. Efremenko, G.T. Garvey, V. Gudkov, *et al.* "Opportunities for Neutrino Physics at the Spallation Neutron Source: A White Paper." (2012). `1211.5199`.

[19] S. Agostinelli *et al.* (GEANT4). "GEANT4: A simulation toolkit." *Nucl. Instrum. Meth.* **A506**, 250–303 (2003).

[20] J. Barranco, O.G. Miranda, and T.I. Rashba. "Probing new physics with coherent neutrino scattering off nuclei." *J. High Energy Phys.* **2005**, 021 (2005). `hep-ph/0508299`.

[21] L.M. Krauss. "Low-energy neutrino detection and precision tests of the standard model." *Phys. Lett.* **B269**, 407–411 (1991).

[22] R. Harnik, J. Kopp, and P.A.N. Machado. "Exploring nu Signals in Dark Matter Detectors." *JCAP* **1207**, 026 (2012). 1202.6073.

[23] B. Dutta, R. Mahapatra, L. E. Strigari, and J.W. Walker. "Sensitivity to Z-prime and non-standard neutrino interactions from ultra-low threshold neutrino-nucleus coherent scattering." (2015). 1508.07981.

[24] J. Dorenbosch *et al.* (CHARM). "Experimental verification of the universality of electron-neutrino and muon-neutrino coupling to the neutral weak current." *Phys. Lett.* **B180**, 303 (1986).

[25] J. Monroe and P. Fisher. "Neutrino Backgrounds to Dark Matter Searches." *Phys. Rev.* **D76**, 033007 (2007). 0706.3019.

[26] A. Gütlein, C. Ciemniak, F. von Feilitzsch, N. Haag, M. Hofmann, *et al.* "Solar and atmospheric neutrinos: Background sources for the direct dark matter search." *Astropart. Phys.* **34**, 90–96 (2010). 1003.5530.

[27] P. Cushman *et al.* "Snowmass CF1 Summary: WIMP Dark Matter Direct Detection." (2013). 1310.8327.

[28] A.J. Anderson, J.M. Conrad, E. Figueroa-Feliciano, K. Scholberg, and J. Spitz. "Coherent neutrino scattering in dark matter detectors." *Phys. Rev.* **D84**, 013008 (2011).

[29] A. Gütlein *et al.* "Impact of coherent neutrino nucleus scattering on direct dark matter searches based on $CaWO_4$ crystals." *Astropart. Phys.* **69**, 44–49 (2015). 1408.2357.

[30] Yu. V. Kozlov, S. V. Khalturtsev, I. N. Machulin, A. V. Martemyanov, V. P. Martemyanov, S. V. Sukhotin, V. G. Tarasenkov, E. V. Turbin, and V. N. Vyrodov. "Anti-neutrino deuteron experiment at Krasnoyarsk." *Phys. Atom. Nucl.* **63**, 1016–1019 (2000). [Yad. Fiz.63,1091(2000)], hep-ex/9912047.

[31] S. Nakamura, T. Sato, S. Ando, T. S. Park, F. Myhrer, Vladimir P. Gudkov, and K. Kubodera. "Neutrino deuteron reactions at solar neutrino energies." *Nucl. Phys.* **A707**, 561–576 (2002). nucl-th/0201062.

[32] J. A. Formaggio and G. P. Zeller. "From eV to EeV: Neutrino Cross Sections Across Energy Scales." *Rev. Mod. Phys.* **84**, 1307–1341 (2012). 1305.7513.

[33] K. Scholberg. "Supernova Neutrino Detection." *Ann.Rev.Nucl.Part.Sci.* **62**, 81–103 (2012). 1205.6003.

[34] P.S. Barbeau, J.I. Collar, and O. Tench. "Large-Mass Ultra-Low Noise Germanium Detectors: Performance and Applications in Neutrino and Astroparticle Physics." *JCAP* **0709**, 009 (2007). nucl-ex/0701012.

[35] P.S. Barbeau. *Neutrino and Astroparticle Physics with P-Type Point Contact High Purity Germanium Detectors*. Ph.D. thesis, U. Chicago (2009). Ph.D. thesis, AAT-3386971.

[36] C. E. Aalseth, P. S. Barbeau, *et al.* (CoGeNT Collaboration). "Experimental Constraints on a Dark Matter Origin for the DAMA Annual Modulation Effect." *Phys. Rev. Lett.* **101**, 251301 (2008). URL https://link.aps.org/doi/10.1103/PhysRevLett.101.251301.

[37] C. E. Aalseth, P. S. Barbeau, *et al.* (CoGeNT Collaboration). "Results from a Search for Light-Mass Dark Matter with a *p*-Type Point Contact Germanium Detector." *Phys. Rev. Lett.* **106**, 131301 (2011). URL https://link.aps.org/doi/10.1103/PhysRevLett.106.131301.

[38] C.E. Aalseth, P.S. Barbeau, J. Colaresi, J.I. Collar, J. Diaz Leon, *et al.* "Search for an Annual Modulation in a P-type Point Contact Germanium Dark Matter Detector." *Phys. Rev. Lett.* **107**, 141301 (2011). 1106.0650.

[39] C.E. Aalseth *et al.* (CoGeNT Collaboration). "CoGeNT: A Search for Low-Mass Dark Matter using p-type Point Contact Germanium Detectors." *Phys. Rev.* **D88**, 012002 (2013). 1208.5737.

[40] N. Abgrall, E. Aguayo, F.T. Avignone III, *et al.* "The MAJORANA DEMONSTRATOR Neutrinoless Double-Beta Decay Experiment." *Advances in High Energy Physics* **2014** (2014).

[41] The GERDA Collaboration. "Background-free search for neutrinoless double-decay of 76Ge with GERDA." *Nature* **544**, 47 EP – (2017). URL http://dx.doi.org/10.1038/nature21717.

[42] W. Zhao *et al.* (CDEX). "Search of low-mass WIMPs with a *p*-type point contact germanium detector in the CDEX-1 experiment." *Phys. Rev.* **D93**, 092003 (2016). 1601.04581.

[43] S.T. Lin *et al.* "New limits on spin-independent and spin-dependent couplings of low-mass WIMP dark matter with a germanium detector at a threshold of 220 eV." *Phys. Rev.* **D79**, 061101 (2009).

[44] M. Lindner, W. Rodejohann, and X. Xu. "Coherent neutrino-nucleus scattering and new neutrino interactions." *Journal of High Energy Physics* **2017**, 97 (2017). ISSN 1029-8479. URL https://doi.org/10.1007/JHEP03(2017)097.

[45] J. Hakenmuller. "CONUS: Towards the detection of coherent elastic neutrino nucleus scattering." Presentation at TAUP 2017. Available from https://indico.cern.ch/event/606690/contributions/2591545/.

[46] G.M. Fuller, W.C. Haxton, and G.C. McLaughlin. "Prospects for detecting supernova neutrino flavor oscillations." *Phys. Rev.* **D59**, 085005 (1999). astro-ph/9809164.

[47] E. Kolbe and K. Langanke. "The Role of neutrino induced reactions on lead and iron in neutrino detectors." *Phys.Rev.* **C63**, 025802 (2001). nucl-th/0003060.

[48] J. Engel, G.C. McLaughlin, and C. Volpe. "What can be learned with a lead based supernova neutrino detector?" *Phys. Rev.* **D67**, 013005 (2003). hep-ph/0209267.

[49] R. Maschuw. "Neutrino spectroscopy with KARMEN." *Progress in Particle and Nuclear Physics* **40**, 183–192 (1998).

What has the COHERENT experiment seen? On coherency and incoherency in neutrino-nucleus scattering

Vadim A. Bednyakov[1] and Dmitry V. Naumov[1]

[1] *Joint Institute for Nuclear Research, Dubna, Moscow Region*

Neutrino-nucleus interaction $\nu A \to \nu A$, when the nucleus conserves its integrity, is discussed with coherent (elastic) and incoherent (inelastic) scattering regimes taken into account. In the first regime the nucleus remains in the same quantum state after the scattering and the cross-section depends on the quadratic number of nucleons. In the second regime the nucleus changes his quantum state and the cross-section has a linear dependence on the number of nucleons. The coherent and incoherent cross-sections are defined by a proton/neutron form-factor squared $|F_{p/n}|^2$ and a $(1 - |F_{p/n}|^2)$-term, respectively. One has a smooth transition between the regimes of coherent and incoherent neutrino-nucleus scattering. In particular, for ^{133}Cs and neutrino energies of 30–50 MeV the incoherent cross-section is about 15-20% of the coherent one. Therefore the COHERENT experiment (with ^{133}Cs) did not see the *true* coherent *elastic* neutrino nucleus scattering (CEνNS). The incoherent (inelastic) admixture at a level of 15-20% is inevitable in the measured data of the experiment. Due to the neutral current nature the coherent and incoherent processes are indistinguishable if the nucleus recoil energy is only observed. Two ways are seen how to detect the *true* CEνNS. One way is to separate the coherent signal from the incoherent one by means of a γ-quantum signal which could be registered from deexcitation of the nucleus excited during the incoherent scattering. For a pulse-beam ν-experiment the γs should be correlated in time with the beam pulse, and the higher energy of the γs allows their detection at a rate governed by the ratio of incoherent to coherent cross-sections. Another way is to use a very low-energy threshold detector and collect data at very low recoil energies, where the incoherent scattering is completely suppressed.

After Freedman's paper [1] it was confirmed [2–5] that in the Standard Model the cross-section of elastic neutrino scattering off a nucleus is amplified with respect to neutrino scattering off a single nucleon. The amplification factor for a spinless even-even nucleus is $|g_V^n N F_n(\boldsymbol{q}) + g_V^p Z F_p(\boldsymbol{q})|^2 \simeq N^2 (g_V^n)^2 |F_n(\boldsymbol{q})|^2$, giving the *coherent* νA-scattering cross section in the well known form [1–12]

$$\frac{d\sigma_{\rm coh}}{dT_A} \approx \frac{G_F^2 m_A}{\pi} \left(1 - \frac{T_A}{T_A^{\rm max}}\right) |F_n|^2 \left(g_V^n\right)^2 N^2. \qquad (1)$$

Here T_A is the kinetic energy of the scattered nucleus, m_A is the nucleus mass, $\boldsymbol{q}$ is the momentum transfer, $G_{\rm F}$ is Fermi constant, Z and N are the numbers of protons and neutrons, $g_V^{p/n}$ are the proton/neutron couplings of the nucleon vector current, and $F_{p/n}(\boldsymbol{q})$ are the proton/neutron form-factors of the nucleus. The form-factors vanish as $|\boldsymbol{q}| \to \infty$ and approach unity ($F_{p/n}(\boldsymbol{q}) = 1$) if $|\boldsymbol{q}| R_A \ll 1$, where R_A is the radius of the nucleus. The famous coherency requirement reads as $|\boldsymbol{q}| R \ll 1$.

Freedman used the terminology "coherent neutrino-nucleus scattering" (CNNS)

[1] to emphasize the fact that the dependence of the corresponding cross-section is quadratic in terms of the number of nucleons.

The importance of the CNNS was demonstrated for a number of observables in astrophysics, like stellar collapse [13, 14], Supernovae [12, 15–17], in studies of physics beyond the Standard Model (SM) [3, 11, 18–28], and investigation of the nuclear structure [4, 29–33]. Due to the neutral-current nature an observation of ν-oscillations with CNNS could be evidence for sterile neutrino(s) [34, 35]. Coherent scattering of atomic systems was studied in [36, 37]. There are some experimental proposals to observe the CNNS [2, 10, 38–51]. This process is an unavoidable background in sensitive direct dark matter searches [52–56]. Due to the CNNS one expects to reduce *significantly the size* of a neutrino detector. It would help to develop neutrino-based applied research (non-intrusive monitoring of nuclear reactors, etc).

The difficulty in observing CNNS lies in the detection of scattered nuclei with low kinetic energy of the order of some keV. This nuclear recoil energy is the only measurable CNNS signature. Detection of neutrinos (with E_ν <50 MeV) via CNNS is a challenge.

The first experimental evidence for CNNS was reported in 2017 by the COHERENT Collaboration [57–59], who used the CsI[Na] scintillator exposed to neutrinos with energies of *tens* of MeV produced by the Spallation Neutron Source (SNS) at the Oak Ridge National Laboratory [60–62]. The COHERENT energy threshold was *5* keV (for caesium). At *these* energies the momentum transfer $\boldsymbol{q}$ is large enough to break the condition $|\boldsymbol{q}|R_A \ll 1$. For example, energy deposits observed in [60] correspond to $1 < |\boldsymbol{q}|R_A < 2.7$, and the *pure* elastic cross-section should be suppressed. At higher energies the elastic cross-section (given in Eq. (1)) vanishes (due to form-factors), but the neutrino-nucleus interaction probability, obviously, does not vanish and must be determined by some inelastic interaction (which is absent in Eq. (1)). In general, the corresponding cross-section should be given by a sum of elastic and inelastic cross-sections, similar to the theory of the scattering of X rays [63] and electrons [64] off an atom and of slow neutrons off matter constituents [65].

In our paper [66] a theoretical framework allowing for elastic and inelastic neutrino-nucleus scattering of the process $\nu A \rightarrow \nu A^{(*)}$, was developed on the basis of calculations from first principles. The possibility that the internal quantum state of a nucleus can be modified after an interaction is labeled by the $(*)$ superscript. The following consideration with some modifications relies on the results of [66].

Neutrinos with energies below tens of MeV predominately conserve the integrity of nucleons allowing usage of an effective neutrino-nucleon interaction in the form $\mathcal{L}(x) = \frac{G_F}{\sqrt{2}} L_\mu(x) H^\mu(x)$. Here $L_\mu(x) = \overline{\psi}_\nu(x)\gamma_\mu(1-\gamma_5)\psi_\nu(x)$ and $H^\mu(x) = \sum_{f=n,p} \overline{\psi}_f(x) O_f^\mu \psi_f(x)$ are the weak currents of neutrinos and nucleons, respectively, $O_f^\mu = \gamma^\mu \left(g_V^f - g_A^f \gamma_5\right) = \gamma^\mu \left(g_L^f(1-\gamma_5) + g_R^f(1+\gamma_5)\right)$, and left- and right-chirality couplings $g_{L/R}^f = \frac{1}{2}\left(g_V^f \pm g_A^f\right)$ are expressed in term of the vector $g_V^{p/n}$

and axial $g_A^{p/n}$ couplings with $g_A = 1.27 \pm 0.003$ [67]:

$$g_V^p = \frac{1}{2} - 2\sin^2\theta_W, \quad g_V^n = -\frac{1}{2}, \quad g_A^p = \frac{g_A}{2}, \quad g_A^n = -\frac{g_A}{2}. \tag{2}$$

In [66] the SM coupling values were used (with $g_A \equiv 1$).

As follows from [66], the neutrino-nucleus ($\nu A \to \nu A^{(*)}$) cross-section is a sum of incoherent and coherent terms (T_A is the kinetic energy of the nucleus)

$$\frac{d\sigma}{dT_A} = \frac{d\sigma_{\text{incoh}}}{dT_A} + \frac{d\sigma_{\text{coh}}}{dT_A}. \tag{3}$$

The incoherent cross-section is

$$\begin{aligned}\frac{d\sigma_{\text{incoh}}}{dT_A} = \frac{2G_F^2 m_A}{\pi} \sum_{f=n,p} \left(1-|F_f|^2\right) \Bigg[A_f \left((g_L^f)^2 + (g_R^f)^2 (1-y)^2 - g_L^f g_R^f \frac{2y m_N^2}{s - m_N^2} \right) \\ + \Delta A_f \left(\Big[g_L^f - g_R^f (1-y) \Big] \times \Big[g_L^f + g_R^f \Big(1 - y \frac{s + m_N^2}{s - m_N^2} \Big) \Big] \right) \Bigg].\end{aligned} \tag{4}$$

Here $y = (pq)/(pk) \simeq T_A/E_\nu$, and m_N is the nucleon mass. The total energy squared $s = (p+k)^2$ of the neutrino and the target nucleon is calculated assuming an effective momentum of the nucleon [66]. In Eq. (4) $A_p = Z$, $A_n = N$ and $\Delta A_p \equiv \Delta Z = Z_+ - Z_-$, $\Delta A_n \equiv \Delta N = N_+ - N_-$, where $Z_\pm, N_\pm$ stand for the numbers of the protons and neutrons with the spin projection on the incident neutrino momentum axis equal to $\pm 1/2$.

If the target nucleus is unpolarized, then terms proportional to ΔA^f in Eq. (4) vanish after averaging, and for an unpolarized target the incoherent cross-section is

$$\frac{d\sigma_{\text{incoh}}}{dT_A} = \frac{2G_F^2 m_A}{\pi} \sum_{f=n,p} \left(1 - |F_f|^2\right) A^f \left((g_L^f)^2 + (g_R^f)^2 (1-y)^2 - g_L^f g_R^f \frac{2y m_N^2}{s - m_N^2} \right). \tag{5}$$

The coherent cross-section has the form (with $\tau = (\sqrt{s} - m_N)/(\sqrt{s} + m_N)$)

$$\frac{d\sigma_{\text{coh}}}{dT_A} = \frac{G_F^2 m_A}{\pi} \left(1 - \frac{T_A}{T_A^{\max}} \right) |G_V + G_A|^2, \qquad \text{where} \tag{6}$$

$$G_V = \sum_f g_V^f F_f \left(A_f \Big[1 - \frac{y\tau}{2} \Big] + \Delta A_f \frac{y}{2} \right), \; G_A = \sum_f g_A^f F_f \left(\Delta A_f \Big[1 - \frac{y}{2} \Big] + A_f \frac{y\tau}{2} \right).$$

Spin averaging in Eq. (6) removes terms linear in ΔA_f. The final formula of the spin-

averaged coherent cross-section is

$$\begin{aligned}\frac{d\sigma_{\rm coh}}{dT_A} = \frac{G_F^2 m_A}{\pi}\left(1-\frac{T_A}{T_A^{\rm max}}\right)\sum_{f,f'} F_f F_{f'}^* \Bigg[\\ g_V^f g_V^{f'}\left(A_f A_{f'}\left(1-\frac{y\tau}{2}\right)^2 + \Delta A_f \Delta A_{f'}\left(\frac{y}{2}\right)^2\right) \\ + g_A^f g_A^{f'}\left(\Delta A_f \Delta A_{f'}\left(1-\frac{y}{2}\right)^2 + A_f A_{f'}\left(\frac{y\tau}{2}\right)^2\right) \\ + 2 g_V^f g_A^{f'}\left(A_f A_{f'}\left(1-\frac{y\tau}{2}\right)\frac{y\tau}{2} + \Delta A_f \Delta A_{f'}\frac{y}{2}\left(1-\frac{y}{2}\right)\right)\Bigg].\end{aligned} \tag{7}$$

Eq. (7) can be simplified if terms proportional to g_V^p are abandoned (because $g_V^p \ll 1$) and terms proportional to $y \approx 3\%E_\nu/(30\,\text{MeV})$ and to $\Delta A_f \Delta A_{f'}$ are neglected. This can be done either for a spinless nucleus or approximately for heavy nuclei with $\Delta A \ll A$. Finally, Eq. (7) arrives at a well-known result given in Eq. (1).

For an unpolarized heavy target (and $y \simeq 0$) one has both terms in a rather simple form

$$\frac{d\sigma_{\rm coh}}{dT_A} = \frac{G_F^2 m_A}{\pi}\left(1-\frac{T_A}{T_A^{\rm max}}\right)\sum_{f=n,p} A_f^2 |F_f|^2 (g_V^f)^2,$$

$$\frac{d\sigma_{\rm incoh}}{dT_A} = \frac{2G_F^2 m_A}{\pi}\sum_{f=n,p} A_f\big(1-|F_f|^2\big)\left((g_L^f)^2+(g_R^f)^2\right).$$

A smooth transition between the coherent and incoherent regimes is the key feature of Eq. (3). The elastic (*coherent*) interactions keeping the nucleus in the same quantum state lead to *quadratic enhancement* ($\propto A_f^2$) of the cross-section in terms of the number of nucleons and is simultaneously proportional to $|F_f|^2$. The cross-section of the inelastic (*incoherent*) processes in which the quantum state of the nucleus is changed has the *linear dependence* ($\propto A_f$) on the number of nucleons and is simultaneously proportional to $\big(1-|F_f|^2\big)$. Both terms in Eq. (3) are governed by the same $F_{p/n}(\boldsymbol{q})$. In the limit $\boldsymbol{q} \to 0$, $F_{p/n}(\boldsymbol{q}) \to 1$, and the contribution of the incoherent cross-section vanishes, while the coherent term totally dominates. In the opposite limit of large $\boldsymbol{q}$, $F_{p/n}(\boldsymbol{q}) \to 0$, and the coherent cross-section vanishes, as the incoherent term dominates. In general, both the coherent and incoherent scatterings contribute.

In what follows we present the results obtained with the Helm form-factors [68] for definiteness. It is convenient to refer to the cross-section integrated over the kinetic energy of the recoil nucleus

$$\sigma(E_\nu) = \int_{T_A^{\rm min}}^{T_A^{\rm max}} \frac{d\sigma}{dT_A} dT_A. \tag{8}$$

This integral depends on the energy threshold $T_A^{\min}$, unique for each detector. As in [66], three experimental setups are considered.

The *first* is a germanium detector with the natural isotope ^{74}Ge only (for illustration). The energy threshold for the electrons of the Ge bolometers in the νGEN experiment at the Kalinin Nuclear Power Plant is 200 eV [49, 69], which roughly corresponds to 1 keV [70] of the ^{74}Ge recoil energy. The differential cross-sections for $E_\nu = 5$ MeV and 7 MeV and the total cross-section for $E_\nu \in (1, 20)$ MeV were calculated. As an estimate, $\Delta\varepsilon = 900$ keV was used for the excitation energy of ^{74}Ge.

The *second* setup is a CsI scintillator exposed to the neutrinos from the SNS [60]. The differential and total cross-sections are calculated for $E_\nu = 30$ MeV and 50 MeV and for $E_\nu \in (1, 150)$ MeV, respectively. It was assumed that $\Delta\varepsilon = 100$ keV for the ^{133}Cs nucleus. A 5-keV energy threshold was set to the ^{133}Cs recoil energy.

The *third* one is a liquid argon detector with an unprecedented low-energy threshold of 0.6 keV for the ^{40}Ar nucleus achieved by the DarkSide Collaboration [71]. The differential and total cross-sections are calculated for $E_\nu = 15$ MeV and for $E_\nu \in (1, 50)$ MeV, respectively.

In Fig. 1 the Helm form-factors for these nuclei as functions of $|\boldsymbol{q}|$ (and $T_{\rm Cs}$) are depicted. At $T_{\rm Cs} = 12$–15 keV, where the maximum of the signal observed by the

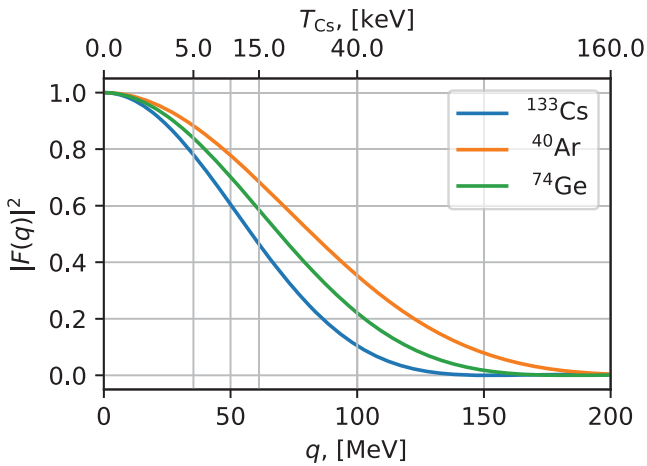

FIG. 1. The Helm form-factor $F^{\rm Helm}$ [68] as a function of the three-momentum transfer $|\boldsymbol{q}|$ (bottom horizontal axis). The upper horizontal axis corresponds to the kinetic energy of the ^{133}Cs nucleus.

COHERENT experiment occurred, $|\boldsymbol{q}| = 50$–60 MeV and $|F(\boldsymbol{q})|^2 = 0.6$–$0.5$. It is seen that the coherent elastic scattering is suppressed, and a contribution from the incoherent transitions should be expected.

In Fig. 2 (Fig. 3) the differential (integral) coherent and incoherent cross-sections are displayed. The following features can be observed in the figures.

As $T_A \to 0$ the coherent cross-section totally dominates, since the incoherent

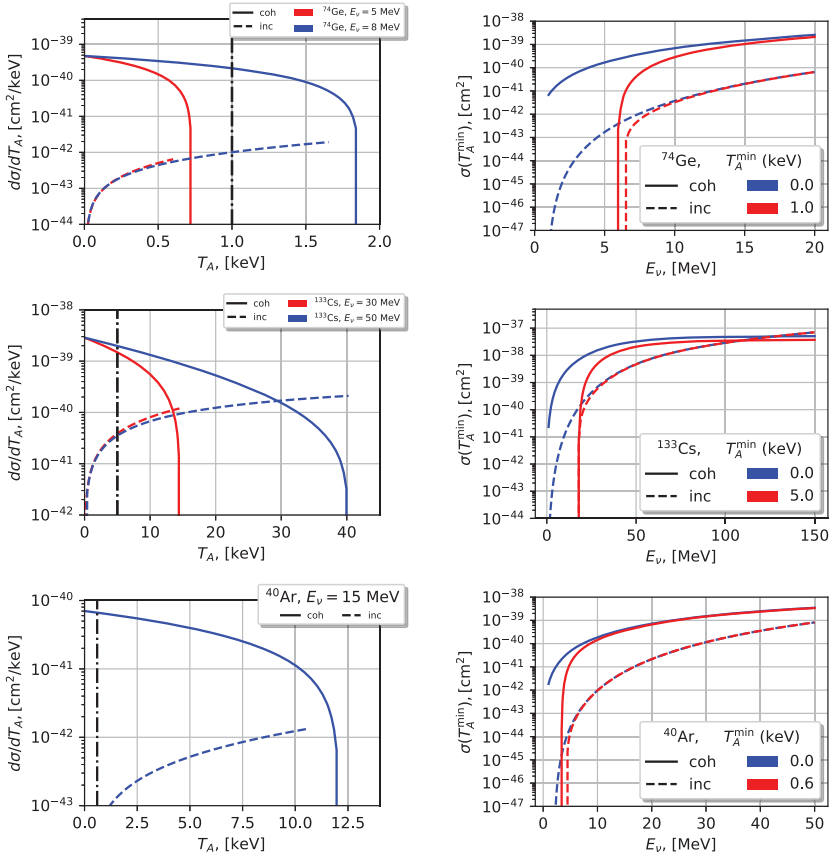

FIG. 2. (Left) Differential cross-sections $d\sigma/dT_A$ for coherent (solid lines) and incoherent (dashed lines) neutrino-nucleus scattering for the ^{74}Ge (top), ^{133}Cs (middle) and ^{40}Ar (bottom) nuclei and different E_ν. Vertical lines correspond to the experimental energy thresholds.

FIG. 3. (Right) Integral cross-sections σ for coherent (solid lines) and incoherent (dashed lines) neutrino-nucleus scattering for the ^{74}Ge (top), ^{133}Cs (middle) and ^{40}Ar (bottom) nuclei and different neutrino energies. The integrals are calculated for idealistic thresholdless ($T_A^{\min} = 0$, blue lines) experimental setups and for state-of-the-art thresholds $T_A^{\min}$ (red lines) achieved by three considered experimental setups.

contribution vanishes. As $T_A \to T_A^{\max}$ the coherent cross-section vanishes due to the factor $1 - T_A/T_A^{\max}$, and the incoherent cross-section rises. For small E_ν the coherent cross-section dominates over the incoherent contribution for any T_A. For larger E_ν there is a value of T_A above which the incoherent cross-section dominates over Ahe Aoherent, as Aan be Aeen An Ahe Aiddle Aanel Af Aig. A Aor E_ν =50 MeV. At

low E_ν the coherent *integral* cross-section is larger than the incoherent one by orders of magnitude because the factors $1 - |F_{p/n}(\boldsymbol{q})|^2$ suppress the latter at small $\boldsymbol{q}$. With increasing neutrino energy, their interrelation changes, and the *integral* incoherent cross-section becomes rather substantial above a certain E_ν.

To quantify this statement, the ratio of integrals given by Eq. (8), $\sigma_{\rm incoh}/\sigma_{\rm coh}$, is displayed in Fig. 4 for the ^{133}Cs nucleus. At $E_\nu \simeq 30$ (50) MeV this ratio is about 5 (10)% for an idealistic thresholdless experiment and reaches about 10 (20)% for $T_A^{\rm min} = 5$ keV (if $g_A = 1$, left panel). For a more realistic case with $g_A = 1.27$

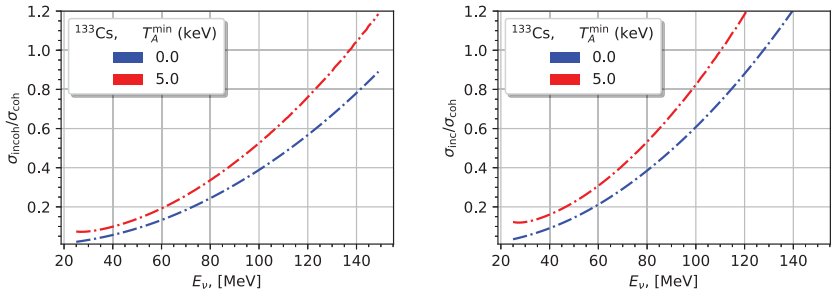

FIG. 4. Ratio $\sigma_{\rm incoh}/\sigma_{\rm coh}$ for the neutrino scattering off a ^{133}Cs nucleus as a function of E_ν. The curves correspond to the $T_A^{\rm min} = 0$ (5) keV threshold. Left (right) is with $g_A = 1$ (1.27).

and $E_\nu \simeq 30$ (60) MeV (right panel), this ratio is about 7 (20)% for $T_A^{\rm min} = 0$ and reaches about 15 (30)% for $T_A^{\rm min} = 5$ keV. In the latter case the incoherent contribution becomes equal to the coherent one at $E_\nu \simeq 110$ MeV. The increasing importance of the incoherent interaction is evident for increasing neutrino energy.

After the interaction the nucleus may remain in the same quantum state, or the internal state of the nucleus could be changed. Experimentally, the scattered nucleus, being in the same or excited state, is practically indistinguishable if one measures only the kinetic energy of the nucleus. Nevertheless, inelastic interaction (for example, nuclear excitation) must be accompanied by some emission of gamma-quanta corresponding to the difference of the energy levels of the nucleus [72]. For example, the time scale of this emission is in the range of picoseconds to nanoseconds for the ^{133}Cs nucleus. The energies of the γs are of the order of hundred keV for ^{133}Cs, and these γs should produce a very detectable signal in the scintillator correlated in time with the beam pulses for an accelerator based experiment. The rate of these γs is determined by the ratio $N_{\rm inc}/N_{\rm coh}$, where

$$N_{\rm inc/coh} = \int dE_\nu \Phi(E_\nu) \int_{dT_A^{\rm min}}^{dT_A^{\rm max}} dT_A \frac{d\sigma_{\rm inc/coh}}{dT_A} \varepsilon(T_A),$$

and $\varepsilon(T_A)$ is the detection efficiency. Fig. 4 suggests that the number of the γ-events due to incoherent interactions could be rather detectable.

Therefore one can *conclude* that due to the high neutrino energy and the high energy threshold (5 keV) the COHERENT experiment (with ^{133}Cs) did not see the *clear* Coherent Elastic Neutrino Nucleus Scattering (CEνNS). This experiment saw a rather substantial *tail* of the neutrino-nucleus neutral-current interaction, the tail of the *wanted* CEνNS, but with 15–20% uncertainty. The incoherent (inelastic) admixture at a level of 15-20% is inevitable in the measured data of the experiment. Therefore, any serious analysis of the COHERENT data (neutron RMS radius, search for physics beyond SM, etc) should take the point into account.

There are two ways for detection of the *true* CEνNS. One is to separate the coherent signal from the incoherent one following the above-mentioned procedure [66]. The incoherent processes, being a relatively small "background" to the coherent interactions provide, an important clue if γ-rays released by the excited nucleus are detected. For a neutrino pulsed-beam experiment the γs should be correlated in time with the beam pulse, and the higher energy of the γs allows their detection at a rate governed by the ratio $N_{\rm inc}/N_{\rm coh}$. Simultaneous detection of both signals due to nuclear recoil and the deexcitation γs provides a sensitive tool for investigation of the *true* CEνNS, studies of the nuclear structure and possible signs of new physics.

The other way is to use an extremely low-energy threshold detector and collect data at recoil energies, where the incoherent scattering is suppressed very significantly. Nowadays, this is an objective for the νGeN experiment with its very-low-energy threshold. Furthermore, the study of the *true* CEνNS is inevitable for significant reduction of a size of an (anti)neutrino detector.

---

[1] D. Z. Freedman, Phys. Rev. **D9**, 1389 (1974).

[2] A. Drukier and L. Stodolsky, Phys. Rev. **D30**, 2295 (1984).

[3] J. Barranco, O. G. Miranda, and T. I. Rashba, JHEP **12**, 021 (2005), arXiv:hep-ph/0508299 [hep-ph].

[4] K. Patton, J. Engel, G. C. McLaughlin, and N. Schunck, Phys. Rev. **C86**, 024612 (2012), arXiv:1207.0693 [nucl-th].

[5] D. K. Papoulias and T. S. Kosmas, Adv. High Energy Phys. **2015**, 763648 (2015), arXiv:1502.02928 [nucl-th].

[6] P. F. Smith, Nuovo Cim. **A83**, 263 (1984).

[7] N. Jachowicz, K. Heyde, and S. Rombouts, *Nuclei in the cosmos. Proceedings, 6th International Conference, Cosmos 2000, Aarhus, Denmark, June 27-July 1, 2000*, Nucl. Phys. **A688**, 593 (2001).

[8] P. C. Divari, V. C. Chasioti, and T. S. Kosmas, Phys. Scripta **82**, 065201 (2010).

[9] G. McLaughlin, *Proceedings, 26th International Conference on Neutrino Physics and Astrophysics (Neutrino 2014): Boston, Massachusetts, United States, June 2-7, 2014*, AIP Conf. Proc. **1666**, 160001 (2015).

[10] J. D. Vergados, F. T. Avignone, III, and I. Giomataris, Phys. Rev. **D79**, 113001 (2009), arXiv:0902.1055 [hep-ph].

[11] J. Papavassiliou, J. Bernabeu, and M. Passera, *Proceedings, 2005 Europhysics Conference on High Energy Physics (EPS-HEP 2005): Lisbon, Portugal, July 21-27, 2005*, PoS

HEP2005, 192 (2006), arXiv:hep-ph/0512029 [hep-ph].
[12] P. C. Divari, Adv. High Energy Phys. **2012**, 379460 (2012).
[13] J. R. Wilson, Phys. Rev. Lett. **32**, 849 (1974).
[14] D. Z. Freedman, D. N. Schramm, and D. L. Tubbs, Ann. Rev. Nucl. Part. Sci. **27**, 167 (1977).
[15] J. Bernabeu, "Low-Energy Elastic Neutrino-Nucleon and Nuclear Scattering and Its Relevance for Supernovae," (1975).
[16] S. Rombouts and K. Heyde, *Nuclei in the cosmos. Proceedings, 4th International Symposium, Notre Dame, USA, June 20-27, 1996*, Nucl. Phys. **A621**, 371C (1997).
[17] P. C. Divari, S. Galanopoulos, and G. A. Souliotis, J. Phys. **G39**, 095204 (2012).
[18] K. Scholberg, Phys. Rev. **D73**, 033005 (2006), arXiv:hep-ex/0511042 [hep-ex].
[19] P. deNiverville, M. Pospelov, and A. Ritz, Phys. Rev. **D92**, 095005 (2015), arXiv:1505.07805 [hep-ph].
[20] I. Esteban, M. C. Gonzalez-Garcia, M. Maltoni, I. Martinez-Soler, and J. Salvado, (2018), arXiv:1805.04530 [hep-ph].
[21] M. Abdullah, J. B. Dent, B. Dutta, G. L. Kane, S. Liao, and L. E. Strigari, (2018), arXiv:1803.01224 [hep-ph].
[22] Y. Farzan, M. Lindner, W. Rodejohann, and X.-J. Xu, JHEP **05**, 066 (2018), arXiv:1802.05171 [hep-ph].
[23] J. Billard, J. Johnston, and B. J. Kavanagh, (2018), arXiv:1805.01798 [hep-ph].
[24] P. B. Denton, Y. Farzan, and I. M. Shoemaker, (2018), arXiv:1804.03660 [hep-ph].
[25] S.-F. Ge and I. M. Shoemaker, (2017), arXiv:1710.10889 [hep-ph].
[26] D. K. Papoulias and T. S. Kosmas, Phys. Rev. **D97**, 033003 (2018), arXiv:1711.09773 [hep-ph].
[27] B. C. Caas, E. A. Garcs, O. G. Miranda, and A. Parada, (2018), arXiv:1806.01310 [hep-ph].
[28] D. Aristizabal Sierra, V. De Romeri, and N. Rojas, (2018), arXiv:1806.07424 [hep-ph].
[29] J. Engel, Phys. Lett. **B264**, 114 (1991).
[30] P. S. Amanik and G. C. McLaughlin, J. Phys. **G36**, 015105 (2009).
[31] P. S. Amanik and G. C. McLaughlin, (2007), arXiv:0707.4191 [hep-ph].
[32] K. M. Patton, G. C. McLaughlin, and K. Scholberg, Int. J. Mod. Phys. **E22**, 1330013 (2013).
[33] M. Cadeddu, C. Giunti, Y. F. Li, and Y. Y. Zhang, Phys. Rev. Lett. **120**, 072501 (2018), arXiv:1710.02730 [hep-ph].
[34] J. A. Formaggio, E. Figueroa-Feliciano, and A. J. Anderson, Phys. Rev. **D85**, 013009 (2012), arXiv:1107.3512 [hep-ph].
[35] A. J. Anderson, J. M. Conrad, E. Figueroa-Feliciano, C. Ignarra, G. Karagiorgi, K. Scholberg, M. H. Shaevitz, and J. Spitz, Phys. Rev. **D86**, 013004 (2012), arXiv:1201.3805 [hep-ph].
[36] Yu. V. Gaponov and V. N. Tikhonov, Yad. Fiz. **26**, 594 (1977).
[37] L. M. Sehgal and M. Wanninger, Phys. Lett. **B171**, 107 (1986).
[38] R. R. Lewis, Phys. Rev. **D21**, 663 (1980).
[39] C. J. Horowitz, K. J. Coakley, and D. N. McKinsey, Phys. Rev. **D68**, 023005 (2003), arXiv:astro-ph/0302071 [astro-ph].
[40] Y. Giomataris and J. D. Vergados, Phys. Lett. **B634**, 23 (2006), arXiv:hep-ex/0503029 [hep-ex].
[41] H. T. Wong, H.-B. Li, J. Li, Q. Yue, and Z.-Y. Zhou, *Proceedings of the 33rd International Conference on High Energy Physics (ICHEP '06): Moscow, Russia, July 26-August 2, 2006*, J. Phys. Conf. Ser. **39**, 266 (2006), [,344(2005)], arXiv:hep-ex/0511001 [hep-ex].

[42] S. Sangiorgio, A. Bernstein, J. Coleman, M. Foxe, C. Hagmann, T. H. Joshi, I. Jovanovic, K. Kazkaz, K. Movrokoridis, and S. Pereverzev, *Proceedings, 2nd International Conference on Technology and Instrumentation in Particle Physics 2011: Chicago, Illinois, 9-14 Jun 2011*, Phys. Procedia **37**, 1266 (2012).
[43] S. J. Brice *et al.*, Phys. Rev. **D89**, 072004 (2014), arXiv:1311.5958 [physics.ins-det].
[44] A. V. Kopylov, I. V. Orekhov, V. V. Petukhov, and A. E. Solomatin, (2013), arXiv:1311.6564 [physics.ins-det].
[45] A. V. Kopylov, I. V. Orekhov, V. V. Petukhov, and A. E. Solomatin, Tech. Phys. Lett. **40**, 185 (2014), [Zh. Tekh. Fiz.40,no.5,1(2014)].
[46] G. Agnolet *et al.* (MINER), Nucl. Instrum. Meth. **A853**, 53 (2017), arXiv:1609.02066 [physics.ins-det].
[47] A. Aguilar-Arevalo *et al.* (CONNIE), *Proceedings, 15th Mexican Workshop on Particles and Fields (MWPF 2015): Mazatln, Mxico, November 2-6, 2015*, J. Phys. Conf. Ser. **761**, 012057 (2016), arXiv:1608.01565 [physics.ins-det].
[48] G. Fernandez Moroni, J. Estrada, E. E. Paolini, G. Cancelo, J. Tiffenberg, and J. Molina, Phys. Rev. **D91**, 072001 (2015), arXiv:1405.5761 [physics.ins-det].
[49] V. Belov *et al.*, JINST **10**, P12011 (2015).
[50] R. Tayloe (for the COHERENT) (2017) arXiv:1801.00086 [physics.ins-det].
[51] J. Billard *et al.*, J. Phys. **G44**, 105101 (2017), arXiv:1612.09035 [physics.ins-det].
[52] H. T. Wong, *Symmetries in subatomic physics. Proceedings, 4th International Symposium, SSP 2009, Taipei, Taiwan, June 2-5, 2009*, Nucl. Phys. **A844**, 229C (2010).
[53] A. J. Anderson, J. M. Conrad, E. Figueroa-Feliciano, K. Scholberg, and J. Spitz, Phys. Rev. **D84**, 013008 (2011), arXiv:1103.4894 [hep-ph].
[54] A. Gutlein *et al.*, Astropart. Phys. **69**, 44 (2015), arXiv:1408.2357 [hep-ph].
[55] V. A. Bednyakov, Phys. Part. Nucl. **47**, 711 (2016), arXiv:1505.04380 [hep-ph].
[56] S. Fallows, T. Kozynets, and C. B. Krauss, (2018), arXiv:1806.01417 [astro-ph.HE].
[57] A. Bolozdynya *et al.* (2012) arXiv:1211.5199 [hep-ex].
[58] D. Akimov *et al.* (COHERENT), (2015), arXiv:1509.08702 [physics.ins-det].
[59] J. I. Collar, N. E. Fields, M. Hai, T. W. Hossbach, J. L. Orrell, C. T. Overman, G. Perumpilly, and B. Scholz, Nucl. Instrum. Meth. **A773**, 56 (2015), arXiv:1407.7524 [physics.ins-det].
[60] D. Akimov *et al.* (COHERENT), Science (2017), 10.1126/science.aao0990, arXiv:1708.01294 [nucl-ex].
[61] D. Akimov *et al.* (COHERENT), (2018), 10.5281/zenodo.1228631, arXiv:1804.09459 [nucl-ex].
[62] D. Akimov *et al.* (COHERENT), (2018), arXiv:1803.09183 [physics.ins-det].
[63] I. Waller and D. R. Hartree, Proceedings of the Royal Society of London A: Mathematical, Physical and Engineering Sciences **124**, 119 (1929), http://rspa.royalsocietypublishing.org/content/124/793/119.full.pdf.
[64] P. M. Morse, Physik. Z. **33**, 443 (1932).
[65] L. Van Hove, Phys. Rev. **95**, 249 (1954).
[66] V. A. Bednyakov and D. V. Naumov, Phys. Rev. **D98**, 053004 (2018), arXiv:1806.08768 [hep-ph].
[67] M. Tanabashi *et al.* (Particle Data Group), Phys. Rev. **D98**, 030001 (2018).
[68] R. H. Helm, Phys. Rev. **104**, 1466 (1956).
[69] V. V. Belov and et al., in *JINR Program Advisory Committee, 2018*.
[70] D. Barker and D. M. Mei, Astropart. Phys. **38**, 1 (2012), arXiv:1203.4620 [astro-ph.IM].
[71] P. Agnes *et al.* (DarkSide), (2018), arXiv:1802.06994 [astro-ph.HE].
[72] T. W. Donnelly and J. D. Walecka, Ann. Rev. Nucl. Part. Sci. **25**, 329 (1975).

The latest results from the long-baseline neutrino experiment T2K

T. WACHALA FOR THE T2K COLLABORATION
The H. Niewodniczanski Institute of Nuclear Physics of Polish Academy of Sciences,
ul. Radzikowskiego 152, 31-342 Krakow, Poland

Abstract

T2K is a long-baseline experiment designed to measure neutrino oscillations. A high intensity beam of muon neutrinos (anti-neutrinos) is produced at the J-PARC accelerator complex and sent towards the near detector station (280 meters away from the neutrino source) and the far detector Super-Kamiokande (295 km).The change in the measured intensity and composition of the beam is used to provide information on the oscillation parameters. The T2K experiment has recently delivered 2σ confidence intervals for δ_{CP} phase and improved the precision of the θ_{23} and Δm^2_{32} measurement. T2K has also provided several useful neutrino-nucleus cross section measurements. A summary of the results for 1.49×10^{21} POT in neutrino-mode and 1.65×10^{21} POT in antineutrino-mode (January 2010 - May 2018) are presented.

1. Introduction

Neutrinos play an important role in the standard model of particle physics and cosmology. They interact both via charged current (CC) and neutral current (NC) exchange but the flavor of the neutrino is determined by the charged lepton that is produced in charged current reaction: electron for ν_e, muon for ν_μ and taon for ν_τ interactions. Neutrinos also oscillate which means that they change their flavor from one to another as they travel. This fact was revealed by several experiments including Super-Kamiokande (Super-K) [1].

From the theoretical point of view neutrino oscillations are a quantum-mechanical effect where the observed in nature neutrino flavor states from the Standard Model ν_e, ν_μ and ν_τ propagate in space as linear combinations of the mass eigenstates ν_1, ν_2 and ν_3. The relation between neutrino flavor states and the mass eigenstates is described by the Pontecorvo-Maki-Nakagawa-Sakata (PMNS) matrix, which can be parametrized using three mixing angles θ_{13}, θ_{23}, θ_{12} and one complex phase δ_{CP} (where $c_{ij} = cos\theta_{ij}$, $s_{ij} = sin\theta_{ij}$).

$$U_{PMNS} = \begin{pmatrix} 1 & 0 & 0 \\ 0 & c_{23} & s_{23} \\ 0 & -s_{23} & c_{23} \end{pmatrix} \cdot \begin{pmatrix} c_{13} & 0 & s_{13}e^{-i\delta_{CP}} \\ 0 & 1 & 0 \\ -s_{13}e^{i\delta_{CP}} & 0 & c_{13} \end{pmatrix} \cdot \begin{pmatrix} c_{12} & s_{12} & 0 \\ -s_{12} & c_{12} & 0 \\ 0 & 0 & 1 \end{pmatrix}$$

The description of the oscillation probabilities requires two more parameters which are two independent differences of mass squared of the neutrinos: Δm^2_{21}, $\Delta m^2_{32\ (13)}$.

Thanks to the discovery of Super-K and other experiments, neutrino oscillation physics became one of the most dynamically developing areas of research in particle physics. Results from Super-K have been confirmed and supplemented later by many experiments which provided information about all mixing angles and mass splittings with a good precision [2].

Although most of the mixing parameters have been measured, there are still open questions in neutrino oscillation physics. Two of the most important questions are: is there a CP violation in the neutrino sector (a non-zero value of δ_{CP} phase?) and what is the neutrino mass ordering related to the sign of $\Delta m^2_{32\ (13)}$: normal ordering (NO), where $m_3 > m_2 > m_1$ or inverted ordering (IO), where $m_2 > m_1 > m_3$?

2. The T2K experiment

The T2K collaboration consists of approximately 500 people from 59 institutions in 11 countries. The goals of the T2K experiment are to look for two channels of neutrino oscillations: ν_e ($\bar{\nu}_e$) appearance in the ν_μ ($\bar{\nu}_\mu$) beam and the disappearance of ν_μ ($\bar{\nu}_\mu$) from the beam. The oscillation probability formulas for neutrino-mode oscillation channels are shown below respectively:

$$P(\nu_\mu \rightarrow \nu_e) = \sin^2\theta_{23}\sin^2 2\theta_{13}\sin^2\left(\frac{\Delta m^2_{31}L}{4E}\right) - \frac{\sin 2\theta_{12}\sin 2\theta_{23}}{2\sin\theta_{13}}\sin\frac{\Delta m^2_{21}}{4E}\sin^2 2\theta_{13}\sin^2\frac{\Delta m^2_{31}L}{4E}\sin\delta_{CP} +$$
$$+ \text{ (CP term, solar term, matter term)}$$

$$P(\nu_\mu \rightarrow \nu_\mu) = 1 - \left(\cos^4\theta_{13}\sin^2 2\theta_{23} + \sin^2\theta_{23}\sin^2 2\theta_{13}\right)\sin^2\frac{\Delta m^2 L}{4E}$$

where Δm^2 is either Δm^2_{32} for normal mass ordering or Δm^2_{13} for inverted mass ordering. It is clear that the ν_e appearance probability is sensitive to θ_{13} and δ_{CP} while ν_μ disappearance formula is sensitive to θ_{23} and $\Delta m^2_{32\,(13)}$. These parameters are in the main scope of the T2K experiment measurements.

T2K is a long-baseline neutrino experiment with ν_μ ($\bar{\nu}_\mu$) beam produced by the J-PARC proton accelerator. Neutrinos (anti-neutrinos) are sent towards the near detector station at 280 m and Super-Kamiokande detector, located 295 km away from J-PARC. A schematic view of the T2K setup is shown in Fig. 1.

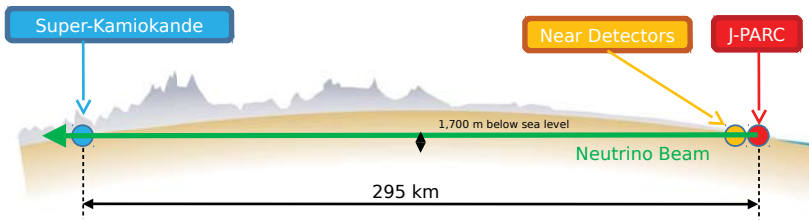

Fig. 1: Schematic view of the T2K experiment including the path of muon neutrinos from J-PARC to the far detector.

T2K uses the off-axis beam idea to produce a narrow-band neutrino beam with one of the near detectors (ND280) and the far detector located 2.5° away from the main axis. This setup allows T2K to produce a neutrino beam with a narrow energy spectrum peaked at 0.6 GeV which is tuned to maximize the neutrino oscillation probability at 295 km. This configuration also minimizes the background to the ν_e ($\bar{\nu}_e$) appearance measurement.

2.1 T2K neutrino beamline

The T2K neutrino beamline consists of two consecutive parts: a primary and secondary beamline. The primary beamline guides the 30 GeV proton beam from the J-PARC's 'Main Ring' (MR) accelerator to the target station. In the secondary beamline, the protons extracted from MR interact with the graphite target and produce secondary pions which are focused by a set of magnetic horns. The polarity of the horns can be changed to focus either positively or negatively charged pions and produce either neutrinos or anti-neutrinos. The pions enter a 96 m-long decay volume where they decay and produce muons which are stopped on the beam dump and neutrinos which travel further away to the near and far detectors.

2.2 Near detectors station

The near detectors station is located 280 m away from the neutrino target and consists of two main parts: off-axis and on-axis detectors. The off-axis detector (ND280) is built of several sub-detectors encapsulated in the UA1/NOMAD magnet which is the source of a 0.2 T magnetic field. The main ND280 components are: Pizero detector (P0D), Tracker – containing two Fine-Grained Detectors (FGDs), three Time Projection Chambers (TPCs) filled with an argon-based gas mixture, Electromagnetic Calorimeter (ECAL) and Side Muon Range Detector (SMRD).
The goal of the ND280 detector is to measure the neutrino flux before the oscillation occurs. The off-axis detector also provides information about the intrinsic ν_e contamination in the beam and measures various neutrino cross sections.
A schematic view of the ND280 detector is shown in Fig. 2.

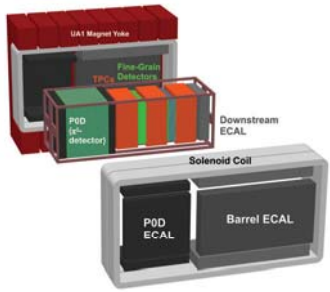

Fig. 2: ND280 off-axis detector and its components. The neutrino beam enters from the left.

The on-axis detector, called INGRID, is composed of 16 iron/scintillator modules and an additional scintillator-only module (proton module). The goal of the INGRID detector is to monitor the beam rate, direction and stability by counting muons from ν_μ charged current interactions. INGRID is also capable of measuring various neutrino cross sections.

2.3 Super-Kamiokande far detector

The Super-Kamiokande detector is the far detector for the T2K experiment. This is the world's largest 'land-based' water Cherenkov detector, which has been operating since 1996 and its technology and operations are well understood [3].

The detector is located 1 km underground in the Mozumi mine and is a cylindrical tank filled with 50 kton of pure water. 13 000 photomultipliers on the walls of the tank detect the Cherenkov light (rings) emitted by the charged particles produced in neutrino interactions.

The Super-Kamiokande detector has a well established electron-muon discrimination technique which is very important for distinguish between ν_e and ν_μ interactions. The Cherenkov rings in the detector can be classified as electron-like or muon-like, depending on their appearance. The muon ring has sharp edges while the electron ring is more fuzzy because of the showering. The mis-identification for a muon as an electron and vice versa is less than 1%.

3. Neutrino oscillation measurements in T2K

The T2K experiment has been collecting physics data since the beginning of 2010 and exceeded 3.16×10^{21} protons on target (POT) as on May 31, 2018. In the analyses presented in this paper 1.49 x 10^{21} POT for neutrino-mode and 1.65 x 10^{21} POT for anti-neutrino-mode has been used.

The strategy for the neutrino oscillation measurements in T2K is based on the data collected by the near and far detector. The data from the near detector (ND280) is fitted using several inputs: neutrino flux prediction, neutrino cross section models and their uncertainties and uncertainties for the event selection in the near detector. The output of the ND280 fit along with the far detector systematic uncertainties are used as inputs for the far detector fit. A fit to the Super-K data is performed using the PMNS neutrino oscillation model and provides the estimates for the oscillation parameters. An alternative approach, where both far and near detector data are fitted simultaneously, has also been developed.

The analysis of the near detector data allows one to reduce the uncertainties in the far detector. Multiple data samples in ND280 are fitted to constrain the combination of the flux and neutrino interaction systematic errors at Super-K. There are six samples (Carbon and Water targets) for neutrino-mode: $\underline{\nu}_\mu$ CC0π, ν_μ CC1π, ν_μ CCOther and eight samples for anti-neutrino-mode: $\overline{\nu}_\mu$ CC1Track, ν_μ CCNTrack, $\overline{\nu}_\mu$ CC1Track, ν_μ CCNTrack. Data on carbon and water targets are binned in outgoing muon momentum and angle. Fitting the near detector data allows the flux and cross-section uncertainties to be reduced from ~15% to ~5%.

Many improvements have also been made to the Super-K data analysis. Apart from the well-established ν_e and ν_μ CCQE samples (only electron/muon in the final state), the new ν_e CC1π sample (additional Michel electron from pion decay) has been introduced into the analysis. Improvements also include: an optimized fiducial volume cut and a new reconstruction algorithm (fitQun).

There are 75 ν_e CCQE, 15 ν_e CC1π and 243 ν_μ candidates selected in the Super-K detector after all analysis cuts. The number of $\overline{\nu}_e$ and $\overline{\nu}_\mu$ anti-neutrino candidates is 9 and 102, respectively. A binned maximum-likelihood fit to all far

detector samples is done simultaneously. The predicted number of events along with the observed ones are shown in Table 1.

Sample	Predicted				Observed
	$\delta_{CP} = -\pi/2$	$\delta_{CP} = 0$	$\delta_{CP} = +\pi/2$	$\delta_{CP} = \pi$	
ν_μ CCQE	268.5	268.2	268.5	268.9	243
$\bar{\nu}_\mu$ CCQE	95.5	95.3	95.5	95.8	102
ν_e CCQE	73.8	61.6	50.0	62.2	75
ν_e CC1π	6.9	6.0	4.9	5.8	15
$\bar{\nu}_e$ CCQE	11.8	13.4	14.9	13.2	9

Table 1: Observed and predicted number of events in the Super-Kamiokande detector.

Observed event rates prefer $\delta_{CP} = -\pi/2$. The marginalization procedure is performed over all nuisance parameters to get the oscillation probabilities as a function of parameters of interest. A detailed procedure of the validation of results is performed including: comparisons across independent fitting approaches (frequentist vs Bayesian statistics), comparisons between different far-detector data binning approaches: (one-dimensional with neutrino energy vs. two-dimensional with outgoing lepton momentum and angle) and pseudo-data fits. The result of the study of atmospheric neutrino oscillation parameters in T2K with additional constraint on θ_{13} angle from reactor experiments is shown in Fig. 3 and Table 2.

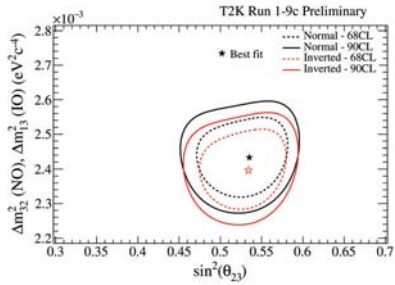

Fig. 3: The 68% and 90% C.L confidence regions for $sin^2\theta_{23}$ and Δm^2_{32} (Normal Ordering) or Δm^2_{13} (Inverted Ordering).

	NO ($\Delta m^2_{32}>0$)	IO ($\Delta m^2_{32}<0$)
$sin^2\theta_{23}$	0.536 (+0.031 - 0.046)	0.536 (+0.031 - 0.041)
$\lvert\Delta m^2_{32}\rvert$ ($\times 10^{-3}$eV^2)	2.434 (±0.064)	2.410 (+0.062 -0.063)

Tab. 2: Best-fit values for $sin^2\theta_{23}$ and $|\Delta m^2_{32}|$ for normal and inverted mass ordering.

One can observe that T2K results are consistent with $\theta_{23} = 45$ degrees. The preferred value of θ_{13} from the T2K experiment alone also agrees with the results from reactor-neutrino experiments within the uncertainties as seen in Fig. 4.

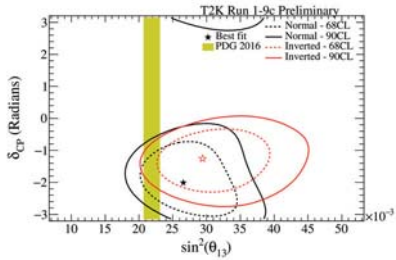

Fig. 4: The 68% and 90% C.L confidence regions for $sin^2\theta_{13}$ and δ_{CP}.

The analysis of the T2K data with the reactor constraint excludes regions of δ_{CP} at 2σ (Fig. 5).

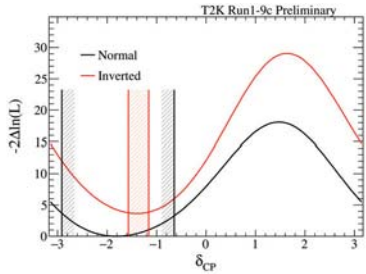

Fig. 5: $\Delta\chi^2$ as a function of δ_{CP} for the analysis with reactor constraint.
2σ confidence regions are also shown.

Values of δ_{CP} which conserve CP symmetry ($0, \pm\pi$) fall outside of 2σ region for both normal and inverted mass ordering and 2σ intervals are as follows: *[-2.914,-0.642]* – for normal ordering and *[-1.569, -1.158]* for inverted. The best fit value of δ_{CP} for normal ordering is *-1.83* rad.

4. Neutrino cross section measurements in T2K

To be able to measure subtle differences in the reconstructed neutrino energy spectra, e.g. induced by the different values of δ_{CP}, it is crucial to understand and reduce the systematic errors.
Currently, the major systematic uncertainties which affect oscillation measurements are the neutrino flux uncertainties and neutrino cross section uncertainties. From the point of view of the neutrino interactions and future neutrino oscillation experiments there is also a need for neutrino-nucleus cross section measurements on various nuclear targets. The near detector of the T2K experiment is a very well suited apparatus to measure neutrino cross sections. Some of the cross sections can be measured at Super-K as well. Extensive work is done in T2K collaboration to test and minimize the model dependence for neutrino-nucleus cross-section measurements and pursue the best methodology. Many measurements for different neutrino interaction channels (CC-inclusive, CC0π, CC1π, CC-Coherent, NC, ν_e) on various targets (carbon, water, iron) and often with novel approaches (eg. Single Transverse Variables) have been performed and many other analyses are ongoing. As an example the measured CC0π cross-section as a function of single transverse variable δp_T is compared with various neutrino interaction models in Fig. 6.

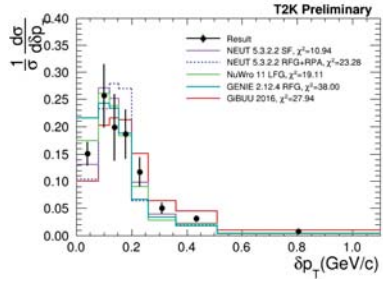

Fig. 6: CC0π cross-section as a function of δp_T compared with various neutrino interaction models [4].

5. ND280 upgrade

An extension of the running period of the T2K experiment has been proposed (T2K-II) [5]. The first stage of the proposal is to extend running from 7.8×10^{21} POT to 20×10^{21} POT. The stage has been approved by KEK and J-PARC. The Main Ring accelerator is planning to be upgraded to reach the beam intensity 1.2 MW. The near detector of the T2K experiment will also be upgraded to increase the angular acceptance and the upgrade will be completed in 2021. The plan is to reduce the systematic errors down to ~4% with the upgraded beam and near detector. T2K-II is expected to reach 3σ CP violation sensitivity.

6. Conclusions

The neutrino oscillation analysis in the T2K experiment presented in this paper uses 1.49×10^{21} and 1.65×10^{21} POT for neutrino-mode and anti-neutrino-mode respectively. T2K is working with high intensity and stable neutrino (anti-neutrino) beam with 470 kW of power. With this amount of data the experiment has provided the world's best measurement of the θ_{23} mixing angle (consistent with θ_{23} = 45 degrees) and delivered 2σ confidence intervals for δ_{CP}: *[-2.914,-0.642]* for normal mass ordering and *[-1.569, -1.158]* for inverted ordering. Many improvements in the analyses have lead to a ~20% increase of number of selected events in the far detector. The T2K experiment also has a broad neutrino cross section program and is producing a lot of important cross-section results. Extensive work is being performed in T2K to search for the best methodology for neutrino-nucleus cross-section measurements with minimal model dependence. The first stage of the proposal to extend the running of the T2K experiment to 2026 to achieve 3σ CP violation sensitivity has been approved.

Acknowledgements

This work was supported by the Polish National Science Centre, project number: 2015/17/D/ST2/03533.

REFERENCES:

[1] Fukuda~Y. et al. (Super-Kamiokande collaboration), *Phys. Rev. Lett.* 81, 1998 (1562); Y. Fukuda et al. (Super-Kamiokande collaboration), *Phys. Rev. Lett.* 81, 1562 (1998).
[2] Particle Data Group, *Phys. Rev. D* 98, 030001 (2018)
[3] Fukuda S. et al. (Super-Kamiokande collaboration), *Nucl. Instrum. Meth. A* 501, 2003 (418); Y. Fukuda et al. (Super-Kamiokande collaboration), *Nucl. Instrum. Meth. A* 501, 2003 (418-462);
[4] arXiv:1802.05078v2 [hep-ex]
[5] arXiv:1609.04111v1 [hep-ex]

The OLVE-HERO calorimeter prototype tests at heavy ion beams of CERN SPS

V.M.Grebenyuk[1,2], A.V.Krasnoperov[1], M.V.Lavrova[1], A.Pan[1,3], D.M.Podorozhny[4], S.Yu.Porokhovoy[1], A.D.Rogov[1], A.B.Sadovsky[1], M.Slunecka[1], A.V.Tkachenko[1] and L.G.Tkachev[1,2]

[1] *Joint Institute for Nuclear Research, Dubna, 141980, Russia*
[2] *Dubna State University, Dubna, 141980, Russia*
[3] *The Institute of Nuclear Physics, Almaty,050032 Kazakhstan*
[4]*Skobeltsyn Institute of Nuclear Physics, Moscow State University, Moscow, 119991, Russia*

Abstract

A project of the OLVE-HERO space detector is proposed for CR measurement in the range of 10^{12}-10^{16} eV and will include a large ionization-neutron 3D calorimeter with a high granularity and geometric factor of ~16 $m^2 \cdot$sr. The main OLVE-HERO detector is expected an image calorimeter of a boron loading of plastic scintillator with a tungsten absorber. Such a calorimeter allows to measure an additional neutron signal which will improve the energy resolution of the detector. More importantly, the rejection power between electromagnetic and nuclear CR components will be increased by factor 30-50 in the whole energy range. The boron loading scintillator detector prototype has designed and tested at the H8 beam test area at CERN SPS during Pb ion run in 2016 and Xe ion run in 2017. The results of the beam tests and the corresponding Monte-Carlo simulation are presented**.**

Introduction

The energy range of 10^{14}-10^{16} eV in the classical "knee" of the galactic Cosmic Rays (CR) spectrum is of great importance for study of the CR acceleration mechanisms and their propagation in our Galaxy. There are no direct measurements of the CR nuclei spectra specifically in the "knee" area. Basic information about CR nuclei in the area 10^{12}-10^{14} eV were obtained in the balloon experiments ATIC [1,2], CREAM [3,4], TRACER[5] and on satellites AMS02 [6,7] and PAMELA [8] . Nowadays the CR study in satellite experiments CALET [9] and DAMPE [10] started.

Determining of the high-energy electron spectrum (> 10^{10} eV) and its possible anisotropy is important to solve a problem of the near CR sources. Extension of the secondary CR spectra by two orders of energy, i. e. CR nuclei (Li, Be, B, sub-Fe etc.), will make it possible to research the processes of CR propagation in the Galaxy in detail.

The fundamental problem of modern physics is to establish the nature of dark matter, the existence of which is firmly established from the different gravitational effects and analysis of the microwave radiation anisotropy. To search for the dark matter particles one requires precise measurements of the electrons and gamma rays spectra up to the tens of TeV.

Therefore additional direct measurements of CR at energies up to 1000 TeV with elemental resolution and measurements of gamma ray flux of TeV energies are needed. Due to the small flux of CR, its effective measurement at such high energies requires a large geometric factor.

Within a framework of the Federal Space Research Program is expected to create the High-Energy Rays Observatory (OLVE - HERO) for the research of the cosmic radiation in the energy range 10^{10}-10^{16} eV. The distinctive characteristic of this project is an unprecedented high exposure factor that will enable to resolve the above mentioned scientific problems.

The main parameters of high-energy cosmic radiation are the type of particle, the value of its kinetic energy and the arrival direction. Therefore, the proposed design of the OLVE-HERO detector is based on the development of a heavy (~10 t) ionization-neutron 3D image calorimeter with a unique high geometric factor (~16 $m^2 \cdot sr$). This geometric factor achieved by optimizing design of the absorber and detecting elements. The three-dimensional structure of the detectors will allow to register particles coming from different directions. As the main detector is expected a scintillation-tungsten image calorimeter with boron loaded scintillator as an active element. This will make it possible to measure an additional signal from neutrons that would improve the energy resolution of the calorimeter, and most importantly, increase 30-50 times the level of rejection between the electromagnetic and hadron-nuclear components of CR in whole energy range [11].

OLVE-HERO detector prototype

It needs to deaccelerate neutrons that produced in calorimeter to measure its additional signal. A prototype of the OLVE - HERO detector is made for the purpose of experimental study of the neutron deceleration effects, schematic view of which is presented on Fig.1. It consists of the 4 boron loaded scintillator planes of 120x120x5 mm^3, collected in pairs (1,2) and (3,4) in the form of 2 modules on the bearing aluminum plate of 1 mm thick, located inside the lightproof container. Charged particles pass through the scintillator with WLS fibers and produce light pulses that are measured by 16-channel PMTs of HAMAMATSU H8711-10. The volume between the modules is filled with a polyethylene granule moderator.

An incoming particle interacts with a target nucleus knocking out secondary particles and leaving the target hit nucleus in a strongly excited state. Removal of the nucleus excitation occurs due to an evaporation of n, p and more complex

nuclear fragments and γ-quanta. The average energy of evaporative neutrons is ~ 2 MeV and they have an isotropic angular distribution. Evaporated neutrons are slowed down to thermal energy and interact with a boron-10 nucleus to produce α-particle and the ^{7}Li nucleus with a total energy 2.78 MeV. The choice of ^{10}B is due to big neutron capture cross section of 755 b and an energetic α-particle production**:**

$$n + {}^{10}B \rightarrow {}^{7}Li + \alpha + \gamma + 2.78 \text{ MeV}.$$

The weight fraction of boron in the scintillator is ~ 5%. Most of the energy in this reaction is carried away by α-particle (1.47 MeV) and spends on generating of a scintillation signal. Its amplitude is equivalent to the signal from an electron with an energy of 76 keV. The typical deceleration time of an evaporative neutron with energy of ~ 2 MeV in polyethylene is 2.7 μs.

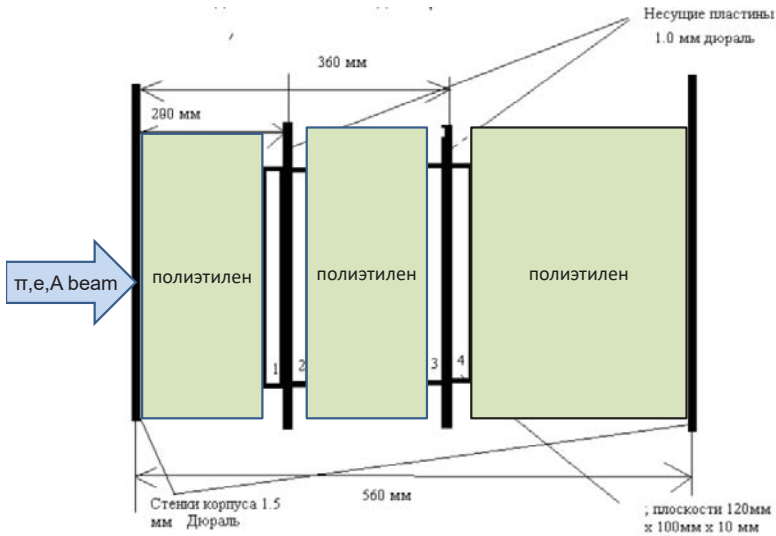

Fig.1 OLVE-HERO detector prototype scheme on the test beam at SPS in CERN.

The prototype tests were carried out at H8 test beam line of CERN SPS in 2016 on the beam of the nuclear fragments with a rigidity A/Z = 2.2-2.5 from accelerated Pb nucleus with an energy of 150 Gev/n. Tests were carried out in 2017 also in a beam of Xe with energy 13 Gev/n or its fragments with rigidity corresponding to A/Z =2.1. The intensity of the nuclei flux in the channel was

~5000 part/sec. Iron or lead bars of different thicknesses used as a target at a distance of 5 cm before of the container.

In Fig. 2 the photo of the detecting plane is presented: the 1 mm grooves were cut in 5 mm thick boron loaded scintillator and WLS fiber by KURARAY was glued. Signals from fibers are gathering via collector to the 16-channel PMT. In detectors 1-3 the fare end of the fiber covered with a layer of silver to the light reflection. In detector 4, as seen in Fig. 2, at the opposite end the fiber makes a loop and returns to the PMT on the other groove, which also increases the amplitude of the light signal on the photocathode. Amplified PMT signal obtained from the last dynode used to organize a trigger.

The neutron signal occurs after the neutron capture by ^{10}B in the scintillator with a delay in comparison with the signals of charged secondary particles from primary vertex that give simultaneous non-delayed counts of all 4 detector planes.

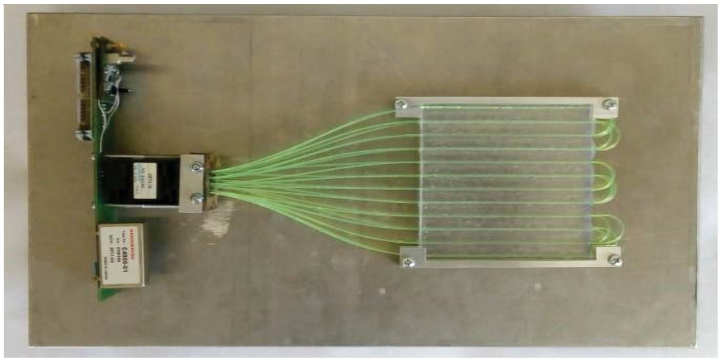

Fig.2 Scintillation plane №4 of OLVE-HERO detector prototype

Evaporation neutrons produced from the exited nuclei and then thermalized by polyethylene moderator. They are registered after thermalization by the same detecting planes. The neutron signal occurs only in one of the planes because a produced α-particle has negligible path and is registered at the place of its formation in the detector. Simultaneous random registration of neutrons in several planes is unlikely. Based on these considerations, the LeCroy electronic blocks was implemented for a measurement scheme, which is shown in Fig.3. The signal from each of the 4 planes is given to the input of the linear adder-splitter "428". Their outputs are connected to the discriminator "623 A" inputs. Their outputs are connected to the inputs of the coincidence circuit"465". This is the trigger generation channel.

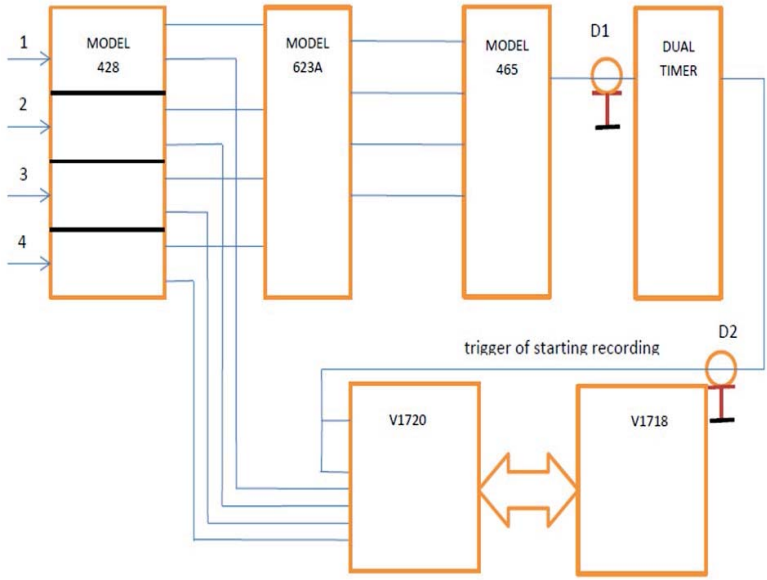

Fig.3.The block scheme of the measurement system

The second outputs of the line splitter are connected to the V1720 digitizer inputs that is located in the VME crate and via the VME USB bridge V1718 connected to a computer. All these units are located in the NIM and VME crates near to the detector. The Dual Timer unit is located in the control room at a distance outside the beam zone. Its input is connected by a cable with a length of about 30 meters with an output of the “465” coincidence circuit which produces a trigger signal. The time position of the output signal from the Dual Timer can be changed from the control room and does not require beam overlap. The signal from Dual Time serves as an event recording trigger which allows measuring the distribution of analog signals up to 16 μs. The timeline of the digitizer V1720 is 4 μs. The same detectors and PMTs were used as in the trigger system as for measuring the delayed neutron signals.

The beam test results of 2017

The test was carried out in a Xe beam with energy 13 Gev/n or its fragments. The linear adder-splitter was excluded from the data taking in the 2917 measurements and signals from the second "623A" outputs were fed to the digitizer inputs with a 30 mV threshold and ~40 ns of the signal duration. The 8-channel digitizer CAEN V1720 was used. In Fig. 4 the examples of events with a

delay ΔT = 4 μs are presented: the amplitude time dependences are shown with a time step of 4 ns in a 4 μs time window. The trigger channel is represented by a dotted line, the amplitudes from 1 to 4 information channels are shown by solid lines. The average values of the signal amplitudes are in the interval <A (t)> = 2160 - 2190 ADC codes and the values are stable over time.

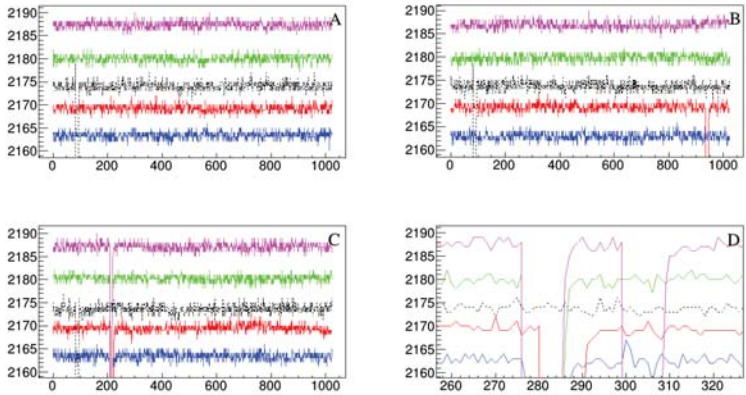

Fig. 4 Time dependences of amplitudes in the 4 ns time steps and in a time window of 1024 time steps of 4 μs.

Figure 4A shows an example of an event when a trigger signal was generated (the peak on the dotted graph in the ~ 100 time step), but there are no signals from the delayed particles. Figure 4B shows an event in which there is both a trigger signal and a single delayed signal in the ~ 950 time step from α-particle, which cannot give a signal in several detecting planes. Figure 4C shows the event when, in addition to the trigger signal, a signal appeared in the ~ 200 time step from another beam particle that passed through the detection planes after a trigger signal. As expected, such a signal occurs almost simultaneously in different planes of the detector. Our beam particles are fragments that fly from the primary target in the accelerator channel. Fragments fly at different speeds, depending on the mass. The difference of speed is small, so we see the appearance of these particles in the window of 4 μs. Figure 4D shows for clarity in more detail the signals from the delayed charged particles in ~280 time step and single signal from α-particle in the ~305 time step. The effective target thickness is 24 mm of Pb plus 20 cm polyethylene to the first detector, which gives ~36% of the nuclear interaction length. That is, with a probability of 30%, secondary charged particles appear from the interactions in the target or retarder.

As shown in Fig.4D, the spread of the appearance of pulses from the delayed beam particles in different channels is ~5 time steps. By selecting the appropriate width of the histogram bin it is possible to obtain the signals from

the delayed particles in different channels in one bin. Accurate to random coincidences neutron will produce a single signal that is used as a criterion for their selection.

Taking into account that a duration range of the delayed neutrons signals reaches 16 μs, an essential limitation of the experiment with this type of digitizer was a restriction due to the width of the time window - no more than 4 μs. With this in mind, the data taken was made with a sequential change in the time delay ΔT after trigger time in 4 μs quanta and subsequent cross-linking of the results obtained at different delays. Fig. 5 shows the results of measuring of the delayed neutron yields in the range from 0 to 4 μs on the Xe beam with a 24 mm thick Pb target in front of the container. The trigger was formed by a condition of the signals coincidence in all 4 detector planes and the data were recorded with a delay ΔT = 0 μs after the trigger. The figure shows that there is a decrease in the yield of delayed neutrons by 1.5-2.0 times. The fourth detecting plane was different from the other ones as described above which is more effective for light collection. This effect is visible in Fig. 5 - the high peak at the first bins in the fourth plane is due to weak signals from the passage of secondary charged particles, which are below the sensitivity threshold on other detection planes.

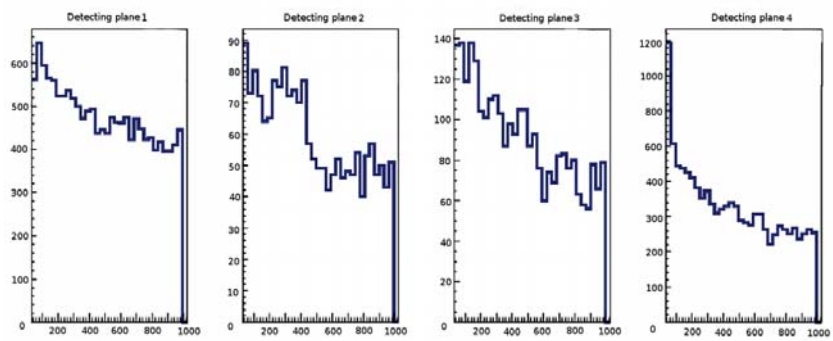

Fig.5. The time dependence of the neutron yield in the range from 0 to 4 μs.

To obtain the time dependence of the neutron signals in the entire interval of 0–16 μs, it is necessary to “sew” the distributions obtained with different delays. The results of the crosslinking is shown in Fig.6. There is a monotonic decrease in the yield of neutrons with increasing time in all channels. Some number of delayed neutrons are lost due to random coincidences in the same time bin. To evaluate this effect, the integral distributions were compared when the interval of 0-1024 time steps was divided into 64 and 32 bins those are represented in Fig.6 by markers "○" and " ∗ " respectively. It seen that the effect of random

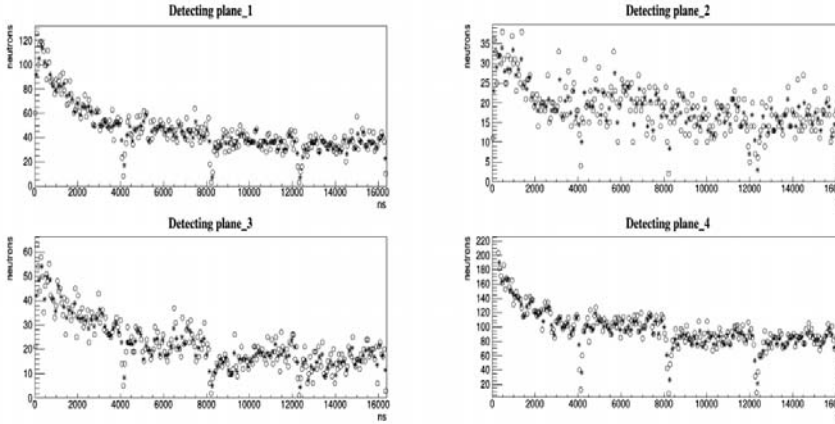

coincidences within the available statistics is insignificant throughout the interval. Visible in Fig. 6 - 8 irregularities at the junctions of distributions with different delays are of a technical nature and have no physical meaning

Fig.6. Integral distributions of neutron yield at a delay of ΔT from 0 to 12 μs with a 24 mm thick lead target and a retarder between detectors.

Fig. 7 shows the integral time distributions of neutron signals with delays from 0 to 12 μs, obtained under the same conditions as in Fig. 6, but without a lead target. It seen that the qualitative behavior of the neutron yield after the removal of the target in front of the detector has changed insignificantly, i.e. most of the registered neutrons are produced and thermalized in a polyethylene moderator.

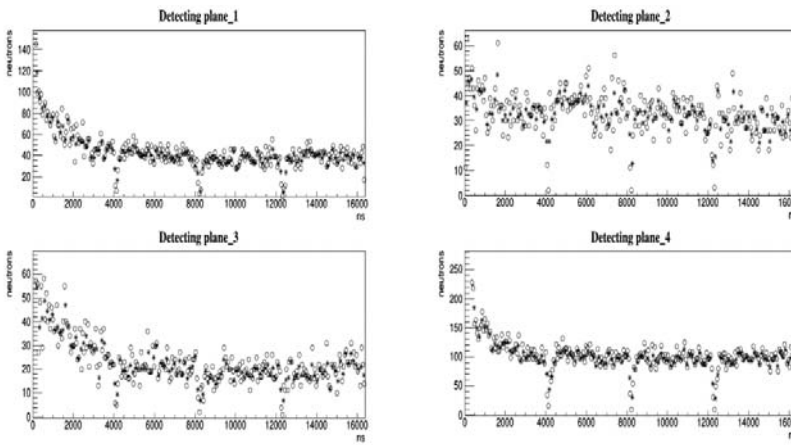

Fig.7. Integral distributions of the neutron yield in the absence of a lead target in front of the detector and a delay of ΔT from 0 to 12 μs.

The beam test results of 2016

The prototype tests were carried on the beam of the nuclear fragments of Pb nucleus with an energy of 150 Gev/n. The test beam was settled in the rigidity interval A/Z from 2.2 to 2.5. Fig. 8 shows the integral time dependence of neutron signals with delays of up to 12 μs. The setup configuration was the same, but in 2016 only three detector planes worked. In addition, the signals of 1 and 2 planes were recorded in one channel and there was no data with zero delay. Obviously, the qualitative behavior of the neutron yields are similar for both tests.

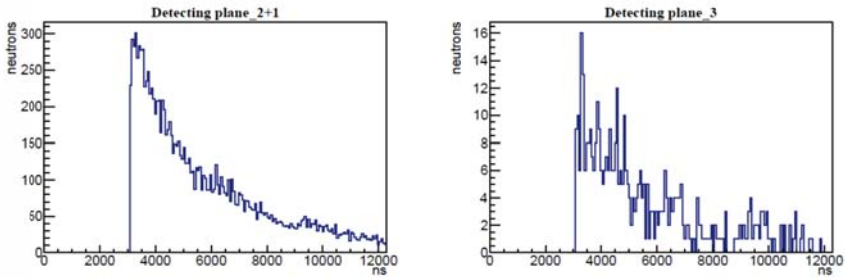

Fig.8. The integral time dependence of the neutron yield with delays from 3 to 9 μs, obtained on a beam of fragments from lead ions with energy 150 Gev/n and with rigidity of A/Z = 2.5.

Monte Carlo simulation results

The following physical models were used in the simulation: the Bertini model of the intranuclear cascade, supplemented by evaporative Dresner model; the intranuclear INCL4 cascade model, together with the evaporation ABLA (GSI) model, It was applied also the CEM03.3 generator of interactions based on the cascade-exciton model using the improved evaporation model for calculating of the evaporation and division processes.

The neutron spectrum and their spatial distribution in the detector were calculated. Neutrons were generated in a lead target from one Xe-132 ion with energy of 13 GeV/n. The neutron spectrum in the detector is shown in Fig. 9. The spatial distribution of evaporated neutron sources of all energies with good accuracy is a narrow beam channel in the detector material surrounded by halo slowed neutrons.

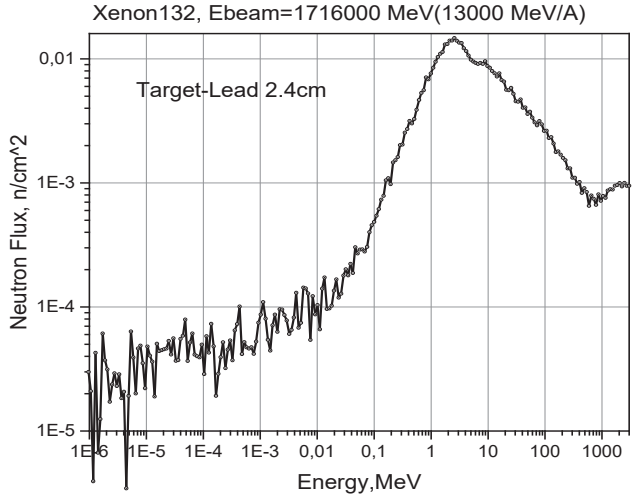

Fig. 9. The Monte-Carlo spectrum of neutrons produced in a lead target from a single ion Xe-132 with an energy of 13 GeV/n.

About 200 evaporative neutrons are born on average per xenon ion in the cascade, 180 of them leave the detector without interaction. To speed up the calculations, the simulation was divided into parts: (1) - neutron source calculation, which one represents as a track ~ 1 cm thick, (2) then one counts only neutron tracks, assuming their source is filamentary and with an evaporative isotropic neutron spectrum.

The simulation result presented in Fig.10, which shows a noticeable discrepancy with the experimentally measured dependence of the neutron signal on the delay time. A possible reason of the discrepancy is the appearance of neutrons from the additional interactions of later-in-time beam particles in the target or moderator. Thus events with different initial time shifts $dT \neq 0$ are superimposed and data cannot be directly compared with the simulation where are no such neutrons. That is, the measurements contain neutron signals that have arisen from later interactions of the beam particles, i.e. having a lower delay and giving the substrate in the measured distribution, which is not in the simulation. From the simulation shown in Fig.10, it seen there should be a large difference in the signals between the first and second pairs of detection. This is due to the thermal neutrons are formed mainly in the first part of the detector, so that the second detector planes located at a distance of 160 mm have smaller angular acceptances. This difference is not visible in the data obtained because detectors

have different sensitivity thresholds and this "covers" the effect of acceptation. Another possible reason is that the simulation did not take into account the events whose primary vertex is not in the target but in the substance of the detector.

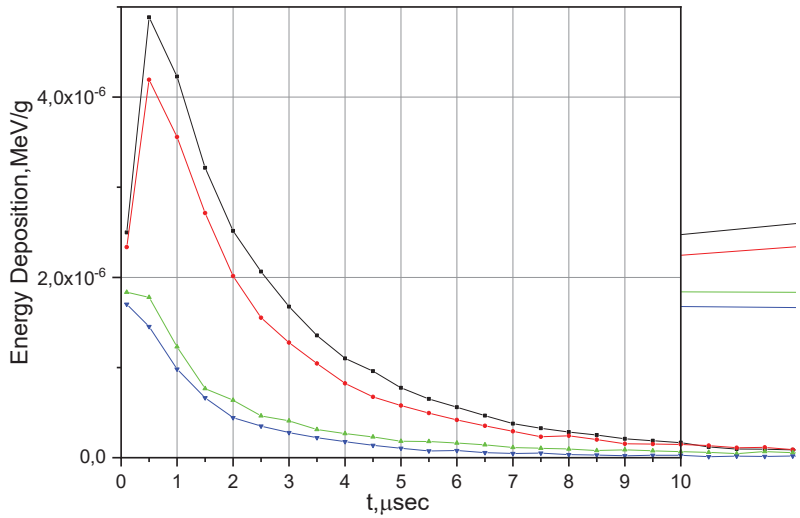

Fig.10. Dependence of the neutron signal value of the delay time

Conclusion

The results of the OLVE-HERO prototype calorimeter tests on lead and xenon ion beams on the SPS of CERN presented. Using a boron loaded scintillator in the prototype together with a polyethylene moderator gives a clear picture of the appearance of delayed signals from the neutron capture of boron-10 in the range of 0 - 16 μs after the primary interaction of the beam particle. The results are in qualitative agreement with the Monte Carlo simulation.

The density of the CR flux in the orbit of the Earth satellite with energy E > 1 GeV/n is ~ $1.2 \cdot 10^8$ /cm^{2}sr·year. For the OLVE-HERO parameters in the form of a cylinder with a diameter of 1.6 m and a height of 1.5 m, the area of the lateral and upper surface is ~10 м^2, so that the total CR flux through the detector from the upper hemisphere is ~$7.5 \cdot 10^6$ с$^{-1}$. This flux will generated evaporative and thermal neutrons. Thus, inside the detector the equilibrium density of thermal neutrons will be established, which will determine the value of the constant background signal in the scintillator, which can "score" the signal from the

charged component of the CR showers, so there is a fear that the detector will "go blind" or give incorrect results. To obtain the final answer, it is necessary to carry out additional tests on the beams, a special simulation of this effect taking into account the spectrum and composition of the CR, as well as the geometry of the detector. The new OLVE-HERO prototype was built and tested at SPS CERN in 2018. Analysis of the new data is in progress.

References

[1] H. S. Ahn et al. // The energy spectra of protons and helium measured with the ATIC experiment. Advances in Space Research, 37 (2006) 1950-1954.
[2] A. D. Panov et al. // The energy spectra of heavy nuclei measured by the atic experiment. Advances in Space Research, 37 (2006) 1944-1949. DOI: 10.1016/j.asr.2005.07.040
[3] Y. S. Yoon et al. // Cosmic-ray proton and helium spectra from the first CREAM flight. The Astrophysical Journal, 728:122 (2011). doi: 10.1088/0004-637X/728/2/122
[4] H. S. Ahn et al. // Energy spectra of cosmic-ray nuclei at high energies. The Astrophysical Journal, 707 (2009) 593-603. doi: 10.1088/0004-637X/707/1/593
[5] A. Obermeier et al. // Energy spectra oprimary and secondary cosmic-ray nuclei measured with TRACER. The Astrophysical Journal, 742:14 (2011). doi: 10.1088/0004-637X/742/1/14
[6] M. Aguilar et al. // Precision Measurement of the Helium Flux in Primary Cosmic Rays of Rigidities 1.9 GV to 3 TV with the Alpha Magnetic Spectrometer on the International Space Station. PRL 115 (2015) 211101. DOI: 10.1103/PhysRevLett.115.211101
[7] M. Aguilar et al. // Precision Measurement of the Proton Flux in Primary Cosmic Rays from Rigidity 1 GV to 1.8 TV with the Alpha Magnetic Spectrometer on the International Space Station. PRL 114 (2015) 171103. DOI: 10.1103/PhysRevLett.114.171103
[8] O. Adriani et al. // Physical Review Letters 106 201101 (2011).
[9] P.Brogi et al. // CALET measurements with cosmic nuclei: expected performances of tracking and charge identification. Proc. 34th ICRC. Hague, Netherlands. PoS ICRC2015 (2016) 595.
[10] X.Wu et al. // The Silicon-Tungsten Tracker of the DAMPE Mission. Proc. 34th ICRC. Hague (2015) PoS.
[11] Aleksandrov K.V., Ammosov V.V., Chubenko A.P. et al. // Nucl. Instr. Meth. in Phys. Res. A 459 (2001) 135

Search and study of extensive air shower events with the TUS space experiment

Andrey Grinyuk[1], *Maria* Lavrova[1], *Ulkhanym* Nurtayeva[1], *Artur* Tkachenko[1], and *Leonid* Tkachev[1,2,*] for Lomonosov-UHECR/TLE Collaboration

[1]Joint Institute for Nuclear Research
[2]Dubna State University

Abstract. The TUS experiment is aimed to study the energy spectrum and arrival direction of Ultra High Energy Cosmic Rays (UHECR) at E ~ 100 EeV from the space orbit by measuring the fluorescence radiation of the Extensive Atmospheric Shower (EAS) in the atmosphere. It is the first orbital telescope aimed for such measurements and is taking data since April 28, 2016. The TUS apparatus structure, methods of UHECR on-line selection and off-line data analysis are described. A few UHECR EAS candidates have been found. Preliminary results of their study are presented.

1 Introduction

The measurements of Cosmic Ray (CR) energy spectrum, composition and arrival directions in the wide energy interval are an important part of modern particle physics and astrophysics. The TUS project's goal is the experimental study of Ultra High Energy Cosmic Rays (UHECR) at energies about ~ 10^{20} eV. The fluorescent and Cherenkov radiation of the EAS generated by UHECR particles should be detected in the Earth's atmosphere on the night side of the orbit at altitudes 400–500 km. An important advantage of space detector is the possibility of taking data from all arrival directions of the sky with the same apparatus and with the same systematic uncertainties. TUS is the first attempt to detect UHECR from space and is a pathfinder for the next more powerful detectors KLYPVE [1] and JEM-EUSO [2].

2 The TUS detector

The TUS detector on board Lomonosov satellite was launched into the orbit on April 28, 2016. It has a sun-synchronous orbit with an inclination of ~ 97°, a period of circulation ~ 94 min, and height about 470-500 km. After a few months of flight tests and tuning of TUS apparatus on the satellite, the regular data taking have been started. During regular operation, the detector measures the UV background level and adjusts the HV and the sensitivity of the PMTs at the background radiation variation [3]. The TUS detector is presented in Fig.1 and consists of two main parts: a modular Fresnel mirror-concentrator and a photo-receiver matrix with 16×16 Hamamatsu R1463 PMT pixels and the corresponding DAQ electronics. TUS optical system field of view (FoV) is ±4.5°, one pixel FoV is ≈ 10^{-4}sr, a PMT quantum efficiency is ~ 20% for the wavelengths of 300-400 nm.

*e-mail: tkatchev@jinr.ru

Figure 1. Schematic view of the TUS detector on-board the Lomonosov satellite: “1” marks the mirror-concentrator, “2” marks the photo-detector.

The TUS detector has a two-level trigger. The first-level trigger is a threshold trigger: the photo-detector modules board calculates a moving sum of PMT signals during 16 time steps in each channel and looks for an moving sum value above a threshold level. The second-level trigger is a pixel-mapping trigger. This procedure selects cases of sequential triggering of spatially contiguous active pixels that are also adjacent in time, allowing for the selection of events with a special spatial-temporal pattern. The TUS DAQ electronics forms a file of 256 time steps for each 256 channels and can operate in four modes intended for detecting various fast optical phenomena in the atmosphere on different time scales. In EAS mode the DAQ electronics works with a time step $\Delta t = 0.8$ μs. The TUS trigger operation is described in more details in [4]. During two years of operation, the TUS detector has measured more than 200000 events most of which are background events. More information about the different types of the background events may be found in [5].

3 The relative PMT calibration

During the first days of operation ≈20% PMTs were broken due to HV tuning system failure. For the same reason, the properties of the remaining PMTs are changed. Calibration of PMT gains was done based on analyzing background data itself.

For this purpose all time sequences (256 time steps) in all pixels (224 working pixels) of all received events were classified into 2 categories: pure “background” pixels and possibly containing signal of any origin. Classification was done by applying multiple cuts on the statistical properties of data of each time sequence. Most important of the cuts are kurtosis, a cut on the slope of the average and cuts on anomalously high and anomalously low mean. Comparison with Monte-Carlo simulated signals shows that the tails of above distributions of real data are significantly wider than what would be expected from pure Poisson based background signal. Therefore the tails are presumed to contain non-background signals and central part to not contain significant contamination to background.

Only events where there were more than 16 "background" pixels (and therefore more than one PMT module) were included in the following steps. Selected in the above way "background" pixels had their mean signal divided by the average mean signal over all "background" pixels in the same event. That ratio was then averaged for that pixel over all the events. The physical background varies in time from event to event across the whole field of view of TUS. Additionally it varies in each event from pixel to pixel due to ground albedo inhomogeneity and clouds. The above order of averaging was chosen so that it should converge under such conditions to real relative PMT gains Grel, given enough data. Division of data into 3 fully statistically independent samples, corresponding to 6 month of operation each, provides con-

sistently repeating coefficients as it presented in Fig. 2 that validate this assumption.
It is expected that this method could introduce systematic bias for pixels with extremely high or extremely low PMT gains. Their signals might get counted at the edge of some of the statistical cuts part of the time. This may lead to their gains evaluated as more moderate than they really are. To counter that it may be sufficient to mark calibration of several pixels as unreliable (though pixels with very low gains were already not considered reliable anyway) and their exclusion from event reconstruction.

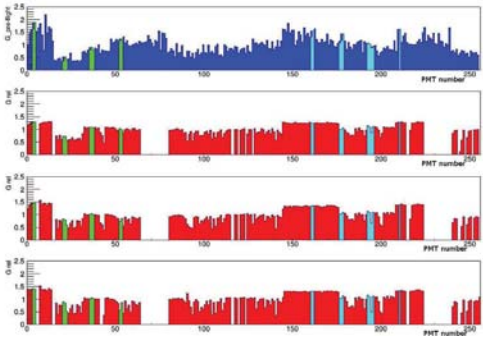

Figure 2. Relative PMT gain coefficients for all 256 channels according to pre-flight measurements (top) and reconstructed from background data for first 3 half-years of operation.

The average value of the absolute relative difference of the PMT coefficients was performed to minimize according to the value of the scale factor for all coefficients. They differ by 0.09, difference from preflight measurements ≈ 0.35. Since these coefficients are approximately normalized by one, it can be said that 0.09 is the error of this relative calibration method.

4 EAS candidates

A few of EAS candidates were found and analyzed according to the understanding of the EAS physics and the TUS detector simulation. The *TUSReadData* program package was elaborated for TUS events analysis [4]. Some details of the analysis criteria may be found in [6].

In Fig.3 the summary of the events is shown: the date and UTC time of the event measurement are the figure title, hit pixels together with dead ones in the upper panel and the amplitude variation (ADC codes) of time for selected hit pixels in the lower panel. The markers and colors of the selected pixels on the upper panel indicate the arrival times for the maximum EAS signals in the time steps. Active pixels are grouped in an oblong spot. It can be seen from the waveforms that characteristic duration of the signal is 70–100μs which is more that one can expect from a vertical EAS. The time position of the maximum of the signal in each pixel has some shift from one pixel to another. This is an argument in favour of a EAS origin for these events. There is a general property of waveforms of two EAS events: the EAS signal starts from dead module then moves across alive pixels and at last go to outside of the PMT matrix and TUS FoV. The EAS movement is shown by arrows and its exit outside of FoV may be a possible reason for the Cherenkov peak absence at the EAS end that presented in the bottom plots. Green and light blue colors in Fig.2 indicate PMTs that

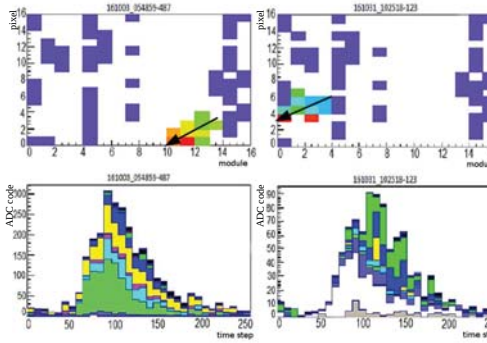

Figure 3. The EAS candidates. Upper plots – image of event with hit pixels and not-working (blue) ones. Bottom plots – the amplitude variation of time for selected hit pixels

correspond to the found EAS candidates: green for event #123 and light blue for event #487
It is important to note that a possible thunderstorm activity was studied in the region of these events measurements. During the time period of the TUS events, no lightning strikes were register in these regions. This provides a strong support for a non-thunderstorm origin of the events.
The next step of the EAS candidate study is a reconstruction of its arrival directions. It is possible to do after the relative calibration coefficient calculated. The *TUSFitData* program package was elaborated for TUS events analysis to do this job. Some details of the event reconstruction procedure and arrival directions measurements are presented in [4].
To check a correctness and reliability of the procedure, the same analysis was fulfilled for MC simulated events that is generated with ESAF package[7] and the TUSSIM program[8]. ESAF simulated events in the energy range logE [eV] = 19.7 – 20.5 and zenith angles θ = 30-50° were analyzed in the same way as for the real events. A difference between the arrival angles of simulated EAS as given by ESAF program generator and the reconstructed zenith θ and azimuth ϕ angles for these events is presented in Fig.4. It gives an evaluation of the systematic errors of these angles measurements. There are rather long tails in the differences those are not exactly understood. Possible reasons: 1) presently the *TUSFitData* program doesn't take into account that TUS detector is out of vertical plane with EAS axes, 2) ESAF generated arrival angles doesn't affected by off axis EAS Cherenkov peak but the reconstructed ones do it. To estimate the statistical errors of arrival angles of the measured EAS events, location of the hit coordinates were randomly variated inside of every pixel at a particular point in time. Afterwards the linear 3D-fit of hit pixels was done and arrival angles calculated by the reasonable number times with a such randomization and real amplitudes of the pixels. The distributions of θ and ϕ angles are plotted on the histograms and are presented in Fig. 5. Variation of the minimum threshold value for the amplitude (in ADC codes) leads to inessential change the angles and presented in Table 1. Finally the following arrival angles were obtained for the EAS candidates: $\theta \approx 28° \pm 2.5°_{\text{stat}} \pm 8.7°_{\text{syst}}$, $\phi \approx 275° \pm 5°_{\text{stat}} \pm 15.5°_{\text{syst}}$ for event #487 and $\theta \approx 54° \pm 2.5°_{\text{stat}} \pm 8.7°_{\text{syst}}$ $\phi \approx 233° \pm 4°_{\text{stat}} \pm 15.5°_{\text{syst}}$ for event #123 in the TUS coordinate system.
Analysis of TUS data shows that most of the events cannot be the EAS candidates. It looks

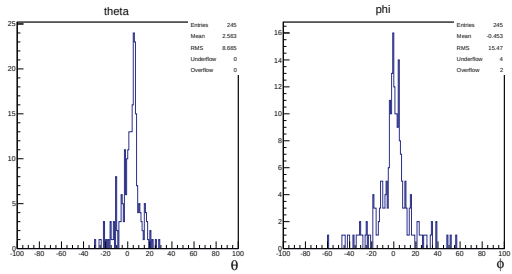

Figure 4. Difference between ESAF simulated and TUSReadData reconstructed zenith θ and azimuth ϕ angles.

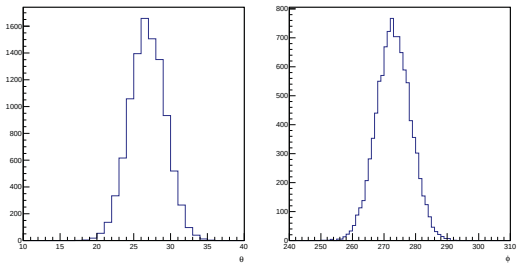

Figure 5. Distributions of the θ and ϕ angles measurements for event #487.

Table 1. Variation of the measured arrival angles and their uncertainties for EAS candidates at different thresholds

threshhold	#487		#123	
	θ	ϕ	θ	ϕ
0	29 ± 2	279,3±4,5	55,82±2,4	234,6±2,8
5	27,9±2,2	273±5,2	54,17±+2,4	233±3
10	27,6±2,4	295,6±5,3	52,7±3	227,7±3,6
15	27,6±2,4	295,8±5	42,9±4,2	218,7±6,3

like a short ≈150μs flash of l ight. Typically such events look like tracks of the few pixels length. The zenith angles of such events are near zero. It means that we have a non-moving flash source of light. There were no Cherenkov flashes at the ends of cascade curves as it may be expected in some EAS events. Besides the time durations of the signals are longer than it should be for vertical EASs. The pseudo EAS events distribution on the PMT matrix is homogeneous that excludes the apparatus nature for these events. The majority of EAS-like events can be related to fast anthropogenic signals.

5 Discussion and conclusion

The TUS detector is operating on board the "Lomonosov" satellite. TUS proved the possibility of registration of UHECR from the space orbit. During TUS data taking in EAS mode and a search for an UHECR a large number of rapid events of the various origins were observed that take place in the atmosphere of the Earth. At least two EAS candidates were selected and their arrival angles were measured. The EAS candidate energy evaluation is not yet obtained due to absence of the absolute PMT calibration. Analysis of TUS data shows that most of the events cannot be the EAS candidates [4]. Their look like short $\approx 150\mu$s flashes of light. Typically such events look like tracks of the few pixels length. The zenith θ angles of such events are near zero. It means that we have a non-moving flash source of light. There were no Cherenkov flashes at the ends of cascade curves as it may be expected in some EAS events. Besides the time durations of the signals are longer than it should be for vertical EASs. The pseudo EAS events distribution on the PMT matrix is homogeneous that excludes the apparatus nature for these events. The majority of EAS-like events can be related probably to fast anthropogenic signals. Nevertheless some of these events may contain genuine EAS events at energy >70 EeV that is lower limit of the sensitivity according to TUS detector simulation [4]. A more detailed analysis of the TUS data is in progress for search of the other EAS candidate events.

6 Acknowledgments

The TUS experiment on board the "Lomonosov" satellite was realized within the Federal Space Program of Russia with funding by the Russian Space Agency. The data analysis is supported by RFBR grants No. 16-29-13065 and No. 15-02-05498.

References

[1] RG. K. Garipov et al., Bulletin of the Russian Academy of Sciences: Physics, **V79 Issue 3**, 326–328, (2015)

[2] The JEM-EUSO Collaboration, Experimental Astronomy, **V40 Issue 1**, 19-44, (2015)

[3] P. A. Klimov et al., Space Science Reviews, **V212 Issue 3–4**, 1687–1703 (2017)

[4] L.G.Tkachev. PoS ICRC2017 527 (2018)

[5] B.A. Khrenov at al., Journal of Cosmology and Astroparticle Physics **V2017 Issue 09**, 006 (2017)

[6] S.V. Biktemerova et al., arXiv:1706.05369v1 [astro-ph.IM] 16 Jun 2017

[7] C. Berat, S. et al., Astroparticle Physics, **V33**, 221-247, (2010)

[8] A. Grinyuk et al., Astroparticle Physics **V90** 93-97 (2017)

Imaging Atmospheric Cherenkov Telescope for the TAIGA experiment – JINR participation

A. Borodin[1]*, V. Grebenyuk[1,2], A. Grinyuk[1], A. Pan[1,3], Y. Sagan[1,2], A. Shalyugin[1], L. Tkachev[1,2]

[1] Joint Institute for Nuclear Research, Dubna, Russia

[2] Dubna State University, Dubna, Russia

[3] The Institute of Nuclear Physics, Almaty, Kazakhstan

E-mail: artur_b@mail.ru

Abstract

TAIGA (Tunka Advanced Instrument for cosmic ray physics and Gamma Astronomy) is designed for the study of gamma rays and charged cosmic rays in the energy range of 10^{13} eV - 10^{18} eV. The JINR full responsibility is design and fabrication of mechanics for the Imaging Atmospheric Cherenkov Telescopes (IACTs). The field of view of the IACT is ~ 10×10 degrees and it has a Davis-Cotton optical system with 34 mirrors, 0.60 m diameter each, a focal length is 4.75 m and a camera of 560 of the XP1911 PMTs. The first IACT has been operating since 2016 in the Tunka valley near Lake Baikal.. Production of the second IACT is in progress. The report will present the procedure and the results of the PMT calibration, the mirror fabrication and its optical parameter measurements. Additionally, a method of mirror alignment is presented. It replaces the present visual assessment of the image

by a pattern recognition program applied to a screen shot of the image of the calibration source.

Introduction

In the last decades many experiments have focused on the identification of Cosmic Ray (CR) sources and on the understanding of their acceleration and propagation mechanisms. It is expected that the Galaxy contains objects that can accelerate CR up to energies above 10^{15} eV ("PeVatrons"), although uncertainty remains about the nature of these objects. Due to the hadronic scenario of CR acceleration, these objects should also be emitters of gamma-rays up to energies of 100 TeV, and gamma-rays observations at ultra-high energies should lead to unambiguous identification of these PeVatrons.

The information about the CR above 100 TeV is provided mainly by ground–based Extensive Air Shower (EAS) experiments. EAS experiments are able to observe a cascade of particles produced by the interaction between CR and the Earth's atmosphere.

Despite a very large amount of data collected so far, the origin and propagation of CR are still under discussion. Until now, no gamma-ray source could be established above 100 TeV, mainly due to the insufficient effective areas of current gamma-ray observatories. To solve this problem, the TAIGA collaboration has created an experimental setup, which contains different types of detectors located on a large area in the Tunka valley near Lake Baikal. IACTs as the part of this array will improve detection sensitivity of the whole setup. This hybrid method will allow to increase PeVatrons detection efficiency.

TAIGA-IACT project

IACTs are the primary instruments for gamma-ray astronomy in the TeV energy range and allow to precisely determine the gamma-ray spectra. The energy of gamma rays is determined from the analysis of IACT images, taking into account the radial distribution of Cherenkov light within EAS. In case of stereoscopic systems of multiple IACTs, which observe EAS from different viewing angles, the location of the shower axis and hence the distance of a given telescope from this axis can be obtained by a simple geometrical reconstruction. For single IACTs, the impact distance can be estimated based on the location and shape of the Cherenkov image within the camera, albeit with larger uncertainty.

The problem of existing experiments with IACTs – HESS [1], MAGIC [2] and VERITAS [3] – is based on the impossibility of scanning the entire sky due to a small viewing angle (3-4°). It leads to insufficient sensitivity to gamma radiation with an energy E > 15-20 TeV, due to small effective detection zone (0.1 km^2). It makes it impossible to detect gamma radiation of more than 100 TeV with their help. For this reason TAIGA setup includes wide-angle Cherenkov detectors HiSCORE timing array with an energy threshold for gamma-ray induced EAS 30 TeV and 100 TeV for hadron CR component. The HiSCORE viewing angle is about 0.6 sr and an angular resolution of 0.1-0.2°, as well as IACTs. IACTs will increase the sensitivity of the array in the low-energy region, while allowing to retain a high angular resolution [4].

The advantage of a few IACTs added to the wide-angle timing array is their better gamma/hadron separation by the analysis of the image parameter information, while core position, direction and energy can be better reconstructed by the timing array. Combination of information from both detector gives a superior result compared to the performance of each single component. This hybrid method allows

to reduce the background hadronic CR showers by about 100 times at the energy of 100 TeV for point-like sources and to increase the distance between IACTs up to 600 m without loss of accuracy of the reconstruction in the measurements of spatial and energy characteristics of EAS.

In 2019 the number of TAIGA-HiSCORE stations will be increased up to 100–120 (area of 1 km^2) and the number of IACTs will be increased up to 3. For more distant future expansion proposal it is expected that the detection sensitivity of such array for local sources of the 5 km^2 observatory in the energy range 30-200 TeV will be 10^{-13} $erg \cdot cm^{-2} \cdot s^{-1}$ for 500 hours of observation or 10 detected events [5].

Fig. 1. presents the EAS events examples on the IACT camera.

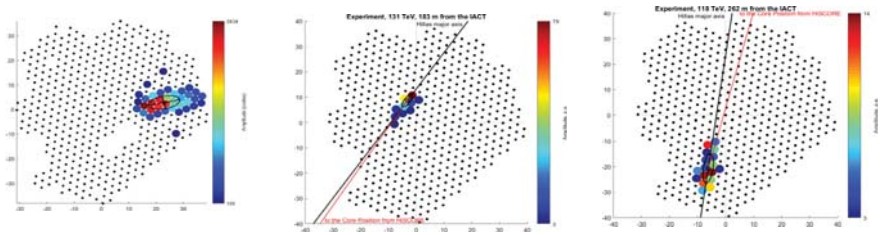

a b c

Fig.1. (a) Example of the image of experimental event together with the Hillas ellipse and major and minor axis. Pixels above threshold are denoted by colored points, pixels below threshold – by gray points. (b,c). The shower axis determined by TAIGA-HiSCORE is projected onto the camera plane (red line). The image major axis (Hillas formalism, black line) is in reasonable agreement with the red line.

Fabrication of the IACT at JINR

The IACT gamma telescope for the TAIGA experiment was fabricated mainly at JINR on the basis of the HEGRA telescope design. IACT represents the atmospheric Cherenkov telescope of Davies-Cotton type. The following requirements were made to the IACT [6]:

- Alt-azimuth mount;
- Spherical shape of 34 mirror modules with a diameter of each ~ 60 cm and with a total mirror area of 9.6 m^2;
- Viewing angle is ± 4.86°;
- Turn around the horizontal axis (zenith angle) -10 + 95°;
- Turn around the vertical axis (azimuthal angle) 0-410°;
- The angular accuracy is 0.01°;
- Driving and positioning system – manual and remote – with the possibility of computer control;
- The rotation speed is ~ 2 deg/sec;
- The detection chamber with diameter of ~ 95 cm (diameter of sensitive area is about 81 cm [7]) represents the matrix of PMTs with FE and DAQ electronics. The weight of the camera is ~ 200 kg and it is fixed at a focal length of 475±1 cm from the mirror. The signals from the Cherenkov radiation of the EAS are focused on the camera by the mirror facets.
- Operating conditions – temperature from minus 40 to plus 30°C and high humidity.

Fig. 2. The first (left) and the second IACT (right) in the Tunka valley (September 2018)

Imaging camera comprises 547 PMTs XP1911. Each one has 1.5 cm photo-cathode diameter. Also each PMT is equipped with Winston cone with diameter of 30 mm which enhances sensitive area by factor of 4 and designed in such a way that a single pixel of the camera views the whole reflector of the telescope. An angular size of a single pixel is 0.36°. The total FOV of the IACT is 9.72° [8].

All PMTs are grouped in an identical clusters of 28 PMTs (Fig.3). Every cluster consists of PMTs with similar dark currents and gains at the same voltage. It allows to simplify the camera tuning procedure and the EAS signals reconstruction.

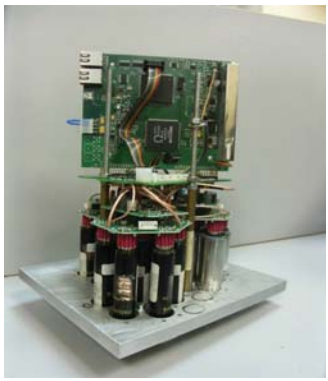

Fig.3. Cluster of 28 PMTs with electronics

Focusing mirrors production method

The method of the focusing mirrors production was developed at JINR. The method is use a mold and a workpiece which are undergoes to controlled heating in the furnace for 48 hours. The glass disk deforms and takes the corresponding spherical shape of steel mold under the action of gravity. A special mode of temperature changing makes it possible to achieve a sufficiently smooth surface and to avoid gluing together of the workpiece and the mold.

Current experiments are aimed to increase the smoothness of the final product and to avoid the subsequent glass polishing and to minimize the curvature errors to the limits permissible for the TAIGA-IACT. As a result, the diameter of the focal spot should not exceed 3 mm. The initial glass disks quality with a mirror diameter of 600 mm the thickness uniformity of about 0.02 mm allows to expect that the bending procedure will minimize subsequent processing.

Driving and positioning system

Rotation around each axis is performed by Phytron ZSH107/4.200.12,5 stepper motors. Each of them is equipped with a planetary gearbox (gear ratio 40, a maximum backlash 16', maximum torque 17 N·m) and a worm gearbox (gear ratio 50, nominal torque 1450 N·m). Each motor performs full turn in 200 steps in the full-step mode. So, the telescope performs full turn in 400000 steps. The angular position monitoring is performed with the Hengstler one-turn absolute encoders (resolution 17 bit, SSI Gray code). Also each axis is equipped with two limit switches. Stepper motors, encoders and limit switches are connected to the PhyMOTION stepper motor controller. In addition to other functions controller supports micro-step mode up to 1/512 of a full step, that can be used for smooth tracking. Remote access to the controller is carried out via Ethernet.

To determine the accurate position of the telescope in the sky a CCD-camera Prosilica GC1380 is used. The field of view of the CCD-camera is approximately 30°x20°, and the angular resolution is about 83 arcseconds that allows to capture image of the sky with observed source as well as the telescope camera. Thus, it is possible to determine the reference to the celestial coordinate system and the position of the Cherenkov camera simultaneously. Position that allows it of the CCD camera is on a frame of the telescope near the mirrors.

The CCD-camera has a resolution 1360x1024 pixels and contains 12-bit ADC. The camera can run up to 20 frames per second, and exposure time can be set from microseconds to one minute. To perform control and data acquisition from the camera remote access is available via Ethernet [9].

Mirrors adjustment system

The mirrors of the IACT are located on separate flanges with the orientation mechanism. The mirrors are adjusted manually. To improve the alignment accuracy a two-stage procedure has been developed. First, the point source image produced by the separate mirror is taken away from the focus in order to be assigned to this mirror. Then, the focal picture is taken by the camera and a special program gives recommendations on the orientation of the mirror for accurate adjustment.

Conclusions

The first IACT has operating as part of the TAIGA setup since 2016. Mechanics of the second one has been fabricated and tested in the JINR. Now it is under field tests in Tunka valley. Also JINR developed a technology for IACT mirror facets manufacturing and control. Fabrication of the third IACT has been started.

References

[1] A. Förster et al., Gamma-ray astronomy with H.E.S.S., Nuclear Instruments and Methods in Physics Research Section A: Accelerators, Spectrometers, Detectors and Associated Equipment, Volume 766, 1 December 2014, Pages 69-72.

[2] Javier Rico, on behalf of the MAGIC Collaboration, Overview of MAGIC results, Nuclear and Particle Physics Proceedings, Volumes 273-275, April–June 2016, Pages 328-333.

[3] Jean-Francois Rajotte for the VERITAS Collaboration, Upgrade and performance of the VERITAS telescope array, Nuclear Instruments and Methods in Physics Research, Section A: Accelerators, Spectrometers, Detectors and Associated Equipment, Volume 766, 1 December 2014, Pages 61–64.

[4] N. Budnev et al., The TAIGA experiment: from cosmic ray to gamma-ray astronomy in the Tunka valley, Journal of Physics: Conference Series 718 (2016) 052006.
[5] E. Postnikov et al., Commissioning the joint operation of the wide angle timing HiSCORE Cherenkov array with the first IACT of the TAIGA experiment, PoS(ICRC2017)756.
[6] N. Budnev et al., The TAIGA experiment: From cosmic-ray to gamma-ray astronomy in the Tunka valley, Nuclear Instruments and Methods in Physics Research A 845 (2017) 330–333.
[7] I.I. Yashin et al., The TAIGA project, Journal of Physics: Conference Series 675 (2016) 032037.
[8] Igor Yashin et al., Imaging camera and hardware of Tunka-IACT, PoS(ICRC2015)986.
[9] D. Zhurov et al., Software design for the TAIGA-IACT telescope pointing and control system, PoS(ICRC2017).

Charged dark matters, missing neutrinos, cosmic rays and extended standard model

Jae - Kwang Hwang
JJJ Physics Laboratory, Brentwood, TN 37027, USA
E-mail: jkhwang.koh@gmail.com

In the present work, the charged B1, B2 and B3 bastons with the condition of k(mm) = k >> k(dd) > k(dm) = k(lq) = 0 are explained as the good candidates of the dark matters. The proposed rest mass (26.12 eV/c^2) of the B1 dark matter is indirectly confirmed from the supernova 1987A data. The missing neutrinos are newly explained by using the dark matters and lepton charge force. The neutrino excess anomaly of the MinibooNE data is explained by the B1 dark matter scattering within the Cherenkov detectors. And the rest masses of 1.4 TeV/c^2 and 42.7 GeV/c^2 are assigned to the Le particle and the B2 dark matter, respectively, from the cosmic ray observations. In the present work, the Q1 baryon decays are used to explain the anti-Helium cosmic ray events. Because of the graviton evaporation and photon confinement, the very small Coulomb's constant (k(dd)) of 10^{x-54}k and gravitation constant (G_N(dd)) of $10^x G_N$ for the charged dark matters at the present time are proposed. The x value can have the positive, zero or negative value around zero. Therefore, $F_c(mm) > F_g(dd)$ (?) $F_g(mm) > F_g(dm) > F_c(dd) > F_c(dm) = F_c(lq) = 0$ for the proton-like particle.

Key words: charged dark matters, missing neutrinos, cosmic rays, gravitation constant, Coulomb's constant, extended standard model, anti-Helium cosmic ray

1. Introduction

The standard model has been well established. However, several new discoveries like the dark matter need the extended standard model. The present extended standard model [1] is compared with the standard model in Fig. 1. For example, the Z, W^- and W^+ bosons in the standard model do not have the lepton charge (flavor) dependence but the quarks and leptons have the lepton charge dependence in Fig. 1. Therefore, the quark mixing (CKM matrix) and lepton mixing (oscillation) are required in order to explain the particle decays. But, in the present extended standard model, the force carrying bosons of Z, W and Y have the lepton charge dependence in Fig. 1 like the quarks and leptons have the lepton charge dependence. In this case, the quark mixing (CKM matrix) and lepton mixing (oscillation) are not needed in order to explain the particle decays. The missing neutrinos are newly explained by using the dark matters and lepton charge force rather than the neutrino oscillation and sterile neutrino in section 3. The neutrino anomalies of the SN1987A data and MinibooNE data are explained by the B1 dark matter scattering within the Cherenkov detectors.

The dark matters have been known to have two properties. First the electromagnetic interactions between the dark matters (d) and normal matters (m) are zero. Secondly, the electromagnetic interactions between the dark matters are zero. Therefore, the zero Coulomb's forces of $F_c(dm) = 0$ and $F_c(dd) = 0$ have been proposed. Here, d and m represent the dark matter and normal matter, respectively. Because of the zero Coulomb's force, the electrically neutral particles have been proposed as the most possible candidates of the dark matters. In other words, the electric charges (EC) of

these dark matters are zero in $F_c(EC) = k\frac{EC1EC2}{r^2}$. Also, the mini-charged particles (or milli-charged particles) with the near-zero EC charge [2] have been proposed as other possible candidates of the dark matters which give the very small Coulomb's forces between the dark matters and normal matters and between the dark matters. In this case, the same Coulomb's constant of k is applied for both of dark matters and normal matters.

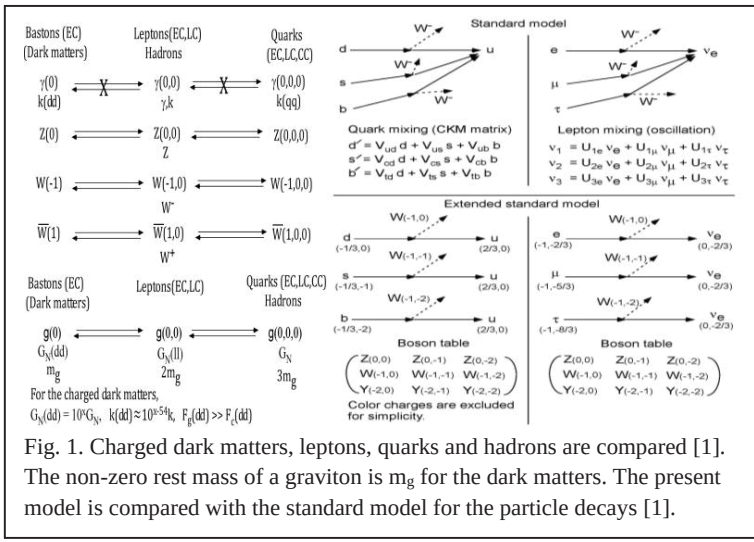

Fig. 1. Charged dark matters, leptons, quarks and hadrons are compared [1]. The non-zero rest mass of a graviton is m_g for the dark matters. The present model is compared with the standard model for the particle decays [1].

In the present work, the zero Coulomb's constant of k(dm) = 0 in Figs. 1 and 2 is applied between the dark matters and normal matters in order to meet the first condition. In order to meet the second condition, the very small k(dd) values for the dark matters and the k(mm) = k values for normal matters are proposed. Therefore, the relation of k(mm) = k >> k(dd) > k(dm) = 0 is shown in Figs. 1 and 2. In this case, the dark matters can have the EC charges close to the EC charge of the electron. The B1, B2 and B3 bastons with the tentative electric charges of -2/3e, -5/3e and -8/3e, respectively, were, for the first time, reported as the possible candidates of the dark matters in Ref. [1]. The B1 and B2 dark matters are expected to be relatively stable because of the lack of the decaying channels. Therefore, in the present work, the B1, B2 and B3 bastons with the condition of k(mm) = k >> k(dd) > k(dm) = 0 are explained as the good candidates of the dark matters. The relations of $G_N(ll) = G_N(qq) = G_N(mm)$ and k(ll) = k(qq) = k(mm) = k are assumed for the simplicity in Figs. 1 and 2. Here, l and q represent the leptons and quarks, respectively. Then, note that k(dm) = k(lq) =0. Then the normal matters consist of leptons, quarks and hadrons, and the dark matters are the three bastons of B1 with -2e/3, B2 with -5e/3 and B3 with -8e/3 [1]. In Fig. 2, the Coulomb's constant (k) and gravitation constant (G) have been changed in terms of the conserved charges and conserved rest masses of the particles. Because the correct evolution curves of k and G are not known, these curves are tentatively drawn for the explanation in Fig. 2. And the effective charges

and effective rest masses of the particles are defined in terms of the fixed Coulomb's constant (k) and fixed gravitation constant (G_N). Then, the effective charge of the B1 dark matter with EC $=-\frac{2}{3}$e is $(EC)_{eff} = -\frac{2}{3}10^{(x-54)/2}$e depending on the x value. Here k(dd) = 10^{x-54}k. And the effective rest mass of the dark matter with the rest mass of m is $m_{eff} = 10^{x/2}$m depending on the x value. Here $G_N(dd) = 10^x G_N$. Therefore, $F_c(mm) > F_g(dd)$ (?) $F_g(mm) > F_g(dm) > F_c(dd) > F_c(dm) = F_c(lq) = 0$ for the proton-like particle in Fig. 2. In Fig. 2, the cases of x = 6 and $F_g(dd) > F_g(mm)$ are shown for the explanation purpose. Note that $F_g(dd) = F_g(mm)$ for the x=0 case and $F_g(dd) < F_g(mm)$ for the x < 0 case in Fig. 2.

In Figs. 1 and 2, the new concepts of the photon confinement and graviton evaporation are introduced. The Coulomb's constant should be constant with increasing of the time because of the photon confinement. The gravitation constant

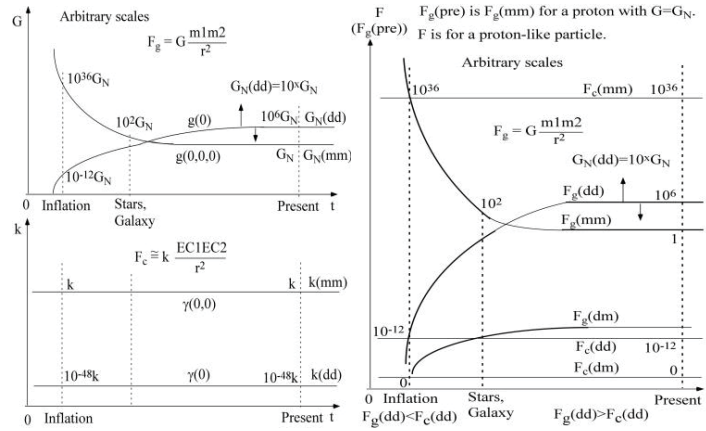

Fig. 2. The G and k values with x=6 are used for the explanation purpose. Here F_g and F_c are the gravitational force strength and electromagnetic force strength, respectively. Here k(dd) = 10^{x-54}k and $F_c(dd) = 10^{x-18}F_g(mm)$. The x value can have the positive, zero or negative value around zero.

has been changed since the big bang because of the graviton evaporation. It is shown that the relation of, at the present time, $F_c(mm) > F_g(dd)$ (?) $F_g(mm) > F_g(dm) > F_c(dd) > F_c(dm) = 0$ for the proton-like particle could explain the universe evolution including the B1, B2 and B3 dark matters by giving the tentative values of the Coulomb's constants (k) and gravitation constants (G) for the explanation purpose in Fig. 2. It is discussed that the gravitation constant ($G_N(mm)$) could be decreased from the very large value like $10^{36}G_N$ down to the very small value like G_N near the inflation period in Fig. 2. Therefore, during most of the universe evolution the gravitation constant could be taken as $G_N(mm) = G_N$. The inflation of the x1x2x3 space is caused by the huge repulsive Coulomb force ($F_c(dd)$) between dark matters in the x1x2x3 space and huge graviton evaporations into the x1x2x3 space in Fig. 2.

The rest mass of 1.4 TeV/c^2 is assigned to the Le particle with the EC charge of -2e from the cosmic ray observations [1]. This rest mass of Le is smaller than the tentative previous rest mass (25.3 TeV/c^2) of Le [1]. The proposed rest mass (26.12 eV/c^2) of the B1 dark matter [1] is indirectly confirmed from the supernova 1987A data. In the present work, the Q1 baryon decays are used to explain the anti-Helium cosmic ray events.

2. Charged dark matters and gravitation constant

The baston dark matters have only the electric charges (EC) [1]. Then, the bastons can be described as (EC). For example, the B1 dark matter with the electric charge of -2e/3 is defined as B1(-2/3). The dark photon of $\gamma(0)$ and the dark graviton of g(0) are associated with the bastons in Figs. 1 and 2. The leptons have the electric charges (EC) and lepton charges (LC). Then, the leptons can be described as (EC,LC) [1]. For example, the electron neutrino and electron are defined as ν_e(0,-2/3) and e(-1,-2/3). The normal photon of $\gamma(0,0)$ and the graviton of g(0,0) are associated with the leptons in Figs. 1 and 2. The quarks have the electric charges (EC), lepton charges (LC) and color charges (CC). And the quarks can be described as (EC,LC,CC) [1]. For example, the u and d quarks are defined as u(2/3,0,CC) and d(-1/3,0,CC). The photon of $\gamma(0,0,0)$ and the graviton of g(0,0,0) are associated with the quarks in Figs. 1 and 2. Also, note that three charges of EC, LC and CC are tentatively quantized based on the systematics [1]. And, the baryons can be described as (EC,LC,-5) or (EC,LC) in Figs. 1 and 2 [1]. For example, the proton is defined as (1,0,-5) or (1,0). The fact that the baryons and mesons can be defined as (EC,LC) in the electromagnetic interactions is called as the hadronization in Figs. 1 and 2 in terms of the electromagnetic interaction. Then, the hadrons can emit and absorb both photons of $\gamma(0,0)$ and $\gamma(0,0,0)$. Therefore, the charged baryons and charged mesons are interacting with the leptons like the electrons through the normal photons of $\gamma(0,0)$ in Fig. 1.

Three things have been observed for the electromagnetic interactions. First the electromagnetic interactions between the dark matters (d) and normal matters (m) are zero. Secondly, the electromagnetic interactions between the dark matters are zero. Thirdly, the independent quarks have never been observed electromagnetically through the normal photons of $\gamma(0,0)$. The third condition indicates that the electromagnetic interactions between the leptons and quarks are zero. Therefore, k(lq) = 0. And the first condition indicates that the electromagnetic interactions between the dark matters and normal matters are zero. Therefore, k(dm) = 0. This indicates that three photons of $\gamma(0)$, $\gamma(0,0)$ and $\gamma(0,0,0)$ are not changed to each other in Figs. 1 and 2. This is called as the photon confinement in the present work. This means that the different Coulomb force should be defined to the bastons, leptons and quarks in Figs. 1 and 2. Second condition can indicate that the F_c(dd) value for the charged

dark matters is nearly zero. So, the very small k(dd) value like k(dd) = 10^{x-54}k for the charged B1, B2 and B3 dark matters can meet the second condition in Figs. 1 and 2.

Three things have been observed for the gravitational force at the present time. First, the gravitational force (F_g(dm)) between dark matters and normal matters is not zero as seen in the galaxy structures. Secondly, the gravitational force (F_g(mm)) between the normal matters is very weak compared with the electromagnetic force (F_c(mm)) between the normal matters. For example, for the proton $F_g(mm) = 0.8\ 10^{-36}\ F_c(mm)$. Thirdly, the gravitational force is dominating over the electromagnetic force for the dark matters. Because F_g(mm) is so small in the second condition, F_g(dd) could be larger than F_g(mm) for the proton-like particle. And the gravitational force of F_g(dm) could be smaller than the gravitational forces of F_g(mm) and F_g(dd) because F_c(dm) = 0 is smaller than the Coulomb forces of F_c(mm) and F_c(dd). This gives the relations of $F_g(dd) > F_g(mm) > F_g(dm) > 0$ and $G_N(dd) > G_N(mm) > G_N(dm) > 0$ because the gravitational force formula is $F_g(dd) = G_N(dd)\frac{m1m2}{r^2}$. The non-zero gravitational force of F_g(dm) indicates that three gravitons of g(0), g(0,0) and g(0,0,0) are changed to each other. This is called as the graviton evaporation in the present work in Figs. 1 and 2. These relations between the gravitational forces can be compared with the relations of $F_c(mm) > F_c(dd) > F_c(dm) = F_c(lq) = 0$ and $k(mm) = k >> k(dd) > k(dm) = k(lq) = 0$. In order to make dark matters to be controlled by the attractive gravitational force in the third condition, the attractive gravitational force (F_g(dd)) between the charged dark matters should be greater than the repulsive Coulomb force (F_c(dd)) between the charged dark matters. Therefore, $F_g(dd) > F_c(dd)$. Therefore, the relation of $F_c(mm) > F_g(dd) > F_g(mm) > F_g(dm) > F_c(dd) > F_c(dm) = F_c(lq) = 0$ for the proton-like particle is obtained for the x = 6 case as shown in Fig. 2.

And why the gravitation force of F_g(mm) is so smaller than the electromagnetic force of F_c(mm) for the proton at the present time is explained as follows. In order to explain this question, we need to consider those forces near the inflation in Fig. 2. Because three photons of $\gamma(0)$, $\gamma(0,0)$ and $\gamma(0,0,0)$ are not changed to each other, the Coulomb's constant of $k(mm)_{inf}$ near the inflation should be equal to the Coulomb's constant of $k(mm)_{pre} = k$ at the present time. This means that $F_c(mm)_{inf}$ is equal to $F_c(mm)_{pre}$ for the proton. Because three gravitons of g(0), g(0,0) and g(0,0,0) are changed to each other, the gravitation constant of $G_N(mm)_{inf}$ near the inflation can be greater than the gravitational constant of $G_N(mm)_{pre} = G_N$ at the present time because of the graviton evaporations. Near the inflation, $F_c(mm)_{inf}$ could be equal or similar to $F_g(mm)_{inf}$ for the proton. Then the F_c(mm) remains constant with increasing of the time since the inflation. However, $F_g(mm)_{inf}$ near the inflation has been decreased to the present value of $F_g(mm)_{pre} = F_g(mm)$ for the proton with increasing

of the time since the inflation in Fig. 2. Therefore, $F_c(mm) >> F_g(mm)$ at the present time in Fig. 2.

Also, in Figs. 1 and 2, the photons are confined within the corresponding space. This indicates that the Coulomb's constant (k) does not change since the inflation. Therefore, always $k(mm) >> k(dd)$ and $k(mm) = k$. However, the gravitation constant of G_N is different because the gravitons can evaporate into other spaces in Figs. 1 and 2. This indicates that the gravitation constant of G has been changing since the inflation. In other words, near the inflation period, $F_g(mm) >> F_g(dd)$ and $F_c(mm) \gg F_c(dd)$ with the condition of $G_N(mm) >> G_N(dd)$ and $k(mm) >> k(dd)$ in Figs. 1 and 2. Then, because of the graviton evaporation, $G_N(mm)$ has been decreased and $G_N(dd)$ has been increased since the inflation. At the present time, $F_g(dd) > F_g(mm)$, $F_g(dd) > F_c(dd)$ and $F_g(mm) \ll F_c(mm)$ with the condition of $G_N(mm) < G_N(dd)$ and $k(mm) >> k(dd)$ in Figs. 1 and 2. At the present time, $F_c(mm) > F_g(dd) > F_c(dd)$ in the force strength and $F_g(dd) > F_g(mm)$. In other words, it is assumed that $G_N(dd) > G_N(mm) = G_N = G_N(qq) \approx G_N(ll)$.

The tentative numerical values of k and G in Fig. 2 are added just in order to show that the graviton evaporation and photon confinement can explain the relative force strengths of the electromagnetic interactions and gravitational interactions well. For example, near the inflation $G_N(mm) \approx 10^{36}G_N$, and $G_N(dd) = 10^{-12}G_N$ in Fig. 2. At the present time, $G_N(mm) = G_N$, and $G_N(dd) \approx 10^6 G_N$ because of the graviton evaporation in Fig. 2. And, always $k(mm) = k \approx 10^{48}k(dd)$. This can be generalized as $G_N(dd) = 10^x G_N$ and $k(mm) = k \approx 10^{x-54}k(dd)$ in Figs. 1 and 2. The x=6 case is shown in Fig. 2. Therefore, in general, $F_c(mm) > F_g(dd)$ (?) $F_g(mm) > F_g(dm) > F_c(dd) > F_c(dm) = F_c(lq) = 0$ for the proton-like particle in Fig. 2. In Fig. 2, the cases of x = 6 and $F_g(dd) > F_g(mm)$ are shown for the explanation purpose. Note that $F_g(dd) = F_g(mm)$ for the x=0 case and $F_g(dd) < F_g(mm)$ for the $x < 0$ case in Fig. 2. It will be interesting to look for the proper x value for the further studies.

At the present time, $F_g(mm) = 8\ 10^{-37}F_c(mm) \approx 10^{-36}F_c(mm)$ for the proton. $F_c = F_c(EC) + F_c(LC) + F_c(CC) \approx F_c(EC) = k\frac{EC1EC2}{r^2}$ because $k(EC) > k(LC) > k(CC)$ [3,4]. The lepton charge force of $F_c(LC)$ plays an important role for the neutrinos with the zero EC charges and non-zero LC charges [3,4]. The missing neutrino fluxes can be studied again by using the lepton charge force of $F_c(LC)$ rather than the neutrino oscillation explanation as shown in section 3. Here it is assumed that the k and G values are similar for the leptons and quarks. Then $F_c(mm) \approx 10^{36}F_g(mm)$, $F_g(dd) = 10^x F_g(mm)$ and $F_c(dd) = 10^{x-18}F_g(mm)$ for a proton-like particle in Fig. 1. This assumption can explain the relation of, at the present time, $F_c(mm) > F_g(dd)$ (?) $F_g(mm) > F_g(dm) > F_c(dd) > F_c(dm) = F_c(lq) = 0$ for the proton-like particle in Fig. 2. For the B1 dark matter with the rest mass of 26.12 eV/c^2 [1], $F_g(dd) \approx 10^{x-16}F_g(mm)$ and $F_c(dd) = \frac{4}{9}10^{x-18}F_g(mm)$ where $F_g(mm)$ is for the proton. Therefore, $F_g(dd) > F_c(dd)$ for the B1, B2 and B3 dark matters in Figs. 1 and 2. This assumption can explain the reason why the gravitational force strength ($F_g(mm)$) between the matters

is so weak compared with the electromagnetic force strength (F_c(mm)) between the matters at the present time. Therefore, it is concluded that the Coulomb's constant is constant because of the photon confinement but the gravitation constant has been changed since the inflation because of the graviton evaporation along with the space evolution in Figs. 1 and 2. It is expected that the changing process of the gravitation constant between the matters from $G_N(mm) \approx 10^{36} G_N$ to $G_N(mm) = G_N$ happened mostly near the inflation period in Fig. 2. Therefore, during most of the universe evolution the gravitation constant could be taken as $G_N(mm) = G_N$. This explanation with the possible numerical values of k and G in Fig. 2 is only the example which needs to be further investigated in the future.

In Figs. 1 and 2, if the gravitons are confined within the corresponding space like the photons, the gravitation constant of G_N(mm) could be much larger than the gravitation constant of G_N(dd) like k(mm) is larger than k(dd). And the gravitation force strength (F_g(mm)) should be similar to the electromagnetic force strength (F_c(mm)). But because the gravitation force strength (F_g(mm)) is much weaker than the electromagnetic force strength (F_c(mm)), it is clear that the gravitons are not confined but evaporated to other spaces as shown in Figs. 1 and 2. In Figs. 1 and 2, it is proposed that k(dd) is much smaller than k(mm) in order to explain the charged dark matter distribution of the galaxy cluster. And if the gravitons are evaporated to other spaces, the gravitation constant of G_N(mm) could be similar to the gravitation constant of G_N(dd). Experimentally, $F_g(mm) = 8\ 10^{-37}\ F_c(mm)$ for the proton. Therefore, the G_N(mm) value is so small at the present time when compared with the k(mm) value in terms of the force strength. This indicates that the gravitons are evaporated as shown in Fig. 2. Because of the huge number (N) of the evaporated gravitons into the x1x2x3 space, the gravitational force between the dark matters on the x1x2x3 space should be stronger than the electromagnetic force between dark matters. Because of the strong gravitational force between the dark matters, the charged dark matters of the B1, B2 and B3 bastons are distributed following the gravitational forces rather than the electromagnetic force between the dark matters. The observed dark matter distributions around the galaxies and galaxy clusters support the strong gravitational force between the dark matters. As shown in Figs. 1 and 2, for the dark matters $F_g(dd) > F_c(dd)$, for the matters $F_g(mm) << F_c(mm)$ and between the matter and dark matter $F_g(dm) > F_c(dm) = 0$. Here F_g and F_c are the gravitational force strength and electromagnetic force strength, respectively. Also, it is assumed that $G_N(dd) = 10^x G_N(mm) > G_N(dm)$ for the gravitation constant and $k(dm) = k(lq) = 0$, $k(mm) = k >> k(dd) = 10^{x-54} k$ for the Coulomb's constant in Figs. 1 and 2. Here d and m mean the dark matter and (normal) matter, respectively. Then, $F_c(dm) = 0$, $F_c(mm) >> F_c(dd)$ for the proton-like particle and $F_g(mm)$ (?) $F_g(dd) > F_g(dm)$ for the proton-like particle. Also, $F_c(mm) > F_g(dd)$ in Figs. 1 and 2.

It has been observed from the gravitational lensing measurements for the bullet cluster [5], Abell 1689 cluster [6] and Abell 520 cluster [7] that the dark matters have been easily separated from the normal matters. The weak gravitational force with the small G_N(dm) value between the dark matters and normal matters can explain why

the dark matters are distributed as observed in the gravitational lensing measurements [5,6,7]. In other words, these gravitational lensing measurements [5,6,7] are the direct evidence of the weak gravitational force with the small $G_N(dm)$ value between the dark matters and normal matters. Therefore, the dark matters and normal matters around the galaxies are connected by the weak gravitational force which can affect the rotational motions of the normal matters. For the bullet cluster [5], the dark matters and normal matters are taking the head and tail parts, respectively, when the

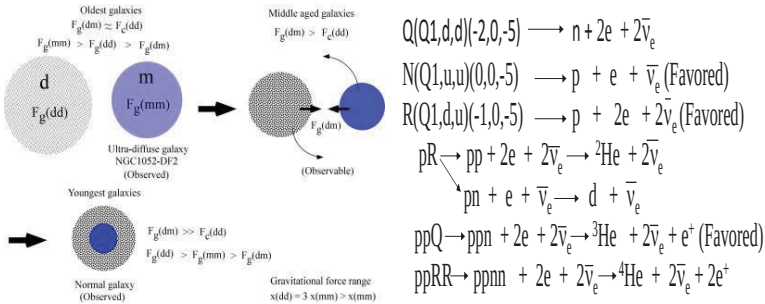

Fig. 3. The transition from the galaxy without the dark matters to the galaxy with the dark matters is shown (see Figs. 1 and 2). The decay channels of several Q1 baryons related to anti-Helium cosmic ray events are shown.

corresponding galaxy cluster is moving. The non-zero rest mass of a graviton is m_g for the dark matters in Fig. 1. Then the non-zero rest mass of a graviton is $3m_g$ for the normal matters of the hadrons in Fig. 1. The strong gravitational force with the longer force range of the g(0) graviton between the dark matters can make the location and shape of the dark matter distributions different from those of the normal matter distributions as observed in the Abell 1689 cluster [6] and Abell 520 cluster [7]. The weak gravitational force with the shorter force range of the g(0,0,0) graviton between the baryonic normal matters can make the location and the shape of the normal matter distributions as observed in the Abell 1689 cluster [6] and Abell 520 cluster [7], which have mostly the normal matters (galaxies) in the outside area and dark matters in the inside center area. Recently, the ultra-diffuse galaxy called as NGC1052-DF2 without the dark matters was found [8]. The formation of the galaxy without the dark matters could be explained with increasing of $F_g(dm)$ as a function of the time as shown in Figs. 2 and 3. The transition from the galaxy without the dark matters to the galaxy with the dark matters could be explained, too, as shown in Fig. 3. Therefore, the galaxies can be classified as the oldest galaxies, middle aged galaxies and the youngest galaxies as shown in Fig. 3. The ultra-diffuse galaxy called as NGC1052-DF2 without the dark matters was found [8] and is classified as the oldest galaxy. Then the dark matter galaxy and matter galaxy classified as the middle aged galaxies can rotate as the pair by the $F_g(dm)$ force. Therefore, looking for the rotating pair of the dark matter and matter galaxies will be interesting. See Ref. [9] for the gravitational force range for the dark matters in Fig. 3.

3. Missing neutrinos, Le lepton, Q1 quark and B1 dark matter

In Ref. [1], three heavy leptons (Le, Lμ, Lτ) with the EC charge of -2 are proposed. The rest mass energy of the Le particle is expected between 3 10^{11} eV and 3 10^{13} eV because the gamma ray excess was reported from the TeV gamma ray spectrum from RX J1713.7-3946 with HESS and Fermi-LAT data [10,11]. In the present work, this gamma ray excess around 1.4 TeV is proposed as the gamma ray peak from the annihilation peak of Le and anti Le particles as shown in Fig. 4. And the cosmic-ray electron and positron excess at the energy range between 10^{11} eV and 2 10^{12} eV was observed from the data of DAMP (Dark Matter Particle Explorer) [12]. Also, the 1.4 TeV electron and positron peak was observed from the same data. And the 1.4 TeV peak observed at the cosmic ray is explained as the annihilation peak of Le and anti

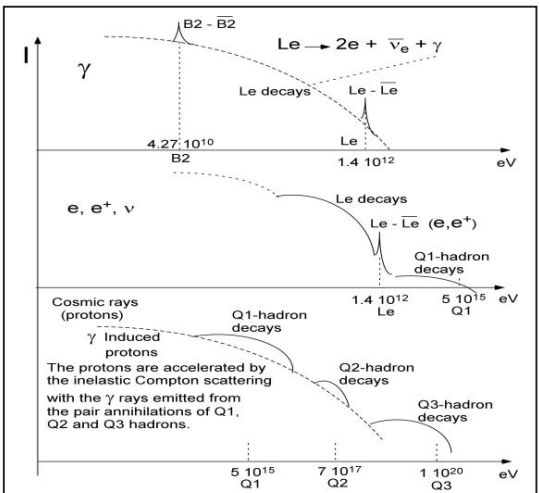

Fig. 4. Cosmic gamma ray and cosmic ray [1,6].

Le particles as shown in Fig. 4. Then, the rest mass of 1.4 TeV/c^2 is assigned to the Le particle with the EC charge of -2e. This rest mass of Le is smaller than the tentative previous rest mass (25.3 TeV/c^2) of Le [1]. And the cosmic-ray electron and positron excess at the energy range between 10^{11} eV and 2 10^{12} eV, which was observed from the data of DAMP (Dark Matter Particle Explorer) [12], is explained to be originated from the decay of Le particle of $L_e \rightarrow 2e + \bar{\nu}$. And the cosmic gamma ray spectrum by CALET 5 year measurements [13] was observed from the Galactic center including galactic diffusing background. The 1.4 TeV gamma ray peak which was originated from annihilation peak of Le and anti Le particles was found [13]. Also, Planck collaboration [14] indicates that the electron and positron cosmic ray data observed around 1.4 TeV by the Fermi/HESS and AMS/PAMELA are excluded from the dark matter candidates by CMB. These electron and positron data can be explained by the decay and annihilation of the new Le particle. The rest masses of Le, Lμ and Lτ leptons can be tentatively calculated by E = 0.4498 10^{38+2F}

and F(EC,LC) = -23.24488 + 7.26341 |EC| - 1.13858 EC^2 + 0.62683 |LC| + 0.22755 LC^2. These data support the existence of heavy leptons like Le, Lμ and Lτ.

In Ref. [1], the B1, B2 and B3 dark matters (bastons) are proposed. These B1 and B2 dark matters are very stable because of the lack of the decaying channels [1]. Their possible rest masses have been tentatively calculated in Ref. [1] under the assumption that the B2 dark matter has the 42.7 GeV/c^2 [12]. The 42.7(7) GeV peak was identified in the gamma-ray spectrum from the Fermi Large Area Telescope (LAT)

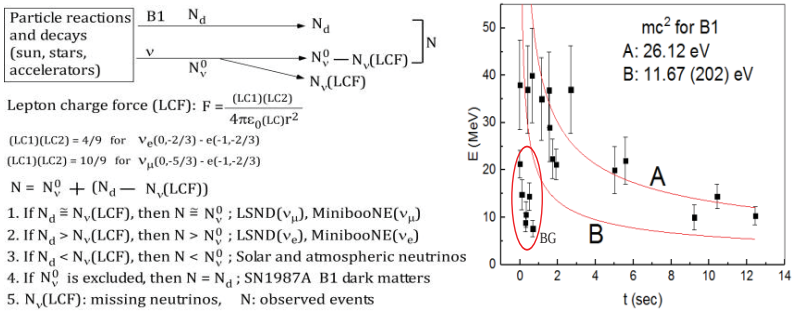

Fig. 5. The B1 dark matter effects (N_d) are considered in the neutrino observation (N) as shown in Fig. 6. The proposed rest mass (26.12 eV/c^2) of the B1 dark matter [1] is indirectly confirmed from the supernova 1987A data [16].

in the directions of 16 massive nearby Galaxy Clusters [1,15]. The 42.7 GeV peak is proposed as the B2 annihilation peak. Then, the rest mass of the B2 dark matter is 42.7 GeV/c^2 [1]. Also, the proposition of the 42.7 GeV/c^2 B2 dark matter is consistent with the dark matter rest mass energy predicted by the Fermi Galactic center excess, AMS anti-proton excess, thermal cross-section and the CMB condition [14]. Planck collaboration [14] reported recently the possible rest mass energy range of the dark matter in Fig. 46 of the paper on Planck 2018 results. VI. Cosmological parameters [14]. This rest mass energy range [14] is consistent with the present B2 dark matter rest mass energy of 42.7 GeV/c^2.

The Cherenkov radiation of the electrons produced from the elastic scattering of the anti-neutrino and electron was observed by the Kamiokande II detector, Irvine-Michigan-Brookhaven detector (IMB) and Baksan neutrino observatory detector (BNO) [16]. And the anti-neutrino data emitted from SN 1987A [16] were explained by using the annihilation of B1 and anti-B1 dark matters [1]. In the present work, the alternative explanation is tried to explain the SN 1987A data [16]. It is proposed in Fig. 6 that the Cherenkov radiation of the electrons produced from the elastic scattering of the B1 dark matter and electron was observed by the Kamiokande II detector, Irvine-Michigan-Brookhaven detector (IMB) and Baksan neutrino

observatory detector (BNO) [16]. In Fig. 5, the curve A fits the observed data well except the 6 BG data. The equation of $2E^2t = m^2c^4t_0$ is taken from the paper by Ehrlich [16]. Here, t_0 is the travel time of the light from SN 1987A to the earth. The background data are expressed as BG in Fig. 5. The 5 data detected by the BNO detector considered as the background data are not shown in Fig. 5 [16]. The curve A uses the proposed dark matter mass of B1. It is proposed that the B1 particles come from SN 1987A to the earth. The energies, E(ν) of the observed neutrinos are re-interpreted as the energies, E(B1) of the B1 dark matters. This supports indirectly that the rest mass of the B1 dark matter is 26.12 eV/c^2. The curve B fitted with all data in Fig. 5 is shown for the comparison with the curve A.

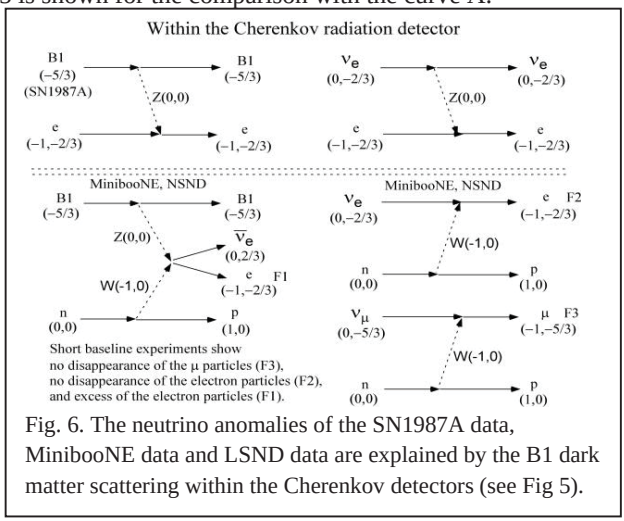

Fig. 6. The neutrino anomalies of the SN1987A data, MinibooNE data and LSND data are explained by the B1 dark matter scattering within the Cherenkov detectors (see Fig 5).

In Figs. 5 and 6, the missing neutrinos are newly explained by using the B1 dark matters and lepton charge force. $F_c = F_c(EC) + F_c(LC) + F_c(CC) \approx F_c(EC) = k\frac{EC1EC2}{r^2}$ because k(EC) > k(LC) > k(CC) [3,4]. The lepton charge force of $F_c(LC) = k(LC)\frac{LC1LC2}{r^2}$ plays an important role for the neutrinos with the zero EC charges and non-zero LC charges in Fig. 5 [3,4]. The missing neutrino fluxes can be studied again by using the lepton charge force of $F_c(LC)$ rather than the neutrino oscillation explanation as shown in section 3.The neutrino anomalies of the SN1987A data, MinibooNE data [17,18] and LSND data [19] are explained by the B1 dark matter scattering within the Cherenkov detectors in Figs. 5 and 6. Also, the reactor missing antineutrino anomaly can be explained by the condition of $N_d < N_v$ (LCF) in Fig. 5. In the present extended standard model, the force carrying bosons of Z, W and Y have the lepton charge dependence in Fig. 1 like the quarks and leptons have the lepton charge dependence. In this case, the quark mixing (CKM matrix) and lepton

mixing (oscillation) are not needed in order to explain the particle decays. Then, it is concluded that the B1 dark matters were already observed in the SN1987A data [16] and MinibooNE data [17,18].

Six anti-^{3}He cosmic ray events and two anti-^{4}He cosmic ray events were observed by AMS-02 measurements [20]. Anti-matter clouds and anti-matter stars are proposed by Poulin et al. as their origins [20]. However, in the present work the Q1 baryon decays are used to explain the anti-Helium cosmic ray events. It indicates that the enhanced anti- ^{3}He events are originated from the anti- (ppQ) decay in Fig. 3. And the anti- ^{4}He events are originated from the anti- (ppRR) decay in Fig. 3. Also, the ultra high energy cosmic rays can be explained by the decaying channels of the Q1, Q2 and Q3 baryons [1] as shown in Fig. 3. This supports the existence of the new heavy Q1, Q2 and Q3 quarks with the charge of EC = -4e/3 [1].

4. Elementary particles and the extended standard model

The relations of $G_N(ll) = G_N(qq) = G_N(mm)$ and $k(ll) = k(qq) = k(mm) = k$ are assumed in Fig. 2. Here, l and q represent the leptons and quarks. Then, note that

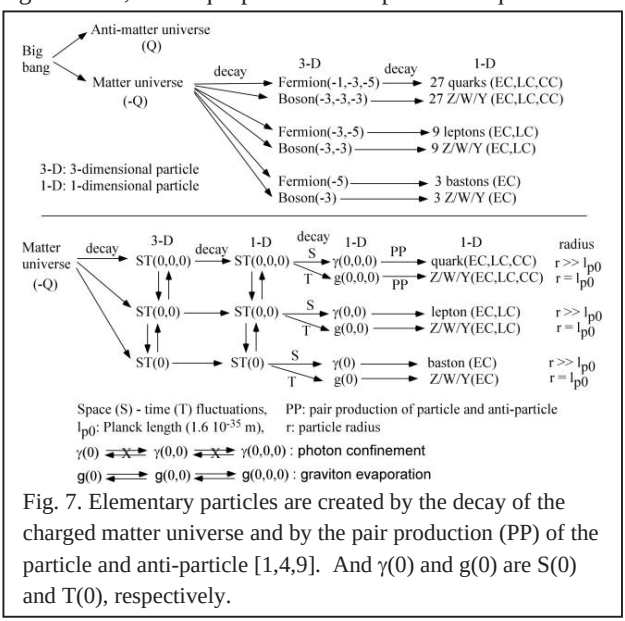

Fig. 7. Elementary particles are created by the decay of the charged matter universe and by the pair production (PP) of the particle and anti-particle [1,4,9]. And γ(0) and g(0) are S(0) and T(0), respectively.

k(dm) = k(lq) =0. And the normal matters consist of leptons, quarks and hadrons, and the dark matters are the B1, B2 and B3 bastons [1]. Then the B1, B2 and B3 dark matter particles exist since the big bang along with the photons and gravitons [9]. Therefore, all elementary particles including the B1, B2, B3 dark matters are created

near the inflation. The particles with the rest mass (m) of $m > E_p/c^2$ and the radius (r) of $r < R$ become the virtual black hole particles from the condition of the Schwarzschild radius of $R = 2Gm/c^2$. $E_p/c^2 = m_p$ is the Planck mass which is the black hole. The real particles are defined as the particles with the radius (r) of $r > R$. Therefore, the B1, B2 and B3 dark matters are the real particles. And it is proposed that the force carrying bosons of gravitons and Z/W/Y bosons with the non-zero rest masses have the radii equal to the Planck length (l_{p0}) in Fig. 7 [9,1,4]. Therefore, the force carrying Z/W/Y bosons and gravitons are always the real particles because the radii of the force carrying bosons and gravitons are $l_{p0} = 1.6\ 10^{-35}$ m larger than their Schwarzschild radii given by $R = 2Gm/c^2$. The size of the photon with the zero rest mass cannot be defined. These Z/W/Y bosons exist only during the very short time allowed by the uncertainty principle. These Z/W/Y bosons are created from the decay of the vacuum energy in Fig. 7. Therefore, the first Z(0,0) and W(-1,0) particles with the rest mass energies of 91 GeV/c^2 and 80 GeV/c^2, respectively, were the real particles that were created from the decay of the vacuum energy. The pair of the matter universe with the charge configuration of -Q and anti-matter universe with the charge configuration of Q could be created from the big bang because our universe is full of the matters in Fig. 7 [9]. In this case, if the matter universe is defined to be negatively charged for the EC, LC and CC charges, the anti-matter universe should be defined to be positively charged for the EC, LC and CC charges. Then, the matters can be created from the decay of the matter universe with decreasing of the gravitation constant (G(mm)) in Fig. 2. Also, the pair of the matter and anti-matter can be created from the vacuum energy fluctuation with decreasing of the gravitation constant (G(mm)) in Fig. 2. The anti-particles created by the pair production of the particle and anti-particle are later changed to the photons by the pair annihilation of the particle and anti-particle. And the particles created by the decay of the matter universe survive to form the galaxies and stars. This is the reason why our matter universe is full of the particles. The decay of the matter universe to create the new particles takes place mostly near the inflation period through the formation of the universe particle and galaxy particles [9,4]. But the pair production of the particle and anti-particle to be created from the vacuum energy fluctuation takes place always from the big bang time up to the present time. Also, the pair production of the matter universe and anti-matter universe can explain the CP symmetry problem of why the matters are dominating over the anti-matters on the present universe.

Elementary particles are created by the decay of the charged matter universe and by the pair production (PP) of the particle and anti-particle in Fig. 7 [1,4,9]. And g(0) and g(0) are S(0) and T(0), respectively in Fig. 7. Also, note that the elementary fermions are created by the particle-antiparticle pair production from the photon and the elementary Z/W/Y bosons are created by the particle-antiparticle pair production

from the high energy graviton. The high energy graviton is made by the constructive interference of the many low energy gravitons. The connection of the elementary bosons with the gravitons are for the first time proposed in the present work in Fig. 7. In other words, the gravitons and the Z/W/Y bosons are created by the fluctuations (T fluctuation) along the time axis of the space and time and the photons and the elementary fermions are created by the fluctuations (S fluctuation) along the space axis of the space and time in Fig. 7 [9,4]. The vacuum energy can be described as the 3-dimensional and 1-dimensional space and time fluctuations of ST(0), ST(0,0) and ST(0,0,0) in Fig. 7. These ST(0), ST(0,0) and ST(0,0,0) fluctuations can be exchanged to each other. Therefore, these vacuum energies are not confined within the corresponding space but evaporated to other space like the gravitons do. And the gravitons (T fluctuation) and photons (S fluctuation) can be combined to form the vacuum energy (ST fluctuation). Also, the vacuum energy (ST fluctuation) can decay to the gravitons (T fluctuation) and photons (S fluctuation). Therefore, the gravitons and photons are originated from the same space-time (ST) fluctuations [4,9]. The vacuum energy density including the photons and gravitons is defined as the ST(0), S(0) and T(0) vacuum energy density of the x1x2x3 space. If the ST(0) vacuum energy is larger than the rest mass energy of two electron neutrinos, the ST(0) energy will be changed to the ST(0,0) energy which makes the pair production of the electron neutrino and anti-electron neutrino. And the increasing of the new g(0) gravitons (T(0) fluctuation) can increase the ST(0) vacuum energy by combining with the γ(0) photons (S(0) fluctuation). The increasing of this ST(0) vacuum energy can cause the accelerated expansion of the x1x2x3 space and the inflation of the x1x2x3 space since the big bang as explained in Ref. [9]. This should be further studied in terms of the 3-dimensional quantized space model.

5. Summary

In the present work, the charged B1, B2 and B3 dark matters are expected to be relatively stable because of the lack of the decaying channels. When the proper values of the gravitation constants and Coulomb's constants are given for the normal matter and dark matters, the charged dark matters like the B1, B2 and B3 dark matters can be the good candidates of the dark matters. Here it is assumed that the k and G values are similar for the leptons and quarks. Then $F_c(mm) \approx 10^{36}F_g(mm)$, $F_g(dd) = 10^{x}F_g(mm)$ and $F_c(dd) = 10^{x-18}F_g(mm)$ for a proton-like particle in Fig. 2. This assumption can explain the relation of, at present time, $F_c(mm) > F_g(dd)$ (?) $F_g(mm) > F_g(dm) > F_c(dd) > F_c(dm) = F_c(lq) = 0$ for the proton-like particle in Fig. 2. For the B1 dark matter with the rest mass of 26.12 eV/c^2 [1], $F_g(dd) \approx 10^{x-16}F_g(mm)$ and $F_c(dd) = \frac{4}{9}\,10^{x-18}F_g(mm)$ where $F_g(mm)$ is for the proton. Therefore, $F_g(dd) > F_c(dd)$ for the B1, B2 and B3 dark matters as shown in Fig. 2. In order to make dark matters to be controlled by the attractive gravitational force, the attractive gravitational force ($F_g(dd)$) between the dark matters should be greater than the repulsive Coulomb's

force (F_c(dd)) between the dark matters. Therefore, F_g(dd) > F_c(dd). Therefore, it is concluded that the Coulomb's constant is constant because of the photon confinement but the gravitation constant has been changing since the inflation because of the graviton evaporation along with the space evolution in Fig. 2. This assumption can explain the reason why the gravitational force strength (F_g(mm)) between the matters is so weak compared with the electromagnetic force strength (F_c(mm)) between the matters.

The rest mass of 1.4 TeV/c^2 is assigned to the Le particle with the EC charge of -2e [2,24,25]. This rest mass of Le is smaller than the tentative previous rest mass (25.3 TeV/c^2) of Le [1]. The proposed rest mass (26.12 eV/c^2) of the B1 dark matter [1] is indirectly confirmed from the supernova 1987A data [16]. The neutrino anomalies of the SN1987A data and MinibooNE data are explained by the B1 dark matter scattering within the Cherenkov detectors. The missing neutrinos are newly explained by using the dark matters and lepton charge force in section 3. Then, it is concluded that the B1 dark matters were already observed in the SN1987A data and MinibooNE data. In the present work the Q1 baryon decays are used to explain the anti-Helium cosmic ray events and ultra high energy cosmic rays.

Finally, I thank the conference organizers for giving me the opportunity to talk on these challenging topics at the 2018 new trends in high energy physics conference.

References

[1] Jae-Kwang Hwang, Mod. Phys. Lett. **A32**, 1730023 (2017).
[2] R. Barkana et al., arXiv:1803.03091v2 (2018).
[3] Jae-Kwang Hwang, https://www.researchgate.net/publication/311312119
[4] Jae-Kwang Hwang, https://www.researchgate.net/publication/297270485
[5] D. Clower et al., Astrophys. J. **604**, 596 (2004).
[6] A.N. Taylor et al., Astrophys. J. **501**, 539 (1998).
[7] M. Jee et al., Astrophys. J. **783**, 1 (2014).
[8] P. van Dokkum et al., Nature **555**, 629 (2018).
[9] Jae-Kwang Hwang, https://www.researchgate.net/publication/325553139
[10] V. Gammaldi, arXiv: 1412.7639 (2014).
[11] S. Federicici et al., arXiv: 1502.06355v1 (2015).
[12] S.F. Ge and H.J. He, arXiv: 1712.02744 (2017).
[13] O. Adriani et al., EPJ Web of Conf. **95**, 04056 (2015).
[14] Planck collaboration et al., Arxiv: 1807.06209v1 (2018).
[15] Y.F. Liang et al., Phys. Rev. **D93**, 103525 (2016).
[16] R. Ehrlich, Astropart. Phys. **35**, 625 (2012).
[17] A.A. Aguilar-Arevalo et al., Phys. Rev. Lett. **121**, 221801 (2018).
[18] G. Cheng et al., Phys. Rev. **D86**, 052009 (2012).
[19] C. Athanassopoulos et al., Phys. Rev. Lett. **81**, 1774 (1998).
[20] V. Poulin et al., arXiv:1808.08961v1 (2018).

Sterile neutrino searches with the ICARUS detector

Filippo Varanini (on behalf of the ICARUS collaboration)

ABSTRACT: The ICARUS-T600 detector is the first large-scale example of a liquid Argon TPC, an ideal detection technology for neutrino physics, combining excellent 3D spatial reconstruction and calorimetry. Its operation with the CNGS neutrino beam proved the maturity of the technique, while providing important results in sterile neutrino searches.
A fully sensitive verification of the existence of sterile neutrinos will be possible with the SBN experiment at the FNAL Booster beam, using three LAr-TPCs at different distances along the beamline. ICARUS, that will act as the SBN far detector, was extensively refurbished in order to adapt to surface operations; data taking is expected to begin during 2019.

THE LIQUID ARGON TPC

The Liquid Argon Time Projection Chamber (LAr-TPC) is one of the most innovative detector technologies now taking a leading role in the field of neutrino physics and other rare phenomena like nucleon decay.
It combines an excellent 3-dimensional imaging capability (with a resolution of the order of the wire pitch, typically a few millimeters) with the properties of a uniform, full-sampling calorimeter, due to the collection of drifting electrons produced by ionizing tracks.
In this detector, the argon acts as both massive target and detection medium at the same time; its accessible cost allows the construction of detectors with huge mass, beyond the kiloton scale.
Moreover, the associated scintillation light in LAr provides a fast signal, that can be used to provide timing information or triggering.
LAr-TPCs were first proposed by C. Rubbia in 1977[1]; a long development, carried out within INFN and in collaboration with industry, culminated in ICARUS-T600, that took data from 2010 to 2013 in the INFN-LNGS underground laboratory in Italy, representing the first application of a LAr-TPC to a large-scale physics experiment.

ICARUS-T600 AT LNGS

The T600 detector[2] is composed of two identical and independent modules, for a total instrumented LAr mass of 476 t; each module consists of two TPCs, sharing a central cathode. Each TPC has a drift length of 1.5 meters; a uniform electric field of 500 V/cm is applied in the TPC, corresponding to an electron drift velocity of ~1.6 mm/μs.

The anode system is composed by three parallel wire planes with different orientations (0°, ± 60° w.r.t. horizontal); both the distance between planes and the wire pitch on each plane are 3 mm. The wire biasing is tuned to guarantee a non-destructive readout of the signals generated by ionization electrons drifting to the anode; in the first two planes a signal is generated by induction, while in the last one all drifting electrons are collected, providing a signal proportional to the deposited energy.
The wire signal is read-out and digitized with a 400 ns sampling time, corresponding to ~0.6 mm; the resolution on the drift coordinate is therefore of the same order.
The LAr scintillation light is read by photomultipliers placed behind the wires; being in the VUV range (~125 nm), it has to be shifted to visible light by a layer of wavelength shifter (tetraphenylbutadiene) deposited on the PMT window. An internal picture of the TPC is visible in **Figure 1**.

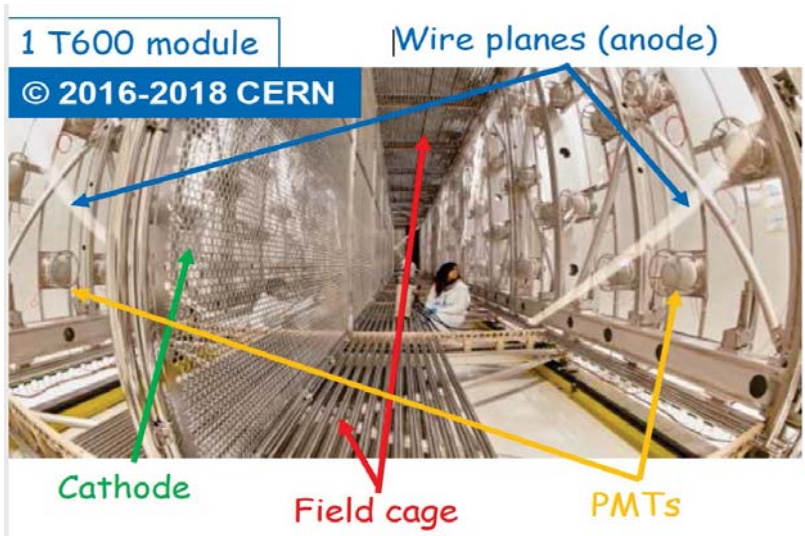

Figure 1: internal photo of one TPC of ICARUS-T600 during the refurbishing at CERN. The wire planes, cathode, PMTs and field cage are visible.

The ICARUS-T600 detector took data for about 3 years at LNGS [100], exposed to both CNGS beam neutrinos (~8.6 10^{19} pot) and atmospheric ones; this very successful data-taking run (live time ~93%) proved the maturity of the LAr-TPC technology, paving the way for future even larger detectors such as DUNE.

In particular, an unprecedented Argon purity of ~20 ppt (O_2 equivalent) [4], corresponding to an electron lifetime of ~15 ms, was reached, limiting the maximal attenuation of the ionization electron signal over the ICARUS drift length to ~7%.

ICARUS RECONSTRUCTION

This run confirmed the expected ICARUS performances, both in spatial and calorimetric reconstruction capability. Their most significant application for current and future neutrino experiments is the identification of electron neutrino interactions, separating them from the background given by neutral current with production of π^0's and relative electromagnetic showers.
The signal/background discrimination is mainly due to the accurate measurement of ionization density dE/dx in the first few centimeters from the neutrino interaction vertex, before the shower onset (**Figure 2**); a genuine electron produces a m.i.p. deposition, unlike π^0 showers, where initial ionization density is at least two times higher. This very detailed reconstruction of electromagnetic showers, made possible by the excellent granularity (3 mm, compared with a radiation length of ~14 cm) represents one of the major advantages of LAr-TPC with respect to other detection techniques.

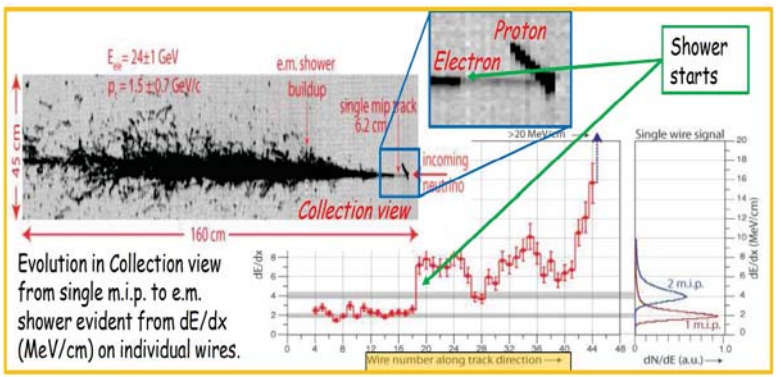

Figure 2: Example of identification of an electron neutrino interaction in the CNGS beam with the analysis of dE/dx. The ionization density is compatible with a m.i.p. for about 15 wires (~4 cm) before the electron develops into a shower.

In the case of non-contained particles, mostly muons, for which a calorimetric measurement is not possible, the only alternative estimate of

energy is from multiple Coulomb scattering (MCS); since the RMS deflection angle of a muon along a track segment of length L is inversely proportional to its momentum p, a measurement of deflection angles allows to estimate momentum.
A new algorithm[5] has been developed for ICARUS, introducing a statistical analysis of observed track deflections, optimizing segment length in order to enhance the genuine MCS effect w.r.t. the apparent deflections due to reconstruction uncertainties, which are estimated on an event-by-event basis. This analysis was validated on a sample of ~400 stopping *rock muons,* i.e. muons produced in the ν_μCC interactions of CNGS beam neutrinos in the rock upstream of the detector, ranging out and possibly decaying in the detector itself. This subsample of contained events provides a direct estimate of momentum from calorimetry, that can be used as a benchmark for the MCS one, in an energy range (0.5-5 GeV) that is typical of future neutrino experiments

The agreement between the two momentum measurements is generally good (**Figure 3**) despite a small underestimation of the MCS estimate w.r.t. the calorimetric one, growing at higher energies (~15% for p>3 GeV/c). This effect is due to the non-perfect planarity of the cathode, that was independently measured with cosmic rays and during the detector overhaul, and could extend up to ~2.5 cm; this causes a distortion of the electric field, resulting in apparent track deflections which mimic a lower momentum value.
This effect was corrected on average, by simulating the electric field resulting from the observed non-planarities and computing the corresponding fake deflections; the correction reduced the maximum underestimation to ~5%.

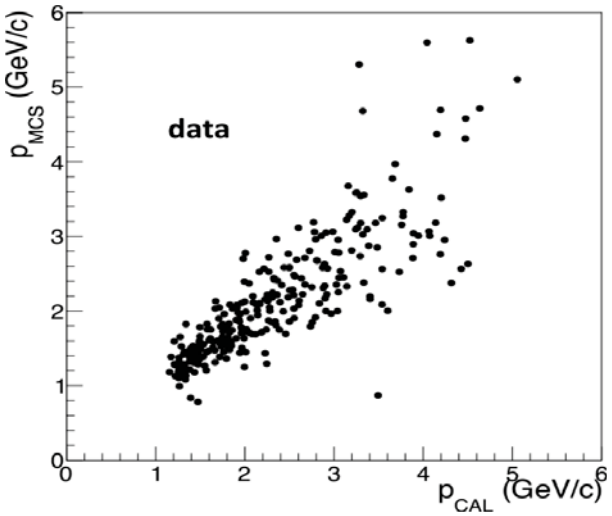

Figure 3:Scatter-plot of the MCS momentum measurement, compared with the calorimetric one, for the CNGS stopping muon sample described in the text.

In addition the CNGS beam neutrinos, ICARUS-T600 could also observe atmospheric neutrinos, with an exposure of ~0.74 kt year. 14 neutrino interactions (6 $\nu\mu$ and 8 νe) were observed (an example is shown in **Figure 4**), while ~18 were expected, taking into account detector live-time and detection efficiencies. This is the first observation ever of atmospheric neutrinos with a LAr-TPC; moreover, it represents an interesting benchmark for the identification and reconstruction of neutrino interaction in a similar energy range to the future SBN experiment.

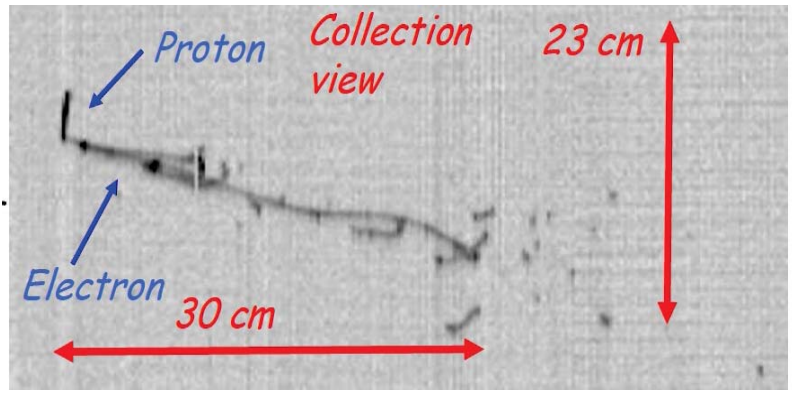

Figure 4: A down-going ne neutrino interaction observed at LNGS. The total deposited energy is ~240 MeV. The electron can be identified by the single-m.i.p. ionization density in the first few wires.

THE STERILE NEUTRINO PUZZLE

While most results in neutrino oscillation physics are consistent with the standard scenario of 3 neutrino flavors and 3 mass eigenstates, a few anomalies, across very different neutrino sources and energy ranges, appear to point to a possible fourth mass eigenstate in the region of 0.1-10 eV^2, corresponding to an L/E ratio of ~ 1 m/MeV. The first of these anomalies was the appearance of anti-νe in the LSND anti-νμ beam, with a ~3.8σ significance[6], later partially confirmed by MiniBooNE. At some reactor experiments a ~3σ deficit of anti-νe was observed w.r.t. expectations[7]. Recent reactor results, however, are somehow contradictory: while some seem to provide alternative explanations for this effect, that do not involve oscillations[8], other measurements at very short baseline [9] appear to point to oscillations with large $\Delta m^2 \sim 7\ eV^2$. A similar disappearance was also found in Mega-Curie neutrino sources, used for the calibration of solar neutrino experiments[10].

ICARUS performed a search for a sterile neutrino in this mass range by looking for νe appearance in the νμ CNGS beam[11]; since the L/E ratio in this case is ~36 m/MeV, much larger than the LSND one, the Δm^2 dependency of the oscillation probability averages out, resulting in $P(\nu\mu \rightarrow \nu e) \sim \frac{1}{2} \sin^2(2\theta)$. The non-observation of νe appearance, consequently, resulted in constraining (together with the similar result by OPERA[12]) the allowed parameter space, identifying a small region around $\Delta m^2 \sim 1\ eV^2$ and small angle, as illustrated in **Figure 5**.

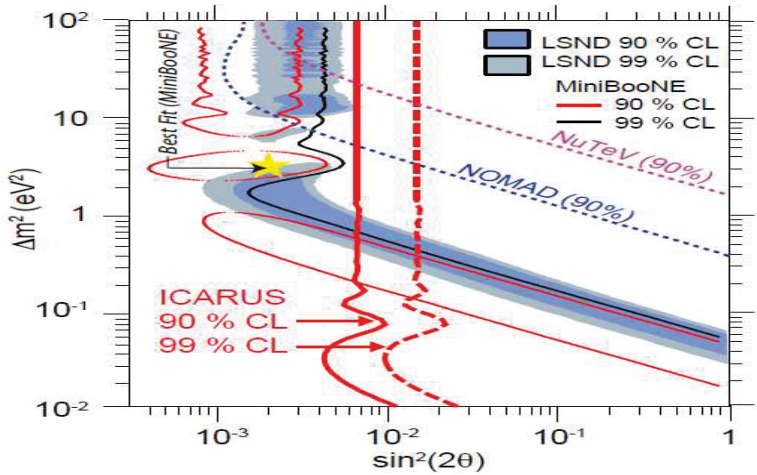

Figure 5: Excluded region from the sterile neutrino search by ICARUS at LNGS, compared with LSND and MiniBooNE allowed regions in parameter space.

Recent cosmological data such as Planck[13] seem to disfavor the sterile neutrino hypothesis, while both reactor and accelerator scenarios present tensions between different results; generally, the sterile neutrino picture appears far from clear, requiring a definitive explanation.

THE SBN EXPERIMENT

The SBN (Short Baseline Neutrino) experiment, under preparation at the Booster neutrino beam at FNAL, has the potential to perform a fully sensitive search of sterile neutrino oscillations, both in the appearance and disappearance channels[14]. In this project, ICARUS will act as the far detector, at 600 meters from the beam target; a near detector (SBND) also based on the LAr-TPC technology, with a mass of 112 tons, will be installed at a ~110 m distance. A smaller LAr-TPC (MicroBooNE, with a mass of ~80 t) is already taking data on the same beamline.
The use of the same detection technology for the far and near detectors will allow to cancel out a large part of the systematics associated to neutrino events identification, reconstruction and detector response. The near detector will provide a basically unperturbed flux composition and spectrum, and any difference between spectra at the near and far locations will imply some unexplained new physics.

Moreover, the νe efficient reconstruction by the LAr-TPC will allow to reject a large fraction of NC-associated backgrounds.

As a consequence, in 3 years of data-taking, SBN will be able to fully cover the region allowed by LSND in parameter space with a νe appearance search, as shown in **Figure 6**, and at the same time extend the present sensitivity in the νμ disappearance channel.

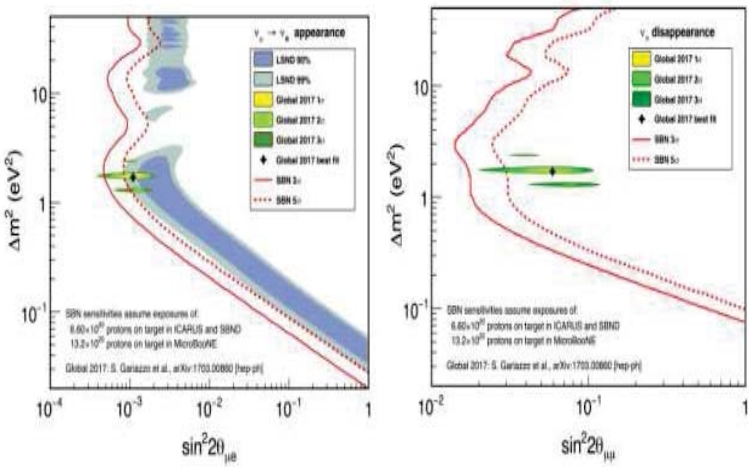

Figure 6: Sensitivity of the SBN experiment in the appearance channel (left) and in the disappearance one (right) for 3 years of data taking, compared with LSND allowed region

THE ICARUS-T600 OVERHAULING

The operation of ICARUS-T600 at SBN will take place at shallow depth, protected by only a 3-meter concrete overburden. These experimental conditions will pose new challenges to the operation of a liquid Argon TPC; the rate of cosmic rays impinging on the detector will be ~11 for each TPC, during each drift window (~1 ms).
Photons associated to incoming cosmic rays will generate, via Compton interaction or asymmetric pair production, electrons that could mimic ν_e interaction and represent an important source of backgrounds for appearance searches.

In order to reduce this background, the absolute position in space and drift time of each ionizing event during the drift window must be unambiguously reconstructed. This will be possible by combining the

TPC information with the scintillation light recorded by a much improved PMT system.
The number of photomultipliers, in view of the SBN experiment, has been increased to 360 (90 per each TPC); the adopted PMTs are characterized by excellent timing features (transit time spread <1 ns, rise time ~ 4 ns) in order to guarantee a ~ns time resolution, allowing reconstruction of the event position within ~50 cm[15]. Moreover, a segmented Cosmic Ray Tagger system (CRT), made of scintillator bars with ~98% detector coverage, will allow identification and tagging of incoming cosmic rays.

In addition to the improvement in the light detection system, the ICARUS detector underwent a major refurbishing at CERN starting in 2015, introducing newer technological developments while maintaining the already achieved performance, before transportation to FNAL in summer 2017. In particular, new cold vessels and purely passive insulation were installed; the cathode was flattened by a thermo-mechanical treatment, reducing the non-planarity to a few mm and removing the largest systematic to MCS muon momentum measurement.
The read-out electronics was also redesigned, introducing a shorter shaping time (~1.5μs) for all wire planes, including the middle Induction one. This resulted in a drastic reduction of the undershoot around signals, allowing a better description of crowded event regions around vertices, and permitted an off-line integration of the Induction signal, providing a calorimetric measurement also in that wire plane.

The installation at the FNAL Far Detector building started in late 2017, with the assembly of warm vessel and the bottom CRT layer; activity on top of the detector was ongoing in September 2018, with the installation of feedthrough chimneys.
Cryogenic work will begin in early 2019, followed by commissioning of the TPC, PMT and CRT subdetector systems. Filling with liquid Argon and start of data taking is planned for summer 2019.

CONCLUSIONS

The ICARUS-T600 detector represents the first large-scale example of a liquid Argon TPC; its very successful operation in tough underground conditions at the LNGS laboratory proved the maturity of this innovative detecting technology, paving the way to further developments in neutrino and rare event physics.
The search for sterile neutrinos through ν_e appearance studies in the CNGS beam provided significant constraints to the allowed sterile neutrino parameter space.

A more thorough verification of the sterile neutrino hypothesis will be possible with the SBN experiment at the Booster beam at FNAL, that will be able to cover the currently allowed appearance region in 3 years of data taking. The use of three LAr-TPCs at different distances – with ICARUS acting as far detector - along the beamline will strongly suppress systematics and allow a very sensitive search also in the disappearance channel.
In order to cope with to its new more challenging shallow depth operation, the ICARUS detector underwent a significant overhauling at CERN from 2015 to 2017. In particular, the scintillation light detection system was fully renovated, increasing the PMT number and their resolution and redesigning the front-end electronics

BIBLIOGRAPHY

[1] C. Rubbia, *The Liquid Argon Time Projection Chamber: A New Concept for Neutrino Detectors*, CERN-EP-INT-77-08, 1977.

[2] M. Antonello et al., *Design, construction and tests of the ICARUS T600 detector,* NIM A 527 329-410, 2004.

[3] M. Antonello et al., *Underground operation of the ICARUS-T600 LAr-TPC: first results,* JINST 6 P07011, 2011.

[4] M. Antonello et al. , *Experimental observation of an extremely high electron lifetime with the ICARUS-T600 LAr-TPC,* JINST 9 P12006, 2014.

[5] M. Antonello et al. , *Muon momentum measurement in ICARUS-T600 LAr-TPC via Multiple Scattering the few-GeV range,* JINST 12 P04010, 2017.

[6] A. Aguilar-Arevalo et al., *Evidence for neutrino oscillations from the observation of anti-neutrino(electron) appearance in an anti-neutrino(muon) beam*, Phys. Rev. D 64 112007 (2001).

[7] G. Mention et al., *The reactor antineutrino anomaly*, Phys. Rev. D 83 073006 (2011).

[8] M. Dentler et al., *Sterile neutrinos or flux uncertainties? Status of the reactor antineutrino anomaly,* JHEP 11 099 (2017).

[9] A.P. Serebrov et al., *The first observation of effect of oscillation in Neutrino-4 experiment on search for sterile neutrino*, arXiv:1809.10561.

[10] J.N. Abdurashitov et al., *Measurement of the solar neutrino capture rate with gallium metal. III. Results for the 2002–2007 data-taking period*, Phys. Rev. C 80 015807 (2009).

[11] M. Antonello et al., *Search for anomalies in the νe appearance from a νμ beam*, Eur. Phys. J. C 73:2599 (2013); M. Antonello et al., *Experimental search for the "LSND anomaly"with the ICARUS LAr-TPC detector in the CNGS beam,* Eur. Phys. J. C 73:2345 (2013).

[12] N. Agafonova et al., *Search for νμ to νe oscillation with the OPERA experiment in the CNGS beam*, JHEP 07 004 (2013).
[13] N. Aghanim et al., *Planck 2018 results. VI: cosmological parameters,* arXiv:1807.06209
[14] R. Acciarri et al., *A proposal for a three-detector Short-Baseline Neutrino oscillation program in the Fermilab Booster neutrino beam*, arXiv:1503.01520.
[15] M. Babicz et al., *Timing properties of Hamamatsu R5912-MOD photomultiplier tube for the ICARUS T600 light detection system,* NIM 912 231-234 (2018).] M. Babicz et al., *Tests and characterization of 400 Hamamatsu R5912-MOD photomultiplier tubes for the ICARUS T600 detector*, JINST 13 P10030, 2018.

NOvA Recent Results with Neutrino+Antineutrino Data

Tomas Nosek[1] on behalf of the NOvA Collaboration

Charles University, Faculty of Mathematics and Physics, Institute of Particle and Nuclear Physics, V Holesovickach 2, 180 00 Prague, Czech Republic

Abstract. NOvA is a long-baseline neutrino oscillation experiment using Fermilab's 700 kW NuMI muon neutrino beam. Two functionally identical scintillator detectors are placed off the beam axis, separated by 810 km oscillation baseline. Both detectors have high active material fractions and are finely segmented allowing for precise identification and analysis of neutrino interactions. By observing both the disappearance of muon (anti)neutrinos and appearance of electron (anti)neutrinos in the beam, NOvA can impose constraints on the yet undetermined parameters of neutrino oscillation phenomenon, such as the neutrino mass ordering, CP violation and the octant of the large mixing angle. NOvA also studies neutral-current neutrino interactions, thus extending its scope beyond the standard three-flavor paradigm. This paper presents the latest NOvA results with the complete neutrino data sample up to date and first antineutrino data collected since February 2017.

1 Introduction

NOvA is a long-baseline neutrino oscillation experiment designed to make measurements of muon neutrinos (ν_μ) disappearance and electron neutrinos (ν_e) appearance in Fermilab's NuMI (Neutrinos at the Main Injector) beam. Well tuned for the first oscillation maximum around neutrino energy of 2 GeV over 810 km baseline, the experiment studies primarily four channels of oscillations: $\nu_\mu \rightarrow \nu_\mu$ or $\nu_\mu \rightarrow \nu_e$ and $\overline{\nu_\mu} \rightarrow \overline{\nu_\mu}$ or $\overline{\nu_\mu} \rightarrow \overline{\nu_e}$. They allow to address several concerns of neutrino oscillations:

1. mass ordering, i.e. normal (NH) or inverted hierarchy (IH) of neutrino masseigenstates,
2. direct CP violation (δ_{CP} phase) and
3. precise determination of θ_{23} and Δm^2_{32} neutrino mixing parameters.

This paper reports the 2018 NOvA combined analysis of 8.85×10^{20} POT (protons on target) neutrino data collected from Feb 2018 to Feb 2017 and

[1] e-mail: tomas.nosek@mff.cuni.cz

6.91×10^{20} POT antineutrino data collected from Feb 2017 to Apr 2018. Neutrino oscillations parametrization, fits, predictions and interpretation of the results were done within the standard oscillation model of 3 active neutrino flavors of electron, muon and tau neutrino (ν_τ) [1].

2 The NOvA Experiment

The experiment consists of two large functionally identical detectors sitting 14.6 mrad off the beam axis 810 km apart. This off-axis configuration reduces uncertainty on energy of incoming neutrinos and suppresses the higher-energy neutrinos background producing neutral current interactions (NC) misidentified as ν_e charged current (CC). On the other hand, it also results in a lower intensity than in the on-axis region, mitigated by the size of the detectors and beam power upgrades.

The detectors are finely grained and high active ($\sim$ 65% active mass) liquid scintillator tracking calorimeters, which allow for precise analysis of investigated neutrino interactions events. They are designed to be as similar as possible aside from size: the far detector (FD) is 14 kt and on surface located in Ash River, Minnesota, the near detector (ND) is located underground in Fermilab, close enough to the neutrinos source to see a far greater flux with only 0.3 kt of mass. Both are constructed out of extruded PVC cells (3.9×6.6 cm in cross section and 15.5/3.8 m in length for FD/ND) filled with scintillator and equipped with a wavelength shifting fiber connected to avalanche photodiode (APD). They collect light produced by charged particles subsequently amplified and digitized by APDs. The cells alternate in horizontal and vertical orientation to allow for a stereo readout. More information on detectors can be found in Ref. [2].

NuMI beam is created following the decay of charged pions and kaons produced by 120 GeV protons hitting a carbon target. These parent mesons are focused by two magnetic horns towards the NOvA detectors and decay in flight through the chain $K^+, \pi^+ \rightarrow \mu^+ + \nu_\mu$, with the muon then decaying as $\mu^+ \rightarrow e^+ + \nu_e + \overline{\nu_\mu}$. By switching the polarity of the horns, opposite charge sign particles can be focused, thus effectively selecting an antineutrino beam. The resulting composition in range 1-5 GeV at ND is of 96% ν_μ, 3% $\overline{\nu_\mu}$ and 1% $\nu_e + \overline{\nu_e}$ in case of neutrino beam and 83% $\overline{\nu_\mu}$, 16% ν_μ and 1% $\overline{\nu_e} + \nu_e$ in case of antineutrino beam.

To identify and classify neutrino interactions NOvA uses a method based on image recognition techniques known as Convolutional Visual Network (CVN), see Ref. [3]. CVN treats every interaction in the detector as an image with cells being pixels and collected charge being their color. When trained with simulated events and cosmic data, CVN can extract abstract topological features of neutrinolike interactions with convolutional filters (feature maps [3]). With an input of calibrated 2D pixelmap (two views of horizontal and vertical event

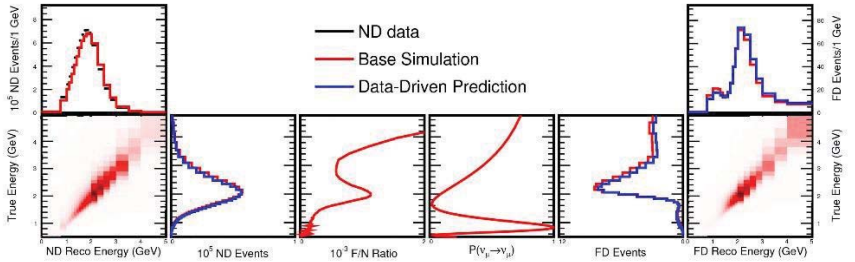

Figure 1: An illustration of NOvA's F/N technique. From left to right: reconstructed to true ν_μ energy translation, F/N ratio, $\nu_\mu \to \nu_\mu$ oscillation probability, true to reconstructed ν_μ energy restoration. Base simulation in red, ND data-driven corrected prediction in blue.

projections), the output is a set of normalized classification scores ranging over hypotheses of beam neutrinos event (ν_μ CC, ν_e CC, ν_τ CC and NC) or cosmics. CVN has been used together with additional supporting PIDs: seperate ν_e and ν_μ cosmic rejection boosted decision trees (BDT) and muon track identification in ν_μ events.

NOvA's two identical detectors design enables to employ data-driven predictions of FD observations. ND neutrinos spectra are considered the effective unoscillated source of oscillated neutrinos measured in FD. FD ν_μ and ν_e signal is predicted using ND ν_μ, whereas FD ν_e beam background is constrained using ND ν_e sample. This Far/Near (F/N) technique includes several steps (Fig. 1). Firstly, the reconstructed neutrino energy spectrum is unfolded to true energy using a simulated migration matrix. Secondly, F/N ratio accounting for geometry, beam divergence and detector acceptance is applied to create unoscillated FD prediction. Then the FD spectrum is weighted by the oscillation probability for a given set of oscillation parameters. Finally, the true energy is smeared back again to the reconstructed energy via the migration matrix. As a reward, F/N technique significantly reduces both neutrino flux and cross section systematic uncertainties. ND reconstructed energy spectra of ν_μ and $\overline{\nu_\mu}$ (the source of FD ν_μ and ν_e signals) can be found in Fig. 2.

3 Muon Neutrino and Antineutrino Disappearance

Muon neutrino disappearance channel is primarily sensitive to $|\Delta m^2_{32}|$ and $sin^2\,2\theta_{23}$ and the precision with which they can be measured depends on the ν_μ

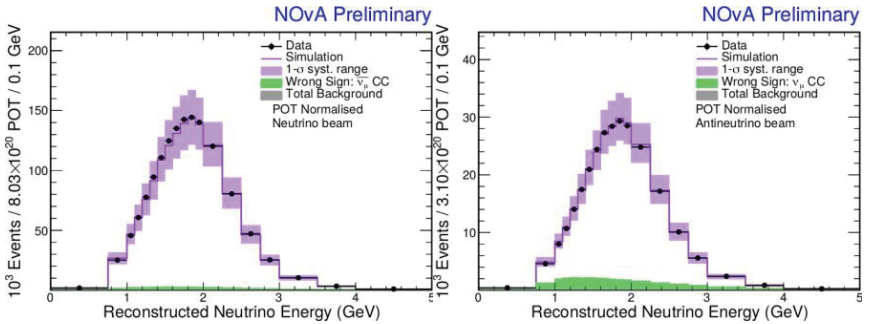

Figure 2: ND selected ν_μ (left) and $\overline{\nu_\mu}$ (right) reconstructed energy in data (black dots) and simulation (purple). Each bin is normalized by its width.

energy resolution. Energy of $\nu_\mu$is reconstructed as a sum of the energy of a muon, estimated from the range of muon track, and remaining hadronic energy. To get best effective use of the energy resolution, the data binning is optimized in two ways. First, the energy binning has finer bins near the disappearance maximum and coarser bins elsewhere. Second, the events in each energy bin are further divided into four populations, or "quartiles", of varying reconstructed hadronic energy fraction, which correspond to different ν_μ energy resolution. The divisions are chosen such that the quartiles are of equal size in the unoscillated FD simulation. The ν_μ ($\overline{\nu_\mu}$) energy resolution is estimated to be 5.8% (5.5%), 7.8% (6.8%), 9.9% (8.3%) and 11.7% (10.8%) for each quartile, ordered from lower to higher hadronic energy fraction. F/N technique is applied separately in quartiles, which has the additional advantage of isolating most of the cosmic and beam NC background events along with events of worst energy resolution (4^{th} quartile).

There are 113 (65) ν_μ ($\overline{\nu_\mu}$) CC candidates observed in FD, whereas with no oscillations, the projected ND flux would result in 730^{+38}_{-49} (syst.) $\pm$27 (stat.) ($266^{+12}_{-14} \pm 16$) events. The total estimated background is 3.76 (1.12) events with 2.07 (0.46) cosmic-ray-induced events, 1.19 (0.39) NC events and 0.51 (0.23) other beam backgrounds. The expected wrong sign contamination is of 7.24 $\overline{\nu_\mu}$ in ν_μ beam and 12.58 ν_μ in $\overline{\nu_\mu}$. FD data and best fit prediction can be seen in Fig. 3. All above show a clear indication of both ν_μ and $\overline{\nu_\mu}$ disappearance.

4 Electron Neutrino and Antineutrino Appearance

In order to maximize the statistical power of the ν_e selected events at FD, the sample is binned in both reconstructed energy and CVN score. There are two CVN bins of low and high purity (low and high PID), or "core" selection, and an

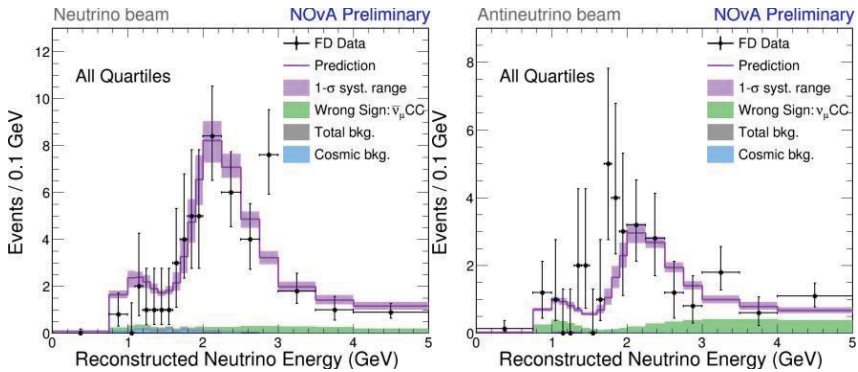

Figure 3: FD data (black dots) selected ν_μ (left) and $\overline{\nu_\mu}$ (right) candidates reconstructed energy compared to the best fit prediction (purple line) with 1σ systematics uncertainty range. Summed over all quartiles of hadronic energy fraction.

additional "peripheral" bin. Events which fail containment or cosmic rejection cuts, but do have a very high CVN ν_e CC score, may be added to the peripheral sample. Because the events on the periphery are not always fully contained they are summed into a single bin instead of estimating their energy (up to reconstructed 4.5 GeV). The overall integrated selection efficiency of ν_e ($\overline{\nu_e}$) is 62% (67%), beam backgrounds are reduced by 95% (99%), the purity of the final predicted FD samples depends on the oscillation parameters, but ranges from 57% (55%) to 78% (77%).

To estimate FD beam background F/N technique is used with ND ν_e sample. It consists of beam ν_e and ν_μ CC or NC interactions misidentified as ν_e CC. Since each of these components oscillate differently along the way to the FD, the sample needs to be broken down into them. In the case of neutrino beam, ν_e component is constrained by inspecting the low-energy and high-energy ν_μ CC spectra to adjust the yields of the parent hadrons that decay into both ν_μ and ν_e (track ν_μ and ν_e to their common parents). The ν_μ component is estimated from observed distributions of time-delayed electrons from stopping μ decay. The rest is attributed to NC interaction. In the case of antineutrino beam, the components are only evenly and proportionally scaled to match ND data in each bin. ND selections and their breakdowns, or "decomposition", can be seen in Fig. 4. The high PID bin is dominated by the beam $\nu_e + \overline{\nu_e}$, the low PID bin has a significant admixture of ν_μ ($\overline{\nu_\mu}$) CC and NC events. The beam background of FD peripheral bin is estimated from the high PID bin of the core sample.

There are 58 (18) ν_e ($\overline{\nu_e}$) candidates in FD data with the prediction of 30 to 75 (10 to22) depending on oscillation parameters (δ_{CP}, θ_{23} and NH or IH).

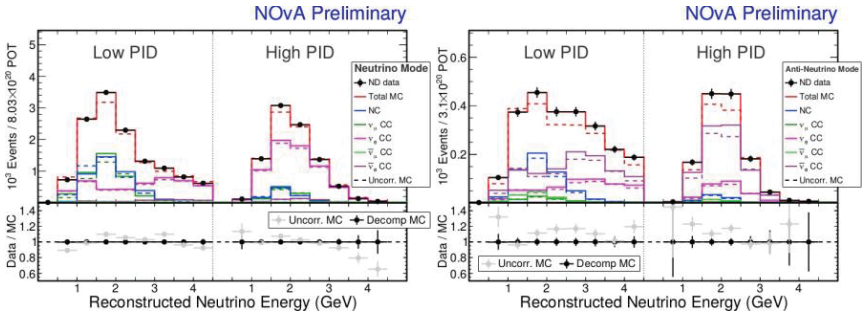

Figure 4: ND selected ν_e (left) and $\overline{\nu_e}$ (right) reconstructed energy data (black dots), uncorrected simulation (dashed red) and data-driven correction (solid red). The selection is decomposed (broken down) into NC (blue), $\nu_\mu/\overline{\nu_\mu}$ CC (dark/light green) and $\nu_e/\overline{\nu_e}$ CC (light/dark magenta). Binned in two PID bins, which are correlated to lower and higher purity of $\nu_e + \overline{\nu_e}$.

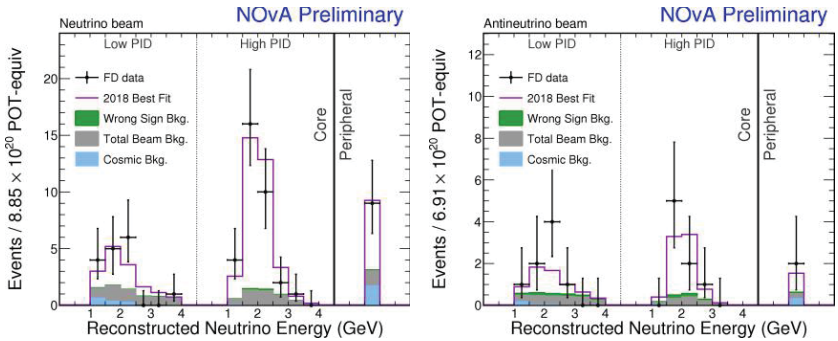

Figure 5: FD data (black dots) selected ν_e (left) and $\overline{\nu_e}$ (right) candidates reconstructed energy binned in low and high PID bins and peripheral sample with energies up to 4.5 GeV. Best fit prediction (purple) shows the expected background of wrong sign (green), other beam background (grey) and cosmics (blue) as shaded areas.

The total expected background is 15.1 (5.3) events of 6.85 (2.57) beam $\nu_e + \overline{\nu_e}$, 0.63 (0.07) $\nu_\mu + \overline{\nu_\mu}$, 0.37 (0.15) $\nu_\tau + \overline{\nu_\tau}$, 3.21 (0.67) NC events, 3.33 (0.71) cosmic-ray-induced events and 0.66 $\overline{\nu_e}$ (2.57 ν_e) from wrong sign component of the ν_μ ($\overline{\nu_\mu}$) sample. The FD data and best fit predictions can be seen in Fig. 5. Antineutrino data gives more than 4σ evidence of $\overline{\nu_e}$ appearance in $\overline{\nu_\mu}$beam.

5 Constraints on Oscillation Parameters

To obtain oscillation parameters, a simultaneous fit of joint $\nu_e + \nu_\mu$ and both neutrino and antineutrino data was performed. Systematic uncertainties are incorporated as nuisance parameters with Gaussian penalty term, appropriately correlated between all the data sets. The leading systematics are worth a note: detector calibration (calorimetric energy scale), light production and collection model and muon energy scale (abs.+rel.) for ν_μ disappearance; detector response and calibration, neutrino cross-sections and actual ND to FD differences for ν_e appearance. Several oscillation parameters are taken as inputs from other measurements: solar parameters θ_{12} and Δm^2_{12}, the mixing angle θ_{13} and its uncertainty was taken from reactor experiments, all in Ref. [1]. The best fit is

$$\Delta m^2_{32} = 2.51^{+0.12}_{-0.08} \times 10^{-3}\text{eV}^2, \qquad sin^2\,\theta_{23} = 0.58 \pm 0.03, \qquad \delta_{CP} = 0.17\pi,$$

which corresponds to normal hierarchy and the upper θ_{23} octant (UO, $\theta_{23} > 45°$). All confidence levels (C.L.) and contours are constructed following the Feldman-Cousins approach [6].

The 90% C.L. allowed region for a combination of Δm^2_{32} versus $sin^2\,\theta_{23}$ in the $\Delta m^2_{32} > 0$ half-plane, together with other results from MINOS+ (2018) [7], T2K (2017) [8], IceCube (2017) [9] and Super-Kamiokande (2017) [10] overlaid is shown in Fig. 6. There is a clear consistency within all experiments despite that NOvA data asymetrically points to UO and rejects maximal 23 mixing ($sin^2\,\theta_{23} = 0.5$) at about 1.8σ C.L.

Fig. 7 shows the 1, 2 and 3σ C.L. allowed regions for $sin^2\,\theta_{23}$ versus δ_{CP} in both cases of NH and IH (mass ordering). It is worth noticing, that the values of δ_{CP} around $\pi/2$ are excluded at $> 3\sigma$ C.L. for IH, similarly to previous NOvA neutrino only analysis [4]. On the other hand, rather weak constraints on δ_{CP} itself allow all possible values $[0,2\pi]$ in 2σ interval for the case of NH and UO.

6 Future Prospects

NOvA is expected to run until 2024 with about an equal total exposure of neutrino and antineutrino beam. Moreover, several accelerator upgrades to enhance the beam performance are planned for the next years. Based on these prerequisities and projected 2018 analysis techniques there is a possibility of more than 3σ sensitivity to hierarchy resolution by 2020 in case of favorable true values of oscillation parameters (NH and $\delta_{CP} = 3\pi/2$), or by 2024 for 30-50% of all possible δ_{CP} otherwise. Besides that, about 3σ sensitivity to θ_{23} octant determination and more than 2σ to CP violation in case of $\delta_{CP} = \pi/2$ or $3\pi/2$ (maximal violation) are expected by 2024.

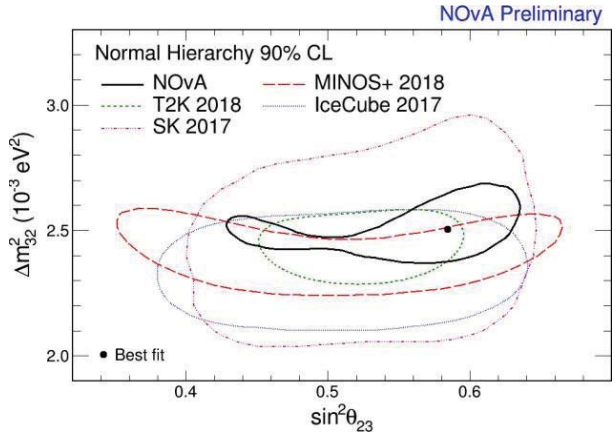

Figure 6: Comparison of the allowed regions of Δm^2_{32} vs. $sin^2\,\theta_{23}$ parameter space at 90% C.L. as obtained by recent experiments: NOvA (black solid, black dot labels the best fit value), T2K (green dashed), MINOS+ (red dashed), IceCube (blue dotted) and Super-Kamiokande (purple dash-dotted).

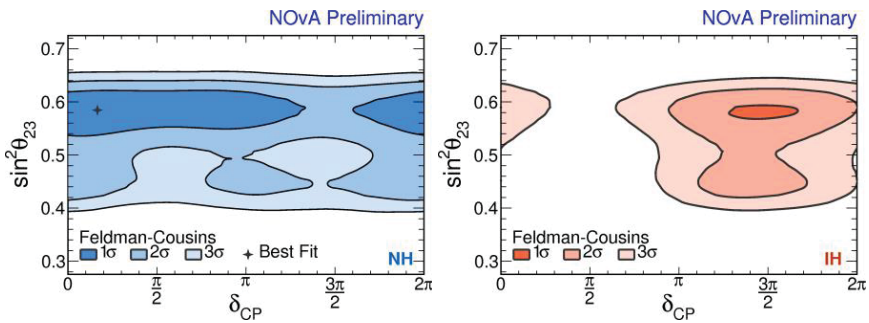

Figure 7: 1, 2 and 3σ allowed regions of $sin^2\,\theta_{23}$ vs. δ_{CP} neutrino oscillation parameter space consistent with ν_e appearance and ν_μ disappearance data. The left plot corresponds to the case of normal hierarchy of neutrino masses ($\Delta m^2_{32} > 0$), the left one to the inverted hierarchy ($\Delta m^2_{32} < 0$).

To further improve neutrino oscillation analysis and to extend the reach of the experiment, NOvA plans to start an intensive test beam program in early 2019. The main focus will be on simulation tuning, systematics study and their reduction, validation and training of reconstruction or machine learning algorithms.

7 Summary

The first antineutrino data from NOvA (6.91×10^{20} POT) has been analyzed together with existing neutrino data (8.85×10^{20} POT). The measurements are well consistent with the standard oscillation model of 3 active neutrino flavors. NOvA observes more than 4σ evidence for $\overline{\nu_e}$ appearance in $\overline{\nu_\mu}$ beam. The results of joint analysis of neutrino and antineutrino and both ν_μ disappearance and ν_e appearance channels give the parameters estimates of $sin^2\,\theta_{23} = 0.58 \pm 0.03$ and $\Delta m^2_{32} = 2.51^{+12}_{-0.08} \times 10^{-3}\text{eV}^2$, which are in a good agreement with other accelerator and atmospheric oscillation experiments. There is an indication of nonmaximal 23 mixing at 1.8σ and inkling of upper octant of θ_{23} angle. Data also prefers normal hierarchy of neutrino masses at 1.8σ, while simultaneously disfavoring inverted hierarchy for δ_{CP} around $3\pi/2$ at more than 3σ. NOvA plans to continue running until 2024 in both neutrino and antineutrino beam modes.

Acknowledgments. I would like to thank the organizers for a great conference of NTIHEP 2018. This work is supported by MSMT CR (Ministry of Education, Youth and Sports, Czech Republic).

References

[1] M. Tanabashi *et al.* [Particle Data Group], *Review of Particle Physics*, Phys. Rev. D 98, 030001 (2018)

[2] D. S. Ayres *et al.* [NOvA Collaboration, *The NOvA Technical Design Report*, FERMILAB-DESIGN-2007-01

[3] A. Aurisano *et al., A Convolutional Neural Network Neutrino Event Classifier*, JINST 11, P09001 (2016), arXiv:1604.01444 [hep-ex]

[4] P. Adamson *et al.* [NOvA Collaboration, *New constraints on oscillation parameters from* ν_e *appearance and* ν_μ *disappearance in the NOvA experiment*, Phys. Rev. D 98, 032012 (2018), arXiv:1806.00096 [hep-ex]

[5] P. Adamson *et al.* [MINOS Collaboration], *The NuMI Neutrino Beam*, Nucl. Instrum. Meth. A 806, 279 (2016), arXiv:1507.06690 [physics.acc-ph]

[6] G. J. Feldman and R. D. Cousins, *A Unified approach to the classical statistical analysis of small signals*, Phys. Rev. D 57, 3873 (1998), arXiv:physics/ 9711021 [physics.data-an]

[7] A. Aurisano [on behalf of the MINOS+ Collaboration], *Recent Results from MINOS and MINOS+*, presented at Neutrino 2018, Heidelberg, doi:10.5281/zenodo.1286760

[8] K. Abe *et al.* [T2K Collaboration], *Search for CP Violation in Neutrino and Antineutrino Oscillations by the T2K Experiment with* 2.2×10^{21} *Protons on Target*, Phys. Rev. Lett. 121, 171802 (2018), arXiv:1807.07891 [hep-ex]

[9] M. G. Aartsen *et al.* [IceCube Collaboration], *Measurement of Atmospheric Neutrino Oscillations at 656 GeV with IceCube DeepCore*, Phys. Rev. Lett. 120, 071801 (2018), arXiv:1707.07081 [hep-ex]

[10] K. Abe *et al.* [Super-Kamiokande Collaboration], *Atmospheric neutrino oscillation analysis with external constraints in Super-Kamiokande I-IV*, Phys. Rev. D 97, 072001 (2018), arXiv:1710.09126 [hep-ex]

II "ADVANCES IN THEORETICAL PHYSICS, STANDARD MODEL AND BEYOND"

Recent results with ALICE experiment

Marek Bombara for the ALICE Collaboration
Pavol Jozef Safarik University
E-mail: marek.bombara@cern.ch

1 Introduction

ALICE experiment is dedicated to study the hot and dense nuclear matter produced in heavy ion collisions at the Large Hadron Collider (LHC). In this way we can explore QCD matter phase diagram and study strong interaction at distances larger than hadron size. Also, it is an unique opportunity to probe primordial matter from the Big Bang epoch in the laboratory.
A critical energy density needed for the creation of partonic degree state of matter (also known as Quark-Gluon Plasma, QGP) is $\sim 1\text{GeV/fm}^3$ [1]. In the heavy ion collisions at the LHC TeV scale this density is easily surpassed by factor 12 [2]. Results from RHIC and LHC showed that quarks and gluons are strongly coupled to their neighbours and as a consequence, the QGP behaves like a relativistic hydrodynamic fluid. The partons undergo a collective expansion until the critical energy density is reached and they convert to hadrons. Most of the QGP signatures are thus inevitably indirect - they can be studied via hadron properties measured by the detector.
A crucial part of the ALICE physics programme is to study pp and p–Pb collisions and compare them with heavy ion collisions in order to disentangle effects coming from individual nucleon-nucleon interactions or from cold nuclear matter.
Some of the notable QGP signatures and their corresponding experimental variables are elaborated in following sections.

2 Strangeness enhancement

Enhancement of strangeness was originally proposed among first signatures of QGP [3]. Production of strange quarks in QGP should be energetically favoured and faster than production in hadron gas. Experimental variable based on comparison of strange hadron production in nucleus-nucleus (A–A) collisions with nucleon-nucleon (or nucleon-nucleus) collisions indeed confirmed strangeness enhancement at SPS [4], RHIC [5] and LHC [6].
A variable representing a size of the system is the number of nucleons participating in the collision (N_{part}). Since at the LHC the N_{part} does not scale with particle multiplicity [7] a different experimental variable is used to study the strangeness enhancement: a ratio to pion production as a function of multiplicity. An outstanding LHC performance allows to study not only multiplicity dependence in nucleus-nucleus collisions, but also in pp

and p–Pb collisions. In Fig. 1 we can see a remarkable overlap of the ratio in pp, p–Pb and peripheral Pb–Pb collisions at various energies. There is a smooth transition among those three different collision systems with various energies. It seems that the variable driving the strangeness production is the produced multiplicity. We also see a rising trend for multistrange hyperons

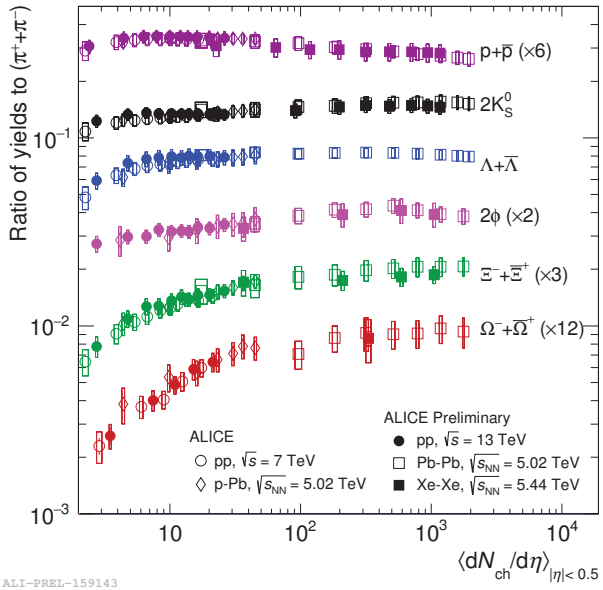

Figure 1: p_{T}-integrated yield ratio to pions as a function of $\langle dN_{\mathrm{ch}}/d\eta \rangle$ measured in $|y| < 0.5$ in different collision systems

from low multiplicity pp collisions which can be better appreciated in Fig. 2. Strange particle-to-pion ratios are normalized to the ratio in multiplicity-inclusive sample and plotted as a function of multiplicity in pp and p–Pb. The strangeness enhancement is clearly visible for high multiplicity pp and p–Pb collisions and the hierarchy of the enhancement is determined by the hadron strangeness content. The observation of the enhancement in small system questions paradigm of QGP being solely produced in A–A collisions. On the other hand there are also other effects (like colour reconnection or colour ropes) which can produce more strangeness and hence mimic the QGP signature [9].

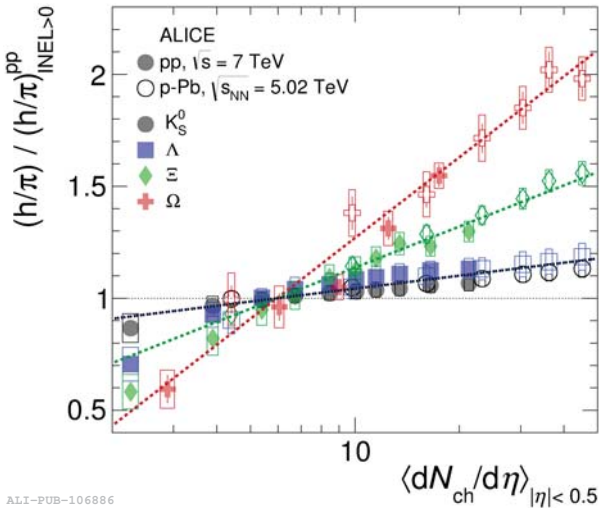

Figure 2: Particle yield ratios to pions of strange and multi-strange hadrons normalised to the values measured in the inclusive pp sample (INEL > 0), both in pp and in p–Pb collisions [8].

3 Azimuthal anisotrophy

A consequence of collisions with not fully overlapping nuclei is an almond shaped fireball formed by hot and dense matter. In such asymmetrical shape the pressure gradient is higher in in-plane direction than in out-of-plane direction. Initial spatial asymmetry of partonic matter then leads to azimuthal momentum space anisotropy in hadron distribution due to the different pressure gradients. Anisotropy can be quantified by second Fourier coefficient of the particle distribution (v_2 a.k.a. elliptic flow):

$$E\frac{d^3N}{d^3p} = \frac{1}{2\pi}\frac{d^2N}{p_T dp_T dy}\left(1 + 2\sum_{n=1}^{\infty} v_n(p_T, y)\cos[n(\phi - \Psi_R)]\right) \qquad (1)$$

where

$$v_n(p_T, y) = \langle\cos[n(\phi - \Psi_R)]\rangle \qquad (2)$$

and Ψ_R is reaction plane angle. "Lumpiness" of the fireball (due to fluctuations in the initial energy density of the colliding nucleons) can give rise to higher harmonics (v_n, $n = 3, 4, ..$). Measured azimuthal anisotropy as a function of system size is in a very good agreement with corresponding predictions from hydrodynamic models [10]. This is an indication of strongly coupled matter. Multiplicity dependence of different flow coefficients for various collisional systems and energies is plotted in Fig. 3. The results

should not contain any contribution from other effects resembling collectivity like jets or resonance decays. It is intriguing to observe that non-zero collectivity is also present in pp and p–Pb collisions.

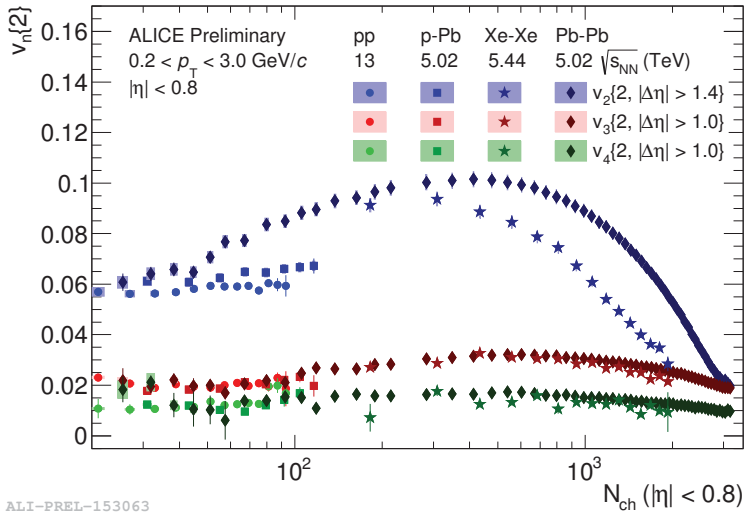

Figure 3: Multiplicity dependence of different flow coefficients $v_n\{2\}$ in 13 TeV pp, 5.02 TeV p–Pb, 5.44 TeV Xe–Xe and 5.02 TeV Pb–Pb collisions.

4 Hard probes

High p_T partons are produced by hard scattering at early times and can hence probe all stages of collision. Measurements so far suggest enormous energy losses at the LHC about 10 GeV per 1 fm [2]. One of the most common variable for studying interactions of high p_T partons with QGP medium is nuclear modification factor:

$$R_{AA}(p_T) = \frac{d^2N_{AA}/dydp_T}{\langle N_{coll}\rangle d^2N_{pp}/dydp_T} \quad (3)$$

The R_{AA} represents a ratio of production in A–A and binary scaled production in pp. N in the formula could be particles or jets. $\langle N_{coll}\rangle$ (number of binary collisions of nucleons) is calculated by Glauber model [11]. The factor should be 1 for colourless objects in QGP like γ or intermediate bosons as it is in Fig. 4. The factor is 1 also for high p_T hadrons in p–Pb. On the other hand, we see a strong suppression of high p_T hadrons measured in central Pb–Pb collision which indicates energy loss at partonic level.

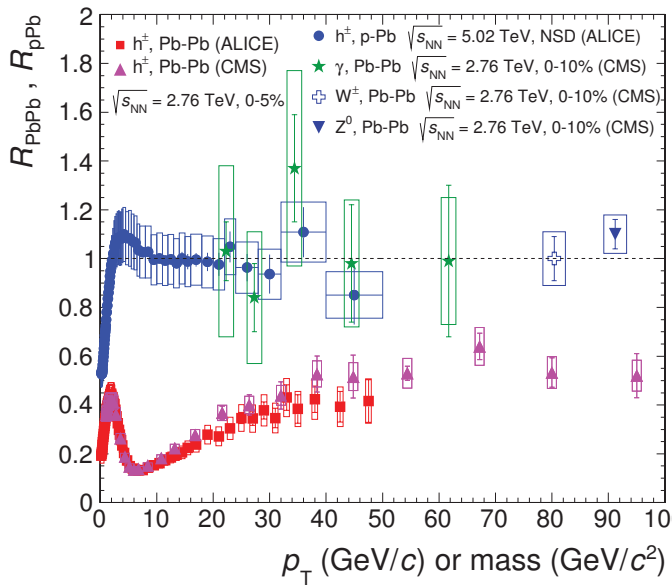

Figure 4: Transverse momentum dependence of the nuclear modification factor of various particles ($h^{\pm}$) measured in minimum-bias (NSD) p-Pb collisions at $\sqrt{s_{\rm NN}} = 5.02$ TeV in comparison to data on the nuclear modification factor $R_{\rm PbPb}$ in central Pb-Pb collisions at $\sqrt{s_{\rm NN}} = 2.76$ TeV [12, 13].

5 Summary

The ALICE experiment studies properties of QGP in nucleus-nucleus collisions. Studying pp and p–Pb collisions is also important in order to disentangle effects not related to QGP. Strangeness enhancement, as one of the original proposed signatures of QGP, is also seen in high multiplicity pp and p–Pb collisions. Elliptic flow in A–A and suppression of R_{AA} confirm existence of dense and strongly coupled plasma of quarks and gluons. Non-zero flow and strangeness enhancement observation in pp and p–Pb collisions raises questions: Is high multiplicity pp (p–Pb) collision a small droplet of QGP? If yes, why there is no evidence for the suppression of particle production at high-p_{T}?

References

[1] J. D. Bjorken, *Phys. Rev.* D **27** (1983) 140-151

[2] W. Busza, K. Rajagopal and W. van der Schee *Ann. Rev. Nucl. Part. Sci.* **68** (2018) 1–49

[3] J. Rafelski and B. Müller, *Phys. Rev. Lett.* **48** (1982) 1066-1069; Erratum: *Phys. Rev. Lett.* **56** (1986) 2334

[4] F. Antinori *et al.* (NA57 Collaboration), *J. Phys.* G **32** (2006) 427

[5] B. I. Abelev *et al.* (STAR Collaboration), *Phys. Rev.* C **77** (2008) 044908

[6] B. Abelev *et al.* (ALICE Collaboration), *Phys. Lett.* B **728** (2014) 216

[7] K. Aamodt *et al.* (ALICE Collaboration), *Phys. Rev. Lett.* **106** (2011) 032301

[8] J. Adam *et al.* (ALICE Collaboration), *Nature Physics* **13** (2017) 535

[9] C. Bierlich and J. R. Christiansen, *Phys. Rev.* D **92** (2015) 09401

[10] J. Adam *et al.* (ALICE Collaboration), *Phys. Rev. Lett.* **116** (2016) 132302

[11] M. L. Miller, K. Reygers, S. J. Sanders and P. Steinberg *Ann. Rev. Nucl. Part. Sci.* **57** (2007) 205–243

[12] B. Abelev *et al.* (ALICE Collaboration), *Eur. Phys. J.* C **74** (2014) 3054

[13] S. Chatrchyan *et al.* (CMS Collaboration), *JHEP* **03** (2015) 022

Diffraction in lepton-hadron and hadron-hadron scattering

Roberto Fiore
Department of Physics, University of Calabria, I-87036 Arcavacata di Rende, Cosenza, ITALY
robertofiore1943@gmail.com

László Jenkovszky
Bogolyubov Institute for Theoretical Physics (BITP),
14-b, Metrologicheskaya str., Kiev, 03680, UKRAINE
jenk@bitp.kiev.ua

Nadya Maslova
Physics Department, Taras Shevchenko National University of Kyiv,
03127, Kyiv, Hlushkova Avenue, 4, UKRAINE
nadiiamaslova@gmail.com

Rainer Schicker
Physikalisches Institut, Im Neuenheimer Feld 226,
Heidelberg University, 69120 Heidelberg, GERMANY
schicker@physi.uni-heidelberg.de

Jolán Turóci
Uzhhorod National University,
14, Universytetska str., Uzhgorod, 88000, UKRAINE
turocijolika@gmail.com

We study diffractive phenomena in proton-proton and electron-proton collisions at the LHC and DESY using analyticity, crossing symmetry and unitarity, particularly the Regge-pole model realizing these concepts. Fits to the data are presented and tensions between theoretical predictions and the data that may indicate the way to further progress are in the focus of our paper. Elastic *pp* (LHC) and DIS *ep* scattering (DESY) usually are considered by means of two pomerons, "soft" and "hard" or with a single one, but varying intercept. We introduce a reggeometric pomeron replacing the above objects.

Keywords: LHC; Regge-poles; pomeron; odderon; duality; unitarity; diffraction; CED; DIS.

1. Introduction

In this paper we present our study of diffractive proton-proton and electron-proton collisions in the framework of the Regge pole model (we recall that Regge poles lie on the so called Regge trajectories $\alpha(t)$, in the t channel) through the introduction of a reggeometric pomeron $\alpha_P(t)$. First of all, we start with a brief recapitulation of the present state of the theory. The construction of the scattering amplitude implies two steps: choice of the input (Born term) and subsequent unitarization. The better the input (*i.e.*,the closer to the expected unitary output), the better are the chances of a successfully converging solution (*i.e.*, the smaller are the unitarity corrections). The standard procedure is to use a simple Regge-pole amplitude as input with subsequent eikonalization.

The common feature in many papers studying this problem (see Refs. 1-7) is the use of a supercritical pomeron, $\alpha_P(t=0) > 1$, as input, motivated by the rise of the cross sections

and by perturbative QCD calculations (for instance, Ref. 8, where the BFKL theory is introduced). The next indispensable step is unitarization, usually realized in the eikonal formalism. Unitarization is necessary at least for two reasons: to reconcile the rise of the total cross sections with the Froissart-Martin bound and to generate the diffractive dip-bump structures in the differential cross sections. The latter issue is critical for most of the theoretical constructions since the standard eikonalization procedure results in a sequence of secondary dips and bumps, while experimentally a single dip-bump is observed only, as confirmed by all measurements including those recent, at highest LHC energy. This deficiency is usually resolved e.g. by introducing the so-called enhanced diagrams, or extra free parameters. Still, none of the above-mentioned models was able to reproduce the whole set of pp and $p\bar{p}$ a data from the ISR to the LHC in the dip-bump region. This is a crucial test for all existing models. These models did not predict the unexpected rapid rise, as $\ln^2 s$, of the forward slope revealed by the experiment TOTEM (see Ref. 9) or the drastic decrease of the parameter $\rho(s,0)$, ratio of the real to imaginary part of the elastic scattering amplitude, reported in Ref. 10. The latter (a single data point) was fitted a posteriori by an odderon [11], although in an earlier paper by one of the authors the model predicted quite a different trend. To summarize, the existing Regge-eikonal models are compatible with the general trend of high-energy diffractive scattering, but many details, such as the dynamics of the dip-bump, the role of the odderon still remains open and controversial.

The TOTEM Collaboration announced [12] new results of the measurements on the proton-proton elastic slope at 7 and 8 TeV, B(7 TeV)= 19,89$\pm$0,27 and B(8 TeV)= 19,9$\pm$0,3 GeV^{-2}, showing that the logarithmic approximation, with a ln(s) behavior, an exponential fit over the large |t|-range from 0.005 to 0.2 GeV^2 describes the differential distribution well. These data offer new information concerning the burning problem of the strong interaction dynamics, namely the onset of (or the appoach to) the asymptotic regime of the strong interaction.

The approach to the expected asymptotic behavior has two stages. One is the onset of pomeron dominance, *i.e.*, of the domain where secondary reggeon contributions become negligible. It can be shown that in the nearly forward direction, at LHC energies the contribution from secondary trajectories is negligible, smaller than the error bars in the measured total cross section, *i.e.* "soft" physics at the LHC is pomeron-dominated. The next question is where does the pomeron itself reaches its asymptotics. Below we address these questions.

2. *S*-matrix theory, Regge-pole models

Regge-pole theory is the adequate tool to handle "soft" or "forward" physics. It is a successful example of the analytic S-matrix theory, based on analyticity, unitarity and crossing symmetry of the scattering amplitude. It was developed in the 60-ies of the past century, culminating in discovery of duality and dual amplitudes, whereupon, in the 70-ies was overshadowed by local quantum eld theories, more specifically by quantum chromodynamics (QCD).

2.1. Regge poles and trajectories; factorization

Below we introduce the Regge-pole model with emphases on its practical applications. Its derivation from potential scattering, the Schrödinger equation and its relation to quantum mechanics can be found in many textbooks (see, e.g., Refs. 13-15).

In relativistic S-matrix theory we do not have a Schrödinger equation, and the existence of Regge poles is conjectured by analogy with quantum mechanics. The use of the complex angular moments results (for details, see Refs.13-15) in a representation for the amplitude,

$$A(s,t) = \beta(t)\xi(t)s^{\alpha(t)},$$

valid in all channels, where $\beta(t)$ is the residue and

$$\xi(t) = -\frac{1 \pm e^{-i\pi\alpha(t)}}{sin\pi\alpha(t)}$$

is the signature factor.

Baryon and meson trajectories are nearly linear functions in a limited range of their variables. This is suggested by the (nearly) exponential shape of forward cone in elastic scattering and by the meson and baryon spectrum. In Fig. 1 a typical Chew-Frautschi plot is shown. Similar nearly linear plots are known for other mesons and baryons [13-15]. Whatever appealing, this simplicity is only an approximation to reality: analyticity and unitarity as well as the finiteness of resonances require Regge trajectories to be non-linear complex functions (see, for instance, Refs. 16-18**)**.

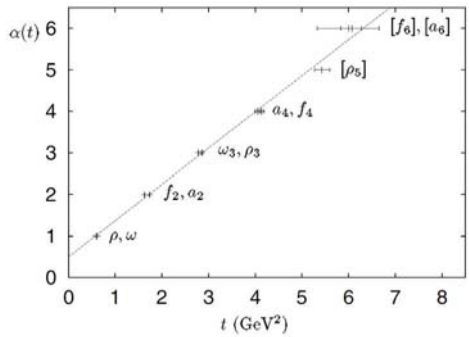

Fig. 1. Linear mesonic Chew-Frautschi plot (spin vs. squared masses, $Re\alpha(t)$).

Let us reiterate that Regge trajectories are building blocks of the scattering amplitude. In dual models (see below) they appear as the only variables. By crossing symmetry, they connect (smoothly interpolate between) the resonance formation – which implies positive *x*=*s* or *t*) with scattering (negative *x*), thus anticipating duality.

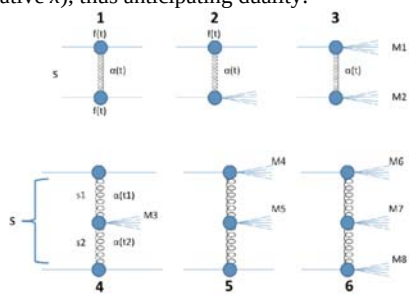

Fig. 2. Diagrams describing Regge-pole factorization.

Factorization of the Regge residue $\beta(t)$ and the "propagator" $(s/s_0)^{\alpha_P(t)-1}$ is a basic property of the theory (see Ref. 14). As mentioned, at the LHC for the first time, we have the opportunity to test directly Regge-factorization in diffraction, since the scattering amplitude here is dominated by a pomeron exchange, identical in elastic and inelastic diffraction. Simple factorization relations between elastic $d\sigma_{el}/dt$, single σ_{SD}/dt and double $d^3\sigma_{DD}/dtM_1^2dM_2^2$

cross-sections are known from the literature [19]. By writing the scattering amplitude as a product of vertices, the elastic f and the inelastic F, multiplied by the (universal) propagator (pomeron exchange), $f^2 s^\alpha$, fFs^α, $F^2 s^\alpha$, respectively for the elastic scattering, single (SD) and double (DD) diffraction dissociation (see Fig. 2) one gets

$$\frac{d^3\sigma_{DD}}{dtdM_1^2 dM_2^2} = \frac{\frac{d^2\sigma_{SD_1}}{dtdM_1^2}\frac{d^2\sigma_{SD_2}}{dtdM_2^2}}{\frac{d\sigma_{el}}{dt}}. \quad (1)$$

Assuming exponential residua $\exp(Bt)$ for both the elastic scattering and SD, and integrating over t one obtains

$$\frac{d^3\sigma_{DD}}{dM_1^2 dM_2^2} = \frac{k\frac{d^2\sigma_{SD_1}}{dM_1^2}\frac{d^2\sigma_{SD_2}}{dM_2^2}}{\frac{d\sigma_{el}}{dt}}, \quad (2)$$

where

$$k = r^2/(2r-1), r = B_{SD}/B_{el}.$$

To summarize this discussion, we emphasize the important role of the ratio between the inelastic and elastic slope, which at the LHC is close to its critical value, $B_{SD}/B_{el} = 0.5$, which means a very sensitive correlation between these two quantities. The right balance may require a correlated study of the two quantities, by keeping the ratio above 0.5. This constrain may guide future experiments on elastic and inelastic diffraction.

2.2. Pomeron and odderon

Regge trajectories (reggeons), introduced in the 60-ies of the past century correspond to a family of mesons or baryons sitting on the real part of the trajectories – the so-called Chew-Frautschi plot, to which their parameters (intercept and slope) are adjusted. There are two exceptions, namely the pomeron and odderon. The pomeron was introduced by I.Ya. Pomeranchuk as a fictive trajectory with postulated unit intercept to provide for non-decreasing asymptotic total cross-sections. In those days, the common belief was that asymptotically the cross sections tend to a constant limit. This has changed after the rise of cross sections was discovered at the ISR. The new, fictitious trajectory accommodates the asymptotically constant or rising cross section provided its intercept is respectively one or bigger, $\alpha_P(0) \geq 1$. The so-called supercritical pomeron, typically with $\alpha_P(0) \approx 1.1$ violates the Froissart bound (and unitarity) at very high energies, beyond any credible extrapolation. Nevertheless, formally and for aesthetic reasons, the input amplitude should be subjected to unitarization.

Unlike the case of ordinary (called also secondary or sub-leading) reggeons the pomeron trajectory was considered, since the beginning, as not connected to any observed particle. This assumption changed in the 70-ies with the advent of the quark model and the QCD. Nowadays the pomeron trajectory has its own Chew-Frautschi plot with glueballs, bound states of gluons. Glueballs are eventually mixed with quarks, forming "hybrids": this makes difficult their experimental identification.

The existence of the pomeron makes plausible the existence of its odd-C counterpart – the odderon. While the pomeron is made of an even number of gluons, the odderon is a bound state of an odd number of gluons. Moreover, the pomeron is "seen" as the imaginary part of the forward amplitude (total cross section), instead the identification of the odderon is not so unique.

2.3. Duality

The notion of duality, discovered in 1968 [20], has many facets values. Here we deal with resonance-Regge duality (or the Veneziano model [21]), discovered by saturating the so-called nite energy sum rules. Their analysis showed that, contrary to expectations, the proper sum of resonances produces a smooth Regge behavior and vice versa, their sum producing double counting. As a next step, an explicit dual amplitude was constructed. It is an Euler *B*-function:

$$A(s,t) = \int_0^1 dx x^{-\alpha(s)-1}(1-x)^{\alpha(t)-1} = B(-\alpha(s),-\alpha(t)) = \frac{\Gamma(-\alpha(s))\Gamma(-\alpha(t))}{\Gamma(-\alpha(s)-\alpha(t))}. \quad (3)$$

The Veneziano amplitude has several remarkable properties: it is crossing symmetric by construction, can be expanded in a pole series (resonance poles) in the *s* and *t* channel, and at large *s*, by the Stirling formula it is Regge-behaved, thus explicitly showing resonance-Regge duality - see, for instance, Fig. 3. At the same time, the model is not free from difficulties or limitations: it is valid only in the so-called narrow-resonance approximation, bringing to real and linear trajectories only, and as a result analyticity and unitarity are violated. A solution was found in dual amplitudes with Mandelstam analyticity (DAMA) [22], replacing Eq. (3) with

$$A(s,t) = \int_0^1 dx \left(\frac{x}{g}\right)^{-\alpha(s,x)-1} \left(\frac{1-x}{g}\right)^{\alpha(t,1-x)-1}, \quad (4)$$

where g > 1 is a parameter.

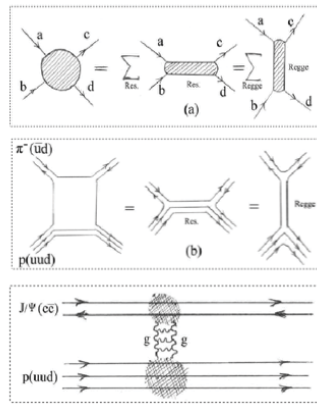

Fig. 3. Diagrams describing the resonance-Regge duality

Its low-energy pole decomposition the amplitude has the form

$$A(s,t) = \sum_{n=0}^{\infty} g^{n+1} \sum_{l=0}^{n} [-s\alpha(s)]^l \frac{C_{n-l}(t)}{[n-\alpha(s)]^{l+1}}, \quad (5)$$

where $C_{n-l}(t)$ is the residue, whose form is fixed by the *t*-channel Regge trajectory.

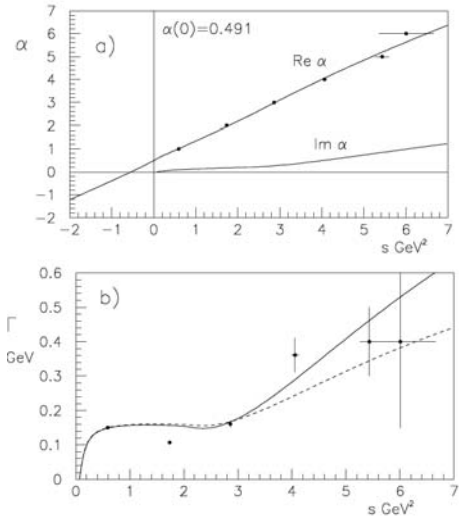

Fig. 4. (a) Re $\alpha(s)$ and Im $\alpha(s)$ for the degenerate $\rho - a_2$ trajectory; (b) continuous line: Γ(s) for the degenerate $\rho - a_2$ trajectory, dashed line: Γ(s) for the nondegenerate ρ trajectory.

As an example of typical terms in Eq. 3, in Fig. 4 we present the Chew-Frautschi plot of the degenerate $\rho - a_2$trajectory (real and imaginary parts) in Fig. 1(a), together with, in Fig. 1(b) the width $\Gamma(s)$ for the degenerate $\rho - a_2$ trajectory (continuous line) and the nondegenerate ρ trajectory (see, on this, Ref. 23), by means of a dispersion relation.

Resonance-Regge duality is applicable also in relating resonances in the missing mass of the DD to the high-mass smooth asymptotics, as shown in Fig. 5.

Finally, we mention the parton-hadron (Bloom-Gilman) duality [24]: it relates resonance production in deep-inelastic scattering to the smooth scaling behaviour of structure functions and may be a clue to the confinement problem!

2.4. Geometry and the black disc limit

The unitarity condition is simple in the impact parameters representation of the scattering amplitude; it is

$$h(s,b) = \frac{1}{4s}\int \frac{d^2\vec{k}}{(2\pi)^2} e^{i\vec{k}\vec{b}} A(s,t) = \frac{1}{8\pi s}\int_0^\infty dk k J_0\left(b\sqrt{-t}\right) A(s,t)\,, \tag{6}$$

with the inverse transformation

$$A(s,t) = 16\pi^2 s \int \frac{d^2\vec{b}}{(2\pi)^2} e^{-i\vec{k}\vec{b}} h(s,b) = \frac{1}{8\pi s}\int_0^\infty db b J_0\left(b\sqrt{-t}\right) h(s,b)\,. \tag{7}$$

In these equations $h(s,b)$ is called elastic impact parameter profile, *A(s,t)* is the elastic amplitude, $J_0(z)$ is the Bessel function of the zeroth order, $\vec{k}$ is a two-dimensional vector, $t \approx -k_\perp^2$ and *b* is the impact parameter.

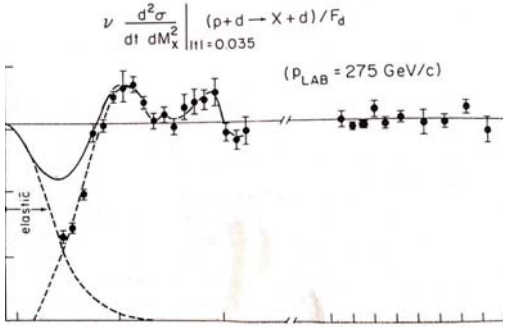

Fig. 5. Finite-mass sum rules (FMSR), Ref. 17, relating low missing-mass resonances (horizontal axis) with high mass production (vertical axis) in diffraction dissociation, are shown.

For the observables the following expressions hold, see Refs. 5-7:

$$\sigma_t(s) = \frac{1}{s} ImA(s,0) = 8\pi \int_0^\infty dbb Imh(s,b), \tag{8}$$

$$\sigma_{el}(s) = \frac{1}{16\pi s^2} \int_{-\infty}^0 dt |A(s,t)|^2 = 8\pi \int_0^\infty dbb |h(s,b)|^2, \tag{9}$$

$$\sigma_{inel}(s) = 8\pi \int_0^\infty dbb (Imh(s,b) - |h(s,b)|^2)\,, \tag{10}$$

where, in the impact parameter *b* representation, *h*(*s*, *b*) is the elastic-scattering amplitude at the center-of-mass energy and *Imh*(*s*, *b*), usually called the profile function, represents the hadron opacity. The eikonal and u matrix approaches differ dramatically concerning the "black disc limit", absolute in the eikonal model, but merely transitory for the u matrix. A large number of paper appeared, e.g. Refs. 5-7, dramatizing the "dangerous" vicinity of the black disc limit $Imh(s,b) = 0.5$, reached or even crossed at the LHC. The transformation of the experimental data, including the differential cross sections measured at the LHC can be always questioned because the real part of the amplitude (or the phase) is not measured directly.

Contrary to the eikonal, in the u matrix approach the black disc is not an absolute limit. Having reached $Imh(s,0) = 0.5$, the nucleon will tend to be more transparent [25]. This phenomenon was discussed in a number of papers by S.M. Troshin and N.E. Tyurin (see, for instance, Ref. 25 and references therein). In Sec. 3 we come back to the predictions of this unorthodox unitarization scheme.

3. Unitarity and "asymptopia"

3.1. Unitarity

We find approximate solutions of the u-matrix unitarization with a double pole (DP) as input. Postponing a detailed fit to the data, here we explore the general trend in the behavior of the observables, concentrating on the expected transition to the asymptotic regime of the strong interaction.

In the u matrix approach, the unitarized amplitude is [25]

$$h(\rho,s) = \frac{u(\rho,s)}{1 - iu(\rho,s)}\,, \tag{11}$$

where $u(\rho, s)$ is the input "Born" term.

We obtain for the forward measurables, in the $O(L^{-1})$ approximation ($L = \ln(s/s_0)$, s_0 being a scale for the square of the total energy s)

$$\sigma_{tot} = \frac{4\pi\alpha'_P}{\lambda}\ln(1+g)\,(1+\lambda L), \tag{12}$$

$$\sigma_{in} = \frac{4\pi\alpha'_P}{\lambda}\frac{g}{1+g}(1+\lambda L)\,, \tag{13}$$

$$\sigma_{el} = \frac{4\pi\alpha'_P}{\lambda}\left(\ln(1+g) - \frac{g}{1+g}\right)(1+\lambda L)\,, \tag{14}$$

where λ is a parameter, whose typical value is 0.06 [17].

One can see from Eqs. (12)-(14) that, in the leading $O(L^{-1})$ approximation, the energy dependence of the cross sections is not affected by unitarization if g is constant, that was typical for the ISR era with geometrical scaling (GS). The GS is violated beyond the ISR energies, requiring the energy dependence, $g \to g(s)$, to be discussed in what follows.

Furthermore, in the *O(1/L)* approximation, the amplitude can be written as

$$A(s,0) = A_B(s,0)\frac{\ln(1+g)}{g}\ . \tag{15}$$

In the "Born approximation" we have the McDowell-Martin limit [26] for the slope:

$$B(s,0) = \frac{\sigma_{tot}^2(1+\rho^2)}{16\pi\sigma_{el}}\ . \tag{16}$$

The parameter g may be found from the ratio

$$\frac{\sigma_{el}}{\sigma_{tot}} = 1 - \frac{g}{(1+g)\ln(1+g)}, \tag{17}$$

where g is constant in the case of unit dipole pomeron (DP) intercept, sharing the property of geometrical scaling (GS), typical of the ISR energy region, with

$$\sigma_t \sim \sigma_{el} \sim \sigma_{in} \sim B(s) \sim \ln(s). \tag{18}$$

Beyond the ISR the ratio (17) starts rising, braking the GS. This phenomenon is related with the rise of the parameter *g(s);* that can be calculated (and parametrized) uniquely from the experimental data on the the ratio (17). Consequently, the GS relation will be replaced by the asymptotic formulas to be discussed in the next Subsection.The results of the "perturbative" (due to smalleness at high energies of the parameter L^{-1}) expansion are attractive for their simplicity and the possibility to perform the calculations analytically. Evaluation of higher-order, subleading corrections is possible but was not done as yet. Even more interesting are exact numerical calculations with simultaneous fits to the date. They are feasible, although require huge machine resources (two-fold numerical Fourier-Bessel transforms with minimization (through MINUIT procedure at each step).

3.2. Asymptotic universality

In this Subsection we use the obtained results to predict future trends. Our first conclusion is the existence of two regimes: the first is the "low-energy" ISR-FNAL region, which shows modest (logarithmic) rise of the cross section with constant ratios σ_{el}/σ_{tot} and σ_{tot}/B, i.e. GS; the second is asymptotic, with Froissart saturation and $\sigma_{el}/\sigma_{tot} \to 1$. The transition between the two regimes and the onset of the asymptotic behavior is quantified by the "running constant" *g(s)*.

One can see from Eq. (12) that the rise of σ_{tot} is a combined effect coming from two factors: increasing intensity of the interaction $\mathcal{L}_1 = ln[1 + g(s)]$ and increasing interaction radius $\mathcal{L}_2 = 1 + \lambda L$. Their product results in the Froissart saturation,

$$\sigma_{tot} \sim c ln^2 s. \tag{19}$$

Eq. (19) relates the coefficient *c* with the slope of the pomeron trajectory α'_P. Setting $\alpha'_P = 0.394$ GeV^{-2}, we get $c = 0.088$ mb, close to its fitted value.

4. Diffractive deep-inelastic scattering: how many pomerons?

Let us establish two postulates:

1. Regge factorization holds, *i.e*. the dependence on the virtuality of the external particle (virtual photon) enters only the relevant vertex, not the propagator;
2. there is only one pomeron in Nature and it is the same in all reactions. It may be complicated, e.g. having many, at least two, components (soft and hard?).

The first postulate was applied, for example, in Refs. 27 and 28 to study the deeply virtual Compton scattering (DVCS) and the vector meson production (VMP). In Fig. 6, where diagrams (a) and (b) represent the DVCS and the VMP, respectively, the Q^2 dependence enters only the upper vertex of the diagram (c), where we explicitate the Regge-factorized form of the amplitude for both processes. The particular form of this dependence and its interplay with t is not unique.

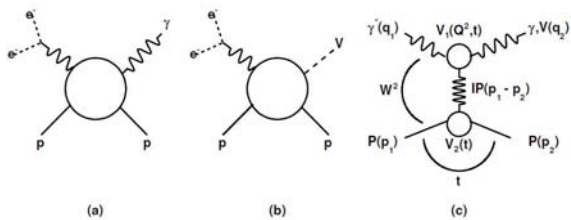

Fig. 6. Diagrams of DVCS (a) and VMP (b); (c) DVCS (VMP) amplitude in a Regge-factorized form

Hadron-hadron elastic scattering is different from exclusive VMP and DVCS not only because the photon is different from a hadron (although they are related by vector meson dominance), but even more because of the transition between space-and time-like regions: while the virtual photon's "mass square" q^2 is negative, that of the hadron is positive and that makes this attempt interesting!

4.1. Reggeometric pomeron

We start by reminding the properties and some representative results of the single-term Reggeometric model (see Ref. 27).

The invariant scattering amplitude is defined as

$$A(Q^2,s,t) = \widetilde{H} e^{-i\pi\alpha(t)/2} \left(\frac{s}{s_0}\right)^{\alpha(t)} e^{2\left(\frac{a}{Q^2}-\frac{b}{2m_N^2}\right)t}. \tag{20}$$

Here

$$\alpha(t) = \alpha_0 + \alpha' t \tag{21}$$

is the linear pomeron trajectory, a and b are two parameters to be determined with the fitting procedure and m_N is the nucleon mass. The coefficient $\widetilde{H}$ is a function providing the right behavior of elastic cross section in $\tilde{Q}^2 = Q^2 + M_V{}^2$ (M_V being the vector meson mass):

$$\widetilde{H} \equiv \widetilde{H}(\tilde{Q}^2) = \frac{\widetilde{A_0}}{\left(1+\frac{\tilde{Q}^2}{Q_0^2}\right)^{n_S}}, \tag{22}$$

where $\widetilde{A_0}$ is a normalization factor, Q_0^2 is a scale for the virtuality and n_S is a real positive number. Notice that we use the variable $\tilde{Q}^2$ as a measure of "hardness". By using Eq. (22) with the norm and

$$\frac{d\sigma_{el}}{dt} = \frac{\pi}{s^2}|A(Q^2,s,t)|^2, \tag{23}$$

the differential and integrated elastic cross sections become

$$\frac{d\sigma_{el}}{dt} = \frac{A_0^2}{\left(1+\frac{\tilde{Q}^2}{Q_0^2}\right)^{2n}} \left(\frac{s}{s_0}\right)^{2(\alpha(t)-1)} e^{4\left(\frac{a}{Q^2}-\frac{b}{2m_N^2}\right)t} \tag{24}$$

and

$$\sigma_{el} = \frac{A_0^2}{\left(1+\frac{\tilde{Q}^2}{Q_0^2}\right)^{2n}} \frac{\left(\frac{s}{s_0}\right)^{2(\alpha_0-1)}}{4\left(\frac{a}{Q^2}-\frac{b}{2m_N^2}\right)+2\alpha' ln\left(\frac{s}{s_0}\right)}, \tag{25}$$

where

$$A_0 = -\frac{\sqrt{\pi}}{s_0}\widetilde{A_0}.$$

Eqs. (24) and (25) (for simplicity we set $s_0 = 1\ \mathrm{GeV}^2$) were fitted [29] to the HERA data obtained the by ZEUS and H1 Collaborations on exclusive diffractive VMP.

A shortcoming of the single-term Reggeometric pomeron model, expressed by Eq. (20), is that the fitted parameters in this model acquire particular values for each reaction.

4.2. Two-component Reggeometric pomeron

In this Subsection we try to approach a complicated and controversial subject, namely the existence of two (or more) different pomerons: one "soft" responsible for on-mass-shall hadronic reactions, and the other one(s) "hard" applicable to of-mass-shall deep inelastic

scattering (DIS). There are similarities between the two soft and hard models (e.g., Regge behavior), but also differences. The main difference is that the Regge pole model, being part of the analytic S matrix theory, strictly speaking, is applicable to asymptotically free states on the mass shall only. Another difference is that the hard (or "Lipatov") pomeron is assumed to follow from the local quantum field theory (QCD) with confined quarks and gluons. We do not know how can these two extremes be reconciled. Below we try to combine these two approaches by using a specific model, a "handle" combining three independent variables: *s*, *t* and Q^2:

We introduce an universal, "soft" and "hard", pomeron model (see Ref. 27). Using the Reggeometric ansatz expressed by Eq. (20), the amplitude is written as a sum of two parts, corresponding to the "soft" and "hard" components of a universal, unique pomeron:

$$A(Q^2,s,t) \equiv A_s(Q^2,s,t) + A_h(Q^2,s,t) \; = \\ \widetilde{H_s} e^{-i\frac{\pi}{2}\alpha_s(t)} \left(\frac{s}{s_{os}}\right)^{\alpha_s(t)} e^{2\left(\frac{a_s}{Q^2}-\frac{b_s}{2m_N^2}\right)t} + \\ \widetilde{H_h} e^{-i\frac{\pi}{2}\alpha_h(t)} \left(\frac{s}{s_{os}}\right)^{\alpha_h(t)} e^{2\left(\frac{a_h}{Q^2}-\frac{b_h}{2m_N^2}\right)t} \; . \tag{26}$$

Here s_{os} and s_{oh} are squared energy scales, and a_i and b_i, with i=*s*,*h*, are parameters to be determinated with the fitting procedure. The two coefficients $\widetilde{H_s}$ and $\widetilde{H_h}$ are functions similar to those defined in Ref. 25.

Each component of Eq. (26) has its own, "soft" or "hard", pomeron linear trajectory:

$$\alpha_s(t) = \alpha_{os} + \alpha_s' t, \qquad \alpha_h(t) = \alpha_{oh} + \alpha_h' t.$$

As input we use the parameters suggested by Donnachie and Landshoff [30], so that

$$\alpha_s(t) = 1.08 + 0.25t, \qquad \alpha_h(t) = 1.40 + 0.1t.$$

Let us illustrate the important and delicate interplay between the "soft" and "hard" components of our unique pomeron. Since the amplitude consists of two parts, according to Eq. (26), it can be written as

$$A(Q^2,s,t) = A_s(Q^2,s,t) + A_h(Q^2,s,t) \; . \tag{27}$$

As a consequence, the differential and elastic cross section contain also an interference term between the "soft" and "hard" parts, so that they read

$$\frac{d\sigma_{el}}{dt} = \frac{d\sigma_{s,el}}{dt} + \frac{d\sigma_{h,el}}{dt} + \frac{d\sigma_{interf,el}}{dt} \tag{28}$$

and

$$\sigma_{el=}\sigma_{s,el} + \sigma_{h,el} + \sigma_{interf,el} \, . \tag{29}$$

Given Eqs. (28) and (29), we can define the following ratios for each component:

$$R_i\left(\widetilde{Q^2},W,t\right) = \frac{\frac{d\sigma_{i,el}}{dt}}{\frac{d\sigma_{el}}{dt}} \tag{30}$$

and

$$R_i\left(\widetilde{Q^2}, W\right) = \frac{\sigma_{i,el}}{\sigma_{el}}, \tag{31}$$

where *i* stands for *s*, *h*, *interf.*

Fig. 7 shows the interplay between the components for both $\sigma_{i,el}$ and $R_i\left(\tilde{Q}^2, t\right)$, as function of $\tilde{Q}^2$, for $W = 90$ GeV. In Fig. 8. both diagramts show that not only $\tilde{Q}^2$ is the parameter defining softness or hardness of the process, but such is also the combination of $\tilde{Q}^2$ and *t*, similar to the variable $z = t - Q^2$ introduced in Ref. 27. On the whole, it can be seen from the diagrams that the soft component dominates in the region of low $\tilde{Q}^2$ and *t*, while the hard component dominates in the region of high $\tilde{Q}^2$ and *t*.

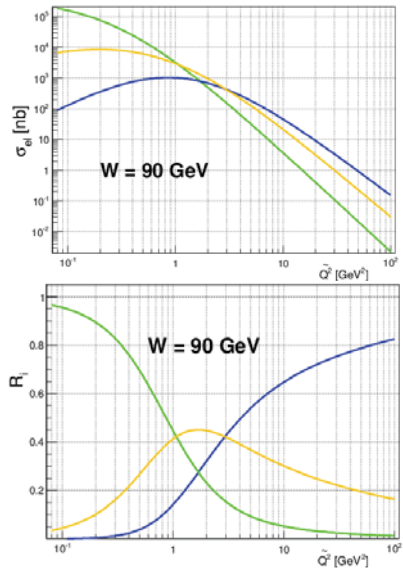

Fig. 7. Interplay between soft (green line), hard (blue line) and interference (yellow line) components of the cross section $\sigma_{i,el}$ (upper Figure) and the ratio $R_i\left(\tilde{Q}^2, t\right)$ (lower Figure) as function of $\tilde{Q}^2$, for W = 90 Gev.

5. Conclusions

The total, elastic and inelastic cross sections at the LHC did not reveal surprises; the rate of their rise (not predicted by the theory) follows extrapolations of phenomenological models, typically $\ln^2 s$ or, equivalently that of Donnachie and Landshoff 's supercritical pomeron with $\alpha(0) \approx 0.08$.

Forward physics at the LHC is dominated by the pomeron exchange, the role of secondary (e.g. f of ρ) exchanges is negligible, their relative contribution there being smaller than the experimental uncertainties. The odderon is not “seen” in fits to total cross sections. Although the common belief is that cross sections will continue rising indefinitely, alternatives, e.g. tending to a constant, oscillations etc. are not excluded by the theory.

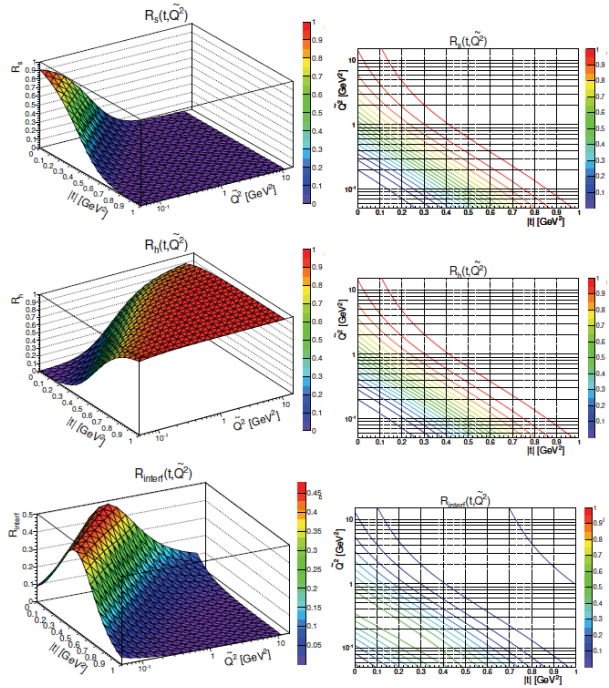

Fig. 8. Left column: soft (upper surface), hard (middle surface) and interference (bottom surface) components of the ratio $R_i(\tilde{Q}^2, W, t)$ are shown as functions of $\tilde{Q}^2$ and t, for W=90 GeV. Right column: some representative curves of the surfaces projected onto the $(t, \widetilde{Q^2})$ plane.

Contrary to total cross sections, the data on the forward slope $B(s,0)$ and the phase (the $\rho(s,0)$ parameter) offers surprises, triggering theoretical work. The forward slope $B(s,0)$, typically logarithmic in Regge-pole models, was found by the TOTEM collaboration to accelerate from $\ln(s)$ to $\ln^2(s)$ at highest LHC energy [9,12], needing theoretical explanation and understanding. Another news from TOTEM is the surprisingly low value $\rho(13,0) = 0.10\pm0.01$ [10]. The low value of the ratio $\rho(13,0)$ is almost a direct evidence for the odderon, predicted many years ago and discussed in numerous papers, see e.g. Refs.17 and 31 and references therein. Recent fits to the TOTEM data with its low ρ value cannot prove or disprove the existence of the odderon until larger values of t, namely those at the dip will be shown to work.

There is little doubt about the existence of the odderon, just because nothing forbids its existence. Its parameters are not predicted from theory. By a plausible estimate, based on the string model, the odderon's slope is roughly $\alpha_0' \approx 2\alpha_P'/3$. The odderon could be detected directly by measuring pp and $\bar{p}p$ differential cross sections at the same energy, e.g. by rescaling the LHC down to the closed Tevatron energy,v $\sim$2 TeV^2.

The pomeron is the central object in forward physics at the LHC. As repeatedly stressed in this paper, in the LHC energy region one for the first time has a chance to identify the pomeron, uncontaminated by secondary exchanges. Perturbative quantum chromodynamics

(pQCD) predicted that the intercept of the (bare) pomeron is much higher than its "canonical" value 0.08.

Finally we note that we ignore the so-called rapidity gap survival corrections that brought much confusion in studies of diffraction dissociation. In our opinion, the confusion comes from the mixture of the space-time treatment of inelastic processes with the analytic S matrix theory, part of which are Regge-poles, operational only for asymptotic states. A reasonable Regge-pole model compatible with unitarity should not contain "rapidity gap survival corrections", otherwise it should be improved within its own formalism. In other words, the size of these corrections reflect the "goodness" of the model.

Acnowledgement

We thank Chung-I Tan and István Szanyi for usfull discussions. L.J. thanks the Organizers of the Montenegro conference on New Trends in High-Energy Physics for their invitation and support.

References

1. S. Donnachie and P.V. Landshoff, Phys. Lett. **B727** (2013) 500, and earlier references therein.
2. D.A. Fagundes, M.J. Menon, and P.V.R.G. Silva, Nucl. Phys. **A966** (2017) 185.
3. D.A. Fagundes, G. Pancheri, A.Grau, S. Pacetti, Y.N. Srivastava, Phys. Rev. **D88** (2013) 094019.
4. V. A. Khoze, A.D. Martin, and M. G. Ryskin, Eur. Phys. J. **C74** (2014) 2756; V. A. Khoze, A. D. Martin, and M. G. Ryskin, Int. J. Mod. Phys. **A30** (2015) 1542004; V.A. Khoze, A.D. Martin, and M.G. Ryskin, Phys. Rev. **D97** (2018) 3,034019.
5. A. Alkin, O. Kovalenko, and E. Martynov, EPL **102** (2013) 3, 31001.
6. A.A. Godizov, Phys. Rev. **D96** (2017) 3, 034023.
7. A.K. Kohara, E. Ferreira, T. Kodama, and M. Rangler, *Description of pp forward elastic scattering at 7 and 8 TeV*, Proc. of EDS Blois 2017: 17th conference on Elastic and Diffractive scattering, Prague, Czech Republic, JUNE 26-30, 2017; A.K. Kohara, E. Ferreira, T. Kodama and M. Rangler, Eur. Phys. J. **C77** (2017) 12, 877.
8. V.S. Fadin, E.A. Kuraev, and L.N. Lipatov, Phys. Lett. **B60** (1975) 50; I.I. Balitsky, L.N. Lipatov, Sov. J. Nucl. Phys. **28** (1978) 822, Yad. Fiz., **28** (1978) 1597.
9. G. Antchev et al. (TOTEM Collab.), Nucl. Phys. **B899** (2015) 527.
10. E.S. Martynov and E. B. Nicolescu, Phys. Lett. **B778** (2018) 414.
11. A. Alkin, O. Kovalenko, and E. Martynov, EPL **102** (2013) 3, 31001.
12. G. Antchev et al. (TOTEM Collab.), (2017), *First determination of the ρ parameter at √s = 13 TeV - probing the existence of a colourless three-gluon bound state*, arXiv:1812.04732; CERN-EP-2017-335; CERN-EP-2017-v3:
13. P. D. B. Collins, *An introduction to Regge Theory and High Energy Physics*, Cambridge University Press (1977).
14. V. Barone and E. Predazzi, *High-energy particle diffraction*, Springer-Verlag Berlin Heidelberg NewYork, ISBN 3540421076, (2002).
15. S. Donnachie, H.G. Dosch, O. Nachtmann, and P. Landshoff, *Pomeron physics and QCD*, Camb. Monogr. Part. Phys. Nucl. Phys. Cosmol. **19** (2002) 1.
16. A.O. Barut and D.E. Zwanziger, Phys. Rev. **127** (1962) 974.
17. L.L. Jenkovszky, Riv. Nuovo Cim. **10N 12** (1987) 1.
18. R. Fiore, L.L. Jenkovszky, V. Magas, F. Paccanoni, and A. Papa, Eur. Phys. J. **A10** (2001) 217.
19. V.N. Gribov and I.Ya. Pomeranchuk, Phys. Rev. Lett. **9** (1962) 238.

20. R. Dolen, D. Horn, and C. Schmid, Phys. Rev. **166** (1968) 1768.
21. G. Veneziano, Nuovo Cim. **A57** (1968) 190.
22. A.I. Bugrij et al. Fortsch. Phys. **21** (1973) 427.
23. R. Fiore, Laszlo L.L Jenkovszky, V. Magas, F. Paccanoni, and A. Papa, Phys. Element. Part. Atom. Nucl. **31** (2000) n° 7B, 47.
24. E.D. Bloom and E.J. Gilman, Phys. Rev. Lett. **25** (1970) 1149; Phys. Rev. **D4** (1971) 2901.
25. P. Desgrolard, L.L. Jenkovszky, and B.V. Struminsky, Phys. Atom. Nucl. **63** (2000) 891, Yad. Fiz. **63** (2000) 962; Eur. Phys. J. **C11** (1999) 145.
26. S.W. MacDowell and A. Martin, Phys. Rev. **135** (1964) B960.
27. M. Capua, S. Fazio, R. Fiore, L.L. Jenkovszky, and F. Paccanoni, Phys. Lett. **B645** (2007) 161.
28. S. Fazio, R. Fiore, L.L. Jenkovszky, and A. Lavorini, Phys. Rev. **D85** (2012) 054009.
29. S. Fazio, R. Fiore, L.L. Jenkovszky, and A. Salii, Phys. Rev. **D90**, (2014) 016007.
30. A. Donnachie and P.V. Landshoff, *Elastic Scattering at the LHC*, arXiv:1112.2485 [hep-ph].
31. L.L. Jenkovszky and I. Szanyi, Phys. Part. Nucl. Lett. **14** (2017) 687.

Probing QCD at high energy

Yuri Kulchitsky[1]
on behalf of ATLAS Collaboration
Joint Institute for Nuclear Research, Dubna, Russia

Abstract. Perturbative QCD calculations at next-to-next-to-leading-order are available for many processes since several years and can be rigorously tested with a large variety of final s tates. The latest results from the ATLAS Collaboration at the LHC (CERN) involving jets, dijets, photons in association with heavy flavors and vector bosons in association with jets, measured at center-of-mass energies of 8 and 13 TeV are presented. All measured cross-sections are compared to state-of-the art theory Monte Carlo predictions. The paper concludes with the results of jet-substructure studies at 13 TeV, in particular the measurement of the jet soft-drop mass.

1 Introduction

Precise measurements of jet cross-sections are crucial in understanding physics at hadron colliders. In quantum chromodynamics (QCD), jets are interpreted as resulting from the fragmentation of quarks and gluons produced in a short-distance scattering process. Jet cross-sections provide valuable information about the strong coupling constant, α_s, and the structure of the proton. Inclusive jet and dijet events represent a background to many other processes at hadron colliders. The predictive power of fixed-order QCD calculations is therefore relevant in many searches for new physics. The ATLAS collaboration[2] [1] at the LHC (CERN) [2] have measured inclusive jet cross-sections in pp collisions at centre-of-mass energies of 13 TeV [3] and 8 TeV [4]. Dijet production at the LHC has been measured at 13 TeV [3]. The production of isolated prompt photons in association with a heavy flavour (HF) j et c ontaining a b o r c h adron a t 8 TeV [5] p rovides a testing ground for perturbative quantum chromodynamics (pQCD), the content of the proton and the treatment of heavy quarks (HQ) in matrix element (ME) and parton shower (PS) computations. Prompt photons, which refer to those not arising from hadron decays, are targeted by requiring that their

[1] E-mail: Iouri.Kultchitski@cern.ch

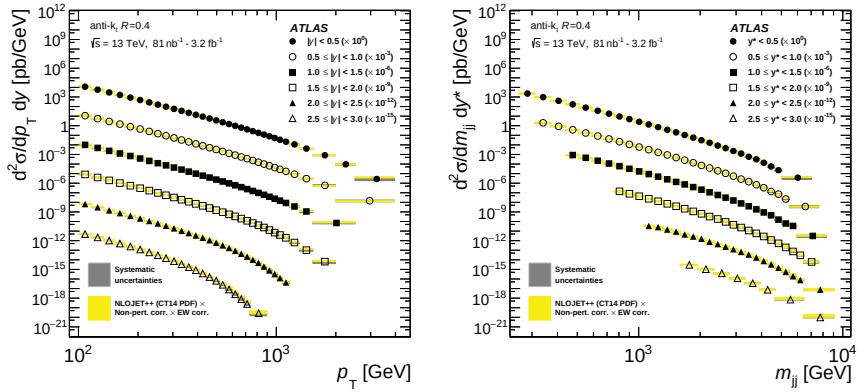

(a) (b)

Figure 1: Inclusive (a) jet and (b) dijet cross-sections as a function of transverse momentum for jet and m_{jj} for dijet and absolute jet rapidity, for anti-k_{t} jets with $R = 0.4$ in pp collisions at 13 TeV. The statistical uncertainties are smaller than the size of the symbols used to plot the cross-section values. The dark gray shaded areas indicate the experimental systematic uncertainties. The data are compared to NLO pQCD predictions calculated using NLOJET++ with $p_{\mathrm{T}}^{\mathrm{max}}$ for jet and $p_{\mathrm{T}}^{\mathrm{max}} \exp(0.3\, y^*)$ for dijet as the QCD scale and the CT14 NLO PDF set. The yellow shaded areas indicate the predictions with their uncertainties. (a) At low and intermediate transverse momentum bins the experimental systematic uncertainties are comparable to the theory uncertainties (drawn on top) and therefore are barely visible. (b) In most m_{jj} bins the experimental systematic uncertainty is smaller than the theory uncertainties and is therefore not visible. Taken from Ref. [3].

signals are isolated. A measurement of the W boson production cross section and the W^+/W^- cross-section ratio, both in association with jets, in pp collisions at 8 TeV are presented in Ref. [6]. A measurement of the first jet substructure quantity was calculated at next-to-next-to-leading-logarithm (NNLL) accuracy are presented in Ref. [7].

2 Inclusive jet and dijet cross-sections at 13 TeV

This paper presents measurements of the inclusive jet and dijet cross-sections in pp collisions at center-of-mass energy 13 TeV corresponding to an integrated luminosity of 3.2 fb^{-1} [3]. The inclusive jet cross-sections are mea-

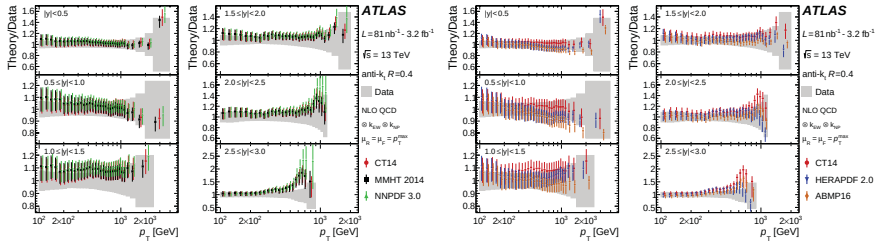

Figure 2: Comparison of the measured inclusive jet cross-sections and the NLO pQCD predictions shown as the ratios of predictions to the measured cross-sections in pp collisions at 13 TeV. The ratios are shown as a function of the jet transverse momentum in six absolute jet rapidity bins for anti-k_t jets with $R = 0.4$. The predictions are calculated using NLOJET++ with three different PDF sets (a) [CT14, MMHT2014, NNPDF3.0] and (b) [CT14, HEPAPDF3.0, ABMP16]. The NP and EW corrections are applied. The gray bands show the total data uncertainty including both the systematic and statistical uncertainties. Taken from Ref. [3].

sured double-differentially as a function of the jet transverse momentum, p_T, and absolute jet rapidity, $|y|$. The double-differential dijet production cross-sections are presented as a function of the invariant mass of the dijet system, m_{jj}, and as a function of half the absolute rapidity separation between the two highest transverse momentum jets satisfying $|y| < 3$, denoted y^*. Jets are reconstructed using the anti-k_t jet clustering algorithm with a radius parameter value of $R = 0.4$. The measurements cover the kinematic region of $.1 < p_T < 3.5$ TeV and $|y| < 3$ for the inclusive jet cross-section, and of $0.3 < m_{jj} < 9$ TeV and $y^* < 3$ for the dijet cross-section. NLO pQCD predictions calculated using several parton distribution function (PDF) sets, corrected for electroweak (EW) and non-perturbative (NP) effects, are quantitatively compared to the measurement results. In addition, the inclusive jet cross-sections are compared to the recently published complete next-to-next-to-leading-order (NNLO) pQCD calculation. The measured double-differential inclusive jet cross-sections are shown in Fig. 1(a) as a function of transverse momentum for the six jet rapidity bins, and the measured double-differential dijet cross-sections are shown in Fig. 1(b) as a function of m_{jj} for the six y^* bins. The NLO pQCD predictions using the CT14 PDF set corrected for NP and EW effects are also shown in Fig. 1. The ratios of the NLO pQCD predictions to the measured inclusive jet cross-sections as a function of transverse momentum in the six absolute jet rapidity bins are shown in Fig. 2 for the CT14, MMHT214, NNPDF3.0, HERAPDF2.0, ABMP16 PDF sets. No significant deviation

of the data points from the predictions is seen; the NLO pQCD predictions and data agree within uncertainties. In the forward region ($|y| > 2$) there is a tendency for the NLO pQCD prediction using the CT14, MMHT214 and NNPDF3. PDF sets to overestimate the measured cross-section in the high transverse momentum range, although the difference from data does not exceed the range covered by the experimental and theoretical uncertainties. A quantitative comparison of the measurements to fixed-order NLO QCD calculations shows overall fair agreement when considering jet cross-sections in individual absolute jet rapidity bins independently. In the inclusive jet measurement, a significant tension between data and theory is observed when considering data points from all jet transverse momentum and absolute jet rapidity regions. No significant differences between the inclusive jet cross-sections and the fixed-order NNLO QCD calculations corrected for NP and EW effects are observed when using $p_{\mathrm{T}}^{\mathrm{jet}}$ as the QCD scale. The NLO pQCD predictions using $p_{\mathrm{T}}^{\mathrm{max}}$ as the scale overestimate the measured inclusive jet cross-sections.

3 Inclusive jet cross-sections at 8 TeV

The measured double-differential inclusive jet cross-sections at center-of-mass energy 8 TeV are shown in Fig. 3 as a function of the jet transverse momentum for anti-k_{t} jets with $R = 0.4$ and $R = 0.6$ for each absolute jet rapidity bin [4]. The cross-section covers 11 orders of magnitude in the central absolute jet rapidity region and nine orders of magnitude in the forward absolute jet rapidity region. Jet transverse momenta above $p_{\mathrm{T}} = 2$ TeV are observed. In the most forward region, the jet transverse momentum reaches about .5 TeV. The measurement is compared to an NLO QCD prediction using the MMHT214 PDF set based on NLOJet++ corrected for NP and EW effects. This theory prediction describes the gross features in the data. The ratio of NLO QCD calculations to data corrected for NP and EW effects for various PDF sets is shown in Fig. 4(a) for anti-k_{t} jets with $R = 0.4$ [4]. At low transverse momentum, the level of agreement is very sensitive to NP effects. When using Pythia8 as the nominal NP correction, the NLO QCD prediction is typically about 10– 20%above the data at low transverse momentum, whereas the NLO QCD prediction corrected with Herwig++ follows the data well for jets with $R = 0.4$, while it is $5 - 10$%below the data for jets with $R = 0.6$. The comparisons of the Powheg predictions with the measurement for jets with $R = 0.4$ are shown in Fig. 4(b) as a function of the jet transverse momentum in absolute jet rapidity bins. The measurements are also compared to the NLO QCD prediction using the CT1 PDF set and corrected for NP effects with the same Monte Carlo (MC) generator configuration as was used for Powheg. Strong tension between data and theory is observed when considering data points from all jet transverse

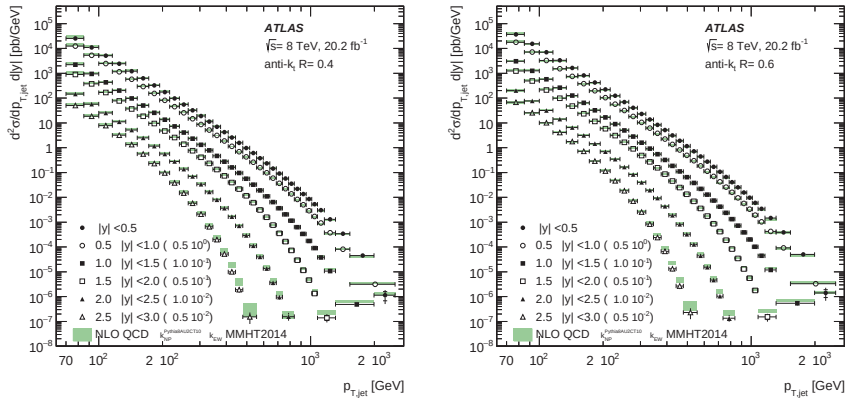

(a) (b)

Figure 3: Inclusive jet cross-section as a function of jet transverse momentum in bins of absolute jet rapidity in pp collisions at 8 TeV. The results are shown for jets identified using the anti-k_t algorithm with (a) $R = 0.4$ and (b) $R = 0.6$. For better visibility, the cross-sections are multiplied by the factors indicated in the legend. The data are compared to the NLO QCD prediction with the MMHT2014 PDF set. The error bars indicate the statistical and the systematic uncertainties in the measurement added in quadrature. The inner vertical line shows the statistical uncertainty separately. Taken from Ref. [4].

momentum and rapidity regions, with a full treatment of the correlations. This tension can be reduced, but not completely resolved, using alternative correlation scenarios for the experimental and theoretical systematic uncertainties [4].

4 Differential cross-sections of γ with b or c jet at 8 TeV

Prompt photons (γ) can be used as a colourless non-hadronizing probe of parton dynamics that yields a clean experimental signature. Processes containing final state b or c quarks play an important role in many LHC physics analyses and therefore the accuracy of the description of this HF content of the proton must be investigated. HF jets are defined as jets, which contain either a b or c hadron. In Fig. 5 the values for the measured differential γ+c cross sections are plotted and in Fig. 6 the ratios of γ+b and γ+c for central and forward regions are given at center-of-mass energy 8 TeV, with the relevant theory predictions [5]. In general, considering the LO predictions in

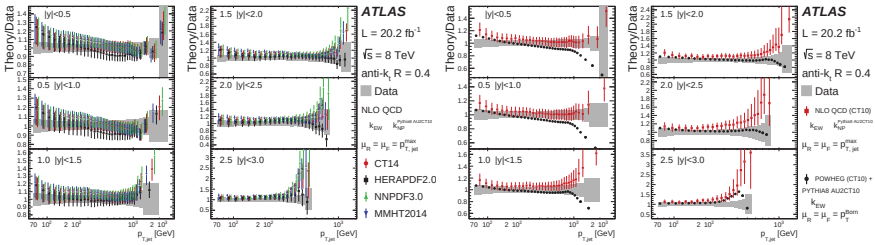

Figure 4: (a) Ratio of the inclusive jet cross-section predicted by NLO QCD corrected for NP and EW effects to the cross-section in data as a function of the jet transverse momentum in each jet rapidity bin in pp collisions at 8 TeV. Shown are the predictions for various PDF sets for anti-k_t jets with $R = 0.4$. The points are offset in jet transverse momentum for better visibility. The error bars indicate the total theory uncertainty. The gray band shows the total uncertainty in the measurement. (b) Ratio of the inclusive jet cross-section predicted by the POWHEG MC event generator with respect to the cross-section in data as a function of the jet transverse momentum in each jet rapidity bin for anti-k_t jets with $R = 0.4$. Only the nominal values of this ratio are indicated. Also shown is the prediction by NLO QCD corrected for NP effects, where the error bars indicate the total theory uncertainty. EW corrections are applied for both theory predictions and the CT10 PDF set is used. Taken from Ref. [4].

pQCD, those from Sherpa agree well with the measured values and provide a better description of the data than those from Pythia. Comparisons of the γ+c measurement to NLO+PS predictions from MadGraph5_aMC@NLO in the $5F$ scheme using NNPDF3.1nlo with .26% of the intrinsic charm (IC) and CT14nnlo are shown in Fig. 5. The predictions are found to agree with the data within the uncertainties across the entire E_{T}^{γ} range. However, those using the BHPS or the fitted charm PDF sets predict higher cross-section values in the forward region at high E_{T}^{γ}, above 105 GeV, than those using the nominal PDF sets. As shown in Fig. 6(a), the $4F$ and $5F$ NLO predictions for the cross-section ratios consistently overestimate the data for $E_{\mathrm{T}}^{\gamma} > 65$ GeV; the $5F$ predictions are at the edge of agreement with the measured values within uncertainties. Sherpa, which generates additional partons in the ME and uses a massive $5F$ scheme, provides a better description of the measured cross sections and cross-section ratios than MadGraph5_aMC@NLO in either the $5F$ or $4F$ scheme. The predicted values for the cross-section ratios, shown in Fig. 6(b), are smaller for the predictions using the BHPS or the fitted charm sets than for those using the nominal sets. This is the expected behaviour of the IC contributions from

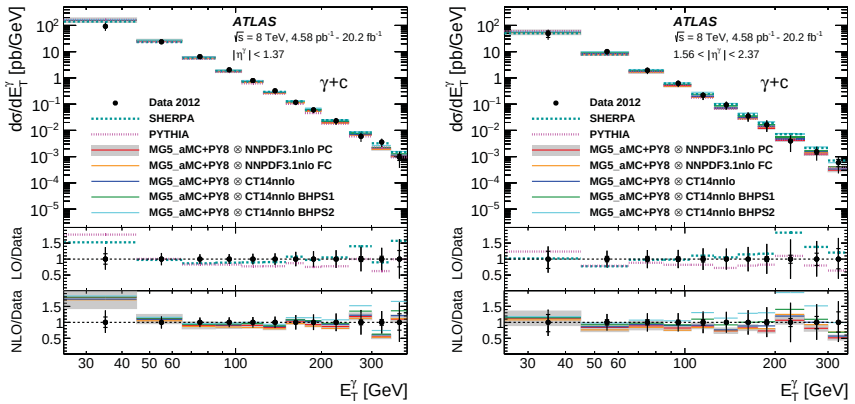

(a) (b)

Figure 5: Differential cross sections as a function of the photon transverse energy, E_{T}^{γ}, for γ+c in (a) the central and (b) the forward regions in pp interactions at 8 TeV. The statistical uncertainty is represented as horizontal marks on the error bars of the data points, while the complete length of the error bars represents the total measurement uncertainty. The MG5_aMC+PY8 label in the legend refers to the MadGraph5_aMC@NLO calculations interfaced to Pythia8. The $5F$ and $4F$ labels in the legend refer to PDF sets with five and four quark flavours, respectively. The PC and FC labels in the legend refer to perturbative charm and fitted charm PDF sets, respectively. All of the predictions for γ+c use $5F$ PDF sets. The theoretical uncertainty in the MadGraph5_aMC@NLO predictions is displayed for a single PDF set since it is similar for each of the PDF sets. The Sherpa and Pythia cross sections are not normalized to data and no uncertainties are provided for them. Taken from Ref. [5].

these PDF sets in the theory predictions. The predictions with the BHPS2 PDF set (2.1% of the IC) deviate the most from those using the nominal PDF sets, by about a factor 1.5, while those using the BHPS1 (.6% of the IC) and the fitted charm PDF sets give intermediate values. The precision of the data is comparable to the size of these deviations in the predictions. For the γ+b final state, the best description of the data is provided by the Sherpa predictions, which include up to three additional partons and are computed in the massive $5F$ scheme. The NLO predictions underestimate the data in the highest E_{T}^{γ} intervals measured. The $5F$ scheme of the theoretical calculations provides a better description of the data than the $4F$ scheme. For the γ+c final state, which exhibits larger measurement uncertainties, all the predictions are in agreement with the data. Differences

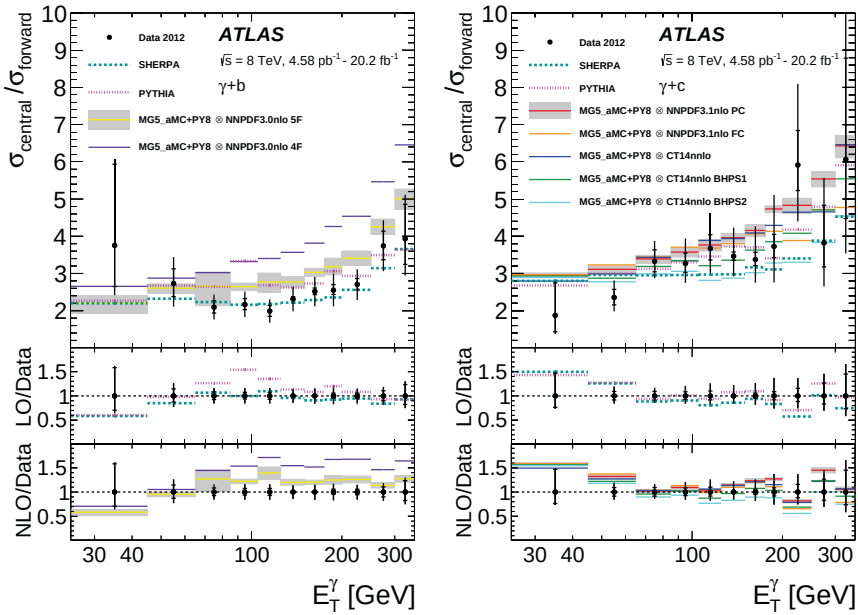

(a) (b)

Figure 6: Cross-section ratios of the central region, $|\eta^{\gamma}| < 1.37$, to the forward region, $1.56 < |\eta^{\gamma}| < 2.37$, as a function of the photon transverse energy, E_{T}^{γ}, for (a) γ+b and (b) γ+c. The statistical uncertainty is represented as horizontal marks on the error bars of the data points, while the total measurement uncertainty is represented by the complete length of the error bars. The MG5_aMC+PY8 label in the legend refers to the MadGraph5_aMC@NLO calculations interfaced to Pythia8. The $5F$ and $4F$ labels in the legend refer to PDF sets with five and four quark flavours, respectively. The PC and FC labels in the legend refer to perturbative charm and fitted charm PDFs, respectively. All of the predictions for γ+c use $5F$ PDF sets. The theoretical uncertainty in the MadGraph5_aMC@NLO predictions is displayed for a single PDF set since it is similar for each of the PDF sets, except for NNPDF3.1nlo FC for which the total uncertainty is similar to that in NNPDF3.1nlo PC at a value of 25 GeV in E_{T}^{γ}, but rises steadily relative to it to be a factor of three larger at 35 GeV. No uncertainties are provided for Sherpa and Pythia. Taken from Ref. [5].

of about the size of the measurement uncertainties are seen between the predictions using PDF sets with IC contributions and those without. These measured cross sections provide a test of pQCD calculations with HQs and

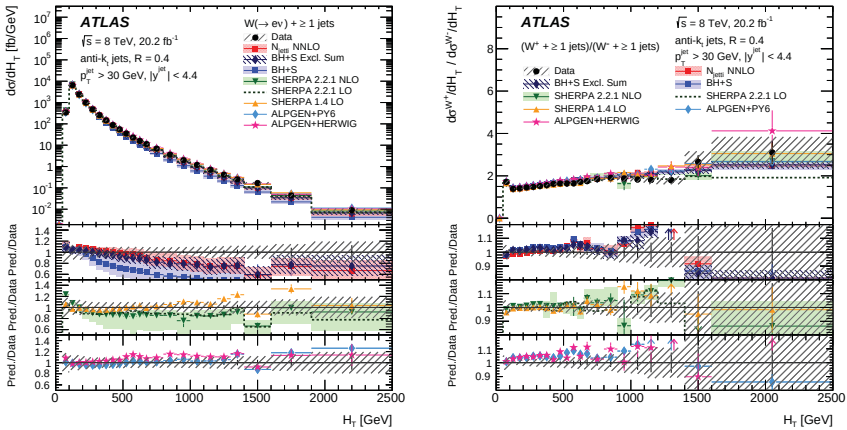

(a) (b)

Figure 7: Differential cross sections for the production of (a) W bosons and (b) the W^+/W^- ratio as a function of H_{T} for events with $N_{\mathrm{jets}} \geq 1$. The last bin in the figure (a) includes values beyond the shown range. For the data, the statistical uncertainties are indicated as vertical bars, and the hatched bands show the combined statistical and systematic uncertainties. The uppermost panel in plot shows the differential cross sections. The lower panels show the ratios of the predictions to the data. The arrows on the lower panels indicate points that are outside the displayed range. Taken from Ref. [6].

are sensitive to the b and c quark PDFs.

5 Differential cross-sections of W + jets and W^+/W^- ratios at 8 TeV

Using data corresponding to an integrated luminosity of 20.2 fb^{-1} at center-of-mass energy 8 TeV, the results for W +jets production in final states containing one electron and missing transverse momentum, focusing on events with one or two additional jets are presented [6]. The data are measured for W production as well as for W^+ and W^- production and the cross-section ratio of W^+/W^- as a function of the number of jets (N_{jets}). For events with at least one jet, the differential cross sections are shown as a function of the scalar sum of the transverse momenta of electron, neutrino and jets (H_{T}), the transverse momentum of the W boson, and the transverse momentum and rapidity of the most energetic jet (leading jet). These observables are sensitive to higher-order terms in the prediction as well as the PDFs. For

events with at least two jets, the differential cross sections are shown for W boson production only and include distributions as a function of the transverse momentum and rapidity of the second leading jet, the dijet angular separation, and the dijet invariant mass. These observables are sensitive to hard parton radiation at large angles and different ME/PS matching schemes. The differential cross section for W production and the ratio of W^+ and W^- as a function of H_{T} are shown in Fig. 7 for $N_{\mathrm{jets}} \geq 1$. The H_{T} distribution is a very important test of pQCD as the higher values are sensitive to higher jet multiplicities and topologies such as $qq \to qq'W$. The LO predictions of Sherpa and Alpgen, which both include multiple jets in the ME calculation describe the data best, although these predictions have large theoretical uncertainties. The BlackHat+Sherpa predictions underestimate the data at large values of H_{T}. This is expected since, at these large values of H_{T}, contributions from additional jets are important, which are only partially present in this calculation. The predictions from the BlackHat+Sherpa exclusive sums method and from the NNLO N_{jetti} calculation, which include an additional jet emission at NLO, provide better agreement with the data. At the largest measured values of H_{T}, where the measured cross section is small, the total experimental uncertainty in the W^+/W^- cross-section ratio increases due to larger statistical uncertainties in the data and some systematic uncertainties that do not fully cancel out in the ratio. Overall, the measured distributions show that NNLO and NLO predictions are able to describe the data. However, at high transverse momenta, large jet rapidities, or large dijet angular separations, many of these predictions underestimate or overestimate the cross sections. In many places, multi-leg LO generators, such as Alpgen and Sherpa, which consider a larger number of parton emissions from the ME calculation, model the data best, although with large theoretical uncertainties. The H_{T}, jet rapidity, and dijet invariant mass distributions are in general the least well described, suggesting that better modelling of events with energetic jets as well as jets with large rapidities is needed.

6 Measurement of the soft-drop jet mass at 13 TeV

Calculations of jet substructure observables that are accurate beyond LL accuracy have recently become available. In the Ref. [7] the normalized, differential cross-section is measured as a function of $\log_{10}(\rho^2)$, where ρ is the ratio of the soft-drop mass to the ungroomed jet transverse momentum. This quantity is measured in dijet events from 32.9 fb^{-1} of center-of-mass energy 13 TeV pp collisions. The soft-drop procedure acts on the clustering history of a sequential recombination jet algorithm. In these algorithms, all inputs to jet-finding start as a proto-jet and are combined pairwise using a

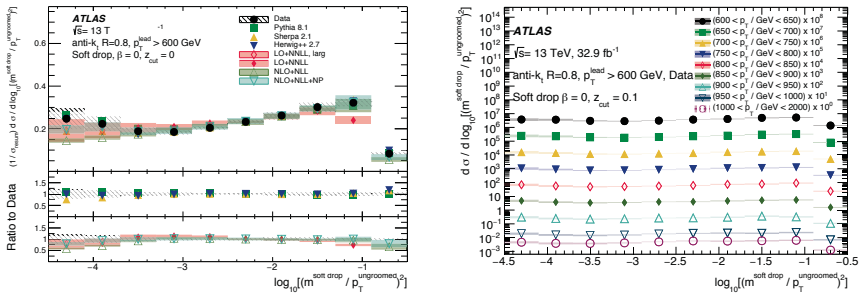

(a) (b)

Figure 8: (a) The unfolded $\log_{10}(\rho^2)$ distribution for anti-k_t $R = 0.8$ jets with $p_T^{lead} > 600$ GeV, after the soft drop algorithm is applied for $\beta = 0$, in data compared to PYTHIA, SHERPA, and HERWIG++ particle-level, and NLO+NLL+NP and LO+NNLL theory predictions. The LO+NNLL calculation does not have NP corrections; the region where these are expected to be large is shown in an open marker, while regions where they are expected to be small are shown with a filled marker. The distributions are normalized to the integrated cross section, σ_{resum}, measured in the resummation region, $-3.7 < \log_{10}(\rho^2) < -1.7$. The NLO+NLL+NP cross-section in this resummation regime is 0.14 nb for $\beta = 0$. (b) The unfolded $\log_{10}(\rho^2)$ distribution in data for each of the transverse momentum bins in the analysis, overlaid with a multiplicative factor indicated in the legend. Taken from Ref. [7].

distance metric in (y, ϕ)-space. When the smallest distance is above some threshold R, the algorithm terminates and the remaining proto-jets are the final jets. The clustering history is the sequence of pairwise combinations that lead to a particular jet. The soft-drop algorithm starts by re-clustering anti-k_t jet's constituents. Next, the clustering tree is traversed from the latest branch to the earliest and at each node, the following criterion is applied to proto-jets j_1 and j_2:

$$min(p_{T,j_1}, p_{T,j_2})/(p_{T,j_1} + p_{T,j_2}) > z_{cut}\,(\Delta R_{12}/R)^{\beta},$$

where p_T is the momentum of a jet transverse to the beam pipe, z_{cut} and β are algorithm parameters, and

$$\Delta R_{12} = \sqrt{\Delta y^2 + \Delta\phi^2}\,,$$

is the distance in (y, ϕ)-coordinate system between the proton–jet. The data are unfolded to correct for detector effects, compared to precise QCD calculations and LL particle-level MC simulations, and are shown in Fig. 8(a).

They are compared to the predictions of the Pythia, Sherpa, and Herwig++ generators, as well as the NLO+NLL and the LO+NNLL. The NLO+NLL calculation includes NP corrections based on the average of various MC models with NP effects turned on and off; the envelope of predictions is added as an uncertainty. The LO+NNLL predictions do not contain NP effects, but the open makers in Fig. 8(a) indicate where NP are expected to be large. The $\log_{10}(\rho^2)$ distribution in data for $\beta = 0$ and each transverse momentum bin is shown in Fig. 8(b). There is no strong dependence of the shape on transverse momentum.

7 Summary

The latest results from the ATLAS collaboration at the LHC (CERN) involving jets, dijets, photons in association with HF jets and vector bosons in association with jets, measured at center of mass energies of 8 and 13 TeV are obtained. The first measurement of γ+HF jet at the LHC are presented. All measured cross-sections are compared to state-of-the art theory predictions.

References

[1] ATLAS Collaboration, JINST **3**, S08003 (2008).

[2] L. Evans and P. Bryant (editors), JINST **3**, S08001 (2008).

[3] ATLAS Collaboration, JHEP **1805**, 195 (2018)

[4] ATLAS Collaboration, JHEP **1709**, 020 (2017)

[5] ATLAS Collaboration, Phys. Lett. B **776**, 295 (2018)

[6] ATLAS Collaboration, JHEP **1805**, 077 (2018)

[7] ATLAS Collaboration, Phys. Rev. Lett. **121**, 092001 (2018)

Experimental search of nuclear fusion reactions in a ptμ system

A. Adamczak[1], V.V. Baluev[2], L.N. Bogdanova[3], D.L. Demin[4], V.N. Duginov[4], M.P. Faifman[5], S.V. Filchagin[2], K.I. Gritsaj[4], A.D. Konin[4], I.P. Maksimkin[2],T.N. Mamedov[4], R.K. Musyaev[2], A.I. Rudenko[4], Z.U. Usubov[4], O.P. Vikhlyantsev[2], V.P. Volnykh[4], A.A. Yukhimchuk[2]

[1] *Institute of Nuclear Physics, The Polish Academy of Sciences, Krakow, Poland;*

[2] *RFNC - VNIIEF, Sarov, Russia;*

[3] *NRC "Kurchatov Institute"- ITEP, Moscow, Russia;*

[4] *DLNP, JINR, Dubna, Russia;*

[5] *NRC "Kurchatov Institute", Moscow, Russia;*

Abstract

We present the most recent study of nuclear reactions, proton and tritium fusion, catalyzed by negative muons. The experiment was performed at TRITON installation in JINR, in 2016. This phenomenon of light nuclei pt-fusion at low temperatures was so far investigated in the only experiment (PSI, 1993). The yeilds of main reaction channels, gamma rays and conversion muons, were measured for two different tritium concentrations, and the rates didn't match theoretical expectations. To study this problem in detail and to observe other possible channels predicted by the theory, namely, electron-positron and gamma-gamma pairs, we carried out the experiment at the negative muon beam (10^4 s^{-1}, 100 MeV/c) from the JINR Phasotron with a specially created target of 50 c.c. volume, filled with a liquid hydrogen-tritium H/T mixture (tritium concentration of 1% and 0.1%). The experiment used an effective detection system containing two gamma-detectors which ensured reliable registration and identification of pt-reaction products at different relative dispositions of target and detectors. In three experimental runs with a total duration of 300 hours, besides the channels of pt-fusion with single gamma-quanta and conversion muons, electron-positron (e^+e^-) and gamma-gamma ($\gamma\gamma$) pairs in the output channels were detected, which were not observed before, either "in-flight" (beam-target experiments), or in *ptμ*- muonic molecules. The measured yields of γ- and μ- channels of pt-fusion are in a good agreement with the results of PSI experiment, what makes a major challenge for the nuclear physics theory to explain the results. The description of TRITON installation and the methods developed for the experimental search of the pt-fusion within the *ptμ* molecule are presented. Further analysis of the experimental data and their interpretation will be performed on the basis of the Monte Carlo simulations to describe the kinetics of processes of muon catalysis in a hydrogen-tritium H/T mixture and taking into account the actual geometry of the experiment. As a result of the time and energy experimental spectra analysis, the yields of pt-fusion

products (for the first time for e^+e^- pairs and $\gamma\gamma$ pairs) will be determined. This will allow extracting the nuclear reaction constants for magnetic dipole M1- and electric monopole E0-transitions in the A = 4 nucleon system.

1 Introduction

High fusion probability for nuclei of hydrogen isotopes in muonic molecules was theoretically predicted by F.Ch. Frank and A.D. Sakharov at the end of the 1940s and later experimentally confirmed by L. Alvarez (1957). The first strict scientific concepts regarding a complex chain of reactions induced by a muon in a mixture of hydrogen isotopes H/D/T (muon catalysis) were formulated in the papers of J. Jackson, Ya.B. Zel'dovich, and S.S. Gershtein in the early 1960s. In 1964, V.P. Dzhelepov initiated systematic experimental research of muon catalysis at the Laboratory of Nuclear Problems, JINR, which resulted in what could be regarded as fundamental achievements in physics: resonant formation of muonic deuterium molecules was discovered. A high rate of the muon catalysis cycle in a mixture of deuterium and tritium (D/T) predicted by L.I. Ponomarev and colleagues at JINR was experimentally confirmed for the first time, and spin and temperature dependences of muonic molecule formation rates in liquid and solid deuterium were obtained for the first time. For decades, these results stimulated muon catalyzed fusion research both in our country (JINR, PINP) and abroad (United Kingdom, Canada, United States, Switzerland, Japan).

The muon catalysis research at DNLP continued in fruitful cooperation with experimenters from VNIIEF (Sarov) initiated by V.G. Zinov. Systematic studies on the specially developed TRITON facility [1] resulted in obtaining parameters of the muon catalysis cycle in a D/T mixture under a variety of experimental conditions (temperature 20–800 K, pressure up to 1500 atm) and acquiring experimental data of record high amount and accuracy [2]. Muon catalysis in a dense triple H/D/T mixture of hydrogen isotopes was investigated for the first time, epithermal effects predicted for this mixture were observed [3], and a conclusion was drawn about a possibility of diluting the D/T mixture by hydrogen to a level of about 10% to save tritium, which is important for developing nuclear energy sources based on muon catalysis. Parameters of the cycle in pure tritium were measured [4] with a record accuracy, the mechanism for fusion of tritium nuclei was studied [5], and considerable α - n correlations in the final state of that reaction were inferred. Also, the yield of the radiative deuteron capture channel $dd\mu \rightarrow {}^4He + \gamma$ with respect to the main channels of the dd reaction in the muonic molecule $dd\mu$ was experimentally estimated for the p-wave state [6].

Muon catalysis is an unique profitable tool for studying fusion reactions of hydrogen isotopes, especially at low, "astrophysical", nuclear collision

energies. It helps one obtaining or refining constants of various reactions at particular spin states of nuclei and to observe fusion channels forbidden in collisions of free nuclei. By now, all kinds of muon-catalyzed nuclear reactions in mixtures of hydrogen isotopes have been well studied. An exception is fusion of proton and tritium nuclei.

2 Background

The latest experiment on the study of muon catalysis in the H/T mixture was carried out by an international team of experimenters at PSI (Switzerland) in 1993 [7]. Two exit channels of this reaction were observed: M1 transitions with emission of a gamma ray and, for the first time, E0 with conversion on the muon. The measured yields of these pt reaction channels are appreciably larger than the expected values based on the experimental data on the in-flight radiative capture pt and the reaction n + ^{3}He, which is a mirror reaction relative to the radiative channel of the p + t reaction, and also the values calculated from the data on the ^{4}He(e,e')pt reaction (for the conversion channel). No explanation for this disagreement has been found so far. In addition, the conversion channel with the formation of e^+e^- pairs was not observed though its yield was predicted to be about the muon yield [8,9].

The so far unsolved problems in the description of the muon-catalyzed pt fusion aroused interest of the DNLP scientific experimental group headed by D.L. Demin, and they proposed investigation of the pt-fusion channels with energy output about 20 MeV:

$$pt\mu \rightarrow {}^4He\mu + \gamma, \quad (1)$$

$$pt\mu \rightarrow {}^4He + \mu, \quad (2)$$

$$pt\mu \rightarrow {}^4He\mu + e^+ + e^-, \quad (3)$$

$$pt\mu \rightarrow {}^4He\mu + \gamma + \gamma. \quad (4)$$

The TRITON project was prepared and soon supported by the JINR Programme Advisory Committee for Nuclear Physics in year 2011. The team established for conducting the experiment had an appreciable background to allow successful implementation of the project. By that time, Demin's group had accomplished the experiment at DLNP on the search for the rare radiative deuteron capture reaction using specially designed "gamma" detectors [10] with a measurement range up to 30 MeV. With this unique experience, the Dubna experimenters were prepared for studying characteristic features of the pt reaction.

The motivation to observe ptμ fusion is as follows. One can not observe the reaction channels (2), (3), (4) in a beam-target experiment. The reaction

channels (1), (2) had had the only previous observation [7]. The reaction channels (3), (4) were not observed previously. The knowledge of the reaction channels' (1), (3), (4) yield is critical for primordial nucleosynthesis in astrophysics [11]. The reaction channels (1), (3), (4) are the perfect probe for developing four-body problem in nuclear physics.

3 Experimental method

The experimental methodology was proposed by Prof. V.V. Fil'chenkov. The experimental setup scheme is shown in the Fig.1. A detailed description of the experimental methodology is given in [12]. The Liquid tritium target (Fig.2) [13] was designed according to the JINR specification by VNIIEF group headed by I.P. Maksimkin and was able to contain 50 c.c. of liquid hydrogen at 22 K with up to 1% tritium admixture during hundreds of hours.

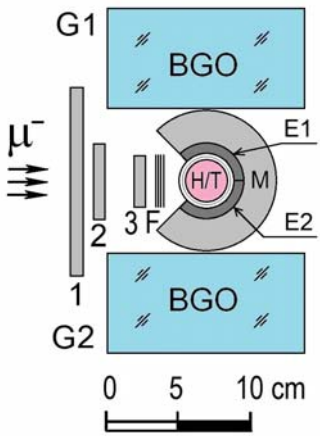

Fig.1. Experimental setup:
1-3 – plastic counters,
BGO – crystal,
E1-E2 – electron telescope,

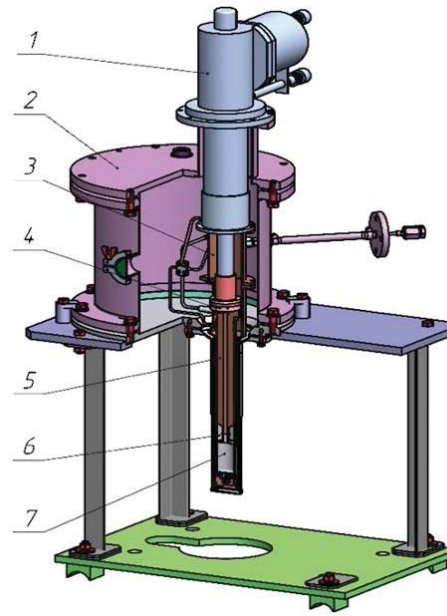

Fig.2. Liquid tritium target:
1—cryogenic refrigerator,
2 – vacuum chamber,
3 – vacuum insulation,

F – copper degrader,
G1-G2 – gamma-detector,
H/T – target containing H/T mix,
M – muon detector (full absorption)
4 – heater,
5 – cold duct,
6 – container,
7 – liquid H/T mix

The cylindrical geometry of the target was chosen to provide higher registration efficiency with respect to that in PSI experiment [7]. In this geometry the "electron" detectors E1, E2 (Fig.1) envelope the target tightly and serve to detect e^+e^- pairs (3). Cylinder-shaped "muon" detector M is designed to absorb conversion muon (2). Electron–positron pair E1, E2 detectors and conversion muon M detector were developed to suit the compact geometry. Two BGO-based "gamma" detectors G1, G2 mentioned above [10] are placed around and close to muon detector (at the distance 56 mm from the center of the target) to detect gamma particles (1), (4). The detectors are shown in the Fig.3.

Fig.3. Detectors: E1, E2 – in the front, G1 – in the depth, scintillator with light-guide for detector M – in the middle

The two "electron" detectors E1, E2 and two "gamma" detectors G1, G2 allow registering $\boldsymbol{e^+e^-}$ pairs and $\boldsymbol{\gamma\gamma}$ pairs. Detectors E1, E2 are supplied with a fiber light-guide as shown in the Fig.4. This feature provides compact design together with spectrometric quality of the device (due to light collection uniformity). Plastic scintillator in detectors E1, E2 are of thickness 5 mm and that in detector M of thickness 19 mm. The heights of the plastics are both equal to about 110 mm. The design of "gamma" detector is shown in the Fig.5. The BGO crystal Ø127x60 mm is surrounded with a plastic shell, which makes possible to

lower the cosmic background by two orders using pulse-shape analysis [14].

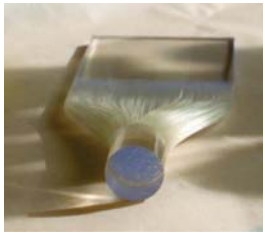

Fig.4. Make-up of the fiber light-guide

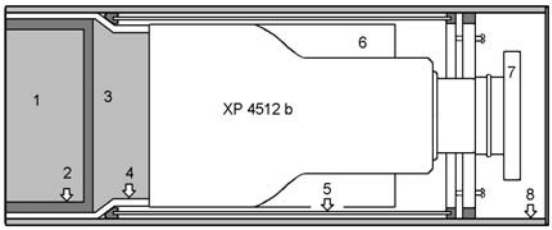

Fig.5. Gamma detector: 1 - BGO crystal, 2 – plastic scintillator shell, 3 – light-guide, 4 – Teflon, 5 – iron magnetic shield, 6 – permalloy magnetic shield, 7 – electronics, 8 – iron case

The simplified scheme of the electronics is shown in the Fig.6. The coincidence signal **1,2,3,E1,E2** starts the timing gate with the duration of 20 μs when the γ-particle or conversion muon (or electron-positron pair) signals are expected to be registered. The necessary condition is an absence of other incoming muon, detected as coincidence signal **1,2**, during preceding 5 μs. The Trigger block [15] selects the useful events. It monitors the detectors and produces the signal permitting the FADCs output (digitized from detectors E1, E2, M, G1, G2) to be "written" to a PC.

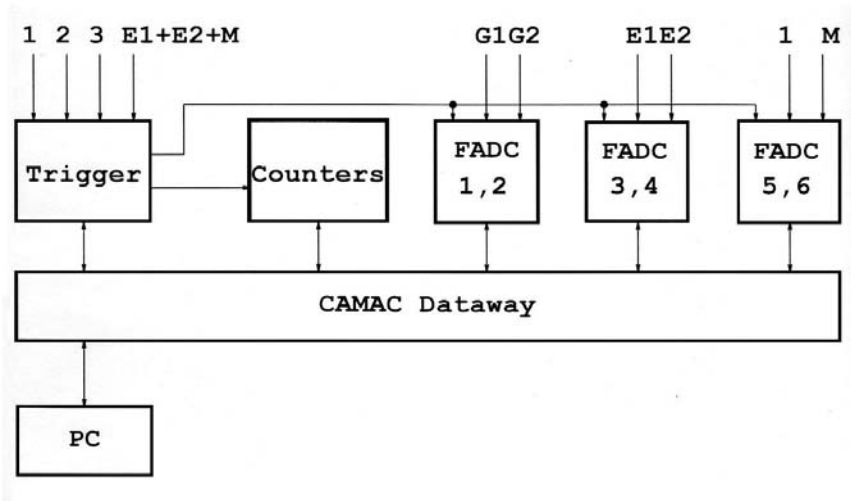

Fig.6. Electronics of the experiment

One of the goals of our experiment was detecting the yield of e^+e^- pairs, which were not observed in the PSI experiment [7] with **ptμ** molecules. The conviction in the productivity to do so is supported by the theoretical results [8,9] predicting the conversion muons yield (2) and the yield of e^+e^- pairs (3) to be close within 25%. Equipped with the knowledge of the angular correlation in e^+e^- pair emission for nuclear E0-transition [16], the problem of parameterization of angular correlation of pair emission in the p + t reaction (3) was solved and the Monte Carlo simulation of corresponding physical processes in the TRITON installation was performed. The result of simulation of pair emission (3) is shown in the Fig.7. together with that for conversion muon (2), the proposed yields of both channels being set equal. The results of the simulation for the registration efficiencies ϵ pertinent to the experiment are also given in the Table. 1: marker **γ** corresponds to gamma-particle (1) registration in detectors G1 or G2; marker **μ** corresponds to conversion muon (2) stop registration in detector M; marker **pairs 1** attributes to signal $\mathbf{(E1 + E2) \cdot M}$ and corresponds to detection at least one particle of e^+e^- pair (3); marker **pairs 2** attributes to signal $\mathbf{E1 \cdot E2 \cdot M}$ and corresponds to simultaneous detection of both particles of e^+e^- pair (3); marker $\mathbf{e_d}$ corresponds to electron from muon decay. The latter is the logical sum $e_d = e_d1 + e_d2$, where $\mathbf{e_d1}$ is the coincidence signal $\mathbf{(E1 + E2) \cdot M}$, responsible for the muon stop in the target; $\mathbf{e_d2 = M \cdot (G1 + G2)}$ means that a conversion muon decays in detector M.

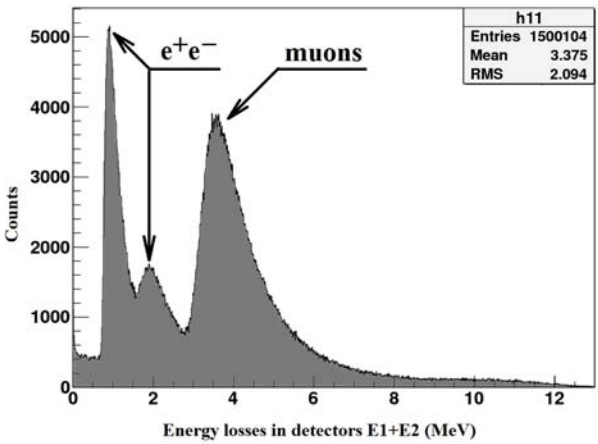

Fig.7. The Monte Carlo simulation of physical processes in TRITON installation: **muons** – process (2), e^+e^- - process (3)

Table. 1: Registration efficiencies ϵ

Particles	Registration efficiency, %
$\epsilon(\gamma)$	20
$\epsilon(\mu)$	66
ϵ (pairs 1)	90
ϵ (pairs 2)	16
$\epsilon(e_d1)$	70
$\epsilon(e_d2)$	30

The calibration of the TRITON experimental equipment (Fig.8.) using electron beam (electron energy E_e up to 20 MeV) of LINAC-200 during commissioning works [17] and Monte Carlo simulation (Fig.9.) for electron

registration have been performed. Beam energy determination (the order of accuracy 1%) [18] was performed by the method of the ratio of photoactivation of ^{114}In-^{115}In isotopes [19].

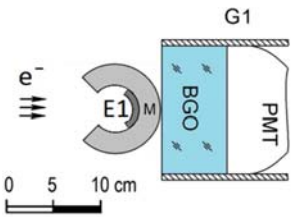

Fig.8. Setup for calibration using electron beam

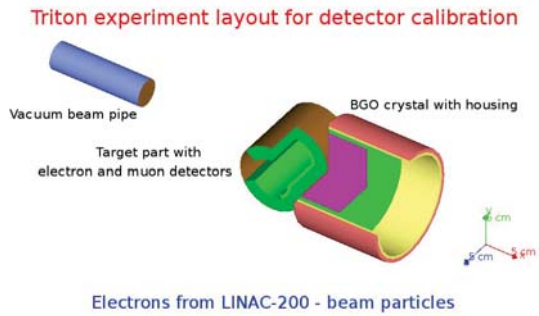

Fig.9. Monte-Carlo geometry to simulate the calibration of the TRITON experimental equipment

The results of the Monte Carlo simulation fit well with the measurements using electron beam of LINAC-200. The example of the energy deposited by a single electron in detector G1 is shown in the Fig.10. The detector apparatus line broadening was obtained as a function of energy of an incident electron, see Fig.11. The detector calibration using electron beam is necessary in data analysis handling the **complicated** scheme of muon catalyzed fusion processes in the TRITON installation.

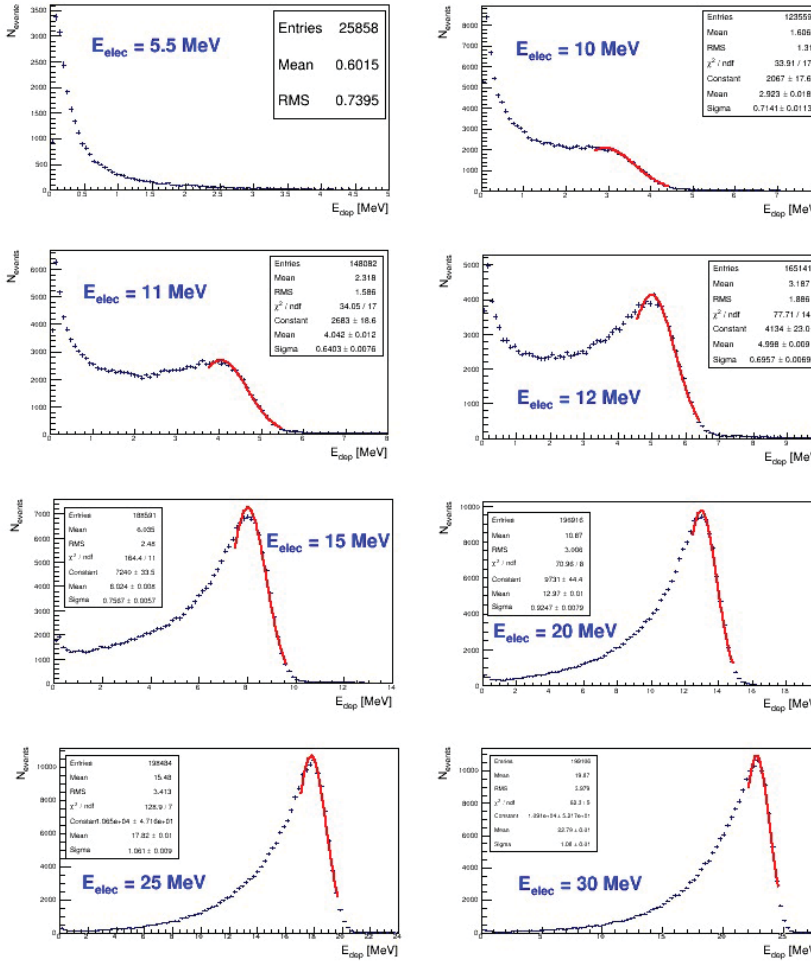

Fig.10. Monte Carlo simulation - energy deposited by a single electron of energy E_{elec} in detector G1

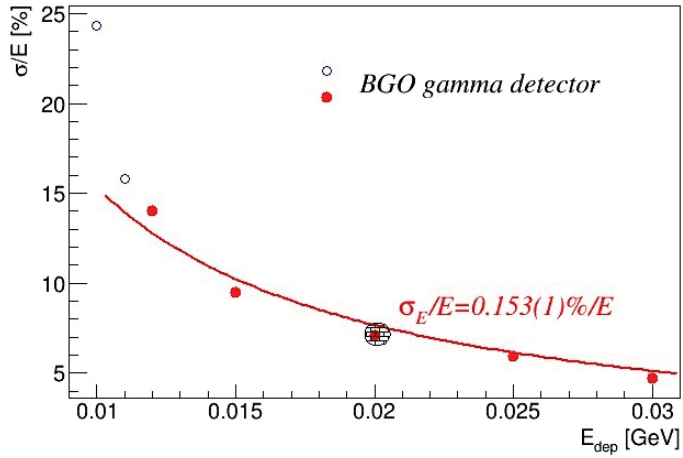

Fig.11. The detector G1 apparatus line broadening was obtained as a function of energy E_{dep} of an incident electron

The **simplified** scheme of muon catalyzed fusion processes in the double H/T mixture is shown in the Fig.12. The dependences, obtained by two different (PSI [7] and our) calculating programs of kinetics modelling the muon catalyzed fusion processes, are in quite good agreement, see the Fig.13.

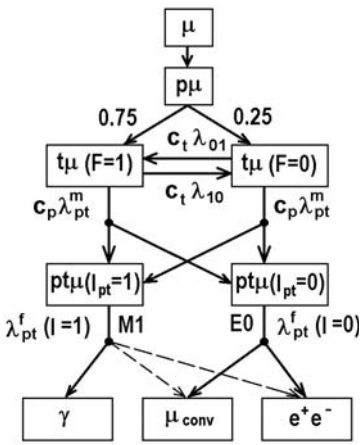

Fig.12. The simplified scheme of muon catalyzed fusion processes in the double H/T mixture (Figure taken from [7] and the designations

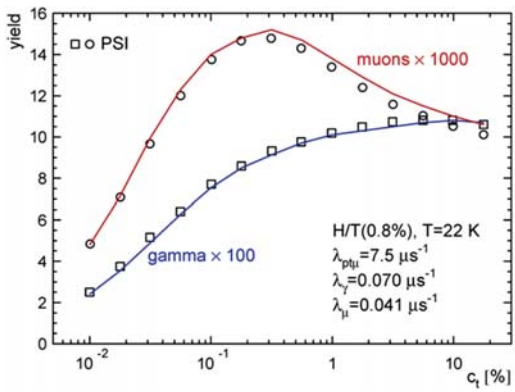

Fig.13. Yields for conversion muons (circles) and gamma emissions (squares) in pt-fusion as a function of tritium concentration c_t [7]. Respective curves correspond to results of our Monte Carlo

therein) simulations at fixed muon catalyzed fusion parameters (presented on plot)

4 Experiment

From May till November 2016 the experiment on the search for muon catalysis in an H/T mixture was carried out on the DNLP Phasotron, JINR, in collaboration with VNIIEF specialists. The condition of the beam was as follows: internal proton current - 1 μA, negative muon pulse - 100 MeV/c, pulse uncertainty ±5%, beam spot FWHM - 4·4 cm^2, intensity – 10^4 μ/s [20]. The mean counting rate was maintained at the level of a hundred muon stops per second (Fig.14) in the H/T mix inside the target (Fig.15). The run parameters and the target contents are summarized in the Table. 2.

Table. 2: The run parameters and the target contents

Run No.	Tritium content	Deuterium content	Gamma-detectors' angle	Triggers	Run time
Dec.'13	0%	10^{-4}	180°	10^6	20 h
I (May'16)	0.8%	10^{-4}	180°	10^7	100 h
II (Nov.'16)	0.08%	10^{-4}	180°	10^7	100 h
III (Nov.'16)	0.08%	10^{-4}	110°	10^7	100 h

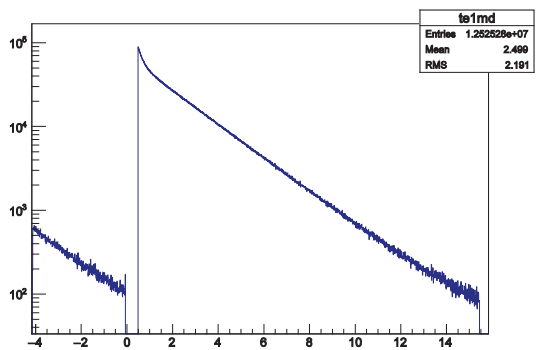

Fig.14. Time spectrum in microseconds of μ-decay electrons (used for normalization)

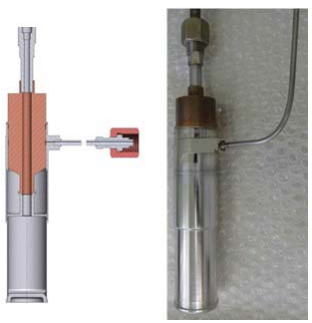

Fig.15. Make-up of the target

Earlier known pt-fusion channels (1), (2) with the yield of single gamma rays and conversion muons were observed in the experiment (Figs. 16, 17).

For the first time the pt-fusion channel with the yield of electron-positron pair (3) was observed. The sum energy spectrum of conversion muon and electron-positron pairs in electron telescope E1+E2 is shown in the Fig.18.

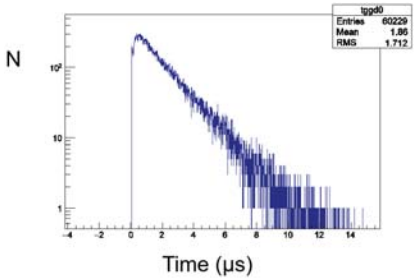

Fig.16a. Timing spectrum of process (1)

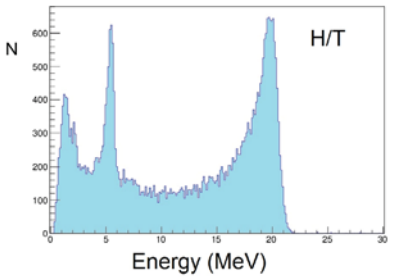

Fig.16b. Energy spectrum of process (1). The gamma line at 5.5 MeV corresponds to natural admixture of deuterium

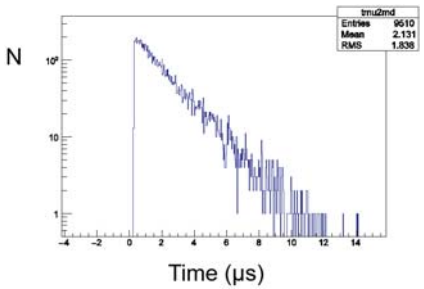

Fig.17a. Timing spectrum of process (2)

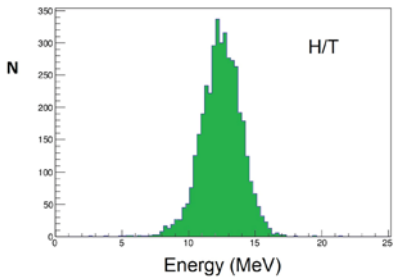

Fig.17b. Energy spectrum of process (2)

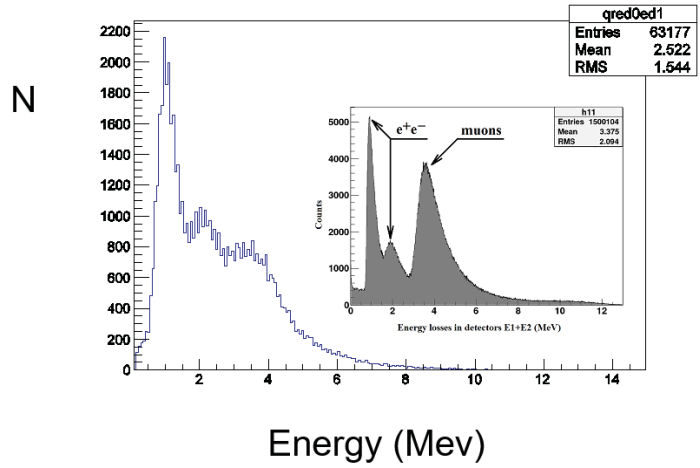

Fig.18. Experimental energy spectrum of electrons/positrons from process (3) registered by the detectors E1+E2 together with experimental energy spectrum of conversion muons from process (2) detected by the same detectors. The Monte Carlo simulation plot performed before the experiment is also given

Quite unexpectedly, the process (4) with the yield of two gamma particles (Fig.19) simultaneously registered in two different detectors G1 and G2 was observed for the first time in run I (May'16) at the level comparable to that of the process (1).

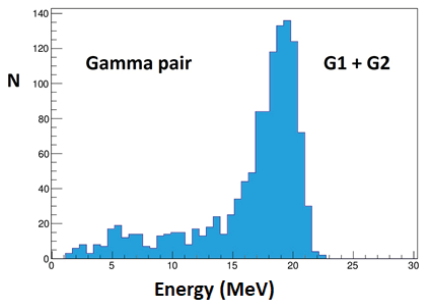

Fig.19a. The sum G1+G2 energy spectrum of process (4)

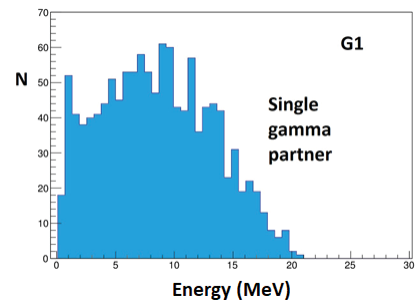

Fig.19b. The G1 energy spectrum of one partner of two-gamma process (4)

The measurements were repeated in runs II and III (Nov.'16) with lower content of tritium and different relative positions of gamma detectors G1 and G2 in order to observe the angular correlation between gamma particles in process (4). The tritium content 0.08% was chosen for runs II, III in the way (Table.2)

that the yield of conversion muons (the E0-transition) remains the same, the gamma emission yield (the M1-transition) being lower. And the observations confirmed this suggestion, based on kinetics calculations (Fig.13). However, no severe angular correlation for process (4) was observed, as seen from the Fig.20. But another process was noted. The gamma line at 5.5 MeV corresponding to natural admixture of deuterium appears in the sum energy spectra of double gamma events more clearly as relative content of tritium/deuterium decreases (Figs.19a, 20). This appearance can be accounted for the fusion reaction not observed yet:

$$pd\mu \rightarrow {}^{3}He\mu + \gamma + \gamma + 5.5\ MeV. \qquad (5)$$

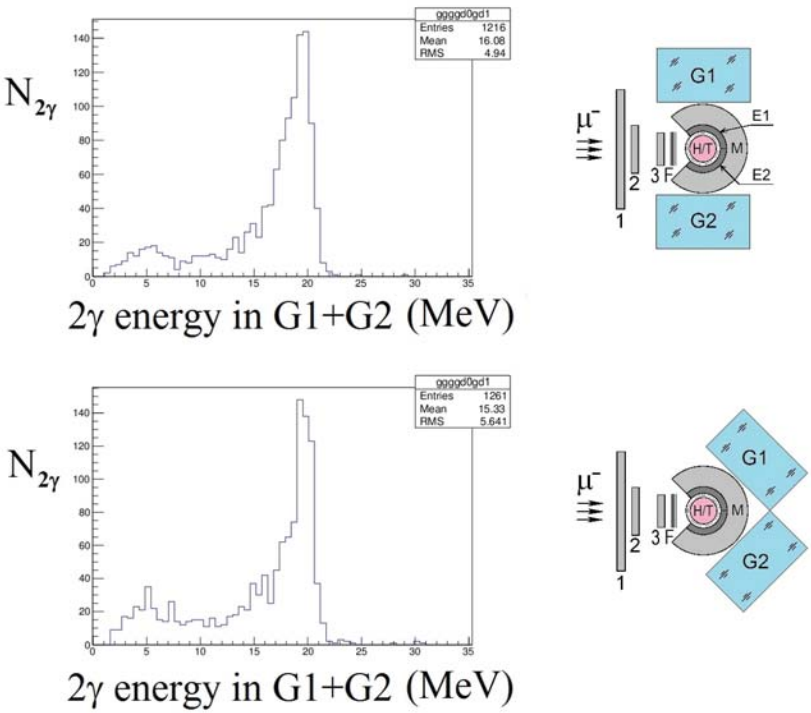

Fig.20. The sum energy spectra of process (4) registered in G1+G2 at tritium concentration c_t = 0.08% with the same beam statistics for two different relative positions of gamma detectors G1 and G2: relative angle of 180^{O} (top), 110^{O} – (bottom)

Following the recommendations of the 46-th Session of JINR Programme Advisory Committee for Nuclear Physics, 14–15 June 2017 (Dubna), we plan to perform further data analysis: modeling of kinetics of mesoatomic and mesomolecular processes in the target; development of a technique for modeling the channel registration process with the emission of two gamma quanta from the pt-fusion reaction in the TRITON installation; in-depth analysis of the experimental data obtained.

5 Results

The analysis of the main pt-reaction parameters (radiative fusion rate and muon conversion rate) has been already accomplished in the Table. 3 except for the systematical errors, estimated below 10%.

Table. 3: Comparison of the rates of nuclear reaction from different spin states of the pt-system, corresponding channels (1), (2) - the analysis of time spectra

	Fusion rate λ_{pt}^{γ} (μs^{-1}) **Channel (1), I_{pt}=1**	Muon conversion rate λ_{pt}^{μ} (μs^{-1}) **Channel (2), I_{pt}=0**
PSI results [7]	$0.067\pm0.002_{-0.002}^{+0.005}$	0.15±0.02
The preliminary results of **TRITON** experiment (2016y.)	0.065±0.004(stat.)	0.11±0.01(stat.)

The further analysis of the experimental data is now under way, and the following important conclusions can already be drawn:

1. The **obtained results confirm** theoretical predictions of Ya.B. Zel'dovich and S.S. Gershtein (1960) [21] on the output products of nuclear reactions in cold hydrogen isotope mixtures caused by muons;

2. The preliminary analysis of data and obtained rates of previously observed pt-fusion channels (1), (2) with the yield of single gamma quanta and conversion muon **agree well** with results of PSI experiment [7];

3. The pt-fusion channel with the yield of electron-positron pairs (3) as well as the channel with the yield of a pair of gamma quanta (4) was **observed for the first time**;

4. The **first indication** was made for the channel with a yield of pair of gamma quanta in pd-fusion (5).

Acknoledgements

The authors appreciate help from Professors L.I. Ponomarev, C. Petitjean and V.V. Kobets. The work was done with the aid of RFBR Grant #12-02-00089-a.

References

[1] A.A. Yukhimchuk et al., **Hyp. Int.** 119(1999)341.

[2] V.R.Bom et al., **JETP** 100(2005)663.

[3] Yu.P. Averin et al., **Hyp. Int.** 138(2001)249.

[4] L.N.Bogdanova et al., **JETP** 108(2009)216.

[5] L.N. Bogdanova et al., **Phys. At. Nucl.** 78(2015)10.

[6] V.V. Baluev et al., **JETP** 113(2011)68.

[7] P. Baumann et al., **Phys. Rev. Lett.** 70(1993)3720.

[8] J.R. Oppenheimer and J.S. Schwinger, **Phys. Rev.** 56(1939)1066.

[9] L.N. Bogdanova and V.E. Markushin, **MCF** 4(1989)103.

[10] L. N. Generalov et al., **Preprint VNIIEF** 104-2009, Sarov, Russia, 2009.

[11] V.A. Bednyakov, **Phys. Part. Nucl.** 33(2002)915.

[12] L.N. Bogdanova, et al., **Phys. Part. Nucl. Lett.** 9(2012)605.

[13] R.K. Musyaev et al., *"Zhidkotritievaya mishen' dlya issledovaniya ptμ sinteza"*, XII Mezhdunarodnaya Shkola molodykh uchenykh i specialistov

IHISM'17 Junior imeni A.A. Kurdyumova “Vzaimodeistvie isotopov vodoroda s konstrukcionnymi materialami”, 10-15 June, 2017, Protvino, Russia.

[14] D.L. Demin et al., **Preprint JINR** E15-2012-107, Dubna, Russia, 2012.

[15] V.G. Zinov et al., **Preprint JINR** P13-96-439, Dubna, Russia, 1996.

[16] C.P. Montoya et al., **NIM** A334(1993)437.

[17] V.V. Kobets et al., **LINAC2018**, 16-21 Sept., 2018, Beijing, PRC.

[18] M.I. Gostkin, U. Kruchonak, A.S. Zhemchugov, to be published.

[19] M. Krmar et al., **NIM** A 901(2018)133.

[20] A.V. Demianov et al., **Preprint JINR** P9-93-374, Dubna, Russia, 1993.

[21] Ya.B. Zeldovich and S.S. Gershtein, **Sov. Phys. Uspekhi** 3(1961)593.

III "NEW COLLIDERS, FACILITIES, DETECTORS, COMPUTING AND DATA ANALYSES TECHNIQUES"

Radiation hardness of scintillation detectors based on organic plastic scintillators and optical fibers

Yu.N. Kharzheev

The scintillation detectors (SDs) based on the organic plastic scintillators and the optical fibers are one of the basic detectors used in the all modern accelerator, astrophysics, and neutrino experiments. They are multifunctional being used in calorimeters, triggering, tracking, TOF, Veto systems are. This is due to the remarkable properties of the organic scintillators and the optical fibers such as good optical and mechanical properties, short decay time, reliability and stability of their characteristics, ease manufacture and operation, compactness, and cheapness [1-3].

In recent years, interest in using SDs has significantly increased due to the forthcoming upgrade of the LHC [4] and the construction of new accelerators FCC [5], FAIR [6], NICA [7], and others, since their energy and luminosity significantly exceed the currently achieved values (Table 1). However, under the influence of high radiation loads, the light output and transmission of both scintillators and optical fibers deteriorate. Requirements on stability and reliability of SD operation in new conditions became strickler and their fulfillment largely depends on the radiation hardness of the scintillators, optical fibers, and photodetectors. In the framework of the upgrade the spectrometers ATLAS [8], CMS [9], LHCb [10] research is being carried out on both known and new materials capable of meeting the increasing requirements of radiation hardness.

Accelerator	Luminosity	Particles	Energy	Refer.
LHC HL-LHC	10^{34} cm^{-2} s^{-1} (in present) $5x10^{34}$ cm^{-2} s^{-1}(2025)	P+P P+P	14 TeV 14 TeV	4
FCC	$5x10^{34}$ cm^{-2} s^{-1} (2035)	P+P	100 TeV	5
FAIR(HESR)	10^{34} cm^{-2} s^{-1} (~2025)	anti P+ions	1-16 GeV	6

NICA	10^{27} cm^{-2}s^{-1} (~2020)	Au^{79+} ions	4-12 GeV	7

Table 1. Luminosity and energy of modern and planned accelerators

A charged particle passing through on organic scintillator excites and ionizes its molecules, and free π-electrons are transferred to high-energy states, return of which to the ground state occurs through a singlet or triplet state accompanied by emission of fast (luminescence) or slow (fluorescence) photons. However, the most popular polystyrene (PS) and polyviniltoluene (PVT) scintillators have large self-absorption: therefore, they are usually used as three-component scintillators (Fig. 1a,b). The energy of the excited molecules of the scintillator (base) is transferred to the primary fluor (activator), return of which to the ground state accompanied by emission of light with λ ~ 370 nm. Secondary fluor (shifter) absorbs this light and re-emits it with λ ~ 420 nm or more. Transformation of light wavelength from the short (UV of base) to the long (blue or green of shifter) waves leads to a decrease in the transmission loss of light as the light with shorter λ is absorbed and scattered more intensively than that with longer λ.

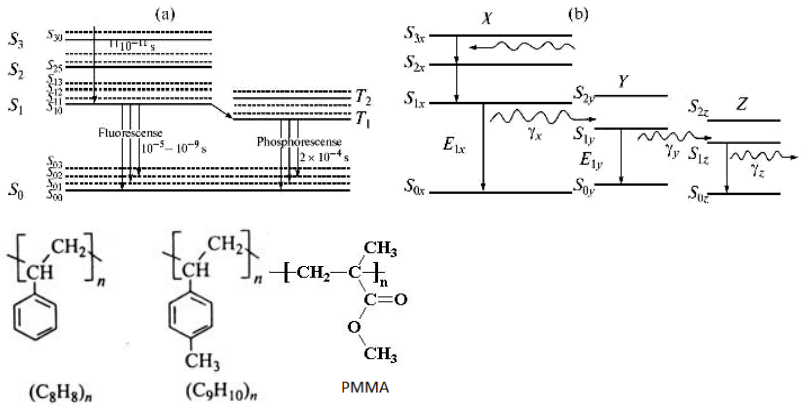

Fig.1. Light emission mechanism in one-component (a) and three-component OPS (b); and molecular structure of PS (c), PVT (d) and PMMA (e) polymers.

The efficiency of light transmission in this chain depends on the shift value between absorption and emission spectra (Stokes shift) of the fluors - the greater the shift, the less in the light transmission. The peak values of

absorption and emission as well as their differences for the most popular fluors compiled from [11] are given in Table 2.

Table 2. Absorption and emission peaks and their differences of some popular flours [11]

Item	Absorption peak, nm	Emission peak, nm	Difference, nm
b-PBD	305	360	55
BDB	360	405/425	45/65
Y7	437/460	490	63/30
3HF	350	530	180
Y11	400	476	76
pTP	290	360	70
POPOP	385	420	35
K27	355	492	37
PPO	310	365	55
Naphthelene	310	325/340	15/30
X25, X31	400	500	100

Under the influence of radiation molecular structures of polymers break down as scission or cross-linking between adjacent chains of the polymers both in the base of the scintillator and fluors occurs [12]. Molecular structures of the most popular PS and PVT scintillators and also PMMA often used in the inner cladding of fibers are shown in Fig.1(c, d, e). Irradiation results in formation of free radicals (color centers) on which the scintillation light is absorbed and scattered, and various gaseous products are released. Radicals are unstable formations that can decay or interact with each other. Damage and recovery of the irradiated scintillators depend on many factors – the materials of the base and the fluors, the absorbed dose and dose rate, irradiating particles, environments [13-15], etc.

During irradiation scintillators lose their transparency and turn yellow or dark brown depending on the absorbed dose. After irradiation bleaching and recovery of irradiated materials occur. Bleaching of PS- and PMMA- based K27 WLS light guides after immediate irradiation by γ rays at 27 kGy and their full annealing in O_2 and air is shown in Figs.2a and 2b [13]. In dry air the bleaching time of the 10.1- mm- thickness SCSN-38 is about 40 hours while that of PMMA is greater than 1 year. Thickness of bleaching zone (z) behaves as $z^2 \sim t$. Such behavior is similar to diffusion of O_2 into materials. Recovery of SCSN-38 proceeds very fast in O_2 (2-3 days) and very slowly in inert gases (> 200 days) (Fig.2c). Radical concentration in PMMA is 60 times larger than in PS, and the

diffusion rate in O_2 is about 10 times larger than in PS [13].

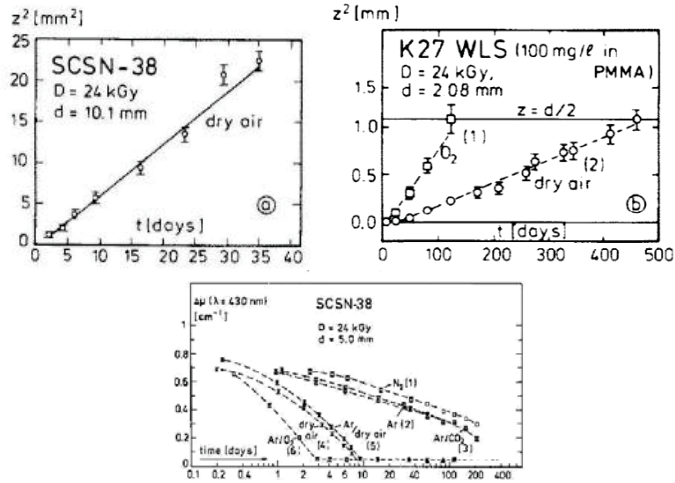

Fig.2. Bleaching of the PS (a) and K27 WLS (b), and recovery of SCSN-38 under different gas atmospheres (c) [13]

Light yield and recovery of the scintillators to a large extent depend on the fluors and are influenced by environments (temperature, presence of O_2). Comprehensive studies were carried out on a large number (~ 30) of fluors irradiated by ^{137}Cs source at doses of 2.3, 10 and 14.3 Mrad [11]. It was shown that primary fluors pTP, PPO, PBD, bPBD show good radiation hardness, and their characteristics do not differ much from one another. Secondary fluors 3HF, M3HF, X25 and X31 are most radiation resistant among many examined ones. Adding naphtaline and increasing its concentration provide higher radiation resistance.

Light yield of pure PS and PS with primary fluors with concentration (0.05% - 2.0) % 3HF and, as a reference, BC-408, two ternary scintillators PS+pTP(1%)+3HF(0.01%) and PS+pTP(1%)+3HF(0.10%) were investigated by ^{60}Co γ-rays at integrated doses of 10 Mrad and 30 Mrad (Fig.3). PS with 3HF concentrations of 1.0%, 0.10%, 0.05% showed 3%, 12%, and 17% light loss respectively for 10 Mrad (minimal light loss is at 1% 3HF). The ternary scintillator PS +1%pTP with 0.01%3HF and 0.10% 3HF concentration showed 17% and 6% light loss respectively for 10 Mrad. Transmittance losses remain small (~12%) even for the 10-cm-thick 3HF scintillator with the 3HF concentration 1% and at 10 Mrad irradiation. The main causes of the LY loss are destructions in the scintillator base but not in the 3HF [14].

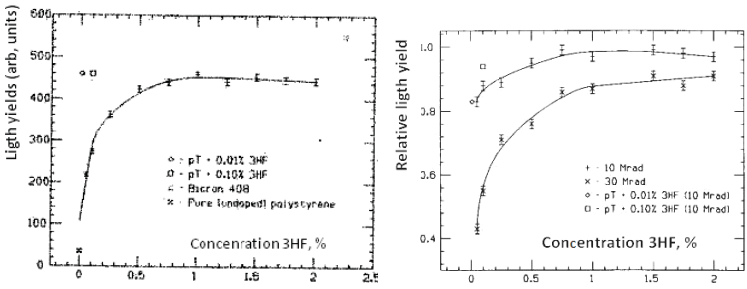

a b

Fig.3. 3HF scintillator light yield as a function of the 3HF concentration (a) and ratio of the light yield measured after 10 Mrad and 30 Mrad exposure and annealing to the initial light yield for the intrinsic 3HF samples (b) [14]

In the frame of upgrade of the ATLAS spectrometer it is planned to replace the scintillators used in the gap region between the barrels of the tile calorimeter. The samples (5x5x3.5) mm^3 of the scintillators made of the different manufacturers (ISMA [17], Protvino [18], Bicron[19], and ELJEN [20]) were investigated at high radiation doses 0.8, 8, 25, and 80 MGy by the 6 MeV protons beam[21]. The samples of ISMA (designated in Table 3 as Dubna) and Protvino are made of PS, and Bicron and ELJEN are made of PVT. It was interest to investigate the transmittances and recovery properties of the various grades of the ELJEN samples (EJ -200, EJ-208, EJ-260), which were no previously used in ATLAS detectors in contrast to the others. The transmission losses of all these samples at a wavelength λ= 420 nm for different doses are presented in the Table 3. Transmission losses of all scintillators were almost identical for the lowest dose (D=0.8 MGy). EJ scintillators have better transmission than the others especially for a high dose of radiation.

Table 3. Transmission losses of all samples at λ= 420 nm for different doses [21]

Sample	Dose (MGy)	% Trans. loss	Sample	Dose (MGy)	% Trans. loss
EJ 200	80	42.9	Protvino	80	60.8
	25	28.6		25	34.8
	8	14		8	7.4
	0.8	3.9		0.8	3.3
EJ 208	80	29.1	Dubna	80	51.3
	25	14.9		25	35.1
	8	4.7		8	26.6
	0.8	2.5		0.8	5.5
EJ 260	80	44.8	Bicron	80	45.5
	25	15.5		25	39.5
	8	14.3		8	11.5
	0.8	6.6		0.8	8.7

Light transmission of all EJ scintillators behaves in a similar way. With increasing doses, their transmission spectra move to longer λ and transmission losses increase (Fig.4a). Significant recovery occurs during 2-3 days (Fig.4b). EJ - 208 is the best one, and in addition the emission peak (435 nm) well matches the absorption peak 430 nm of Y11 used in WLS fibers. At higher doses some structural changes in the base and fluors were observed in Raman spectra [22].

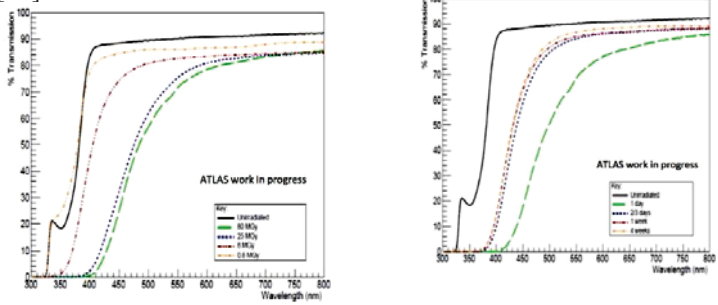

a b

Fig.4. Transmission versus wavelength for EJ-208 for different exposure doses (a) and on different days after irradiation (b) [21]

In the frame of the upgrade of the hadron calorimeter of the CMS spectrometer a search for new scintillators instead of SCSN-81 was performed. The EJ-200, EJ-200 P2, EJ-200 2X, EJ-260 scintillators [20] and SCSN-81 as a reference were irradiated by 150 GeV μ-meson beam at H2 line SPS CERN [23]. The EJ-200 P2 and EJ-200 2X scintillators are two special version of EJ-200

having different types of primary fluors and primary fluors with the concentration twice as high as in EJ-200 respectively. The scintillators under tests have the form of tiles with dimensions 100x100x4mm^3 with a σ-shaped groove on the surface of the plastic in which the WLS fiber was embedded. It was shown that such tiles provide highly uniform light collection from the tile. Integrated charge distribution of the different samples showed that the light output of over-doping EJ-200 2X and green EJ-260 scintillators are less than SCSN-81 (Fig.5a) [23]. Differences of the time signals arriving from SCSN-81 and from different flavors of EJ-200 are roughly centered near at 0 ns whilst EJ-260 signals are slower than those of SCSN-81 by about 5 ns. The investigation of light yield, light collection and signal timing shows that the over-doping the scintillators (EJ-200 2X) and shifting to a longer wavelength (green-emitted EJ-260) are two viable methods for improving radiation hardness.

Structural and optical properties of EJ-200, EJ-208, EJ-260 (ELJEN) and UPS-923A (ISMA) were studied by irradiation them with a neutron beam with E>1 MeV and fluencies (1.2, 3.6, 9.4) x 10^{12} neutrons/cm^2 [24] at IBR-2 JINR[25]. No structural and optical changes were observed in the Raman and the light output spectra (Figs.5b, c).

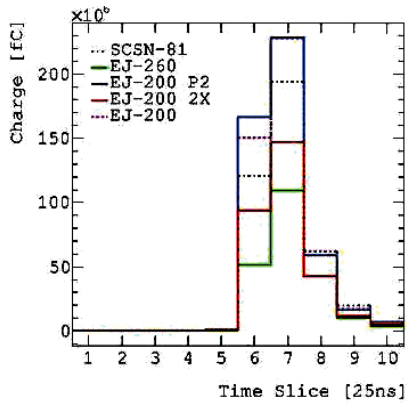

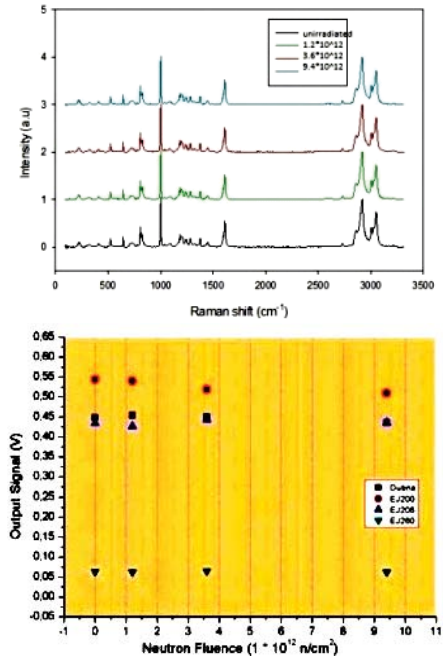

Fig.5. Distribution of the integrated charge per 25 ns time slice in the whole data sample (a) [23], Raman spectra for the EJ200 sample (b), and light yield output spectra versus neutron fluencies for different samples (c) [24].

In modern and future experiments, scintillators not only with higher radiation resistance but also with excellent time characteristics are required. New scintillator materials (custom polyester used in the production of plastic bottles and containers), - Polyethylene Naphthalate (PEN) (100x100x1mm^3, $\lambda_{peak}\approx$ 450 nm) and Polyethylene Terephthalate (PET) (100x100x 2mm^3, $\lambda_{peak}\approx$350nm), were irradiated by ^{137}Cs γ rays at doses of 1.4 Mrad and 14 Mrad. Light yield (Fig. 6), light yield and time recoveries (Table 4) were tested [26]. It was shown that PEN is more radiation hard than PET (factor of 2 for 1.4 Mrad and 3.8 for 14 Mrad). Also, PEN has much shorter recovery time than PET [26].

	Initial Light Yield (%)		Recovered Light Yield (%)		Recovery Time (days)	
	1.4 Mrad	14 Mrad	1.4 Mrad	14 Mrad	1.4 Mrad	14 Mrad
PEN	71.4	46.7	85.9	79.5	5	9
PET	35.0	12.2	93.5	80.0	22	60

Table 4. Summary of the PEN and PET light yield and recovery time results [26]

Recovery tests of PEN and some other materials in the form of tiles (lab-produced elastomer (ES), EJ-260(EJN), and EJ-260(EJ2P)) were performed by using blue LED stimulation after ^{137}Cs γ irradiation at doses of 100 kGy (PEN) and 75 kGy (ES, EJN,EJ2P)[27]. After 40 days, recovery was measured of two samples of each tile, one exposed to RGB LED and other was kept in a dark box. After 7 days PEN tiles recovered to 72% in LED and only to 40% in the dark box. The corresponding values for ES were 56% and 46%. Neither EJN nor EJ2P showed a significant effect due to LED simulation (24% and 26% for LED and dark box respectively). Note that PEN and ES are “blue” scintillators whereas Eljien samples are “green” (Table 5) [27].

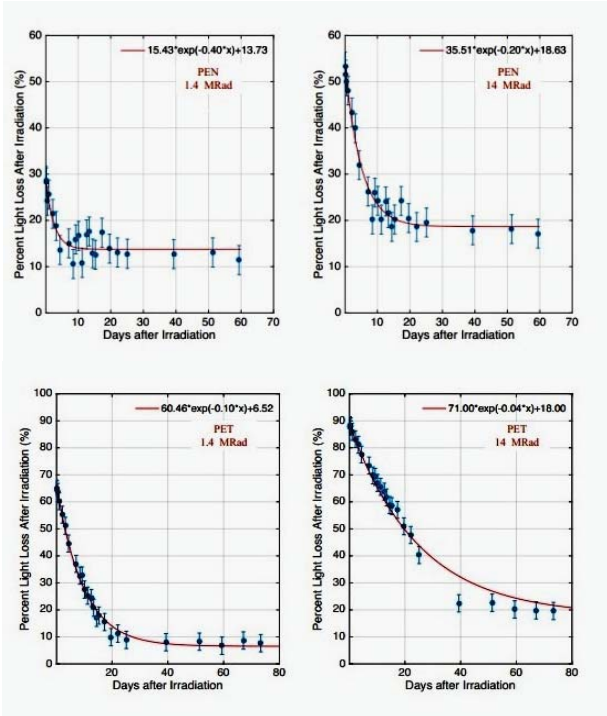

Fig.6. PEN light yield at 1.4 Mrad and 14 Mrad over 50 days after irradiation respectively (a, b) and the same for PET at 1.4 Mrad and 14 Mrad (c, d) [26]

Tile	'*a*', Total recovery	'*c*', Permanent damage	'*b*', Recovery constant ($days^{-1}$)
ES RGB	56.3 ± 2.4%	30.7 ± 1.6%	0.22 ± 0.03
ES dark box	45.7 ± 2.5%	44.1 ± 1.9%	0.18 ± 0.03
EJN RGB	24.0 ± 2.2%	6.92 ± 0.7%	0.64 ± 0.16
EJN dark box	21.1 ± 1.8%	15.9 ± 0.6%	0.50 ± 0.11
EJ2P RGB	26.9 ± 3.1%	15.2 ± 0.9%	0.75 ± 0.22
EJ2P dark box	26.5 ± 2.2%	13.7 ± 0.7%	0.62 ± 0.14

Table 5. Fit parameters of the exponential functions a*exp(-bx) + c used for decribining the recovery of the tiles where 'a' is the difference between the initial and permanent damage, 'b' is the recovery constant, and 'c' is the permanent damage[27]

Radiation damage depends not only on the dose, but also on the dose rate. Detailed studies were carried out on the scintillators SCSN-38, SCSN-81 and Bicron 499-35 irradiated with dose rates of 2.3 krad/h - 1.05 Mrad/h and absorbed dose of 10 Mrad [28]. The final light output (LO) of all samples versus of dose rate shows the semi-logarithmic behavior. LO significantly decreases with decreasing dose rate. On the immediate LO curves of all samples one can see the convergence points. Above that points when the dose rate decreases, the immediate LO can either increase (SCSN-38), or stay constant (SCSN-81), or decrease (BC-499-35) (Fig.7). Such behavior depends on the O_2 permeability, chain mobility of the scintillators and glass transition temperatures.

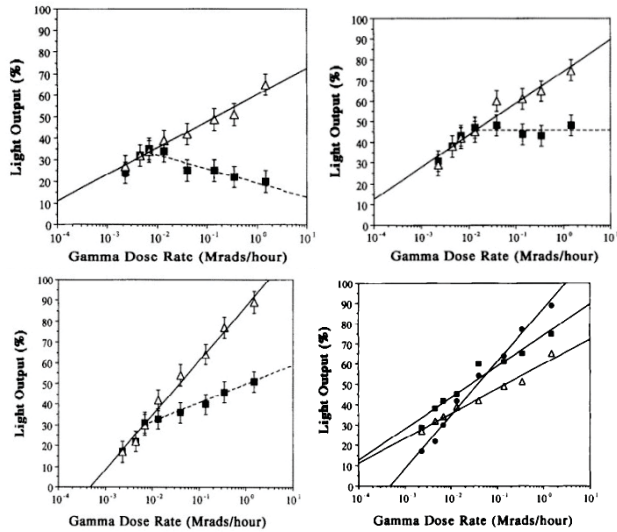

Fig.7. Immediate (triangle) and final (squares) LO of SCSN-38 (a), SCSN-81 (b), BC-499-35 (c) and their final LO after seven days of recovery (d) versus dose rate. Final LO of all scintillators in Fig. 7d are denoted by triangles (SCSN-38), black squares (SCSN-81), and circles (BC-499-35) [28].

Light output of SCSN-81 were investigated by ^{60}Co γ rays at very low dose rates of 10^{-4} -0.1 krad/h and dose D = 0.01-0.2 Mrad (Fig.8) [29]. The results were compared with that measured at a high dose rate of 14 krad/h [28]. Light loss in CMS scintillators as a function of dose rate is obeys the power law

as predicted by the diffusion of O_2 into scintillator. The measured light loss is in reasonable agreement with the results from γ irradiation [28]. Light loss at low dose rates is larger than at high dose rate.

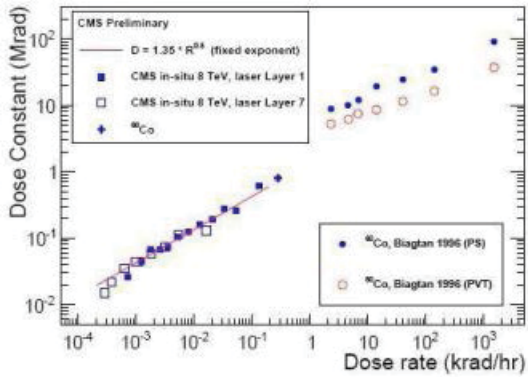

Fig. 8. Exponential constant as a function of the dose rate. Results from scintillators based on PS are shown in blue, while those based on PVT are shown in red. Results from the scintillators in layer 1 (7) of the CMS HE detector are denoted by filled squares (open squares)[29].

Investigation of radiation hardness of the scintillators irradiated with neutrons is very important since in the electromagnetic and hadron calorimeters of the modern accelerators, as well as in some of their other parts, neutrons are produced in large quantities. For example, in the most radiation-loaded parts on the LHC, more than 10^{15} neutrons / cm^2 per are expected for 10 years [4].

Investigations were carried out on pure PS, SCSN38 and pure PMMA using fast neutrons produced in the reaction $^{9}Be(d,n)^{10}B$ (with low gamma background) at the PTV cyclotron (Germany) and neutrons from the reactor (Belgium) [30]. It was shown that neutrons produced about 5 times more radiation damage in PS and SCSN38 than γ rays (Fig.9a). This effect is explained by the fact that in Polystyrene, the protons produced during the elastic scattering of the fast neutrons on them, have much larger interaction cross sections than gamma quanta. On the contrary, in PMMA γ-rays produce ~1.5 times more damage than neutrons (Fig.9b).

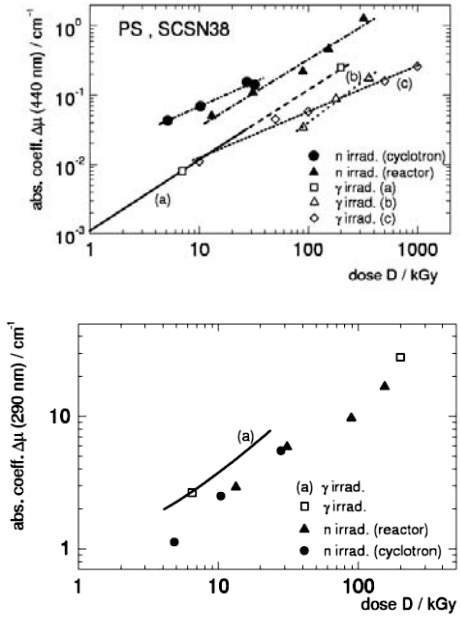

Fig.9. Compilation of radiation-induced permanent optical absorption coefficients at 440 nm for PS and SCSN38 (a) and the same at 290 nm for PMMA (b) [30].

The possibility of increasing light yield and radiation hardness of the scintillators was shown by "fingering" of a tile [31]. The tile of 100x100x4 mm^3 and 16 strips of 6x100x4 mm^3 were irradiated by electrons of ^{90}Sr ($E_e \approx 4$ MeV) for D=0.5, 1, 5, 10 and 30 Mrad (Minsk Belarus). Light yields of 16 "fingered" strips were summarized and compared with light yield of the tile. The positive effect achieved in LY was about 40% for k=0.8 (k is the transmission loss coefficient of light collection in the optical "OR" coupler used). Radiation hardness was increased up to 20 Mrad (Fig. 10a).

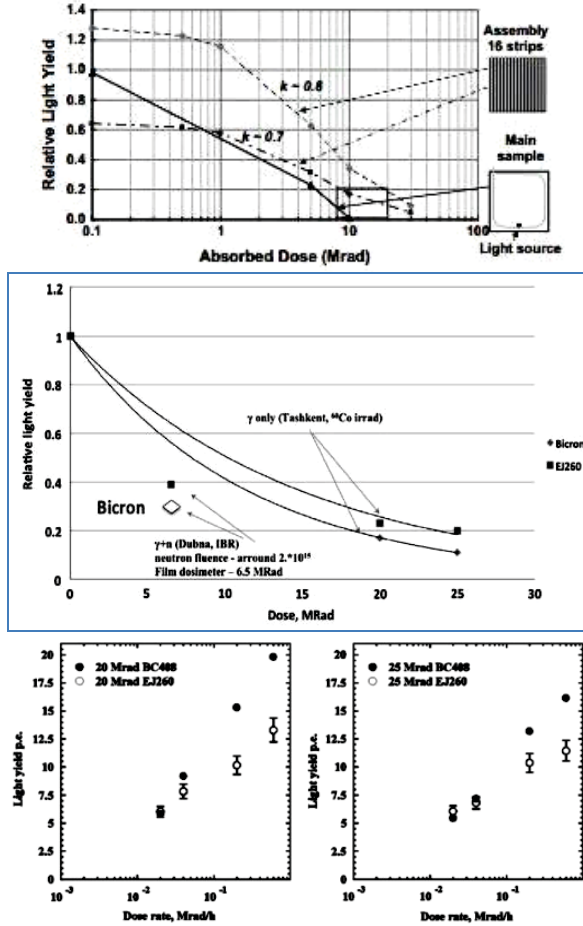

Fig.10. The calculated relative light yields from different samples based on measurements (a) [31]. Comparison of the experimental data from the gamma-neutron exposure (IBR-2 JINR) and γ rays exposure (^{60}Co, Tashkent) (b). Light yield from the strips irradiated with up to 20 Mrad (c) and 25 Mrad (d) at different dose rates [29].

Relative LY of the "fingered" BC-408 and EJ-260 irradiated with neutrons from IBR-2 (JINR) [25] and ^{60}Co γ rays (Tashkent) was measured [32]. The fluence of the neutrons and the mean energy of the γ rays were $3x10^{15}$ n/cm^2 and <Eγ>~1.5-2 MeV respectively. The dose rate was changed to 500 krad/h. At

the same dose neutrons have a larger impact on the light yield than γ rays (Fig.10b). LY from the strips irradiated by ^{60}Co γ rays at 20 Mrad and 25 Mrad shows that light loss at lower dose rates is greater than at high dose rates (Fig. 10c, d).

Scintillating fibers (SciFi) are used in the most radiation-loaded areas of accelerates for measuring in luminosity (ALFA at LHC [33]), for tracking (D0 [34], LHCb [35,36]), and for beam hodoscopes (COMPASS [37], MUSE [38]) etc.

The SciFi hodoscope for COMPASS comprising 3 layers of 1mm SCSF-78MJ (Fig. 11a) was used in the intensive (100-200) GeV/c muon beam of 10^8 muons/s (10^6 muons/s for fiber channel). The hodoscope allowed collecting up to 20 photoelectrons per pixel of the multi-anode H6568 photo detector and provided excellent space and time resolution (400 ps). The light output losses in the 8 mm of the fiber portion irradiated by electrons from ^{90}Sr with a dose of 100 kGy were no more than 15% (Fig.11b). To efficiently transport light from the SciFi fiber to the photo-detector the fiber was connected to the clear fiber by melting their ends at a temperature of 105^0C-110^0C. Such connected fibers allowed to transmit light with loss less than 10% [37].

The SciFi Tracker of LHCb at the High Luminosity Colllider was proposed instead of gas straw tubes and silicon microstrip detectors. It is composed of mats of six densely packed fibers layers with dimensions 131x2424x1.4 mm^3 [35, 36]. The tracker will cover total area of the detector 340 m^2 and made of 250-μm-diameter 2.4-m-long SCSF-78MJ fibers on the basis of PS+pTP+tetra butadiene. These fibers have longer L_{att}, more LY and fast scintillation time. It allows significantly minimizing the material budget and achieving the efficiency of ~99%, and space resolution of 70 μm. Irradiation of the detector shows that the reduction in SciFi L_{att} as a function of the accumulated dose for different particles (protons, γ rays, X rays) and for D=35 kGy may be estimated at a level of 40% (for 10 years of irradiation).

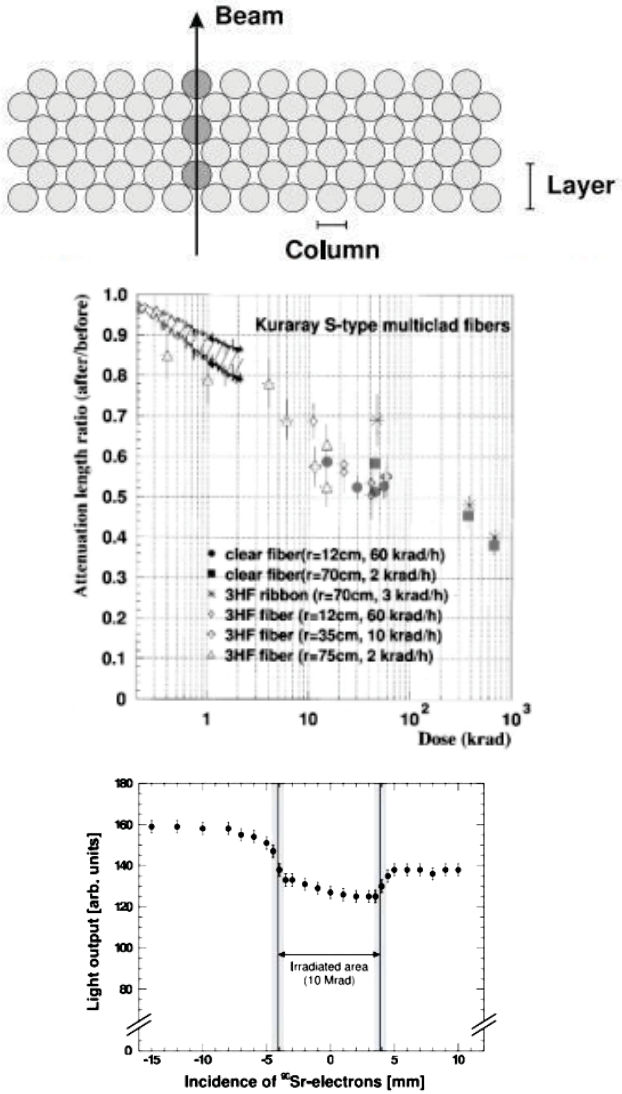

Fig.11. Fiber configuration for the scintillating fiber hodoscope with 3 layers of fibers (a) and light output of Kuraray SCSF-78MJ SciFi after local irradiation at 10Mrad (b) [37], and the ratio of the attenuation lengths of 3HF and clear fibers after /before irradiation (c) where data of 3HF fibers, 3HF fiber ribbons and clear fibers are denoted by open symbols, crosses and filled marks respectively [39].

Radiation hardness and mechanical durability of Kuraray Scintillating 3HF and clear S-type fibers were tested by ^{60}Co γ rays at D=0.4 – 500 krad [39]. It was shown that the ratio of the L_{att} after/ before irradiation is similar for both CF and 3HF fibers as a function of the dose for different dose rates and fiber curvature (Fig.11c). Recovery 3HF fibers is rather insensitive to the dose rates 2-12 krad/h and accumiulated dose 6-48 krad. L_{att} as well as LY decrease with increasing S-parameter. For example, LY(S40) is 30% greater than LY(S70).

A new class of scintillating fibres with Nanostructured Organosilicon Luminofores (NOL) has been developed at the Enikolopov Institute of Synthetic Polymer Materials, Moscow [40, 41]. Unlike the case in traditional plastic scintillators, where molecules of activators and wavelength-shifting fluors are independently and randomly distributed in the PS matrix, in the new scintillator they are connected via "bridges" of silicon nanoparticles (Fig.12). The close geometric correlation of the activator and the WLS complexes is expected to reduce the losses of UV photons and to increase the overall efficiency of the conversion process by non-radiative energy transfer (Forster transfer).

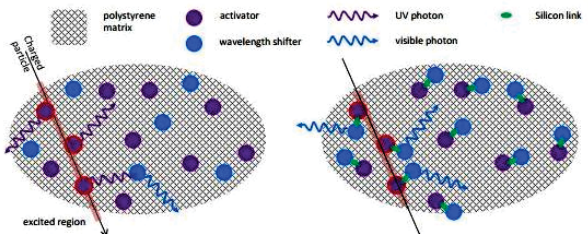

Fig.12. Simplified principle of light yield increase in NOL fibers - conventional plastic scintillator (left) and NOL scintillator (right) [35]

Absorption and luminescence spectra of the NOL11 and NOL19 used in the production 250 μm diameter BPF-11 and GPF-19 fibers are given in the Figs.13. LY of NOL11 and NOL19 is ~3 times larger than that of POPOP. The NOL11 (NOL19) emits light in the blue (green) region with the photoluminescence quantum yield of 96% (87%) and decay time of 0.98 ns (0.93ns). Decay time of the green GPS-19-1 is ~ 6 times shorter than that of the SCSF-3HF and of the blue BPF-19-1 fiber is ~2 times shorter than that of SCSF-78 (Table 6). NOL fibers may be atractive option for the LHCb SciFi tracker.

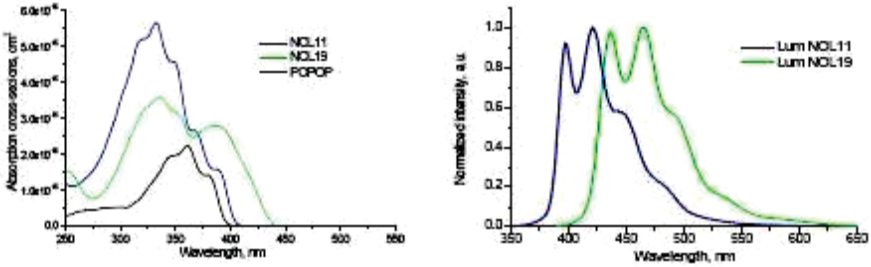

Fig.13. Absorption spectra of NOL11, NOL19, POPOP (left) and luminescence spectra of NOL11, NOL19 (right).

Table6. Peak wavelength, attenuation length, light yield and decay time of different fibers [41]

Fibre type	λ_{peak} [nm]	Λ [cm]	LY [p.e./mm]	τ [ns]
BPF-11-1	430	263	23.2	1.34
GPF-19-1	470	294	14.2	1.18
SCSF-78	440	351	27.8	2.36
SCSF-3HF	530	330	23.6	6.18

Radiation hardness of the GPS-19-1 and BPF-19-1 fibers after X-rays irradiation with dose of 1 kGy and dose rate of 23 Gy/min is about the same as that of the SCSF-3HF and SCSF-78 fibers, but further testing of the fibers with other particles is required.

Wave-length shifting (WLS) fiber collect the light from the scintillator, convert its wavelength so that it matches to the spectral sensitivity of the popular photo-detectors and transfer it to the latter. WLS fibers are mostly used as active elements in the calorimeters, TOF and veto-systems, etc. The effect of radiation on the fiber is manifested in deterioration of its light output and transmission, and it depends on its material, absorbed dose, dose rate, and environment.

Light yield of 1mm WLS fibers BCF91A-MC (Bicron), Y11(200)MSJ (Kuraray) and S250-100 (Pol.Hi.Tech.) was compared under their irradiation by ^{60}Co γ rays at the doses of D=1.16 kGy and 6.93 kGy [42]. Kuraray fibers have

the best LY and L_{att}. Immediate relative light losses are 17(46)% (BCF91A), 13(29)% (Kuraray) and 40(48)% (Pol-Hi.Tech) at D=1.16(6.93) kGy. After 10 days the recovery in the light output of Bicron and Kuraray fibers is a few percent at both doses but the recovery of Pol.Hi.Tech.is much larger (Table 7).

Table7. Relative light output at x=140 cm and for total doses of 1.16 and 6.93 kGy [42]

Fiber type	$\frac{R(140)}{R(30)}$ for 1.16 kGy			$\frac{R(140)}{R(30)}$ for 6.93 kGy		
	0 days	1 day	10 days	0 days	1 day	10 days
BCF91A MC	0.83	0.86	0.85	0.54	0.56	0.56
Y11(200)MSJ	0.87	0.92	0.91	0.71	0.72	0.74
S250-100	0.60	0.70	0.81	0.52	0.55	0.64

Radiation hardness of the BC9929 WLS fiber and the BC404 scintillator with WLS fiber embedded in it was investigated [43]. BC9929 WLS fibers were irradiated by ^{60}Co γ rays at the doses D=50,100,200,300,650 krad and 1 Mrad using 7 krad/min dose rate, and the scintillator + WLS fiber was irradiated with D=200 krad and dose rate of 4.4 krad/min.

The WLS fiber was recovered a hundred times faster than that of the scintillator + WLS fiber system (Fig. 14 a, b). In the latter 80% permanent level was reached after 300h (Fig. 14a). At the doses D=1 Mrad and 650 krad the permanent level of the BC9929 WLS is 50(70) % and its recovery time increases significantly at these doses (Fig.14 c).

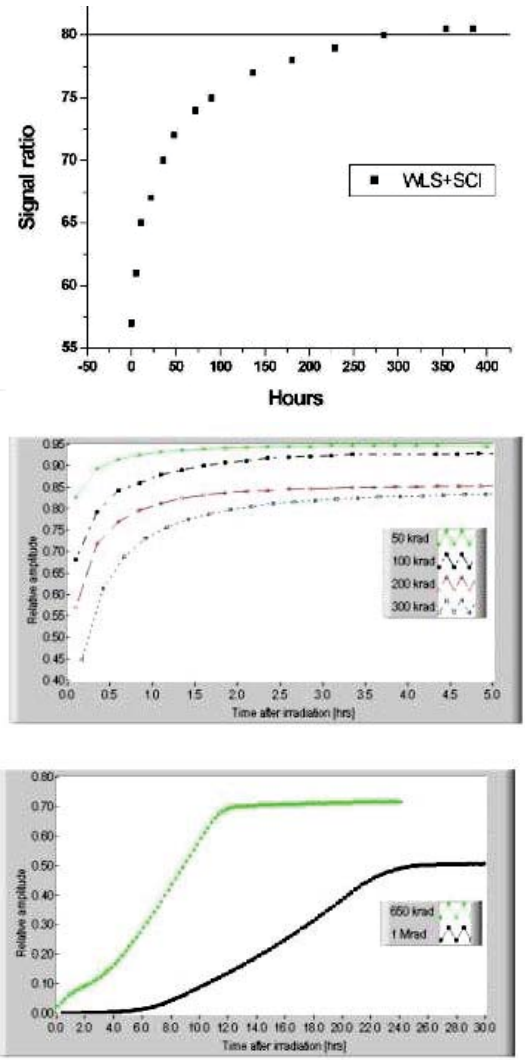

Fig.14. Relative PMT signal amplitude of post-irradiated to pre-irradiated scintillator +WLS for dose 200 krad (a) and WLS fibers for doses 50 krad, 100 krad; 200 krad, 300 krad (b), and 650 krad and 1 Mrad (c). The horizontal axis shows the time elapsed from the end of the irradiation [43].

Optical glues

Light collection from tiles or strips is usually carried out by WLS fibers inserted into the groove on the surface of the tile or strip and the hole in the strip filled with air ("dry" case). However, gluing the WLS fiber into the groove by some high transparent optical fillers increases the light collection by a factor of up to 1.8 [44] and 1.6 [45] against the "dry" case. High transparent optical glues on the epoxy base (EJ-500, Aqua E-300, BC-600, and Araldite Crystal) are often used as filler in the groove of tiles or strips. The transmission of these unirradiated glues is more than 90% in the visible region [46].

The high-transparency (T>95% for λ>400nm) and high-viscosity (10 - 20 Pa*s) low molecular weight synthetic resin SKTN-MED(E) [47] as a filler in the hole of the strip (up to 5m long) have been studied [48]. It was demonstrated that this filler increases the light collection by a factor of 1.5 -1.9 in comparision with "dry" case depending on the strips length, and presence (absence) reflective coating at the end of the strip [48]. As the filler has high viscosity a special technique for injection it into the small hole (2.6 mm) of a long strip (with length up to 5m) was developed and realized. It is of great interest to study radiation hardness of the optical glues used as fillers. The radiation resistance of the SKTN-MED (grades E and D) and BC-600 [49] under irradiation by the fast neutron beam (E>1 MeV) with fluencies $16x10^{14}$, $3.8x10^{14}$ and $1.2x10^{14}$n/cm^2 were tested at IBR-2 (JINR) [50]. Transmittance of these fillers in the form of resin (liquid) and glue (polymerized resin), and short strips with the WLS fiber and with/without filler in it were measured.

Transmittance of the SKTN-MED(D) and SKTN-MED(E) as well as their resins and glues did not differ from each other and was > 90% for λ>400 nm after the irradiation by a neutron beam with the fluencies of $3.8x10^{14}$ and $1.2x10^{14}$ n/cm^2, and the transmittance of the irradiated and non-irradiated samples is almost the same (Fig. 17a and b) [50].

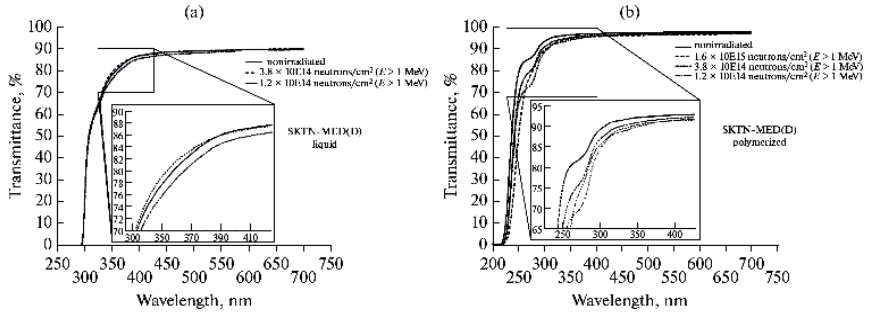

Fig.17. Light transmittance of the resin (liquid (a) and polymerized SKTN-MED(D) (b) before and after irradiation as a function of the wavelength for different neutrons fluencies and E>1 MeV [50].

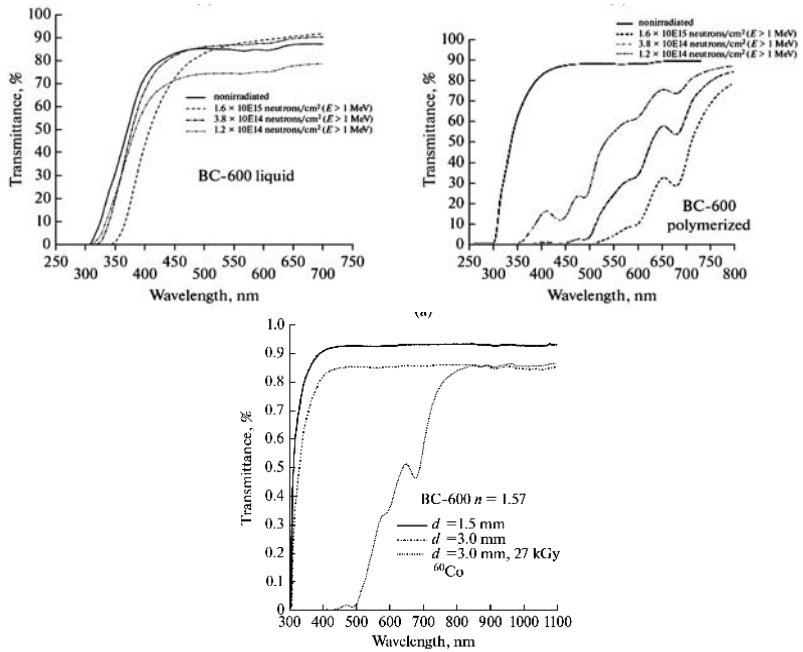

Fig.18. Light transmittance of the resin (a) and polymerized BC-600(b) as a function of the wavelength for different neutron fluencies [43], and of polymerized BC-600 irradiated by γ rays of ^{60}Co at the dose 27 kGy as a function of wavelength (c) [51]

Transmittance of the BC-600 resin as well as its glue is very sensitive to the impact of the neutron beam and wherein BC-600 glue is more sensitive to radiation than its resin (Fig. 18a and b). Similar behavior in the transmittance of BC-600 glue irradiated by γ rays of ^{60}Co at the dose 27 kGy was also observed [51].

Photos of nonirradiated sheets and strips and those irradiated with different neutron fluencies are shown in the (Fig.19). Large changes in transparency are observed in the BC-600 samples (Fig. 19a) whereas in SKTN-MED (D) samples changes are practically not visible (Fig.19b). Noticeable changes are visible in the transparency of irradiated PS strips in comparision of non-irradiated PS strip as neutron fluencies increase (c).

Fig.19. Photos of the SKTN-MED(D) (a) and BC-600 (b) sheets irradiated by the neutron beam with fluencies of $16x10^{14}$ n/cm^2 (samples 1) $3.8x10^{14}$ n/cm^2 (samples 2) and $1.2x10^{14}$ n/cm^2 (samples 3). Samples 0 were not irradiated. Photo of the non-irradiated and irradiated strips (c). The nonirradiated strip is located in the lowest position, followed clockwise by three other strips irradiated by the neutron beam with fluencies of $1.2x10^{14}$, $3.8x10^{14}$ and $16x10^{14}$ n/cm^2 respectively (c).

Radiation influence of different neutron beam on the LY was investigated on the short (15 cm long) strips with the WLS fiber in the hole filled with the various fillers. The measured anode currents of the irradiated strips decreases with increasing neutron fluencies. Decrease in LY is mainly caused by destructions in the strip and fiber but not in the filler, since the transparency of SKTN-MED fillers did not change significantly (see also photo of the irradiated strip) (Fig.19c).

Conclusions.

According to the results of the previous investigations carried out at doses below 1 MGy (predominantly up to 100 kGy) ("old" studies) and during last years ("recent" studies) some conclusions can be drawn:

Part 1 ("old'' studies)

1. Radiation damage of OPS and fibers increases with decreasing dose rates at the same dose.
2. Radiation damage induced in PS by the neutrons is 5 times higher than that by γ rays and vice versa in PMMA.
3. Radiation damage in OPS is mainly due to the destructions of their base and not of the fluors.
4. The position and shape of the emission peak remain unchanged.
5. Recovery of OPS in O_2 much faster than in inert gases while PMMA recovers faster in inert gases than in O_2.
6. The attenuation length of "clear" fibers decreases with increasing parameter S (alignment of base moleculars along the fiber axis).
7. Fibers recover much faster than the system of a scintillator and fiber in it.

Part 2 ("recent" studies)

1. At higher doses (>25 MGy) PVT scintillators (ELJEN) are more radiation hard than BC (Bicron) and PS.
2. Radiation hardness of scintillators can be increased by using fluors with the emission spectrum shifted to the green region.
3. The fibers based on the new type of luminophores NOL11 and NOL 19 (Nanostructured Organosilicon Luminophores) have a high photoluminescene quantum yield and very short decay times of 1.34 ns and 1.18 ns respectively.
4. The new PEN (Polyethelene Naphthalat) scintillator exhibits both good radiation hardness and very short recovery time, being also very inexpensive.
5. Recovery characterictics of PEN and elastomer scintillator (p-terphenil in epoxy) are significantly improved by LED stimulation with the blue emission spectrum.

6. Segmentation of tiles into strips (“finger” strips) provides an increase in the LY and the radiation hardness
7. Deterioration of the LY and transmittance of the scintillator caused by irradiation can be significantly compensated by the synthetic low-molecular weight resin SKTN-MED embedded between the scintillator and the fiber.
8. Along its good optical properties, the SKTN-MED showed high radiation hardness when irradiated by a neutron beam with fluencies up to $1.6x10^{15}n/cm^2$.

Acknowledgements

I am very grateful to V.V Glagolev and Yu.I. Davydov for their attention and support in carrying out this work and M.I. Potapov for language editing and proofreading.

References

1. *Birks J. B.,* The Theory and Practice of Scintillation Counting (Pergamon Press, London, 1964)
2. *Ruchti R. C,* “The use of scintillating fibers for charged particle tracking,” Ann. Rev. Nucl. Part. Sci.46. 281–319 (1996)
3. *Kharzheev Yu.N.* Scintillation Counters in Modern High-Energy Physics Experiments// Physics of Particles and Nuclei 2015 vol. 46. No. 4, p.678-728. *Kharzheev Yu.* Scintillation Detectors in Modern High Energy Physics Experiments and Prospect of Their use in Future Experiments// Journal of Lasers, Optics & Photonics 2017, V.4. issue1. P.1000148
4. LHC Mashine, 2008, JINST 3 S08001
5. Zimmermann Frank, First FCC Physics Workshop, CERN, 16-20 January 2017
6. https://www.gsi.de/forschung_beschleuniger/fair.htm
7. Kekelidze V.D. et.al. (NICA Collaboration) Design and Construction of Nucleon-based Ion Collider facility (NICA) Conceptual Design Report (pttp://nica.jinr.ru)
8. ATLAS Collab., “The ATLAS experiment at the CERN Large Hadron Collider,” J. Instrum. 2008. V. 3. P. S08003
9. CMS Collab., “The CMS experiment at the CERN Large Hadron Collider,” J. Instrum. 2008. V. 3. P. S08004
10. LHCb Collab., “The Large Hadron Collider beauty experiment at the CERN Large Hadron Collider,” J. Instrum. 2008. V. 3. P. S08005.
11. Britvich G.I., Peresypkin A.I., Rykalin V.I., Vasil'chenko V.G., Kornylovskaya L.D., Malinovskaya S.A. Skripkina V.T., Shershukov V.M., Yushko,E.G., Kulichenko A.V., Pyshchev A.I. Radiation damage studies on polystyrene-based scintillators// Nucl.Instr.Meth. A.1993.V.326. P. 483-488.
12.Wood R.J., Pikaev A.K., Science 1994

13. Wick K., Paul D., Schröder P., Stieber V. and Bicken B. Recovery and dose rate dependence of radiation damage in scintillators, wavelength shifters and light guiders// Nucl. Instr. Meth. B. 1991. V. 61. P. 472-486
14. *Bross A. D., Pla-Dalmau A.* Radiation effects in intrinsic 3HF scintillator// Nucl. Instr. Meth. A. 1993. V.327. P. 337- 345
15. *Zorn C. A.* Pedestrian Guide to Radiation Damage in Plastic Scintillators// Nuclear Physics (Proc.Suppl.) 32(1993) 377-383.
16. *Emanuel N. and Buchachenko A.* Chemical Physics of Polymer Degradation and Stabilization, VNU Science Press (1987).
17. ISMA (Institute for Scintillation Materials), Kharkov, Ukraine,www.isma.kharkov.ua/eng/
18. *Rykalin Vladimir, Brekhovskikh Valery, Chernichenko Sergey, GorinAlexandre and Semenov Vitaliy*, Development of the Polystyrene Scintillator Technology and Particle Detectors on Their Base//Jour. of Phys. Sci. and Applications 5(2015)6-13
19. Bicron Corp., 12345 Kisman Rd. Newbury ON 440 USA
20. http://www.eljentechnology.com/
21. *Liao S.* et.al. A comparative study of the radiation hardness of plastic scintillators for the upgrade of the Tile Calorimeter of the ATLAS detector// Journal of Physics: Conference Series 645(2015)012021
22. Jivan H, et. al. Radiation damage effects on the optical properties of plastic scintillators// Nucl. Instr. Meth. B. 2017. V. 409. P. 224-228
23. The CMS HCAL collaboration//Brightness and uniformity measurements of plastic scintillator tiles at the CERN H2 test beam// J. Instrum. 2018. V. 13. P 0100210004
24. *Mdhluli J.E.* et.al. High fluence neutron radiation of plastic scintillators for the TileCal of the ATLAS detector// High Energy Particle Physics Workshop 2017 IOP Publishing IOP Conf. Series: Journal of Physics: Conf. Series 889(2017) 012009
25. *Bulavin M., Cheplakov A., Kukhtin V., Kulagin E., Kulikov S., Shabalin E.A., Verkhoglyadov A*. Irradiation facility at the IBR-2 reactor for investigation of material radiation hardness// Nucl. Instr. Meth. B. 2015. V. 343. P. 26-29.
26. Tiras Emrah, Wetzel James , Bilki Burak, Winn David, Onel Yasar Development of Radiation Hard Scintillators// arXiv: Jame1611.05228v1 [physics.ins-det] 16 Nov 2016
27. Wetzel J, et.al. Using LEDs to stimulate the recovery of radiation damage to plastic scintillators// Nucl. Instr. Meth. B. 2017. V. 395. P. 13-16
28. Biagtan E. et.al. Effect of gamma radiation dose rate on the light output of commercial polymer scintillators// Nucl. Instr. Meth. B. 93. 1994. P. 296-301
29. Khachatryan V. et.al. Dose rate effects in the radiation damage of the plastic scintillators of the CMS hadron endcup calorimeter//J. Instrum. 2016. V. 11. P. T10004

30. *Bodmann B., Holm U.* Neutron-Irradiated plastic scintillators // Nucl.Instr.Meth. B. 2000.V. 185. P.299-304.
31. *Afanasiev S.V. de Barbaro P. , Golutvin I.A. , Emeliantchik I.F. Malakhov A.I. , Moisenz P.V. , Smirnov V.A., Shumeiko N.M.,* Improvement of radiation hardness of the sampling calorimeters based on plastic scintillators// Nucl.Instr.Meth. A. 2013. V. 717. P. 11-13
32. *Afanasiev S.V.* et.al. Light yield measurements of"finger"structured and unstructured scintillators after gamma and neutron irradiation// Nucl. Instr. Meth. A. 2016. V. 818. P. 26–31
33. *Ask S.* et.al. The ATLAS Collaboration, Luminosity measurement at ATLAS – Development, construction and test of scintillating fibre prototype detectors// Nucl.Instr.Meth. A. 2006. V.568. P.588-600
34. *Abazov V.M.* et.al. (D0 Collab.) Upgraded D0 Detector// Nucl.Instr.Meth. A. 2006. V.565. P.463-532
35. *Joram C., Haefeli G., Leverington B.* Scintillating Fibre Tracking at High Luminosity Colliders// J. Instrum. 2015. V. 10. P. CO8005
36. *Hopchev P*., SciFi: A Large Scintillating Fibre Tracker for LHCb// arXiv:1710.08325v1 [physics.ins-det] 23 Oct 2017
37.*Bislinghoff J.* et.al. A scintillating fibre hodoscope for high rate applications// Nucl.Instr.Meth. A.2002. V. 490. P. 101-111
38. *Erez O. Cohen, Eli Piasetzky, Yair Shamai, Nikolay Pilip*. Development of a scintillating-fiber beam detector for the MUSE experiment// Nucl.Instr.Meth. A. 2016. V. 815. P. 75-82
39. *Hara K., Hata K., Kim S., Mishina M., Sano M., Seiya Y., Takikawa K., Tanaka M., Yasuoka K.* Radiation hardness and mechanical durability of Kuraray optical fibers //Nucl. Instr. Meth. A. 1998. V. 411. P. 31 – 40.
40. *Ponomarenko S.A*. et al. Nanostructured organosilicon luminophores and their
application in highly efficient plastic scintillators, Sci. Rep. **4** (2014) 6549.
41.*Borshchev O., Cavalcante A.B.R., Gavardi L., Gruber L.C., Joram C., Ponomarenko S. Shinji O., Surin N.* Development of a New Class of Scintillating Fibres with Very Short Decay Time and High Light Yield //J. Instrum. 2017. V. 12. P05013
42. *Varanda M.J., David M., Gomes A., Maio A.* Recent results of radiation hardness tests of WLS fibers for the ATLAS Tilecal hadronic calorimeters //Nucl.Instr.Meth. A. 2000. V. 453. P. 255-258
43. *Alfaro R., Cruz E., Martinez M. I., Montaño L. M., Paic G. and Sandoval A.* Radiation hardness Tests of a Scintillation Detector with Wavelength shifting Fiber readout // Particles and Fields, Part A: X Mexicon Workshop on Particles and Fields, 2006
44. *Michael D.G., Trevor J., Sousa A., Jensen D., Becker BR.*, et al. The magnetized steel and scintillator calorimeters of the MINOS experiment. Nucl. Instrum. Meth. A. 2008. V. 596. P.190-228.

45. *Britvich G.I., Brekhovskikh V.V., Semenov V.K., Kholodenko S.S.* The main characteristics of polystyrene scintillators produced at the Institute of High-Energy Physics and detectors of their basis// Instruments and Experimental Techniques 2015. T. 58. No.2. P.211-230
46. *Noak Etan, Schneider Thomas* Aida Optical Glue Transmission Tests// CERN Fevr.20, 2013
47. Research and production enterprise SYREL, Russia, CKTN-MED Low molecular-weight rubber, http://www.surel.ru/silicone/77/.
48. *Artikov A., Baranov V., Budagov Yu., Chokheli D., Davydov Yu., Glagolev V., Kharzheev Yu*.,* et al. Optimization of the light yield by injecting an optical filler into the co-extruded hole of the plastic scintillation bar// J. Instrum. 2016. V.11. T05003
49. Bicron Corp., USA, BC-600, Optical Cement, http://www.crystals.saintgobain.com/.../sgc-bc600-data-sheet_69724.pdf
50. *Artikov A., Baranov V., Budagov Yu., Bulavin M., Chokheli D., Davydov Yu.I., Glagolev V., Kharzheev Yu., Kolomoets V., Simonenko A., Usubov Z., Vasiljev I.* Light yield and radiation hardness studies of scintillator strips with a filler // arXiv:1711.11393v1 [physics.ins-det] 30 Nov 2017 (to be published in NIM A)
51. *Kirn Th., Haring M., Schmitz D., Schulz W.*, Absorption length, radiation hardness and ageing of different optical glues //CMS NOTE 1999/003, p.1-6.

The Precision Laser Inclinometer, method of data processing and data storage

I. Bednyakov
JINR
Corresponding Author: bednyakovi@gmail.com

1.Introduction

One of the major parameters of any collider is luminosity. As we know luminosity is affected by many factors. Among them, the least explore: the effect of the oscillation of Earth's surface on the position of beams. This oscillations can have a different origin: industrial noises, oscillations of seismic origin, etc. These oscillations reduce the luminosity in collision area. This effect is expected to be especially noticeable in case of e+ e- colliders, where beam diameters at the meeting point are especially small. The same significant reduction in luminosity may be in future multi-Tev accelerators , like FCC(Future Circular Collider).This research under ATLAS program and the HL LHC project[1]

The Precision Laser Inclinometer (PLI) – a instrument for recording micro-seismic activity of the earth with nano-radian accuracy, developed at the Dzhelepov Laboratory of Nuclear Problems(DLNP) at Joint Institute for Nuclear Research (JINR). Today JINR has manufactured 6 PLI for European Organization for Nuclear Research (CERN), which will be deployed at the Large Hadron Collider(LHC) stop period. This 6 PLI will be deployed full length LHC. Existing software for PLI allow work correct one PLI as unique instrument. For 6 PLI create network is needed, this network allow us to monitor and synchronize all the instruments included at network. Also necessary to provide data corresponding to CALS (CERN Accelerators Logging Service).

At this article discusses software that provides automated data collection and processing. And method for processing and data storage, which makes possible to become part of the CERN computing services .

2. Software and PLI data description:

Currently, data from PLI are processed on computer under Windows operation system, and using LabView[2]. LabView using official drivers for a 24-bit Analog-to-Digital Converter(ADC), this ADC collect information from photodiodes. Figure 1 shows the scheme of photodiodes

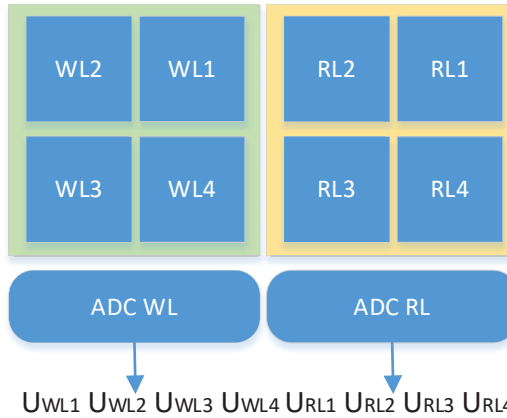

Fig.1. The scheme of photodiodes

The PLI instrument uses 2 photodiodes, which are divided into 4 sectors. The ADC transmits the voltage value from the photodiodes. Two designations for photodiodes are introduced: “WL” (Wanted / Liquid) and “RP” (Reference / Prism). WL – registers the useful signal of the inclinometer reflected from the surface of the liquid. RP – the reference signal of the beam reflected from the prism to compensate for the noises of the laser source.

The PLI data in file introduced below. Time in UTC format, and 8 voltage values from quadrant photodetectors. The general structure of the file looks like:

Time(UTC)	Wl1	Wl2	Wl3	Wl4	Rl1	Rl2	Rl3	Rl4

To calculate the coordinates of the displacement the laser rays can be calculated with formulas:

XWL = (UWL1 + UWL4) – (UWL2 + UWL3)
YWL = (UWL1 + UWL2) – (UWL3 + UWL4)
XRP = (URP1 + URP4) – (URP2 + URP3)
YRP = (URP1 + URP2) – (URP3 + URP4)
X= Xwl-Xrp Y=Ywl-Yrp

Modified data file:

Time(UTC)	X	Y

This format is more preferable, as it directly reflects seismic activity and allows build visual graphs.

3. CALS (CERN Accelerator Logging Service)

The CERN-wide Accelerator Logging Service(CALS)[3] was born out of the LHC Logging Project, which was launched in 2001. The service first became operational in late 2003, and has since become what is considered to be a mission-critical service. The current mandate can be summarized as:

- Information management for Accelerator performance improvement.
- Meet INB* requirements for recording beam history.
- Make available long-term statistics for management.
- Avoid duplicate logging efforts

The logging service persists data of close to 1 million pre-defined signals coming from heterogeneous sources. These signals range from data related to core infrastructure such as electricity, to industrial data such as cryogenics and vacuum, to beam related data such as beam positions, currents, losses, etc.

Java[4] is used to record event in the database, approximately 2TB of data is recoded weekly in the Short-term Change Database(MDB), 1Tb data is stored on the Internet, Long-Term Event Database(LDB). Access to this data is organized using the Java API(application programming interface). For visualization of data using a graphical interface called TIMBER.

4.Timber and pyTimber

Access to the TIMBER graphical interface, performed using software written on Java, pyTimber[5] is a Python language library designed specifically for accessing CALS data, which make it possible to integrate information from the database into their projects. PyTimber include PageStore – this library allow to save information on local hard drive.

5.The PLI data method storage

CALS is a closed system, access to this system provided with approved tool. For software development that meets the requirements of CALS, was decided to locate data from PLI on accessible place – EOS service[6](EOS – disc space with fast access). The structure of our proposed method is presented on figure2.

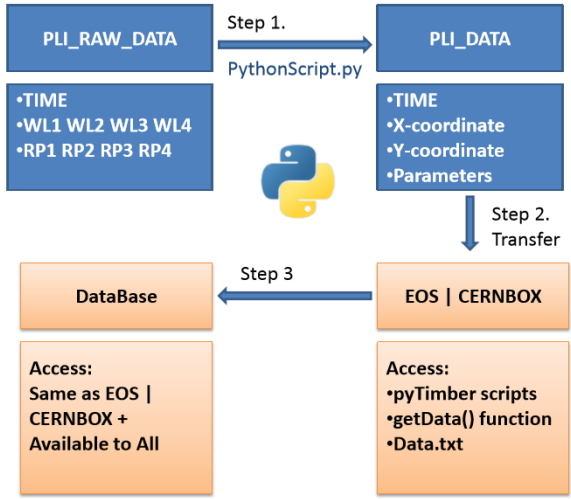

Fig. 2. The structure of our proposed method

The method includes three main components:

1. Conversion data described in section 2.
2. Redirecting processed data to EOS service, CernBox
3. Create SQLite database

This method allow to use PyTimber/PageStore to access PLI data. In the same way as access to the TIMBER database. Also, the data will be available from CernBox (CernBox – provides cloud data storage to all CERN users)
Creating a SQLite database in necessary for retrieving data, it organizes fast access to data.

6.Conclusion

This method provides data processing from one PLI. This method does not depend on the number of instruments, which will further create a network of several PLI. This make possible to be part of the CALS system.

The author of the article expresses the gratitude to Yulian Aramovich Budagov for setting the tast, Nikolai Sergreyevich Azaryan, Mikhail Vasilyevich Lyablin for consulting and clarifying the PLI instrument. Beniamino Di Girolamo,Riccardo De Meria for presenting his software development experience and Jacub Wozniak for clarifying the CALS service specification.

Reference.

1. D. Brünnig and L. Rossi (Eds.) “The High Luminosity Large Hadron Collider”, Advanced Series on Directions in High Energy Physics – Vol. 24, ISSN 1793-1339, World Scientific, (2015)
2. Commissioning of Professional PLI Prototype (EDMS document) 21/09/2017 Nikolay AZARYAN, Mikhail LYABLIN, Alexandre SELETSKIY, Andrei PLUZHNIKOV September 2017
3. Katerina Sigerud WEB: https://be-dep-co.web.cern.ch/content/cals 10/28/2016
4. WEB: https://twiki.cern.ch/twiki/bin/view/ABPComputing/LhcDataStorage
5. Riccardo De Maria GIT: https://github.com/rdemaria/pytimber
6. WEB :http://information-technology.web.cern.ch/services/eos-service

First use of an active polarized Frozen Spin Target in a 4 π detector – Detection of particles under cryogenic conditions below 1 Kelvin

Andreas Thomas
Institut für Kernphysik, Universität Mainz
J.-J.-Becherweg 45, D 55099Mainz, Germany
E-mail: thomand@uni-mainz.de

For the A2-Collaboration

We have developed a Frozen Spin Target in close collaboration with the polarized target group of the Joint Institute for Nuclear Research (JINR, DLNP) in Dubna. The $^{3/4}$Helium dilution refrigerator provides temperatures down to 25 mKelvin. Both longitudinally and transversely polarized protons and deuterons are possible with the help of superconducting holding coils.
The A2 Collaboration at the Mainz Microtron MAMI measures photon absorption cross sections using circularly and linearly polarized 'Bremsstrahlung' photons up to an energy of ~1.5GeV. We use a 4 π detection system with the 'Crystal Ball' as central part.
In this paper the first double polarized experiment with the use of a newly developed active polarized solid target in the year 2016 will be described and new possibilities for the use of this technology in high energy physics experiments will be addressed.

1. The A2 Real Photon Facility at MAMI

The Mainz MAMI electron accelerator with its source of polarised electrons, based on the photoeffect on a strained GaAs crystal, routinely delivers polarised beam with a maximum energy of 1604 MeV and a degree of polarisation of approximately 85%. The last accelerator stage, MAMI C, is realized as a Harmonic Double Sided Microtron (HDSM). Main features of this new machine concept are the four 90° bending magnets and the two LINACs working on 2.45GHz and the first harmonic. Details of the machine can be found in reference [1].

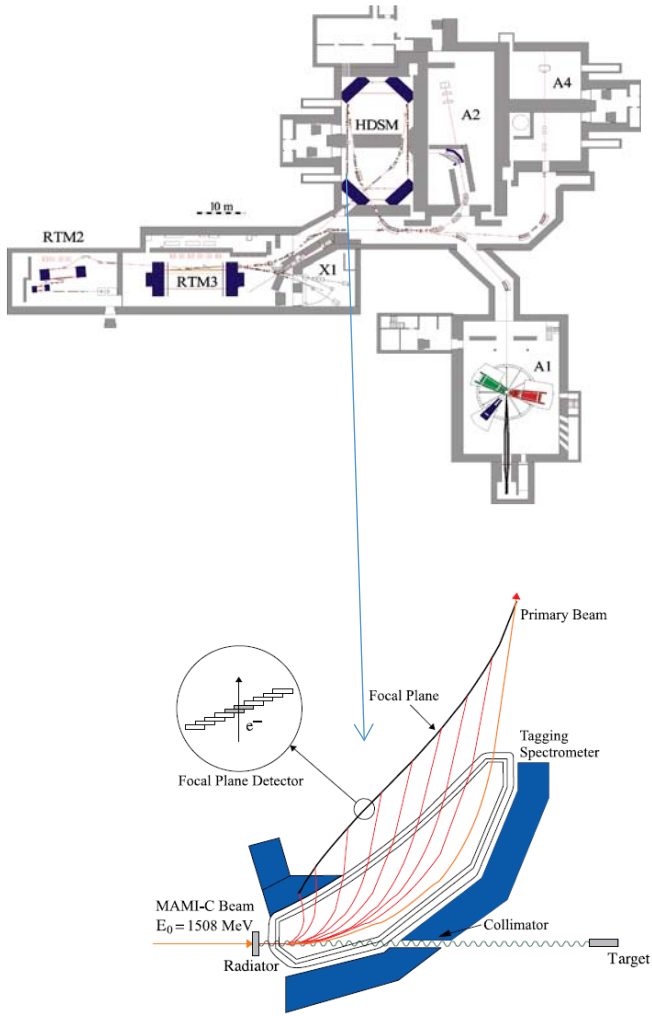

Figure 1. Floor plan (top) of the MAMI accelerator with zoom in the Glasgow-Mainz tagging system (bottom part).

The A2-Glasgow-Mainz tagging facility [2] stands out due to its high photon intensity. The beam is derived from the production of Bremsstrahlung photons during the passage of the MAMI electron beam through a thin radiator. The resulting photons can be circularly polarised, with the application of a polarised electron beam, or linearly polarised, in the case of a crystalline radiator. The tagger

focal plane is segmented into 352 scintillation detectors. Each counter can operate reliably to a rate of 1 MHz, giving high photon flux. The photons can be tagged in the momentum range from 4.7 to 93.0% of E_0. A new detector system with roughly the same segmentation, but even higher count rates is being implemented at the moment.

2. The Crystal Ball detector setup

The central detector system consists of the Crystal Ball calorimeter combined with a barrel of scintillation counters for particle identification and two coaxial multiwire proportional chambers for charged particle tracking. This central system provides position, energy and timing information for both charged and neutral particles in the region between 21° and 159° in the polar angle and over almost the full azimuthal range. At forward angles, less than 21°, reaction products are detected in the TAPS forward wall. The full, almost hermetic, detector system is shown schematically in figure 2.
The full angular coverage of this detector system sets very rigorous condition for the construction of the polarized target.

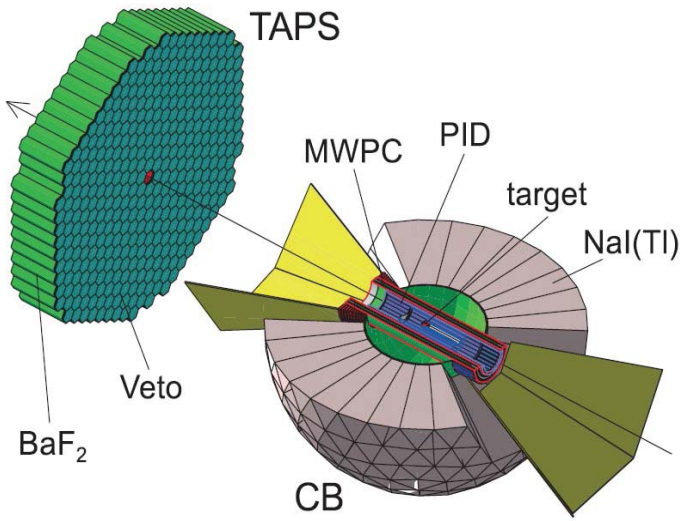

Figure 2. The Crystal Ball calorimeter, with cut-away section showing the inner detectors, and the TAPS forward wall.

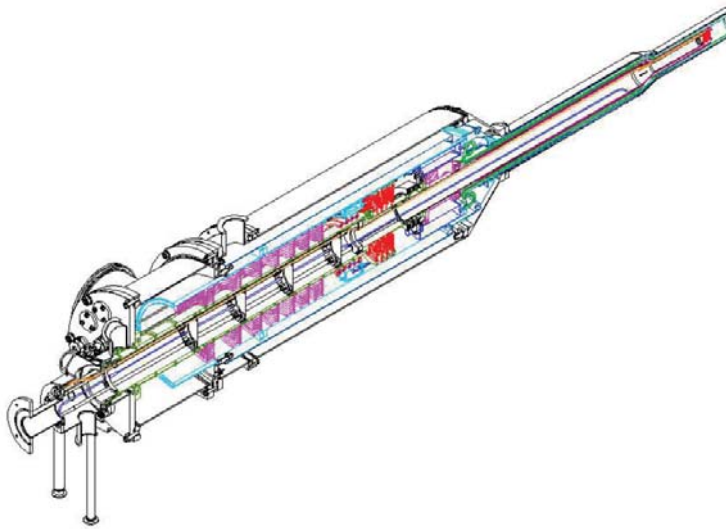

Figure 3. The $^{3/4}$helium dilution refrigerator (magenta - high temperature heat exchanger 300k - 4K; red - low temperature heat exchanger between separator and evaporator helium pot 4K - 1.5K; green - dilution sintered heat exchanger 0.7K - 0.022K).

3. The Polarized Target

The new frozen spin target was designed to retain the high angular acceptance of the detector system. The main boundary condition for the outer diameter of the frozen spin target cryostat was the most inner particle identification detector with a diameter of 104 mm. The internal holding coils had to be as thin as possible to allow particles to punch through (figure 4).

Figure 4. The thin superconducting solenoid (left side) and saddle coil (right side).

Longitudinal and transverse superconducting magnetic holding coils can be integrated to provide all directions of polarization.
The core of the frozen spin target for the Crystal Ball detector is a specially designed, large horizontal ^{3}He/^{4}He dilution refrigerator (see figure 3) that was built in cooperation with the Joint Institute for Nuclear Research (JINR) Dubna. More details about the cryostat design and concept can be found in these proceedings [14].
Several papers have been published in the last years [3-12] about our results concerning Baryon spectroscopy and meson photoproduction.
In addition, we have started an extended program to investigate un-polarized and polarized Compton scattering. Since the cross section is two orders of magnitude smaller compared to pion-production and the final state requires an open trigger the experiment is very challenging. These experiments will lead to a better determination of the scalar polarizabilities [13] and a first independent measurement of the spin polarizabilities [14].
Beside the measurements on a polarized frozen spin target with Butanol, where we use the polarized protons, we have also done a series of measurements with deuterated Butanol, in order to get access to the polarized neutron. In paper [9] the 'Helicity-dependent cross sections and double-polarization observable E in □-photoproduction from quasi-free protons and neutrons' has been presented. Recent other results are presented in these proceedings [16].

4. The Active Polarized Frozen Spin Target

A typical challenge in the analysis of data that stem from experiments using frozen spin target is the determination of low energy recoil particles. This is due to the fact that the actual target material is surrounded by the cooling liquid and several thermal shields and does not consist itself by pure hydrogen. In addition, the particles have to punch through the internal holding coil and the vacuum jacket of the cryostat. To overcome this problems, we have started to develop an active, scintillating polarised target. A series of tests [17, 18] with photodetectors for operation at cryogenic temperatures down to 4.2 Kelvin in order to do a readout of the scintillation-light of our frozen spin target have been performed in the framework of the PhD-thesis of M.Biroth.
Finally, the active polarised proton target was in operation in our detector system in June 2016. A stack of polarisable material polystyrene target plates was used. Figure 5 shows the scintillating head of our system. The 15 SiPMs were operated at the end of a 1.5m long PMMA light guide tube at a temperature level of 150K (figure 7). An operational temperature of 45mKelvin could be reached for 2 weeks during the run. A maximum polarisation of +46% and -49% could be achieved with relaxation times of 78h and 74h at a magnetic holding field of 0.44Tesla (Figure 6).

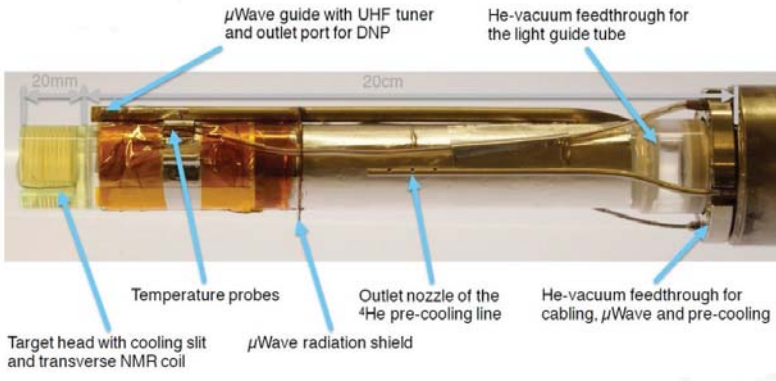

Figure 5. The front end part of the active polarized proton target.

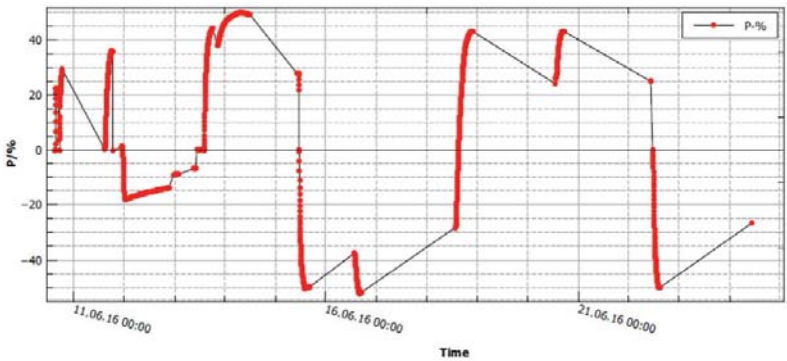

Figure 6. Time dependence of the degree of spin polarization in our first active polarized proton target run.

Figure 7. The SiPMs for the active polarised proton target light readout.

We plan to use this target type in Compton scattering experiments and in threshold meson production, were it is difficult to detect the recoiling target proton or nucleon. In addition, it can be foreseen to use a combination of alcohol–targets (e.g. Butanol) in combination with segmented scintillators inside the $^{3/4}$helium dilution of the refrigerator to get an additional information about the direction of the recoiling particles.

Acknowledgement
The authors wish to acknowledge the excellent support of the accelerator group and operators of MAMI. This work was supported by the Deutsche Forschungsgemeinschaft (SFB1044), the European Community-Research Infrastructure Activity under the FP6 “Structuring the European Research Area” programme (Hadron Physics, Contract No. RII3- CT-2004-506078), Schweizerischer Nationalfonds (Contract Nos. 200020-156983, 132799, 121781, 117601, 113511), the UK Science and Technology Facilities Council (STFC 57071/1, 50727/1), the US Department of Energy (O_ces of Science and Nuclear Physics, Award Nos. DE-FG02-99- ER41110, DEFG02-88ER40415, DE-FG02-01-ER41194), and National Science Foundation (Grant Nos. PHY-1039130, IIA-1358175), INFN (Italy), and NSERC (Canada). We thank the undergraduate students of Mount Allison University and The George Washington University for their assistance.

References

[1] A. Jankowiak, Eur. Phys. J. A 28, s01, 149 (2006)
[2] J.C. McGeorge et al., Eur. Phys. J. A 37, 129 (2008)
[3] P.Adlarson et al., Phys. Rev. C 92, 024617 (2015)
[4] M.Dieterle et al., Phys. Rev. Lett. 112, 142001 (2014)
[5] J.R.Annand et al., Phys. Rev. C 93, 055209 (2016)
[6] J.R.Annand et al., Phys. Rev. C 91, 055208 (2015)
[7] S.Schumann et al., Phys. Lett. B 750, 252 (2015)
[8] A. Käser et al., EPJ A 52, 272 (2016)
[9] L.Witthauer et al., Phys. Rev. Lett. 117, 132502 (2016)
[10] P. Adlarson et al, Phys. Rev. C 95, 035208 (2017)
[11] M.Dieterle et al., Phys. Lett. B, 523 (2017)
[12] A. Käser et al., Phys. Lett. B 786, 305 (2018)
[13] P.P.Martel et al., Phys. Rev. Lett. 91, 112501 (2015)
[14] V. Sokhoyan et al., Eur. Phys. J. A 53, 14 (2017)
[15] I. Gorodnov et al., Proceedings NTIHEP (2018)
[16] V. Kashevarov et al., Proceedings NTIHEP (2018)
[17] M.Biroth et al., Nucl. Inst. Meth. A 787, 68 (2015)
[18] P.Achenbach et al., Nucl. Inst. Meth. A 824, 74 (2016)

New cryostat for the frozen spin target at Bonn electron accelerator "ELSA"

I.S. Gorodnov, Yu.A. Usov, N.S. Borisov, A.S. Dolzhikov
Low temperature sector, Dzhelepov laboratory of nuclear problems (DLNP),
Joint Institute for Nuclear Research (JINR), Dubna, Russia
yuusov@jinr.ru

Abstract. The description of the design, construction and recent results of the horizontal cryostat for the new Bonn frozen spin target developing for the spin physics experiments with tagged photons from the Bonn electron accelerator "ELSA" are given. In addition, the overview of frozen spin polarized targets cooled by the ^{3}He/^{4}He dilution refrigerators developed at the DLNP JINR since 1976 for different accelerators is given.

Introduction

The dilution refrigerator principle was suggested by Heinz London in 1952. H. London, G.R. Clarke, and E. Mendoza proposed a prototype of continuous refrigerator in 1962. Two years later, in 1964, P. Das, R.B. Ouboter and K.W. Taconis realized it in the Kamerlingh Onnes Laboratory at Leiden University. They obtained T_{min}~220 mK. In 1966 B.S. Neganov, N.S. Borisov and M.Yu. Liburg at DLNP JINR created a dilution cryostat that allowed to obtain a temperature of 50 mK in long time mode and up to 25 mK in short time mode [1]. Modern «wet» refrigerators are based on the Grenoble design by Frossati and coworkers. They allow to obtain a stable temperature in the range of 20…50 mK. The lowest temperature obtained in the dilution cryostats T_{min}~2 mK. These cryostats are widely used in various experiments of particle physics.

Theory of operation and schematic diagram of dilution refrigerator

The refrigeration process uses a mixture of two isotopes of helium: helium-3 and helium-4. When cooled below approximately 870 millikelvins, the mixture undergoes spontaneous phase separation to form a ^{3}He-rich phase (the concentrated phase) and a ^{3}He-poor phase (the dilute phase). As shown in the phase diagram (Fig. 1), at very low temperatures the concentrated phase is essentially pure ^{3}He, while the dilute phase contains about 6.6% ^{3}He and 93.4% ^{4}He. The working fluid is ^{3}He, which is circulated by vacuum pumps at room temperature. ^{3}He enters the cryostat at a pressure of a few hundred millibar. In the classic dilution refrigerator (known as a wet dilution refrigerator) (Fig. 2), ^{3}He is precooled and purified by liquid nitrogen at 77 K and a ^{4}He bath at 4.2 K. Next, ^{3}He enters a vacuum chamber where it is further cooled to a temperature of 1.2–1.5 K by the 1 K bath, a vacuum-pumped ^{4}He bath (as decreasing the pressure of the helium reservoir depresses its boiling point). The 1 K bath liquefies ^{3}He gas and removes the heat of condensation. ^{3}He then enters the main impedance, a capillary with a large flow resistance. It is cooled by the still to a temperature 500–700 mK. Subsequently, ^{3}He flows through a secondary

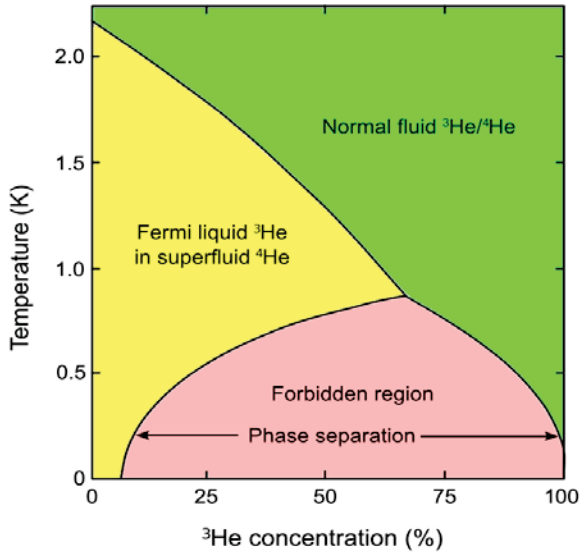

Figure 1. Phase diagram of liquid ^{3}He/^{4}He mixtures showing the phase separation

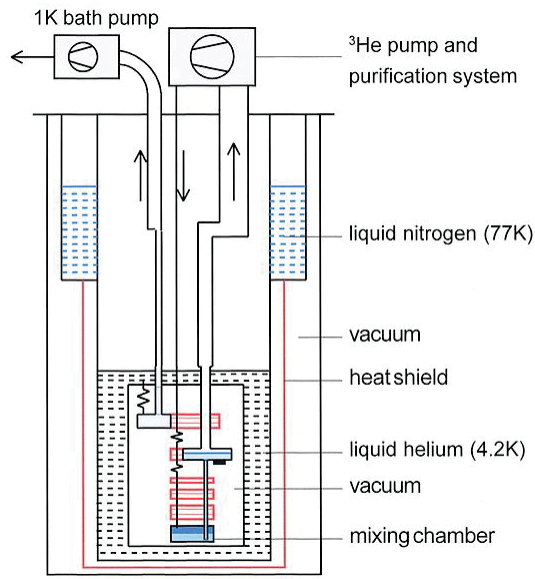

Figure 2. Schematic diagram of a standard, or wet, dilution refrigerator

impedance and one side of a set of counterflow heat exchangers where it is cooled by a cold flow of ^{3}He. Finally, the pure ^{3}He enters the mixing chamber, the coldest area of the device. In the mixing chamber, two phases of the ^{3}He–^{4}He mixture, the concentrated phase (practically 100% ^{3}He) and the dilute phase (about 6.6% ^{3}He and 93.4% ^{4}He), are in equilibrium and separated by a phase boundary. Inside the chamber, ^{3}He is diluted as it flows from the concentrated phase through the phase boundary into the dilute phase. The heat necessary for the dilution is the useful cooling power of the refrigerator, as the process of moving ^{3}He through the phase boundary is endothermic and removes heat from the mixing chamber environment. ^{3}He then leaves the mixing chamber in the dilute phase. On its way up, the cold, dilute ^{3}He cools the downward flowing ^{3}He via the heat exchangers until it enters the still. In the still, ^{3}He flows through superfluid ^{4}He which is at rest. The pressure in the still is kept low (about 10 Pa) by the pumps at room temperature. The vapor in the still is practically pure ^{3}He, which has a much higher partial pressure than ^{4}He at 500–700 mK. The pump therefore creates an osmotic pressure difference, which drives more ^{3}He from the concentrated to dilute phases in the mixing chamber, and then up from the mixing chamber to the still. Heat is supplied to the still to maintain a steady flow of ^{3}He. The pumps compress ^{3}He to a pressure of a few hundred millibars and feed it back into the cryostat, completing the cycle.

An overview of frozen spin polarized targets cooled by the ^{3}He/^{4}He dilution refrigerators developed at the DLNP JINR since 1976

Therefore, after learning how to realize the dilution method, cryostats were used in experiments with a polarized target. In Fig. 3, you can see B.S.Neganov during tuning of 1 K Dynamic Polarized target.

Figure 3. B.S.Neganov during tuning 1 K Dynamic Polarized target (app.1965)

Further development of the dilution method led to the fact that in the laboratory of nuclear problems was created a combined setup including a 1 K dynamic polarized target and a dilution refrigerator where an ultra low temperature 5 mK was reached (Fig. 4).

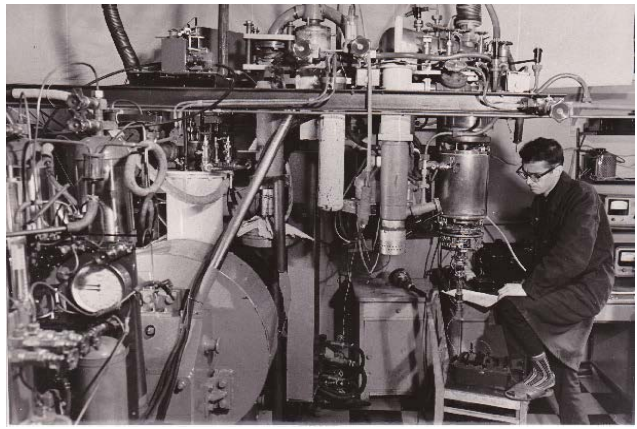

Figure 4. A combined setup including a 1 K dynamic polarized target and a dilution refrigerator where an ultra low temperature 5 mK was reached (1966)

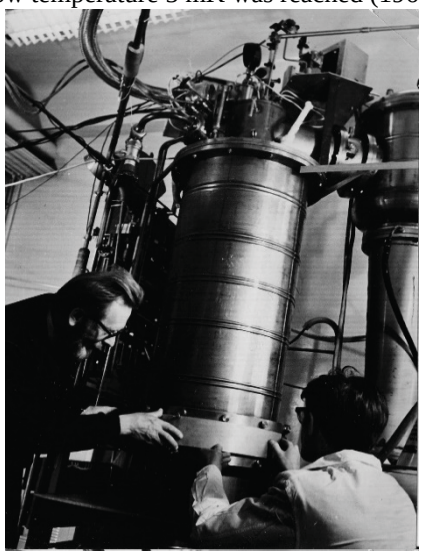

Figure 5. The first Frozen Polarized Target (1975) during tests preparation (B. Neganov and N. Borisov)

The next step was the use of cryostats in experiments with a frozen spin target to achieve very low temperatures. The principle of operation of a frozen spin target is based on long nuclear spin relaxation time at low temperatures (≈ 50 mK) and moderate magnetic fields (≥ 0.3 T). After the polarization build-up with so the spin relaxation time can be many days at about 50 mK.
In 1975 at the Laboratory of Nuclear Problems JINR the experiments at the Phasotron of LNP on measurement of a polarization parameter in the elastic pp-scattering were begun with a newly made frozen spin proton target (Fig. 5). This target is working in Gatchina until now [2].
The next target (Fig. 6) with length 20 cm and 60 cm³ in volume, which has been used for experiments with 40 GeV π^- mesons and 70 GeV protons at the accelerator of the Institute of High Energy Physics in Protvino since 1978 [3, 4]. Lot of articles (over 40) were published since 1976 using these two targets. In 1988 this frozen target was upgraded to deuteron mode.

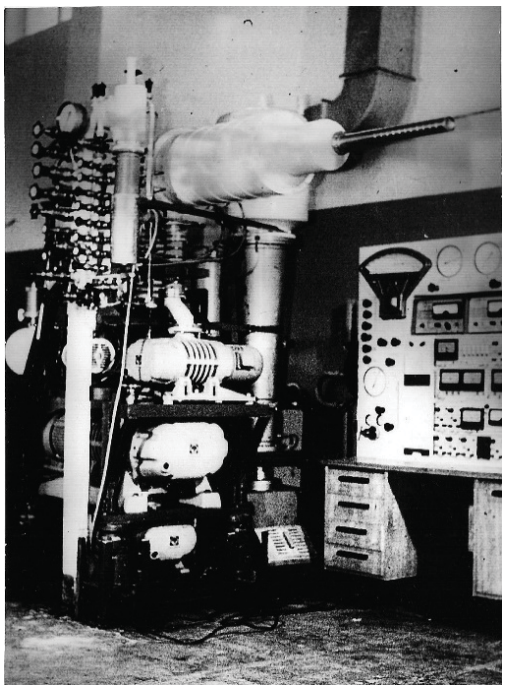

Figure 6. Second FPT before transportation
to IHEP (Protvino) – 1978

Low temperature sector DLNP JINR developed the target with a frozen nuclear polarization for experiments at low energies in Prague (Fig. 7) [5]. In the near future it is planned to conduct new experiments with a polarized target in Prague.

Also our team upgraded the Saclay-Argon frozen polarized target to movable polarized target for high energy spin physics experiments (Fig. 8) [6].

Figure 7. Target with a frozen nuclear polarization for experiments at low energies in Prague

Figure 8. The reconstruction of the Saclay-Argon frozen spin proton polarized target

In our sector, the dilution cryostat (Fig. 9) was manufactured for experiments with Frozen Polarized Target at MAMI C (Mainz) [7]. In the Figure 10, one can see the main parts of the experimental setup including a dilution cryostat with a target container, a superconducting magnet and a Crystal Ball detector. Temperature stability during the experiments is also shown (Fig. 11). At the moment this

cryostat is used in Bonn experiments while another new one is being manufactured by our group in Dubna.

Figure 9. Frozen Polarized Target at MAMI C (Mainz) - 2010

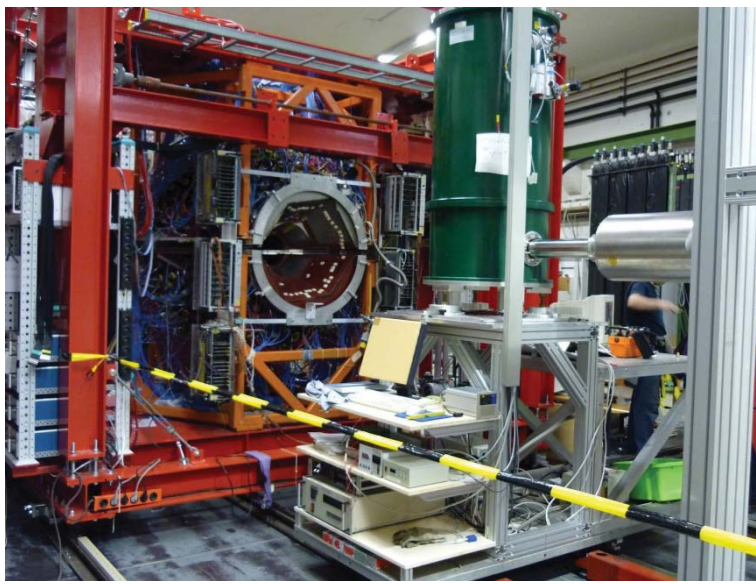

Figure 10. Crystal Ball and Superconducting magnet at MAMI C (Mainz)

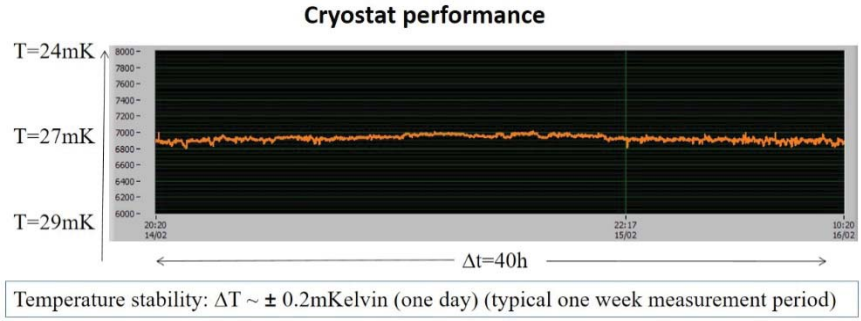

Figure 11. Temperature stability during experiments in Mainz

New ^{3}He/^{4}He dilution cryostat for Bonn electron accelerator "ELSA"

In 2015 the contract on producing new cryostat was concluded between JINR and Bonn University. According to this contract, our team should make a dilution cryostat with the following technical characteristics:

- Mixing chamber temperature < 30 mK is guaranteed in continuous operation. Goal for the base temperature is 25 mK;
- Cooling power at 300 mK > 30 mW at a ^{3}He circulation rate of 10 mmol/sec;
- Evaporator temperature ≈ 1.2 K, Separator temperature ≈ 4 K;
- Temperature of integrated holding or polarizing coil is 1.3 K. A supply of 50 A current to this coil is guaranteed. The design should make a coil current of 100 A possible;
- Liquid ^{4}He consumption < 4 liter/hour;
- Target size: diameter – 20 mm, length – 20 mm.

At the beginning, the design of the cryostat was carried out. Figure 12 shows its cross-section. It shows the main elements of the installation: heat exchangers, evaporator, separator, insert, etc.

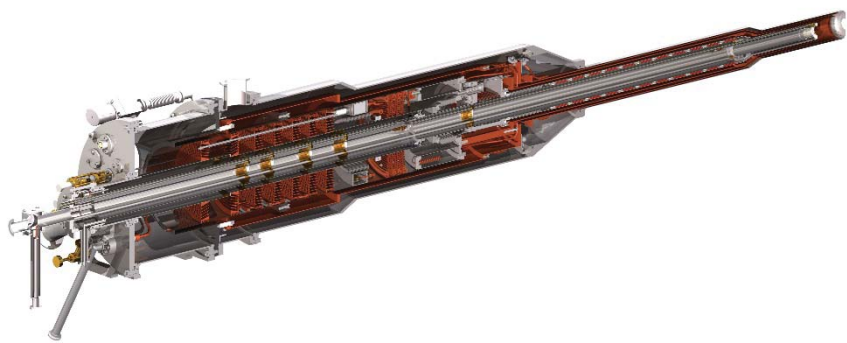

Figure 12. Cross-section of Bonn dilution cryostat

Then the parts were manufactured from which the main elements of the cryostat were assembled (Fig. 13 - 15).

Figure 13. The gas heat exchanger

Figure 14. Vacuum jacket and screen

Figure 15. Pumping flanges and sintered heat exchanger

At the moment we have all the main parts of the Bonn cryostat and we started the general assembling. According to our plans the setup should be finished before new year (2019), and then the cryostat will be transported to Bonn for final tuning (during 2019).

Summary

The team of the low temperature sector DLNP JINR has extensive experience in conducting experiments with polarized targets, as well as designing and manufacturing dilution cryostats. At the moment according to the scheme (Fig. 16), polarized targets and cryostats developed by our team are located in the following cities: Dubna, Protvino, Gatchina, Prague, Mainz and Bonn [8].

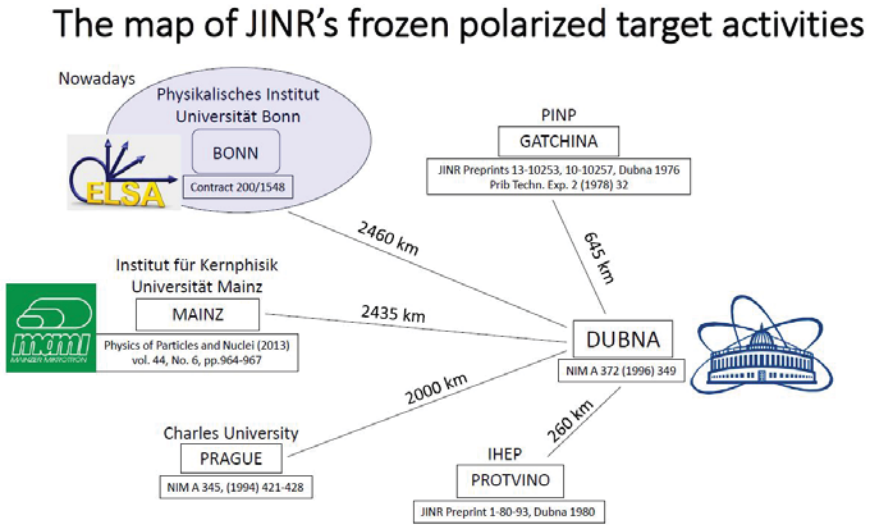

Figure 16. The map of JINR's frozen polarized target activities

References

[1] B.S. Neganov, N.S. Borisov and M.Yu. Liburg, *A Method of Producing Very Low Temperatures by Dissolving ^3He in ^4He*, JINR-P-2480, 1966.

[2] N.S. Borisov, et al., JINR Preprints 13-10253, 13-10257, 1976; Prib. Techn. Exp. 2 (1978) 32.

[3] N.S. Borisov, et al., JINR Preprint 1-80-98, 1980.

[4] N.S. Borisov, E.I. Bunyatova, M.Yu. Liburg, V.N. Matafonov, A.B. Neganov and Usov Yu. A., *Frozen spin polarized deuteron target 60cm in volume*, J.Phys. E: Sci.Instrum., 1988 (21), P. 1179-1182.

[5] N.S. Borisov, V.N. Matafonov, A.B. Neganov, Yu.A. Plis, O.N. Shchevelev, Yu.A. Usov, I. Jansky, M. Rotter, B. Sedlak, I. Wilhelm, G.M. Gurevich,

A.A. Lukhanin, J. Jelinek, A. Srnka and L. Skrbek, *Target with a frozen nuclear polarization for experiments at low energies*. NIM A 345, 1994, P. 421-428.
[6] N.A. Bazhanov, Yu.A. Usov et al., *A movable polarized target for high energy spin physics experiments.* NIM A 372, (1996) 349-351; JINR Preprint E8-96-33, Dubna, 1996.
[7] A. Thomas, N.S. Borisov, A.N. Fedorov, G. M. Gurevich, … Yu.A. Usov, *The new frozen spin target at MAMI.* Physics of Particles and Nuclei, 2013, 44(6), P. 964–967.
[8] Yu.A. Usov, *Frozen Spin targets developed at Dubna. History and traditions*. PoS (PSTP2015-021).

Projects of Future Electron-Positron Colliders at the Energy Frontier

Tadeusz Lesiak*
The Henryk Niewodniczański Institute of Nuclear Physics
Polish Academy of Sciences,Kraków, Poland

March 5, 2019

Abstract

A future giant electron-positron collider, operating at the energy frontier, is a natural next step and a formidable tool to push particle physics into new regime of precise measurements, in particular in the sectors of electroweak observables and Higgs boson parameters. The four projects of such accelerators: two linear (ILC and CLIC) and two circular (FCC and CEPC) have been proposed. The next few years will be of paramount importance for their fate, especially in view of the update of European HEP strategy for particle physics and expectations of important decisions from Japan, China and USA. The paper concisely reviews the relevant aspects and challenges of the proposed accelerators and detectors together with the presumed schedules of construction and operation.

1 Introduction

In the past, the synergic operation of proton-proton and electron-positron colliders was the workhorse of particle physics. The Higgs boson discovery (2012) taking place in pp collisions at Large Hadron Collider (LHC) [1, 2], reinvigorated the projects of new giant e^+e^- colliders, oriented to collect data at the energy frontier. The detailed study of Higgs boson parameters is among the primordial goals of these machines. Two accelerators are proposed in each of the two possible geometries: circular and linear. The former are Circular Electron Collider (CEPC) [3] in China and Future Circular Collider (FCC) [4] in CERN area. The latter are Compact Linear Collider (CLIC) [5] at CERN and International Linear Collider (ILC) [6] in Japan. All four projects will be discussed briefly in the next chapter 2. The physics program of future electron-positron colliders at the energy frontier is discussed, in particular, in [7].

*Tadeusz.Lesiak@ifj.edu.pl

2 Projects of future e^+e^- colliders

The Large Electron Collider (LEP) [8], the largest circular electron-positron collider built so far, was decommisioned in 2000. At this time it was commonly accepted that every LEP successor should realize linear collisions. This conviction was motivated by the fact that for circular accelerators, the beam energy losses due to synchrotron radiation (and operation costs as well) grow rapidly with the centre-of-mass (CM) energy. In parallel, the luminosity of such machines was limited by the level of the beam size reduction (β_y^* - the vertical beta function at the interaction point), which was available at the LEP time ($\beta_y^* \approx 50$ mm). Moreover, for a linear geometry of collisions, the synchrotron radiation is absent and the longitudinal beam polarisation can be implemented relatively easily. However for linear colliders, the beams are accelerated and collided only once. As a result, in order to reach the desired high-luminosity, the beam size must be reduced enormously (even to the of the order of nanometer in the vertical direction), which comprises the technological challenge. In addition, in such conditions the beam-beam electromagneting interaction and the associated beamstrahlung radiation losses should be tamed.

In parallel with the development of linear colliders' technologies, a substantial progress in the circular electron-positron acceleration took place, mainly due to the successful operation of B-factories. In particular, the possibility to reduce significantly the β_y^* parameter (by a factor exceeding 50) have arised. At the same time the instantaneous luminosity could be constantly kept close to the optimal level by exploiting the so called top-up or continuous injection. Here, the additional collider ring, so called booster, periodically top-ups the main rings of the accelerator (adding typically $\sim 10\%$ of beam particles every $\sim$10 s). In this way the booster compensates for the short beam lifetime caused by Bhabha scattering and the loss of particles in collisions. With these and other advances, like e.g. the crab-waist crossing, and assuming a large circumference collider of the order of 100 km, the overall increase of luminosity by a factor exceeding a 1000 (to compare with LEP), is feasible. In view of this progress, the circular geometry is currently considered as a viable option for a future e^+e^- collider, in parallel with the linear one. The brief discussion of the two projects of linear colliders (ILC and CLIC) and two circular ones (FCC and CEPC) is given below.

2.1 The International Linear Collider

The International Linear Collider (ILC) [6] is proposed as a 250 GeV machine, (optionally to be extended up to 1 TeV) with the location in Japan. The Technical Design Report (TDR) [9, 10, 11] of ILC, issued in 2013, assumed a CM energy of 500 GeV. Since 2017, the project was downgraded to 250 GeV with the motivation of cost reduction (by $\sim$40%), while keeping the opportunity of future extensions of the linacs with the associated increase of the collision energy. This so called ILC250 with the total length of 20 km (cf. Fig. 1) would concentrate on the studies

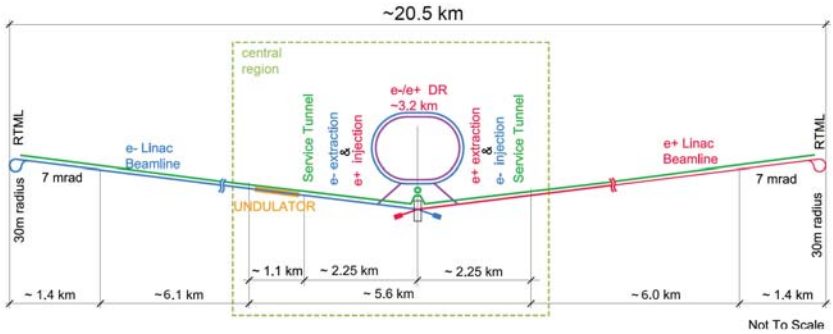

Figure 1: The layout of the ILC250 collider.

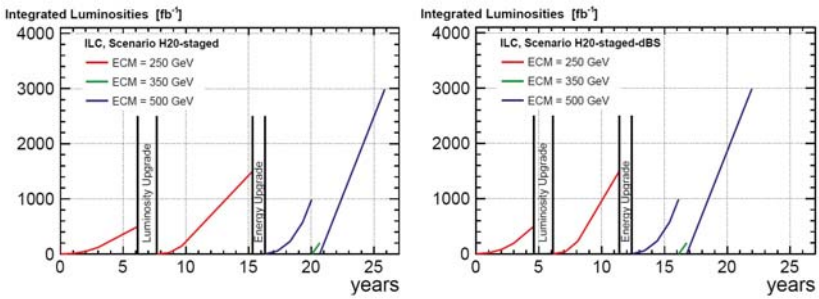

Figure 2: The ILC250 integrated luminosity with two scenarios of staging (from [13]).

of the Higgs boson, with the potential of reaching the $t\bar{t}$ threshold in the upgraded machine.

The ILC would be based on 1.3 GHz superconducting radiofrequency cavities with the acceleration gradient of 31.5 MV/m. This would be a unique new e^+e^- collider with longitudinal polarisation of both beams (80% for electron and 30% for positron beam). The basic parameters of the ILC are collected in Table. 1 and in Fig. 2. It is worthwhile to mention that with the successful commissioning of the European Free Electron Laser (E-XFEL) [14] at DESY (Germany) this acceleration technology has passed the practical test (10% scale of the ILC project). The decision of Japanese government about the realization of the ILC is awaited by the end of 2018.

2.2 The Compact Linear Collider

The Compact Linear Collider (CLIC) [5] is currently a unique project envisioning electron-positron collisions up to multi-TeV range The construction of the CLIC infrastructure is considered in the CERN area. The machine would rely on a novel

Parameter	Unit	Initial	Upgrades	
Centre of mass energy ($\sqrt{s}$)	GeV	250	500	1000
Luminosity ($\mathcal{L}$)	$10^{34}\mathrm{cm}^{-2}\mathrm{s}^{-1}$	1.35	1.8	4.9
Repetition frequency (f_{rep})	Hz	5	5	4
Bunches per pulse (n_{bunch})	1	1312	1312	2450
Bunch population (N_{e})	10^{10}	2	2	1.74
Norm. hor. emitt. at IP ($\gamma\epsilon_{\mathrm{x}}$)	μm	5	10	10
Norm. vert. emitt. at IP ($\gamma\epsilon_{\mathrm{y}}$)	nm	35	35	35
RMS hor. beam size at IP (σ^*_{x})	nm	516	474	335
RMS vert. beam size at IP (σ^*_{y})	nm	7.7	5.9	2.7
Site length (L_{site})	km	20.5	31	40

Table 1: The ILC accelerator parameters. The baseline, "initial" configuration is followed by possible upgrades.

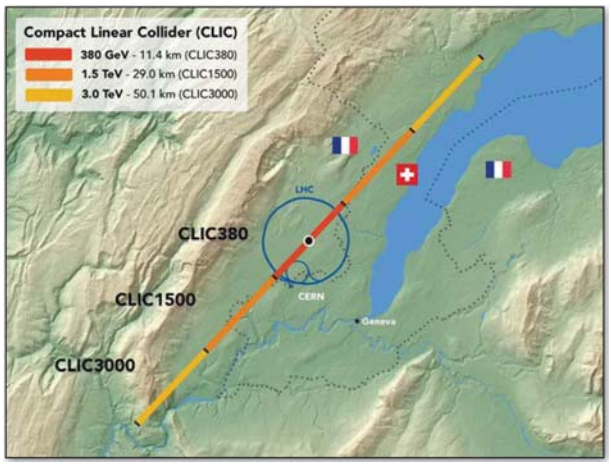

Figure 3: The sketch of the CLIC collider. The three energy stages are shown with different colours (from [16]).

Parameter	Unit	Stage 1	Stage 2	Stage 3
Centre of mass energy ($\sqrt{s}$)	GeV	380	1500	3000
Luminosity ($\mathcal{L}$)	$10^{34}\mathrm{cm}^{-2}\mathrm{s}^{-1}$	1.5	3.7	6.0
Repetition frequency (f_{rep})	Hz	50	50	50
Bunches per pulse (n_{bunch})	1	352	312	312
Bunch population (N_{e})	10^{10}	0.52	0.37	0.37
Norm. hor. emitt. at IP ($\gamma\epsilon_{\mathrm{x}}$)	nm	950	660	660
Norm. vert. emitt. at IP ($\gamma\epsilon_{\mathrm{y}}$)	nm	30	20	20
RMS hor. beam size at IP (σ^*_{x})	nm	149	60	40
RMS vert. beam size at IP (σ^*_{y})	nm	3.0	1.5	1.0
Site length (L_{site})	km	11.4	29.0	50.1

Table 2: The CLIC accelerator parameters, shown separately for the three energy stages.

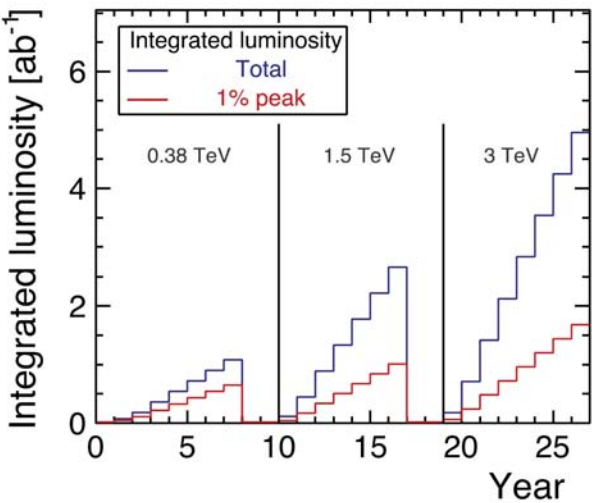

Figure 4: The CLIC integrated luminosity (from [17].

two-beam acceleration scheme. Here the first one, so-called drive-beam is a high-current, low-energy electron beam based on normal-conducting high-frequency (12 GHz, X-band) radiofrequency structures. Such beam would be passed through so-called Power Extraction and Transfer Structures (PETS). There, the drive-beam is decelerated and thereby generates the powerful RF pulse (at 12 GHz). The former is used to accelerate the second so called main-beam, operating at room temperature with the gradient of 100 MV/m. The above described acceleration model appears to be more efficient and less costly to compare with a classical, klystron based, RF powering scheme.

The CLIC Conceptual Design Report [15] foresees 80% polarisation of the electrons at collision. The development of CLIC is planned in three stages with the first one at 380 GeV CM energy, the intermediate phase at 1.5 TeV and the final stage at 3 TeV, with the corresponding length spanning the range from 11 km to 50 km (cf. Fig. 4). The most relevant characteristics of CLIC can be found in Table. 2.

2.3 The Future Circular Collider

The overall goal of the Future Circular Collider (FCC) project [4] is the construction of a 100 km circumference accelerator tunnel in the Geneva area. The first phase of the project, so-called FCC-ee, would correspond to the instrumentation of the tunnel with a high-luminosity e^+e^- collider. This accelerator would accumulate data with CM energies ranging from the Z^0 mass up to beyond the $t\bar{t}$ threshold. The core of the overall project is a 100 TeV proton-proton collider FCC-pp, which is to be commissioned after the e^+e^- phase. The electron-proton collisions are proposed as well with the e^- beam from the Electron Recovery Linac (ERL).

The FCC-ee would collect data in four working points, corresponding to the relevant physics thresholds for the Z, WW, HZ, $t\bar{t}$ production. The collider's parameters are collected in Table. 3. It would be a double-ring accelerator with e^+ and e^- beams circulating in separate vacuum chambers. A top-up injection scheme will be realized with a booster synchrotron located in the collider tunnel itself. The operation model of the FCC-ee is shown in Fig. 6.

2.4 The Circular Electron-Positron Collider

The Circular Electron-Positron Collider (CEPC) [3] is proposed with the setup and parameters very similar to FCC. It would be located in China. The 100 km circumference underground tunnel for such accelerator could also host a Super Proton Proton Collider (SPPC), intended to reach energies beyond the LHC. As shown in Fig. 7, the CEPC will be composed of a linear accelerator, a damping ring, the booster, the collider and the relevant transport lines. The core of the project would compraise the operation as Higgs factory with the CM energy of 240 GeV. The runs at the Z mass peak and WW threshold are planned as well.

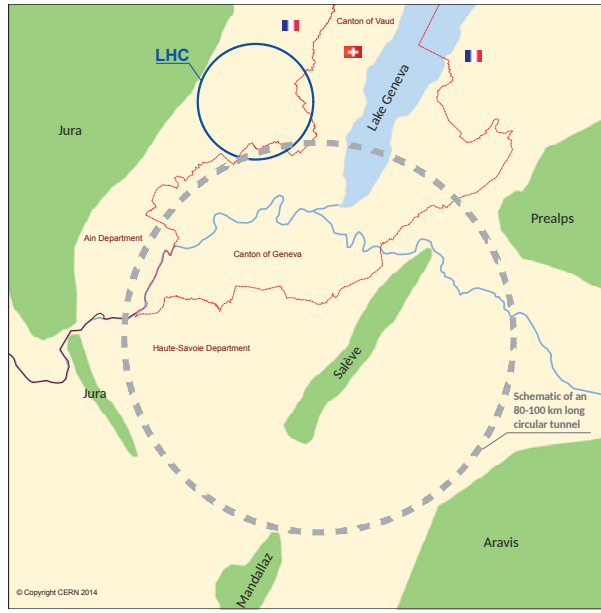

Figure 5: The sketch of the FCC collider (copyright by CERN 2014).

Parameter	Unit	Z	WW	ZH	$t\bar{t}$
Centre of mass energy $(\sqrt{s})$	GeV	91.2	160	240	350
Luminosity/IP $(\mathcal{L})$	$10^{34}\mathrm{cm}^{-2}\mathrm{s}^{-1}$	230	28	8.5	1.8
Beam current (f_{I})	mA	1390	147	29	6.4
Bunches per beam (n_{bunch})		16640	2000	328	59
Bunch population (N_{e})	10^{11}	1.7	1.5	1.8	2.2
Horizontal (H) β_x^*	m	0.15	0.2	0.3	1.0
Vertical (V) β_y^*	mm	0.8	1.0	1.0	1.6
H emittance ϵ_x	nm	0.27	0.84	0.63	1.34
V emittance ϵ_y	pm	1.0	1.7	1.3	2.7
H beam size at IP (σ_{x}^*)	μm	6.4	13.0	13.7	36.7
V beam size at IP (σ_{y}^*)	nm	28	41	36	66
Energy loss/turn	GeV	0.036	0.34	1.72	7.8
RF voltage	GV	0.1	0.75	2.0	4.0/5.4

Table 3: The FCC-ee accelerator parameters, shown separately for the four working points (from [18]).

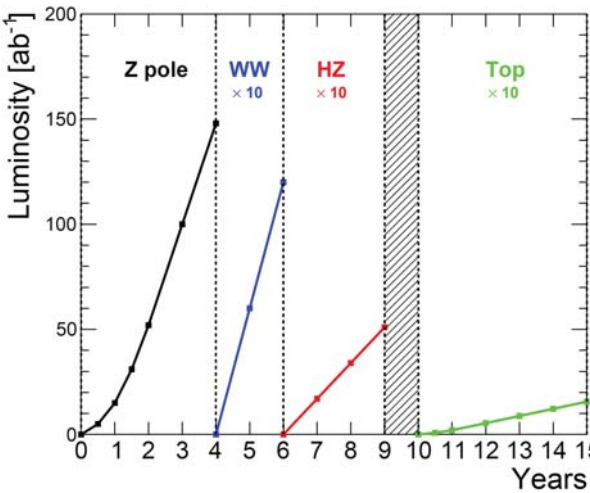

Figure 6: The FCC-ee integrated luminosity (from [17].

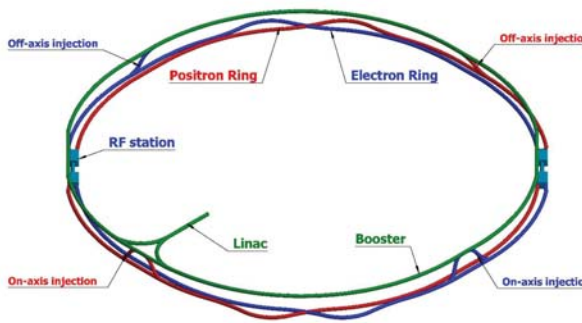

Figure 7: The layout of the CEPC collider (from [19]).

Parameter	Unit	Z	WW	ZH
Centre of mass energy ($\sqrt{s}$)	GeV	91.0	160	240
Luminosity/IP ($\mathcal{L}$)	$10^{34}\mathrm{cm}^{-2}\mathrm{s}^{-1}$	17	10	3
Beam current (f_{I})	mA	461	88	17
Bunches per beam (n_{bunch})		12000	1524	242
Bunch population (N_{e})	10^{11}	0.8	1.2	1.5
Horizontal (H) β_x^*	m	0.2	0.36	0.36
Vertical (V) β_y^*	mm	1.5	1.5	1.5
H emittance ϵ_x	nm	0.18	0.54	1.21
V emittance ϵ_y	pm	4.0	1.6	2.4
H beam size at IP (σ_{x}^*)	μm	6.0	13.9	20.9
V beam size at IP (σ_{y}^*)	nm	78	49	60
Energy loss/turn	GeV	0.036	0.34	1.73
RF voltage	GV	0.1	0.47	2.17

Table 4: The CEPC accelerator parameters (from [19]).

Particle	E_{CM} (GeV)	L per IP (10^{34} cm^{-2} s^{-1})	integrated L per year (ab^{-1}, 2 IPs)	Years	Total integrated L (ab^{-1}, 2 IPs)	Total no. of particles
H	240	3	0.8	7	5.6	1×10^6
Z	91	32	8	2	16	7×10^{11}
W^+W^-	160	10	2.6	1	2.6	1.5×10^7

Table 5: The CEPC operation plan (from [19]).

2.5 Complementarity of circular and linear colliders

The expected luminosities vs the CM energies for all four abovementioned projects are presented in Fig. 8. In the region of relatively low energies, roughly to the $t\bar{t}$ threshold, the expected luminosities of circular colliders are superior to compare with linear ones . For higher CM energies, the linear colliders seem to be the only viable option. Thus both linear and circular geometries are complementary.

The typical timelines of potential future e^+e^- colliders at the energy frontier encompass first the few years of preparatory work devoted in particular to the final R&D work. Next the period of construction would come, spanning the range of 6-8 years. Finally the data taking is expected to take at least a decade (as given in the respective fiures and tables) with various strategies of the time order of different working points.

2.6 Detectors for new e^+e^- colliders

For each of the abovementioned projects of future e^+e^- colliders one-two interaction points equipped with the general purpose, 4π-barrel type detectors, are

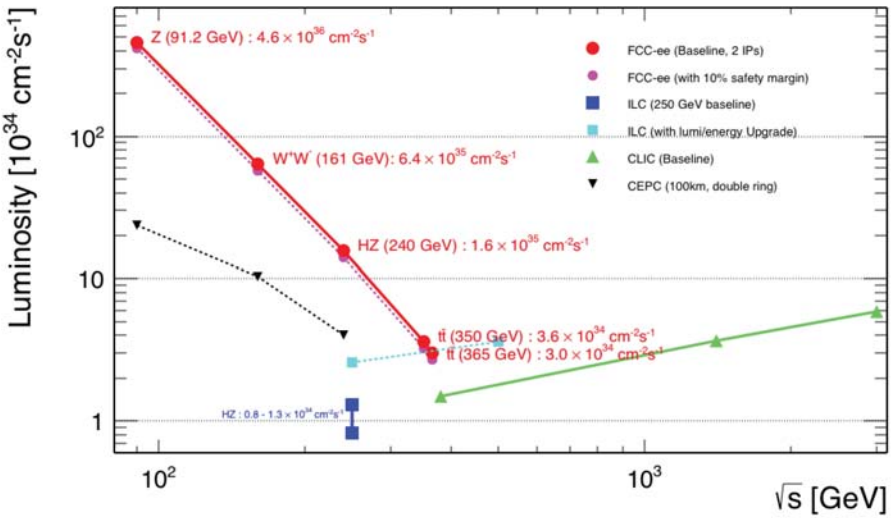

Figure 8: The luminosities vs the CM energies for all four projects of electron-positron colliders discussed in the paper.

planned. They are generally proposed along the same lines as its successful predecessors, designed and built for LEP. The overall scheme of such spectrometer is illustrated with the layout proposed by the CLICdp collaboration [20] (cf. Fig. 9). Generally, such apparatus should be lightweighted in terms of the material content and hermetic. At the same time it should provide also precise tracking and fine-grained calorimetry.

For the tracking system, the Silicon-based spectrometer is usually considerd. The drift chamber solution is also being developed as an alternative solution. The system of calorimeters should meet tights requirements in order to allow for allow for the application of the Particle Flow Algorithms [21]. The intense R&D efforts in calorimetry, carried on by of the CALICE collaboration [22] yielded several proposed setups of calorimeters. The overall ambitious goal of the spectrometers is to reach 3 GeV resolution of jet reconstruction. This would allow to discriminate between jets originating from the W and Z bosons. It is worthwhile to underline that data taking at future e^+e^- colliders will be triggerless i.e. all collisions can be safely recorded for further studies.

3 Summary

The projects of future e^+e^- colliders at the energy frontier have been briefly presented.

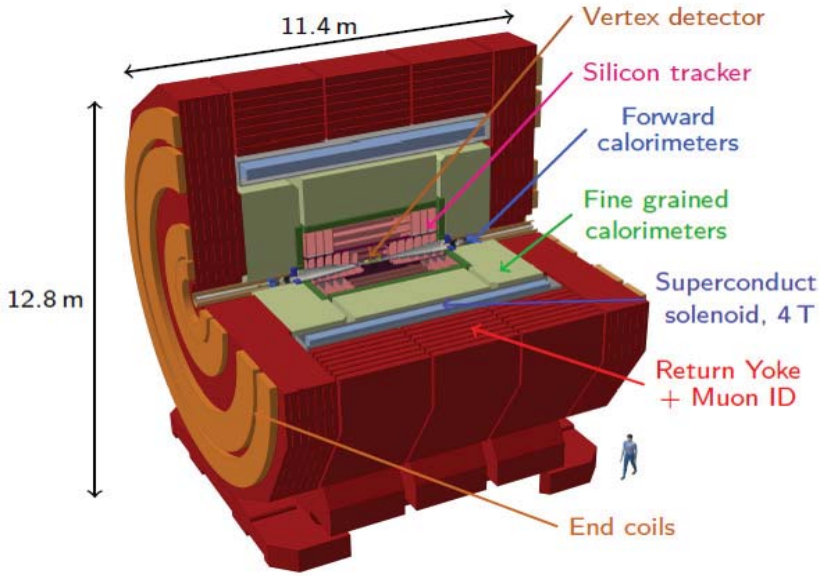

Figure 9: The layout of the CLICdp detector.

Acknowledgements

This research was supported in part by grant of Narodowe Centrum Nauki 2016/23/B/ST2/03927.

References

[1] ATLAS Collaboration, *"Observation of a new particle in the search for the Standard Model Higgs boson with the ATLAS detector at the LHC"*, Phys.Lett. B716 (2012) 1–29.

[2] CMS Collaboration, *"Observation of a new boson at a mass of 125 GeV with the CMS experiment at the LHC"*, Phys.Lett. B716 (2012) 30–61.

[3] http://cepc.ihep.ac.ch

[4] http://fcc.web.cern.ch

[5] http://clic-study.web.cern.ch

[6] http://www.linearcollider.org/ILC

[7] T.Lesiak, Proceedings of the XLVIII International Symposium on Multiparticle Dynamics (ISMD18), submitted to the EPJ Web of Conferences, (2018).

[8] H. Schopper, *"LEP — the Lord of the Collider Rings at CERN 1980–2000"*, 130 Springer Publisher, ISBN 978-3-540-89301-1.

[9] C. Adolphsen et al., *"The International Linear Collider Technical Design Report - Volume 3.I: Accelerator R&D in the Technical Design Phase,"* arXiv:1306.6353 [physics.acc-ph].

[10] C. Adolphsen et al., *"The International Linear Collider Technical Design Report - Volume 3.II: Accelerator Baseline Design,"* arXiv:1306.6328 [physics.acc-ph].

[11] T. Behnke et al., *"The International Linear Collider Technical Design Report - Volume 4: Detectors,"* arXiv:1306.6329 [physics.ins-det].

[12] L. Evans, S. Michizono *The International LInear Collider Machine Staging Rport 2017*, arXiv:1711.00568 [hep-ex].

[13] K. Fuji et al., (LCC Physics Working Group), *Physics Case for the 250 GeV Stage of the international Linear Collider*, arXiv:1710.07621 [hep-ex].

[14] http://www.xfel.eu

[15] http://clic-study.web.cern.ch/content/conceptual-design-report

[16] S. Doebert and E. Sicking, *Towards TeV-scale electron-positron collisions: the Compact Linear Collider (CLIC)* Europhysics News Vol. 49, No 1, (2018).

[17] F. Bordry et al., *Machine Parameters and Projected Luminosity Performance of Proposed Future Colliders at CERN*, arXiv:1810.13022 [physics.acc-ph].

[18] The Future Circular Collider Study - Conceptual Design Report, in preparation.

[19] CEPC Conceptual Design Report, Vol II - Physics & Detector, preprint IHEP-CEPC-DR-2018-02.

[20] http://clicdp.web.cern.ch

[21] M.A. Thomson, *"Particle flow calorimetry and the PandoraPFA algorithm"*, Nuclear Instruments and Methods in Physics A, 611, Issue 1 (2009), 25-40.

[22] https://twiki.cern.ch/twiki/bin/view/CALICE/CaliceCollaboration

CLICdp-Conf-2018-012
21 December 2018

News on physics and detectors at CLIC

E. Brondolin*

On behalf of the CLICdp Collaboration

* *CERN, Switzerland*

Abstract

The Compact Linear Collider (CLIC) is a proposed high-luminosity linear electron-positron collider at the energy frontier. To optimise its physics potential, CLIC is foreseen to be built and operated in three stages, with a centre-of-mass energy from a few hundred GeV up to 3 TeV. In the first stage, CLIC will focus on the Higgs-boson and the top-quark properties, such as a high precision measurement of the Higgs total decay width and couplings and of the top-quark mass. During the subsequent energy stages, the aim of the physics programme will revolve around measurements of rare Higgs-boson processes, as well as direct and indirect searches for new physics, and precision measurements of possible new particles. To pursue this rich physics programme and to face the challenges imposed by the CLIC conditions, an optimised detector design and innovative new technologies are required. In this document, an overview of the CLIC accelerator, the CLICdet detector and its performance, and the CLIC physics programme is given.

Talk presented at New Trends in High-Energy Physics, Budva, Montenegro, 24–30 September 2018

1 Introduction

The Compact Linear Collider (CLIC) [1–3] is a mature options for a future high-luminosity linear electron-positron collider at the energy frontier. It is foreseen to be implemented in several energy stages with increasing centre-of-mass energy with the aim of measuring with high precision the properties of the top quark and the Higgs boson and searching for physics beyond the Standard Model (BSM). A recent update on the CLIC staging baseline scenario can be found in [4], where the assumptions about the accelerator ramp-up and up-time have been harmonised with those of other potential future colliders. In this new staging scenario CLIC is foreseen to run at the centre-of-mass energy of 380 GeV, 1.5 TeV and 3 TeV, and to deliver a total integrated luminosity of 1 ab^{-1}, 2.5 ab^{-1} and 5 ab^{-1}, respectively. The total integrated luminosity at 380 GeV CLIC stage includes about 100 fb^{-1} taken in an energy scan around the $t\bar{t}$ production threshold at 350 GeV. The CLIC baseline foresees also ±80% electron polarisation, and no positron polarisation. The luminosity per year and the total integrated luminosity in the updated scenario can be found in Figure 1.

2 CLIC accelerator

The high centre-of-mass energy of CLIC requires an accelerating gradient of 100 MV/m, using normal-conducting accelerating structure operating at 12 GHz. The CLIC accelerator features a novel acceleration scheme. In this technique, the deceleration of a high intensity beam, the so-called drive beam, in power-extraction and -transfer radio-frequency (RF) structures, is used to generate power in the RF cavities that accelerate particles of the colliding electron/positron beams, also called the main beam. The two-beam technique was demonstrated at CERN in the CTF3 test facility [2].

CLIC achieves high luminosities by using extremely small beam sizes, of the order of (σ_x , σ_y) = (40 nm, 1 nm). The beamstrahlung radiation emitted by the electron and positron bunches traversing the high field of the opposite beam produces two main types of background, incoherent e^+e^- pairs and $\gamma\gamma \rightarrow$ hadron events. While the former impacts mostly the particle occupancy in the detector and is mainly concentrated in the forward region, the latter has a more significant impact on the physics measurement due to the high energy deposits left in the detector. The effect of the beamstrahlung on the occupancy and the collision energy strongly depends on the centre-of-mass energy of CLIC as can be seen in Figure 2 and in Figure 3, respectively [5].

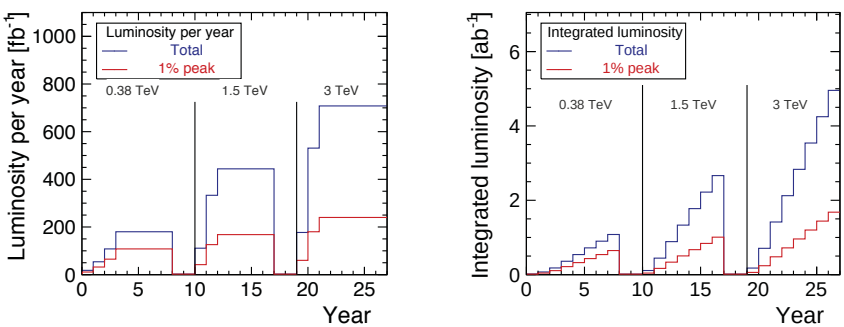

Figure 1: Luminosity per year (left) and the total integrated luminosity (right) in the updated CLIC scenario [4].

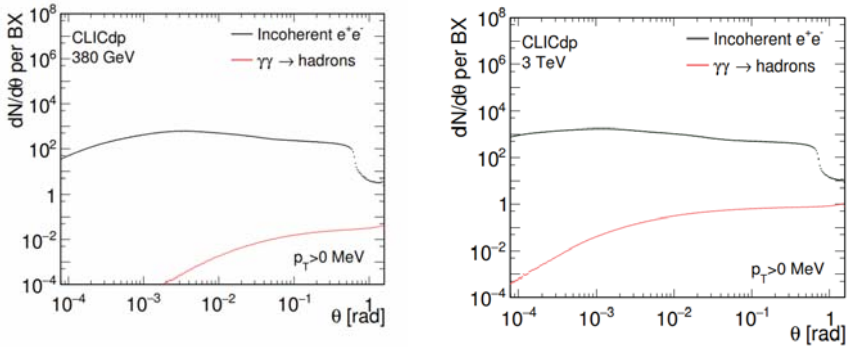

Figure 2: Angular distribution of the produced background particles in the case of 380 GeV (left) and 3 TeV (right) stage of the CLIC accelerator [5].

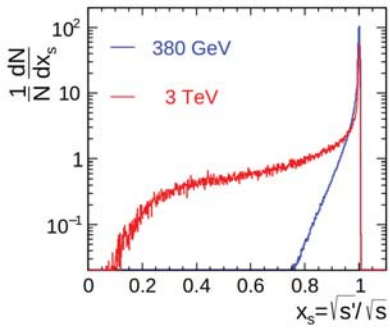

Figure 3: Luminosity spectrum at 380 GeV and 3 TeV stage of the CLIC accelerator [5].

Bunch trains of 312 (352) bunches at the 3 TeV (380 GeV) energy stage separated by 20 ms and single bunch separation of 0.5 ns in each bunch train allow for power pulsing in the detector and a trigger-less readout. To obtain excellent physics performance in trigger-less readout mode and to cope with the $\gamma\gamma \rightarrow$ hadron background, the subdetectors must provide a precise hit timing information which is used in offline software reconstruction as described in Section 3.1.

3 The detector for CLIC

CLICdet is a detector model designed to exploit the physics potential of the CLIC accelerator [6]. It foresees cutting-edge technology and is designed to obtain high performance using the Particle Flow Analysis (PFA). Moreover, it is optimised for the challenging conditions at CLIC, such as the bunches time structure and the high intensity $\gamma\gamma \rightarrow$ hadron background.

3.1 Detector requirements and optimisation

Some of the main detector requirements are the following:

- excellent track-momentum resolution for high-momentum tracks in the barrel, at the level of $\sigma_{p_T}/p_T^2 \leq 2 \times 10^{-5}\,\text{GeV}^{-1}$;
- precise impact-parameter resolution, at the level of $\sigma_{d_0}^2 = (5\,\mu\text{m})^2 + (15\,\mu\text{m GeV})^2/(p^2 \sin^3\theta)$, to allow accurate reconstruction and enable flavour tagging with clean b-, c-, and light-quark jet separation;
- jet-energy resolution for light-quark jets of $\sigma_E/E \leq 3.5\%$ for jet energies in the range 100 GeV to 1 TeV ($\leq 5\%$ at 50 GeV);
- detector coverage for electrons and photons to very low polar angles ($\sim$10 mrad) to assist with background rejection.

In order to fulfil these requirement, CLICdet features an ultra-low mass silicon tracking system, highly granular calorimeters, and subdetectors with a precise hit-timing resolution. The CLICdet layout follows the typical collider detector scheme. In the innermost part are placed a vertex detector composed of 25×25 µm^2 pitched pixels arranged in double-layers and a large tracker volume with barrel and disks of silicon micro-strips. The former is an extremely accurate subdetector with a single point resolution of 3 µm. All silicon tracking elements have a single hit time resolution of about $10/\sqrt{12}$ ns. The total tracker volume has a radius of 1.5 m and a half-length of 2.2 m with a total material budget less than $10\%X_0$ in the barrel region. Surrounding the tracker, an electromagnetic and hadronic calorimeter are placed, all embedded inside a superconducting solenoid providing a 4 T field. The basic ECAL structure of the CLIC detector is a silicon-tungsten sampling calorimeter with 5×5 mm^2 silicon detector cells, while the proposed hadronic calorimeter consists of steel absorber plates interleaved with 3×3 cm^2 scintillator tiles. The hit time resolution for all calorimeter hits is 1 ns. The outermost part of the detector is an iron yoke, interleaved with muon chambers. A quarter-view of CLICdet is shown in Figure 4. In the most forward part of CLICdet are placed two smaller electromagnetic calorimeters are placed, both built with layers of tungsten plates interleaved with sensors: LumiCal, covering an angular range from 39 mrad to 134 mrad, and BeamCal, covering from 10 mrad to 46 mrad.

The CLICdet geometry is optimised using a dedicated software suite which uses the DD4HEP software framework [7] and GEANT4 [8] via the DDG4 [9] package of DD4HEP for the geometry description and simulation. The design of the CLICdet concept ensures that the detector performance meets the requirements, as demonstrated in full simulation. An example of an event fully reconstructed with CLICdet and of an optimisation study aimed at establishing the outer tracker size taking into account the magnetic field and the p_T resolution goal is shown in Figure 5.

In full simulation, several studies were performed on the rejection of the beam-induced background from $\gamma\gamma \to$ hadrons. The energy deposit of these hadrons at the 3 TeV stage is around 20 TeV of energy per bunch train in the central calorimeters and as a consequence, their rejection is imperative to keep high physics performance. This can be efficiently done using the timing information coming from the subdetectors combined with additional p_T information on individually reconstructed particles. Figure 6 show the effectiveness of this selection for a typical $e^+e^- \to t\bar{t}$ event at centre-of-mass energies of 3 TeV [1, 10].

3.2 Detector performance

The CLICdet model fully satisfies the requirements described in Section 3.1. A detailed report on the CLICdet performance can be found in [5]. Some of the main results are summarised here.

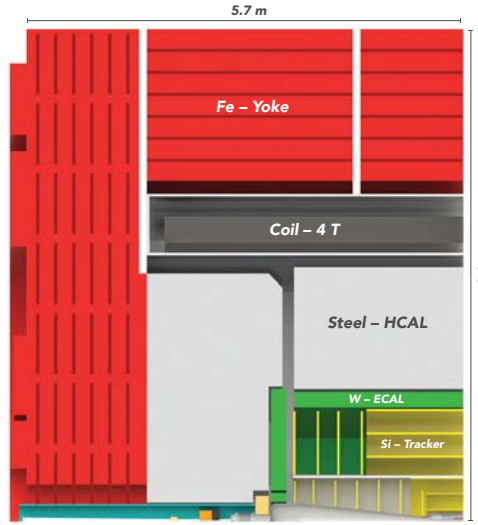

Figure 4: Longitudinal cross section of CLICdet [5].

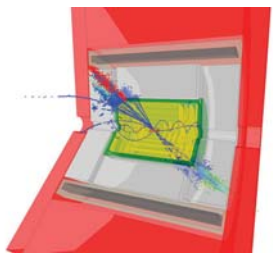

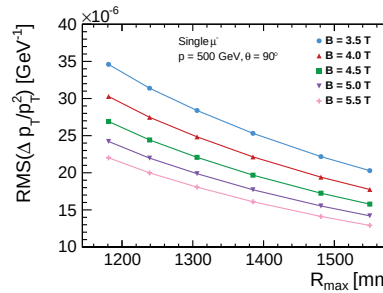

Figure 5: Event displays of $e^+e^- \to t\bar{t}$ events at a centre-of-mass energy of 3 TeV (left). Transverse momentum resolution as a function of tracker radius for different strengths of the B-field (right) [6].

Firstly, some highlights on the tracking performance can be found in Figure 7. On the left, the robustness of the conformal tracking algorithm used at CLICdet is shown in terms of tracking efficiency as a function of p_T for $e^+e^- \to t\bar{t}$ events with and without the $\gamma\gamma \to$ hadron events at the 3 TeV CLIC stage. In Figure 7 (right), the transverse momentum resolution for single muons as a function of the momentum in the case of different polar angles shows that the requirement on the resolution is achieved for high p_T tracks in the barrel.

Moreover, the choice of highly granular calorimeters and the optimisation of CLICdet to make full use of the PFA result in a very accurate jet energy resolution as shown in Figure 8 (left). Di-jet events using

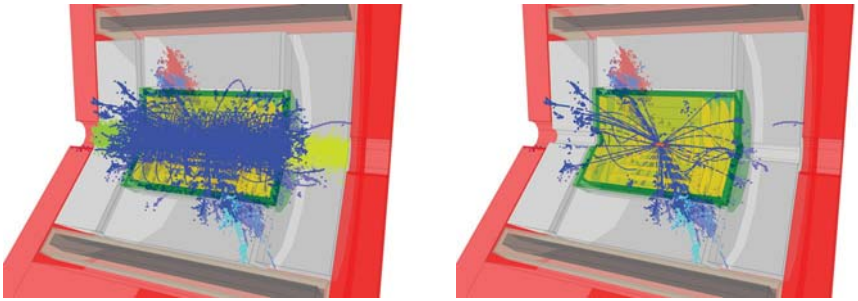

Figure 6: Event displays of $e^+e^- \to t\bar{t}$ events at a centre-of-mass energy of 3 TeV before (left) and after (right) background suppression using a timing selection.

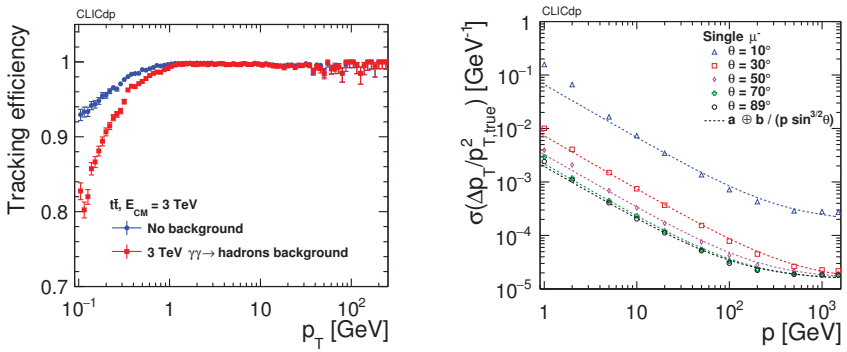

Figure 7: Tracking efficiency for $t\bar{t}$ events at the 3 TeV CLIC stage as a function of p_T with and without 3 TeV $\gamma\gamma \to$ hadron background overlay (left) and transverse momentum resolution for single muons produced at different polar angles as a function of the momentum (right) [5].

decays of a Z/γ^* particle into light quarks (u, d, s) at different centre-of-mass energies are analysed and the energy resolution for light-quark jets is found to be around $3-5\%$ for all jet energies with $|\cos\theta| < 0.925$, where θ is the quark polar angle. In Figure 8 (right) the efficiency for the electron reconstruction in the LumiCal as a function of the polar angle is shown in the case of the 3 TeV CLIC stage. Electrons with energy between 1.5 TeV and 190 GeV are reconstructed in the forward region with an efficiency well above 90% for all polar angles within the fiducial volume of LumiCal.

Finally, the performances of b- and c-flavour tagging at CLICdet are presented in Figure 9. In both cases the tagging results are shown using di-jet samples at 500 GeV without and with overlay of $\gamma\gamma \to$ hadron background produced at 3 TeV CLIC stage. On the left, the beauty quark misidentification probability is plotted as a function of the correct identification efficiency separately for charm and light-flavour contamination. In the right plot, the charm misidentification probability is assessed for beauty and light-flavour contamination. In both cases, the robustness of the flavor jet reconstruction and tagging is proven given that the effect of the background is only increasing the misidentification by a few percent.

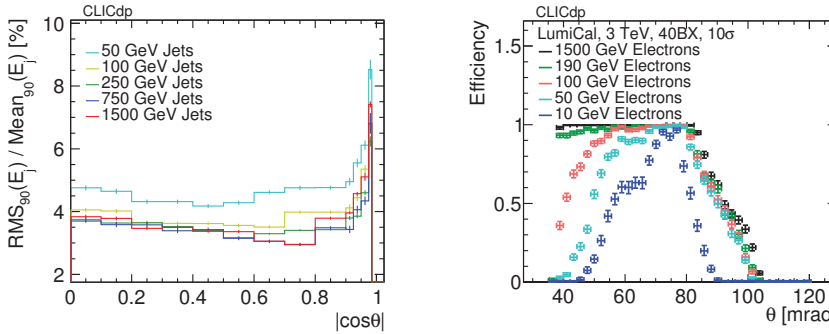

Figure 8: Energy resolution for light-quark jets as a function of the quark polar angle (left). Electron efficiency reconstruction in the LumiCal as a function of the polar angle at the 3 TeV CLIC stage (right) [5].

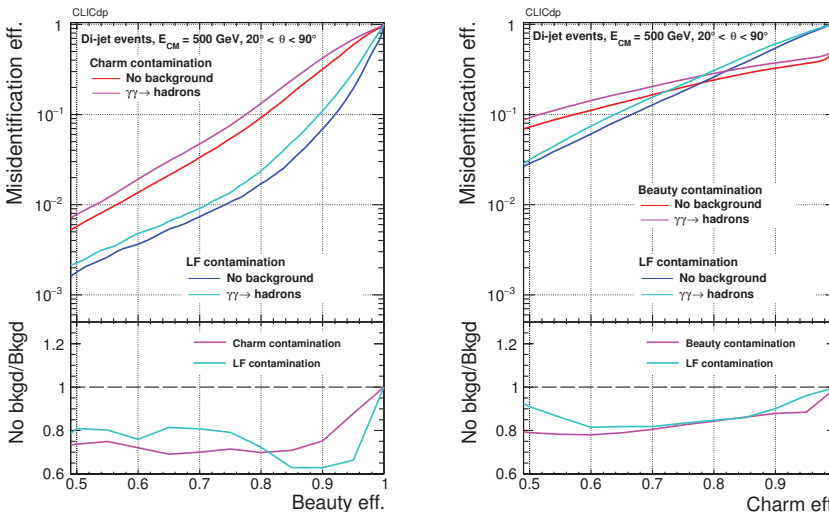

Figure 9: B-tagging (left) and c-tagging (right) performance for di-jet samples at 500 GeV without and with overlay of $\gamma\gamma \rightarrow$ hadron background produced at the 3 TeV CLIC stage [5].

4 Physics potential

CLIC, as a lepton collider with a wide range of energies and high luminosity, can pursue a physics programme with an unprecedented precision on many measurements in the Higgs and top-quark sector as well as potentially addressing several open questions exploring BSM physics.

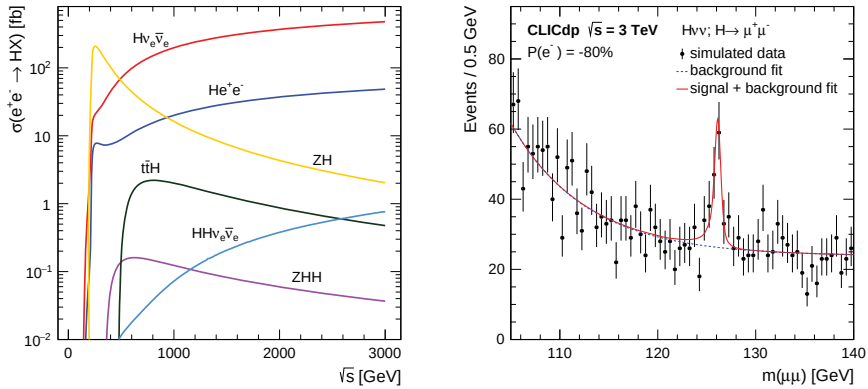

Figure 10: Higgs production cross sections for several production channels as a function of the centre-of-mass energy of an electron-positron collider (left) [1]. Reconstructed di-muon invariant mass distribution of selected $H \to \mu\mu$ events at the 3 TeV energy stage (right) [11].

4.1 Higgs physics

Studying the Higgs boson in great detail is one of the top priorities of the CLIC physics programme. The CLIC accelerator will produce and be able to reconstruct around 160 000 Higgs bosons during its initial stage, and millions are estimated for the highest energy stage. A detailed and comprehensive report on this topic can be found in [11], and including the latest update on the luminosity scenario in [4].

As shown in Figure 10 (left), the different energy stages of CLIC allow the study of several Higgs production channels as predicted in the Standard Model (SM). In the first CLIC stage, the Higgsstrahlung process $e^+e^- \to HZ$ is dominant. The Higgs boson can be identified event-by-event using only the Z boson recoil mass which allows for a measurement of the Higgs branching ratios and decay width without any assumptions about invisible BSM decays of the Higgs boson. At higher energy stages, the contribution from the WW-fusion process $e^+e^- \to H\nu_e\bar{\nu}_e$ becomes significant and can be used to improve the Higgs measurement precision. Moreover, rare processes become available such as the direct double-Higgs production $e^+e^- \to HH\nu_e\bar{\nu}_e$ which allows for the extraction of the trilinear Higgs self-coupling as well as the quartic HHWW coupling. In this study the possibility of polarising the electron beam plays an important role: the negative polarisation of -80% leads to an increase of the double-Higgs production cross section by a factor 1.8, while the positive polarisation of +80% reduces it by a factor of 0.2. The trilinear Higgs self-coupling can be determined at CLIC with a relative uncertainty of -7% and $+11\%$ at 68% C.L. under the SM parameters assumption.

As an example, the $H \to \mu^+\mu^-$ invariant mass distribution is shown in Figure 10 (right). Thanks to the high momentum resolution achieved by the CLIC detector, the peak is well visible on top of the background despite the very low SM branching ratio of 2×10^{-4}. In Figure 11, two results on the Higgs couplings and width are presented. On the left, the results obtained using a model-independent global fit are shown. Sub-percent precision can be obtained for the Higgs couplings (around 1% for rare decays), while the Higgs width can be extracted with precision of 2.5%. On the right, results for a model-dependent fit allow to compare CLIC with HL-LHC projection. It can be noted that, for several couplings, the precision achieved already at the first CLIC stage is significantly better than what is expected at HL-LHC.

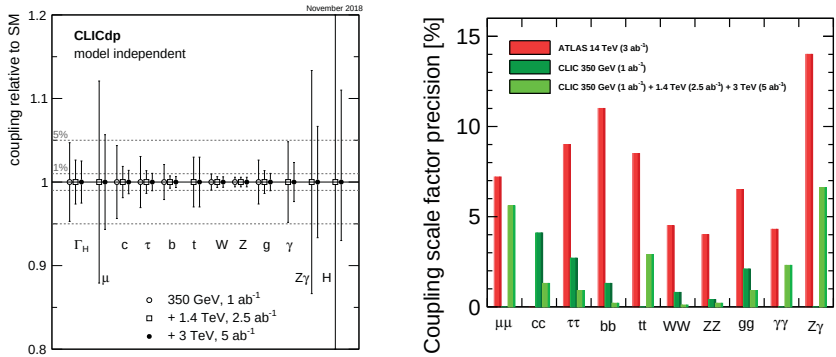

Figure 11: Precision on the Higgs couplings and width extracted from a model-independent global fit (left) [4]. Comparison between model-dependent Higgs coupling sensitivities measured at CLIC and corresponding HL-LHC projections (right) [4].

4.2 Top physics

Until now, the top quark has been produced only at hadron colliders. Therefore, CLIC would provide a unique opportunity to study this particle in detail, testing the SM limits and searching for possible BSM effects [12]. Depending on the energy stage, different aspects of top-quark production and properties can be studied.

In the first stage, CLIC foresees an energy scan around the top-quark pair-production threshold where samples of about 10 fb^{-1} are recorded, separated by 1 GeV in collision energy as shown in Figure 12 (left). From the cross sections measured at each energy point, the top-quark mass, width and other model parameters are extracted using a template fit. The total uncertainty of the measurement on the top-quark mass amounts to about 50 MeV, mainly dominated by the present theoretical uncertainty. Moreover, $t\bar{t}$ events allow to search for top-quark decay modes produced by flavour-changing neutral-current processes which are strongly suppressed in the SM.

The higher energy stages of CLIC open the possibility of studying with high precision the top Yukawa coupling and CP properties in the ttH coupling. As an example, in Figure 12 (right) the sensitivity of the top-quark coupling to Z and γ in terms of form factors is reported [13]. The uncertainty on this measurement is particularly important to search for the existence of new heavy particles predicted by CP-violating new physics models which could modify the top-quark form factors. Already at the first stage, CLIC is able to perform a significantly more precise measurement than the HL-LHC. Finally, thanks to its highest centre-of-mass energy, CLIC is also the only currently proposed accelerator for which the vector boson fusion production process of top pairs $e^+e^- \to t\bar{t}\nu_e\bar{\nu}_e$ is accessible.

4.3 BSM physics

An extensive report on the CLIC potential for new physics was recently published [14]. Given that the relative BSM contribution in many models is expected to increase with centre-of-mass energy, CLIC operating at the highest energy stage provides significant discovery potential for BSM physics. BSM searches can be pursued through direct and indirect measurements.

Direct searches at the highest energy stage of CLIC have the potential to find new particles up to about 1.5 TeV with a 1% accuracy on their mass measurement. Their observation is easier in comparison

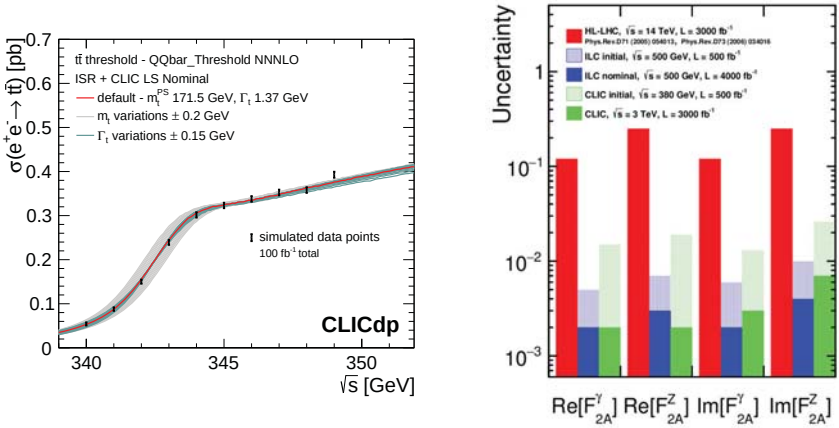

Figure 12: Top-quark threshold scan at CLIC with a total integrated luminosity of 100 fb^{-1} (left) [12]. Comparison of 68% C.L. limits on CP-violating form factors expected at the LHC, ILC and CLIC (right) [13].

to searches at hadron colliders thanks to the low background, and precision measurements of the new particle can also be performed after discovery. Such precise studies could also be conducted on new piarticles discovered at the LHC or the HL-LHC.

For indirect searches of BSM physics the CLIC strategy involves high precision measurements of parameters and couplings of the SM. In this way, the searches can reach sensitivities beyond the centre-of-mass energy of the collider. An example is reported in [15], where the process $e^+e^- \to \mu^+\mu^-$ is studied in the frame of the minimal anomaly-free Z' model. The 5σ discovery limit as a function of the integrated luminosity illustrates how the discovery can be extended to new particles with masses up to tens of TeV (Figure 13).

5 Summary and conclusions

CLIC is a mature international project with the aim of building an electron-positron linear collider with centre-of-mass energy spanning from a few hundred GeV up to 3 TeV. Thanks to its energy staging and the high luminosity foreseen, CLIC is a precision machine with a unique physics potential. Already in the first stage, the Higgs boson couplings and width can be measured with high precision. Moreover, a dedicated programme for the top quark is foreseen to extract its mass, width and other properties with very low uncertainties. At higher-energy stages, the programme will extend to search for rare Higgs processes and decays, as well as for BSM physics up to several tens of TeV with both direct and indirect measurements.

On the accelerator side, the technical challenges of such a high-energy linear collider are solved using a two-beam acceleration scheme, whose proof-of-concept was demonstrated. The CLIC environment and physics goals, especially in the highest energy stage, lead to strict requirements on both the detector and the software. The CLIC detector model, using cutting-edge technology and thoroughly optimised by simulation, has proven to fulfil them all.

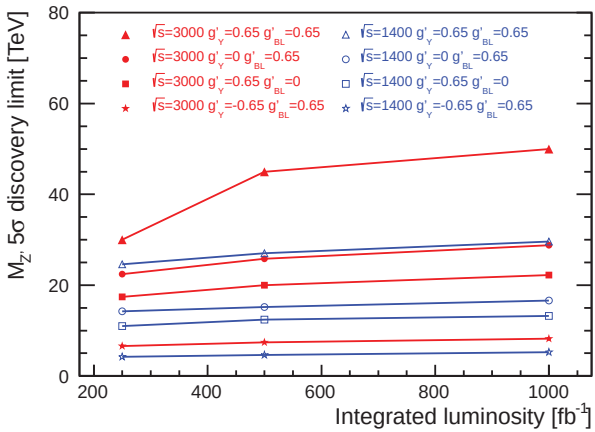

Figure 13: Z' mass discovery limit at 5σ from the measurement $e^+e^- \to \mu^+\mu^-$ as a function of the integrated luminosity and for different coupling values in the minimal anomaly-free Z' model [2].

References

[1] L. Linssen et al., eds., *CLIC Conceptual Design Report: Physics and Detectors at CLIC*, CERN-2012-003, CERN, 2012, arXiv: 1202.5940 [physics.ins-det].

[2] P. Burrows, et al (Eds), *Updated baseline for a staged Compact Linear Collider* (2016), CERN-2016-004, URL: http://dx.doi.org/10.5170/CERN-2016-004.

[3] T. Charles et al., *The Compact Linear e^+e^- Collider (CLIC) – 2018 Summary Report*, arXiv:1812.06018, 2018, URL: https://cds.cern.ch/record/2652188.

[4] P. G. Roloff, A. Robson, *Updated CLIC luminosity staging baseline and Higgs coupling prospects*, CLICdp-Note-2018-002 (2018), URL: https://cds.cern.ch/record/2645352.

[5] D. Arominski et al., *A detector for CLIC: main parameters and performance*, CLICdp-Note-2018-005 (2018), URL: https://cds.cern.ch/record/2649437.

[6] N. Alipour Tehrani et al., *CLICdet: The post-CDR CLIC detector model*, CLICdp-Note-2017-001 (2017), URL: http://cds.cern.ch/record/2254048.

[7] M. Frank et al., *DD4hep: A Detector Description Toolkit for High Energy Physics Experiments*, J. Phys. Conf. Ser. **513** (2013) 022010.

[8] S. Agostinelli et al., *Geant4-a simulation toolkit*, Nucl. Instr. Meth. Phys. A **506** (2003) 250, ISSN: 0168-9002, DOI: https://doi.org/10.1016/S0168-9002(03)01368-8, URL: http://www.sciencedirect.com/science/article/pii/S0168900203013688.

[9] M. Frank et al., *DDG4: A Simulation Framework using the DD4hep Detector Description Toolkit*, J. Phys. Conf. Ser. **664** (2015) 072017.

[10] E. Brondolin, A. Sailer, *Optimization of timing selections at 380 GeV CLIC*, tech. rep. arXiv:1811.00466, Geneva: CERN, 2018, URL: http://cds.cern.ch/record/2645355.

[11] H. Abramowicz et al., *Higgs physics at the CLIC electron-positron linear collider*, Eur. Phys. J. **C77** (2017) 475, DOI: 10.1140/epjc/s10052-017-4968-5, arXiv: 1608.07538 [hep-ex].

[12] H. Abramowicz et al., CLICdp, *Top-Quark Physics at the CLIC Electron-Positron Linear Collider* (2018), arXiv: 1807.02441 [hep-ex].

[13] W. Bernreuther et al., *CP-violating top quark couplings at future linear e^+e^- colliders*, Eur. Phys. J. **C78** (2018) 155, DOI: 10.1140/epjc/s10052-018-5625-3, arXiv: 1710.06737 [hep-ex].

[14] J. de Blas et al., *The CLIC Potential for New Physics*, tech. rep. arXiv:1812.02093, 2018, URL: https://cds.cern.ch/record/2650541.

[15] J.-J. Blaising, J. D. Wells, *Physics performances for Z' searches at 3 TeV and 1.5 TeV CLIC* (2012), arXiv: 1208.1148 [hep-ph].

Muon System for Spin Physics Detector at NICA

V. Abazov, G. Alexeev, G. Golovanov*, S. Kutuzov, A. Piskun, I. Prokhorov, A. Samartsev, A. Skachkova,V. Tokmenin, A. Verkheev, L. Vertogradov, N. Zhuravlev

Joint Institute for Nuclear Research, 141980 Dubna, Russia

Abstract. The SPD project is under preparation at the second interaction point of NICA collider. The main purpose of this experiment is the study of the nucleon spin structure with high luminosity proton and deuteron beams. Both beams will be effectively polarized. One gives us unique possibilities to investigate the wide range of polarized phenomena. One of the main detectors of the installation is the Range System which provides the identification of muons. The latest results on the Range System Prototype tests are presented.

1 Introduction

One of the proposed modes of the Nuclotron-based Ion Collider Facility accelerator complex (NICA) designed at the Joint Institute for Nuclear Research (JINR, Dubna, Russia), is a collision of high luminosity polarized proton and deuteron beams. The plans for basic specification of polarization states and combinations available at NICA include: (a) pp collisions with longitudinal and transverse polarization with respect to a particle velocity; (b) dd collisions up to 4 GeV/c momentum with vertical direction of polarization, changing the polarization direction by 90°; (c) a possibility to collide any available polarized particles (pp, dd and pd). The polarization control system is going to be able to keep longitudinal and transverse polarization degree up to 70% with the collision luminosity $10^{32} cm^{-2} s^{-1}$ over the particle momentum range $(2 - 13.5)$ GeV/c. The above specification offers unique prospects to investigate a wide range of polarized phenomena. The effects of longitudinal and transverse distributions of the partons within a hadron can be experimentally investigated by studying the Drell-Yan (DY) [1, 2] processes in collisions of polarized and unpolarized beams. One provides opportunities to derive transverse-momentum dependent parton distribution functions, e.g. transversity, pretzelocity, Sivers, Boer-Mulders, and Worm-Gears by measuring azimuthal asymmetries [3, 4]. While the unpolarized gluon content of a proton is widely investigated in collider and fix-target experiments the understanding of the polarized parton distribution functions

* E-mail: georgy.golovanov@cern.ch

strongly need an experimental input. Studies of the direct photon production processes allow access to the information of the gluon structure of the nucleon [5]. The opportunity to have high luminosity collisions of polarized and unpolarized protons and deuterons at the NICA collider allows studying the spectroscopy of quarkonia as well as a great variety of spin dependent effects in various exclusive

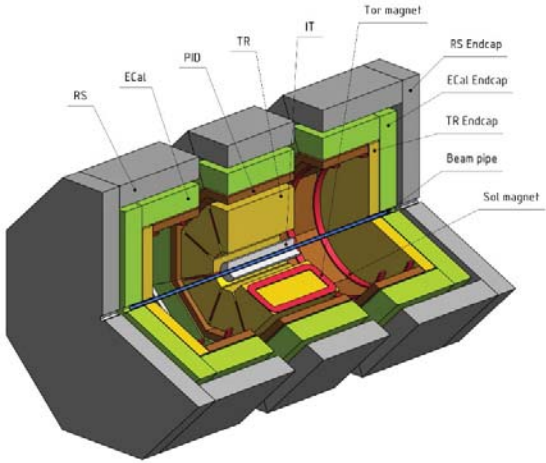

processes, diffraction and elastic reactions.

Figure 1: Schematic view of the SPD detector.

The wide range of physics motivation topics suggests a detector designed to meet the spin physics capabilities of the NICA collider. The Spin Physics Detector (SPD) is a specialized detector aimed at studying nucleon spin structure that remains one of the key topics of the modern high-energy physics. The proposed detector design should satisfy the following requirements: (a) close to 4π geometrical acceptance; (b) high-precision ($\sim 50\mu m$) and fast vertex detector; (c) high-precision ($\sim 100\mu m$) and fast tracking system; (d) good particle identification capabilities; (e) efficient muon range system; (f) good electromagnetic calorimeter; (g) trigger and data acquisition system able to cope with rates at $10^{32} cm^{-2} s^{-1}$ luminosity; (h) modularity and easy access to the detector elements, that makes possible further reconfiguration and upgrade of the facility.

A concept matching these requirements is shown in Fig. 1. The SPD length along the beam axis is 9.2 *m*, the diameter is 6.8 *m* and it consists of 3 parts: two end-caps and a barrel part. Each part has an individual magnet system: the endcaps – solenoidal coils, the barrel – toroidal magnetic system. The main detector systems are as follows: Range System (RS), Electromagnetic Calorimeter (ECal), Time-Of-Flight system (PID), main Tracker (TR) and Vertex Detector (IT). The estimated total weight of the facility is about 1800 ton.

2 SPD Muon Range System

The concept for SPD Muon System is based on a range system technique to register muons in a laminated iron absorber. Mini-Drift Tubes (MDT) [6, 7] with two-coordinate readout of track information (the wires and the orthogonal strips) will be used for charged particle detection in the RS. The Mini-Drift Tube tracking detector is a type of aluminum Iarocci tubes (streamer tubes) that consist of an array of cells with anode wire in the center but uses proportional mode of operation instead of streamer one. The eight-wires MDT detector (see Fig. 2) comprises the following parts: metallic cathode-aluminum extruded comb-like profile, anode wires and plastic envelope for gas tightness. The used gas is a mixture of $Ar: CO_2$ $(70: 30)$ at atmospheric pressure. The chamber with various number of MDT tubes and up to few meters long can be assembled to have hundreds of cells in a detecting plane. One of the advantages of using MDTs for RS lies in a fact that the detector is made of a simple repetitive cell with properties defined by an individual cell.

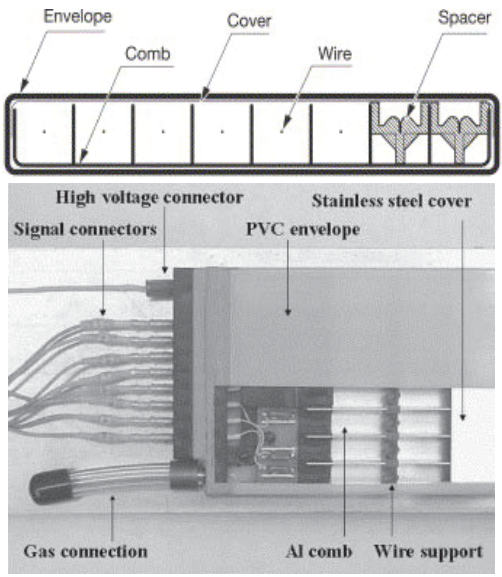

Figure 2: A single MDT tube and its cross section; individual wire cell has $1 \times 1\ cm^2$ cross section; for reading out the induced signals on strips the stainless-steel cover may be removed.

The main purpose of the Muon System is the identification of primary muons with maximal possible separation from background contamination originating mostly from primary low-momenta pions and secondary decay muons in full SPD

energy at $\sqrt{s_{pp}} = 27\ GeV$ resolves muons and hadrons with nearly 100% efficiency above $1\ GeV/c$ by obviously different response pattern. The separation of muons and pions below $1\ GeV/c$ is less efficient and requires test beam measurements for calibration. The resolution of Muon System is enough to use it as a coarse sampling hadron calorimeter (from 30 to 60 mm of iron). It is also very important feature for neutron registration.

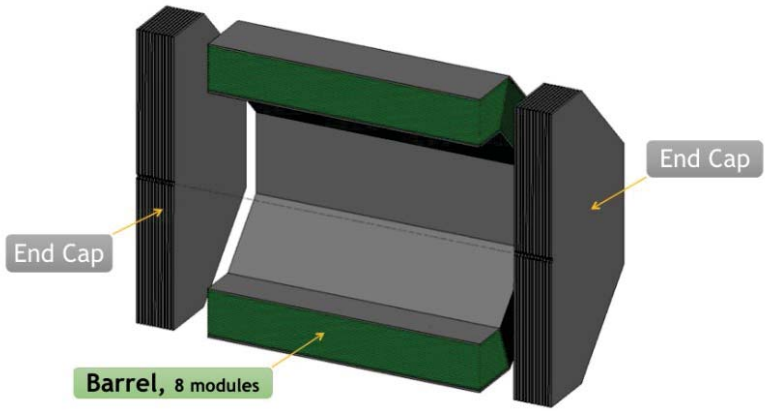

Figure 3: The cross section of the SPD Muon Range System concept.

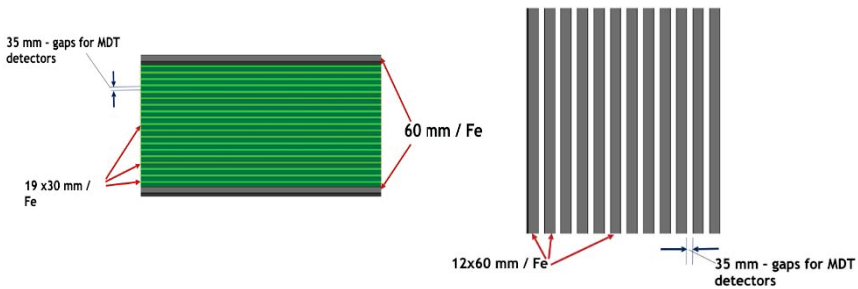

Figure 4: The structure of the barrel (left) and the endcap (right) parts of the SPD Muon Range System.

The Range System is a well-known solution for detecting muons stopped by the absorber and those crossing the iron. In the former case one may even roughly estimate the energy of muons keeping in mind the stopping power of iron absorber (about 1.5 GeV/m) for the relativistic muons with $dE/dx = 2\ MeV/g$. The Muon System consists of eight barrel and two endcap modules. The cross section of the RS 3D model is shown in Fig. 3. Figure 4 illustrates the detailed structure of the barrel and endcaps.

In the barrel part the granularity of the iron absorber is 30 mm (60 mm for the inner and outer layers only). The nineteen 30 mm layers of absorber with 35 mm gaps for MDT detectors in between and two wrapping layers give about 4 nuclear interaction lengths (λ_I) of material. The twelve 60 mm endcap absorber layers giving about $4.2\lambda_I$ of total material thickness are used for better detection/absorption of muons with higher momenta in forward direction. The SPD Muon System weights around 1650 ton considering the designed 8 m length of the barrel part and 8.3 m total height of the endcap modules.

3 SPD Muon Range System R&D program

To test and optimize different aspects of the SPD Muon Range System performance based on MDTs with two-coordinate readout the Range System Prototype (RSP) has been constructed. The Range System Prototype (weighing about 8 ton) has 20 detecting layers of MDTs alternating with 30 and 60 mm thick absorber plates and two "zero" bi-layers. Figure 5 illustrates schematic view of the RSP and its installation on the T9/PS test beam at CERN. It is designed as '2 in 1' device: the structure of the absorber plates reproduces barrel or endcap subsystems of the Muon System depending on the particular direction of the beam and number of engaged layers. The prototype is equipped with 270 (~ 1 m long) MDT detector units, 22 strip boards ($\sim 1 \times 1\ m^2$ size, 3 cm wide strips), and corresponding electronics (2160 channels for wire readout and 760 for strip readout). The R&D program includes calibration of the system response to a variety of particles at different energies, muon/hadron separation performance, pattern recognition algorithm testing as well as tuning of the Monte Carlo (MC) simulation parameters.

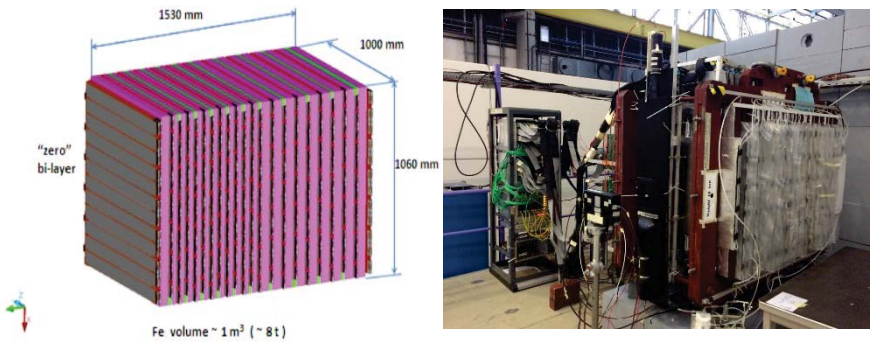

Figure 5 (*color online*): The '2 in 1' RSP scheme: 30 and 60 mm absorber plates (pink color) reproduce barrel and endcap parts of the Muon System; detecting layers of MDTs and strips are positioned in between the plates; two types of "zero"

bi-layers are put outside the absorber (left). The RSP installed on the T9/PS test beam at CERN (right).

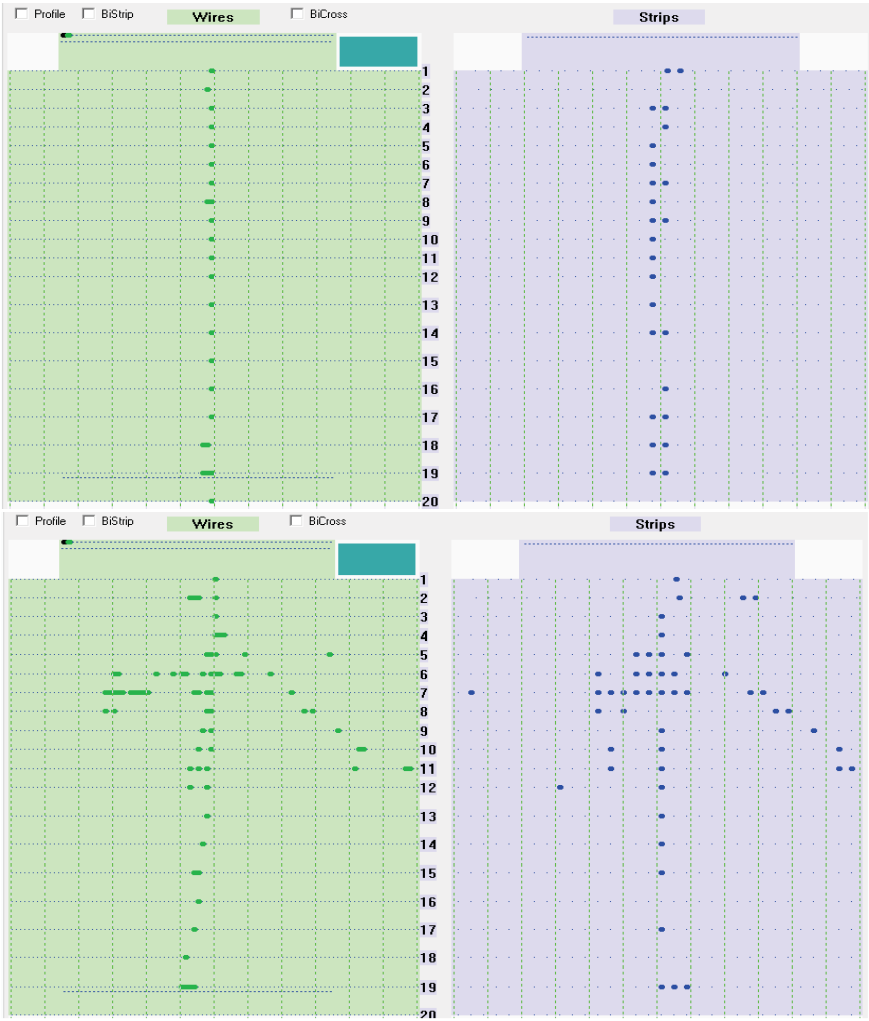

Figure 6 (*color online*): A sample of hit profile in the Range System Prototype for a muon with $p = 10\ GeV/c$ (top) compared to a pion with the same momentum (bottom). Left side plots correspond to hits produced in MDT wires (green) and right plots to the ones received from strips (purple).

A hit profile in RSP corresponding to a particular kind of particles with a certain momentum has a specific pattern. Low momentum pions ($p < 1.0\ GeVc$) are

almost indistinguishable from muons with the same momentum. Finding variables sensitive to differences in such patterns is directly connected to the possibility of separation between muons and pions, e.g. the depth of particles penetration in layered structure of the Range System can be used as an input to various machine learning techniques. Increasing energy of pions significantly changes the profile of hits, forming a shower of secondary particles with momentum up to 10 GeV/c. Figure 6 shows an example of hit profile in the Range System Prototype for a muon with $p = 10\ GeV/c$ compared to a pion with the same momentum.

Hadron calorimetry is implemented by measuring total number of hits in an event (proton and antiproton data are presented in this paper). The prototype's trigger system is equipped with two scintillation counters of time-of-flight (for momenta up to 5 GeV/c) which fixes also a beam entrance spot and Čerenkov counters (for momenta greater than 5 GeV/c) with CO_2 variable gas pressure to separate electrons/pions/muons. Various combinations of layers can be used to represent different parts of Muon Range System. Range System Prototype was calibrated for proton/antiproton responses by selecting of prototype total thickness with chosen sampling (corresponding to barrel and endcap structures). The same calibrations will be repeated once the SPD Muon Range System design is finally established. A proton and antiproton hit multiplicities as a function of particle kinetic energy using RSP sampling equivalent to the barrel part of the SPD Range System are shown on Fig. 7. When proton and antiproton annihilate the energy deposition of the products adds up to twice the rest mass of the proton ($\sim 2\ GeV$). This effect is clearly visible on Fig. 7. Few additional measurements at different momenta for antiprotons will allow to estimate the entire calibration line.

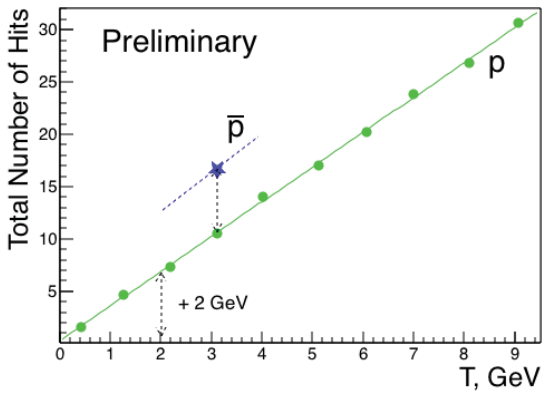

Figure 7 (*color online*): Proton (green points) and antiproton (blue star) total number of hits as a function of particle kinetic energy using RSP sampling and total thickness equivalent to the barrel part of the SPD Range System.

Another very important feature of the proposed SPD Range System is a possibility to identify neutrons and estimate their energy. During the RSP beam tests it was demonstrated by use of the same charged particles monochromatic

(5 GeV/c) beam at T9/PS with a carbon target as a neutron source installed in front of the first prototype's detecting layers along with scintillators for vetoing protons. A distinctive feature of neutron hit profile is an absence of incoming charged track. Figure 8 illustrates an example of a neutron response in the Range System Prototype as compared to a proton's one.

4 Conclusion

The SPD project is under preparation at the NICA collider. The SPD Muon Range System being based on the Mini-Drift Tubes as a detector followed by a robust analogue amplifier/discriminator technique supplemented by a digital data acquisition is up to its tasks: identification of the primary muons, optimal separation from background hadronic contamination, and coarse hadron calorimetry.

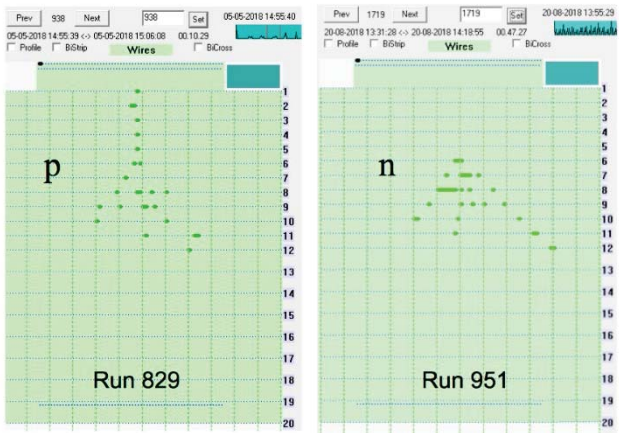

Figure 8: A sample of hit profile in the Range System Prototype for a proton (left) compared to a neutron proton (right).

References

[1] S. D. Drell and T. M. Yan, "Massive Lepton Pair Production in Hadron-Hadron Collisions at High-Energies," Phys. Rev. Lett. **25** (1970) 316 Erratum: [Phys. Rev. Lett. **25** (1970) 902].

[2] S. D. Drell and T. M. Yan, "Partons and their Applications at High-Energies," Annals Phys. **66** (1971) 578 [Annals Phys. **281** (2000) 450].

[3] A. Sissakian, O. Shevchenko, A. Nagaytsev, O. Denisov and O. Ivanov, "Transversity and its accompanying T- odd distribution from Drell-Yan

processes with pion-proton collisions," Eur. Phys. J. C **46** (2006) 147 [hep-ph/0512095].
[4] I. A. Savin *et al*., "Spin Physics Experiments at NICA-SPD with polarized proton and deuteron beams," EPJ Web Conf. **85** (2015) 02039 [arXiv:1408.3959 [hep-ex]].
[5] P. Aurenche, M. Fontannaz, J. P. Guillet, E. Pilon and M. Werlen, "A New critical study of photon production in hadronic collisions," Phys. Rev. D **73** (2006) 094007 [hep-ph/0602133].
[6] V. M. Abazov, G. D. Alexeev, Y. I. Davydov, V. L. Malyshev, V. V. Tokmenin and A. A. Piskun, "Comparative analysis of the performance characteristics of mini-drift tubes with different design," Instrum. Exp. Tech. **53** (2010).
[7] V. M. Abazov, G. D. Alexeev, Y. I. Davydov, V. L. Malyshev, A. A. Piskun and V. V. Tokmenin, "Coordinate accuracy of mini-drift tubes in detection of an induced signal," Instrum. Exp. Tech. **53** (2010) 648.

Selected results of data analysis from the BM@N experiment with ion beams

Julia Gornaya[2], *Mikhail* Kapishin[1], *Vasiliy* Plotnikov[1], *Gleb* Pokatashkin[1,*], *Igor* Rufanov[1], *Veronica* Vasendina[1], and *Alexander* Zinchenko[1]

[1]Joint Institute for Nuclear Research (JINR)

[2]National Research Nuclear University (MEPhI)

Abstract.
The Baryonic Matter at Nuclotron (BM@N) is the first experiment at the NICA-Nuclotron complex, JINR, Dubna. This experiment at fixed target is aimed to study interactions of relativistic heavy ion beams with kinetic energy from 1 to 4.5 GeV per nucleon. First results of the analysis of minimum bias interactions of deuteron and carbon beams with kinetic energy of 4 AGeV with different targets are discussed. Some preliminary results from the data collected in the recent experimental run with the argon beam are also presented.

1 Introduction

A new BM@N experiment is designed to study properties of dense nuclear matter in nucleus-nucleus collisions. The NICA-Nuclotron complex will provide several kinds of heavy ion beams up to gold of kinetic energy from 1 to 4.5 AGeV and intensity up to 10^7 per second. The Nuclotron beam energy range is suitable for studying strange and multi-strange particles (Λ, Ξ, Ω) produced close to the kinematic threshold. As is clear from Figure 1, in heavy ion collisions, strange hadrons can coalesce with light nuclear fragments and form hypernuclei [1]. The maximum in the hypernuclei production rate is predicted at $\sqrt{s_{NN}} \sim$ 4–5 GeV, which is close to the Nuclotron beam energy range. Studying the hypernuclei production processes will provide insight into the properties of the hyperon-nucleon and hyperon-hyperon interactions.
The first methodical paper describing Λ^0-hyperon reconstruction in interactions of the deuteron beam with different targets (December 2016) is published [3]. The paper also describes the data analysis methods such as the detector alignment and Lorentz shift correction, primary vertex reconstruction, and technical details of the central tracker such as the spatial and momentum resolution.
In the last experimental run performed in March 2018, the research program included the measurement of inelastic reactions of the argon and krypton beams with various targets. In particular, the measurement was focused on hyperon reconstruction in the central tracker, identification of charged particles and nuclear fragments with the time-of-flight system, reconstruction of γ and multi-γ states with the electromagnetic calorimeter. A separated run of the BM@N experiment

performed in the carbon beam with the liquid H_2 target was devoted to studies of short-range correlations (SRC) [5].

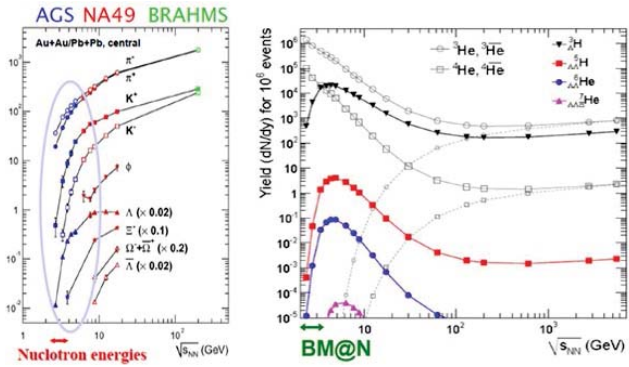

Figure 1. Left plot: Yields of mesons and (anti-) hyperons measured in different experiments as a function of the energy per nucleon- nucleon collision in c.m.s. for Au + Au and Pb + Pb collisions [4]. The Nuclotron beam energy range corresponds to $\sqrt{s_{NN}}$ = 2.3–3.5 GeV. Right plot: Yields of hypernuclei predicted by the thermal model [2] for Au + Au collisions as a function of the nucleon-nucleon collision energy in c.m.s. Predictions for the yields of ^3He and ^4He nuclei are presented for comparison. The Nuclotron BM@N energy range is specified.

2 Detector geometry

2.1 Conceptual detector setup

Figure 2 shows a sketch of the BM@N setup. The detailed description of the BM@N geometry is presented in [6]. The basic detector setup comprises the central tracker inside the analyzing magnet (forward silicon detectors and GEM detectors), outer tracker based on drift chambers (DCH) and cathode strip chambers (CSC), electro-magnetic calorimeter behind the magnet, two time-of-flight detectors (mRPC-1 and mRPC-2), zero degree calorimeter (ZDC), start T0, and trigger detectors around the target.

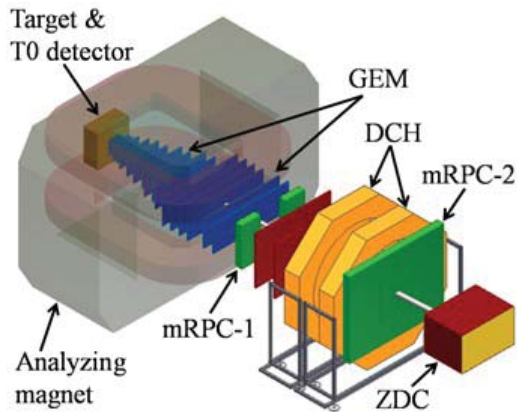

Figure 2. Schematic view of the BM@N setup.

The main advantage of the setup is a large aperture analyzing magnet with a 1 m gap between the poles. The magnet aperture is filled with coordinate detectors, which sustain high multiplicities of particles and are operational in the strong magnetic field. Two walls of time-of-flight detectors situated "near to magnet" and "far from magnet" serve to identify particles with low and high momentum. The link between the central tracker and time-of-flight detectors is performed by the outer tracker.

2.2 Central tracker

The central tracker of the BM@N experiment is based on two-coordinate triple Gas Electron Multipliers (GEM) [7]. The GEM detectors have the established technology developed at the CERN workshop and have been used in various experiments (COMPASS, JLAB, STAR, CMS).
Based on the analysis of experimental data collected in the deuteron run, the central tracker was extended with two-coordinate planes of the forward silicon detector designed to improve the primary vertex reconstruction [8]. The GEM tracker was upgraded to six large area detectors. The central tracker configuration was tuned to measure soft decay products of strange V0 particles. The positions of the GEM and silicon detectors were optimized using Monte-Carlo simulation. Figure 3 shows the central tracker configurations in the recent runs.

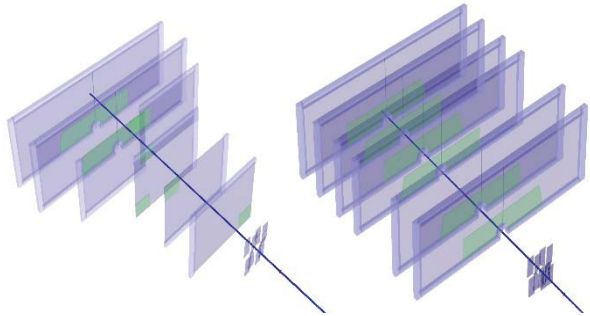

Figure 3. Left plot: BM@N setup used in the carbon run. Right plot: BM@N setup used in the Ar/Kr run.

3. Event reconstruction and Monte-Carlo simulation

The track reconstruction method was based on a so-called "cellular automaton" approach [9]. The tracks found were used to reconstruct primary and secondary vertices using the "KFparticle" formalism [10]. In fact, both (track and vertex) reconstruction packages were adapted from the CbmRoot software framework [11] where they were used extensively for Monte-Carlo performance studies of the CBM detector Silicon Tracking System (STS). The event samples of $C+A$ collisions were produced using the DCM-QGSM event generator [12–15]. The passage of particles through the setup volume was simulated with the GEANT package integrated into the BmnRoot software framework [16]. To describe the GEM detector response in the magnetic field, the microsimulation package Garfield++ [17] was used. The package gives a very detailed description of the processes inside the GEM detector, including the drift and diffusion of ionization electrons in electric and magnetic fields and electron multiplication in GEM foils, so that the output signal from the readout plane can be reproduced.

4. Results and discussion

Some analysis results for the experimental data collected in the carbon and argon beams are presented below.

4.1 Primary vertex reconstruction

Figure 4 shows distributions of the primary vertex along the beam (Z-coordinate) reconstructed in the carbon and argon runs with different targets positions: at -24 cm for the carbon run and at 0.6 cm for the argon run. One can see that the resolution obtained for the argon beam is better because of a higher track multiplicity, a better detector coordinate resolution (in particular, due to additional silicon detector planes), and a smaller distance from the target to the first detector station. The reconstructed experimental Z-coordinate distribution width ($\sigma \simeq 0.6$ cm) for the C + Al interaction vertices was well reproduced by the simulation.

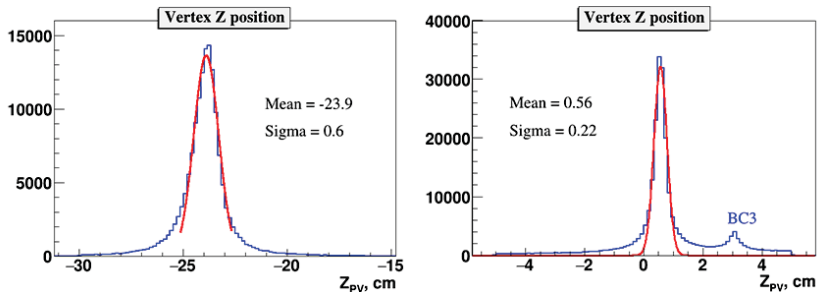

Figure 4. Reconstructed primary vertex along the beam. Left plot: *C + Al* interactions. Right plot: *Ar + Al* interactions. The small bump in the *Ar*-beam distribution is due to interactions in the trigger counter BC3.

4.2 Beam momentum determination

To measure the carbon beam momentum in the central tracker situated in the magnetic field of 0.6 T, the experimental data without a target were collected. Since the carbon ionization is 36 times as large as that of deuteron, the high voltage applied to GEM detectors was reduced in order for the output signal to fit the electronics dynamic range.

Figure 5 shows the momentum distribution for the reconstructed carbon beam particles with a rigidity *p/q* of 8.67 GeV/*c*. Here *p* is the beam particle momentum and *q* is its charge. It is the value that is measured in any magnetic spectrometer. The obtained beam rigidity resolution is ~ 5.5 %. The momentum resolution for reconstructed tracks produced in interactions (like protons or π^--mesons) should be much better because their momenta are lower than the beam particle momentum and their trajectories have larger curvatures.

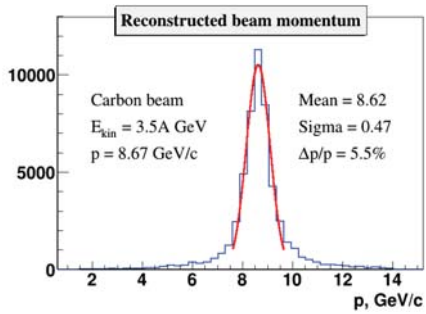

Figure 5. Carbon beam rigidity measured in the central tracker.

4.3 Λ^0 and K_S^0 reconstruction

Λ^0 hyperons were reconstructed using their decay mode into proton and π^-. The signal event topology (decay of a relatively long-lived particle into two tracks) defined the selection criteria: relatively large distance of the closest approach (DCA) of decay products to the primary vertex, small track-to-track separation in the decay vertex, relatively large decay length of the mother particle. Since the particle identification was not used at this analysis stage, all the positive tracks were considered as protons (π^+ for K_S^0) and all the negative tracks as π^-. The kinematic reflection of K_S^0- decay into the (p,π^-) effective mass spectrum contributes to higher masses (around 1209 MeV) of (p,π^-) than the mass of the Λ^0 hyperon of 1115.6 MeV and does not mimic the Λ^0 hyperon signal. Vice versa, the kinematic reflection of Λ^0 - decay contributes to lower masses (around 344 MeV) in (π^+,π^-) effective mass spectra than K_S^0 mass of 498 MeV and is not mixed with the K_S^0 signal. In the Lambda reconstruction algorithm candidates to protons are selected with much higher momentum than candidates to π^-. This requirement eliminates the background from π^+ among the proton candidates.

The data samples collected with three targets (*C, Al, Cu*) were analyzed to reconstruct Λ^0-hyperons and K_S^0 in the carbon run. The left plot of Figure 6 shows the obtained invariant mass distribution of proton, π^--pairs. The right plot of Figure 6 shows π^+, π^- invariant mass spectrum. One can see the Λ^0-peak with $\sigma \sim 2.8$ MeV. The significance of the K_S^0 reconstructed peak in the right plot of Figure 6 is not very high. It can be explained by the fact that the central tracker configuration was tuned to measure relatively high-momentum beam particles and the geometric acceptance for relatively soft decay products of strange V0

particles was rather low. The Monte-Carlo simulation showed that only ~ 4 % of Λ^0 and ~ 0.8 % of K_S^0 could be reconstructed.

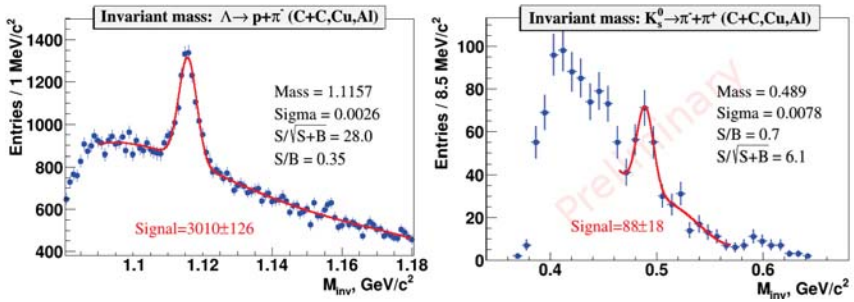

Figure 6. Left plot: Invariant mass spectrum of proton+ π^- pairs. Right plot: Invariant mass spectrum of π^++ π^- pairs.

Figure 7 shows a "first look" result of the invariant mass spectrum of proton-π^- pairs reconstructed in interactions of the argon beam with targets. The result was obtained on a small fraction of the collected statistics and without dedicated tuning of the track reconstruction algorithm.

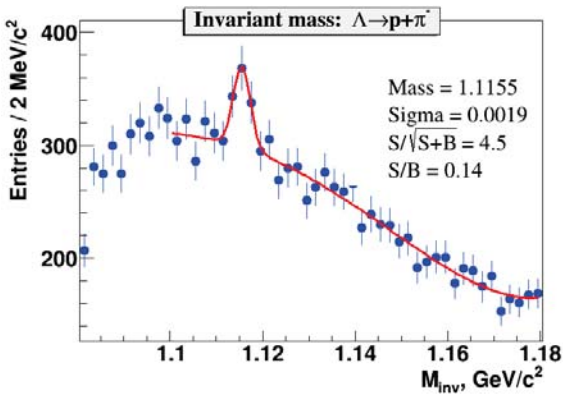

Figure 7. Invariant mass spectrum of proton+ π^- pairs reconstructed in interactions of the argon beam with targets.

5 Summary and plans

The BM@N experiment is in the starting phase of its operation and has recorded data

on interactions of the carbon, argon, and krypton beams of several energies with different targets. Experimental data of minimum bias interactions of the carbon beam with different targets were analyzed with the aim to reconstruct tracks, primary and secondary vertices using the central tracking detectors. The signals of Λ^0-hyperon and K_S^0 were reconstructed in the invariant mass spectra of particles originated from secondary vertices. To improve the vertex and momentum resolution and reduce the background under the Λ^0-hyperon signal, two extra silicon planes were installed into the central tracker. The BM@N setup will be extended to the full configuration to adapt its performance for measurements of interactions of heavier ion beams with targets.

Acknowledgments
This work was partially supported by the Ministry of Science and Education of the Russian Federation, grant N 3.3380.2017/4.6, and by the National Research Nuclear University MEPhI in the framework of the Russian Academic Excellence Project (contract No. 02.a03.21.0005, 27.08.2013).

References

[1] J. Steinheimer, H. Stoecker, I. Augustin, A. Andronic, T. Saito and P. Senger, Strangeness at the international Facility for Antiproton and Ion Research, Prog. Part. Nucl. Phys., **62**, 313 (2009)
[2] C. Blume, J. Phys. G, **S57**, 31 (2005)
[3] D. Baranov et. al (BM@N Collaboration), First results from BM@N technical run with deuteron beam, PEPAN Letters, **15**, 2, 148-156 (2018)
[4] A. Andronic et al., Phys. Lett. B, **695**, 203 (2011)
[5] Probing Short Range Correlations BM@N Project, http://bmnshift.jinr.ru/wiki/lib/exe/fetch.php?media=proposal_bmn_dubna_final.pdf
[6] BM@N Project report, http://bmnshift.jinr.ru/wiki/lib/exe/fetch.php?media=bmnproject_2016.pdf
[7] BM@N Technical Design Report for the GEM Tracking System, http://bmnshift.jinr.ru/wiki/lib/exe/fetch.php?media= tdr_gem_may2017_v1.doc
[8] N. Zamiatin, Status of Silicon Detector for next Run, http://bmnshift.jinr.ru/wiki/lib/exe/fetch.php?media=sildet_bm_n_21.12.17.ppt
[9] V. Akishina, I. Kisel, Time-based Cellular Automaton track finder for the CBM experi- ment J. Phys. Conf. Ser., **599**, 012024 (2015)
[10] S. Gorbunov, I. Kisel, Reconstruction of decayed particles based on the Kalman filter, CBM-SOFT-note-2007-003 (2007)
[11] http://cbmroot.gsi.de
[12] V. Toneev, K. Gudima, Particle Emission In Light And Heavy Ion Reactions, Nucl. Phys. A., **400**, 173 (1983)

[13] N. Amelin, K. Gudima, V. Toneev, Ultrarelativistic nucleus-nucleus collisions within a dynamical model of independent quark-gluon strings, Sov. J. of Nucl. Phys., **51**, 1093 (1990)
[14] N. Amelin, L. Bravina, L. Csernai, V. Toneev, K. Gudima, S. Sivoklokov, Strangeness production in proton and heavy ion collisions at 200-A-GeV, Phys. Rev. C., **47**, 2299 (1993)
[15] K. Gudima, S. Mashnik, A. Sierk, LANL Report LA-UR01-6804 (2001)
[16] http://mpd.jinr.ru
[17] http://garfieldpp.web.cern.ch/garfieldpp/

The front-end electronics of the Mu2e electromagnetic calorimeter

N. Atanov[a], V. Baranov[a], J. Budagov[a], F. Cervelli[e], F. Colao[b], M. Cordelli[b], G. Corradi[b], Y.I. Davydov[a], S. Di Falco[e], E. Diociaiuti[b,j], S. Donati[e,g], R. Donghia[b,k], B. Echenard[c], S. Giovannella[b], V. Glagolev[a], F. Grancagnolo[i], F. Happacher[b], D.G. Hitlin[c], M. Martini[b,d], S. Miscetti[b], T. Miyashita[c], L. Morescalchi[e,f], P. Murat[h], E. Pedreschi[e], G. Pezzullo[e], F. Porter[c], F. Raffaelli[e], M. Ricci[b,d], A. Saputi[b], I. Sarra[b], F. Spinella[e], G. Tassielli[i], V. Tereshchenko[a], Z. Usubov[a] and R.Y. Zhu[c]

a Joint Institute for Nuclear Research, Dubna, Russia
b Laboratori Nazionali di Frascati dell'INFN, Frascati, Italy
c California Institute of Technology, Pasadena, United States
d Università "Guglielmo Marconi", Roma, Italy
e INFN Sezione di Pisa, Pisa, Italy
f Dipartimento di Fisica dell'Università di Siena, Siena, Italy
g Dipartimento di Fisica dell'Università di Pisa, Pisa, Italy
h Fermi National Laboratory, Batavia, Illinois, U.S.A.
i INFN Sezione di Lecce, Lecce, Italy
j Dipartimento di Fisica dell'Università di Roma Tor Vergata, Rome, Italy
k Dipartimento di Fisica dell'Università degli Studi Roma Tre, Rome, Italy

The main goal of Mu2e experiment at Fermilab [1] is to found for Charged Lepton Flavor Violation (CLFV) in the neutrinoless conversion of a negative muon into an electron in the field of nucleus. For 27Al nucleus, which is planed to be used as a target, the energy of such electrons should be at the level E_e = 104:97 MeV [2]. The Standard Model extended with neutrino masses mechanism predicts the rate for this process as $O(10^{-52})$[3], so any signal observed with higher rate would be explained with new physics models. The experiment Mu2e is designed to reach the single event sensitivity (SES) of 2.4*10^-17 in three years of running [1], that improves significantly the current experimental limit of the rate $R\mu e(Au)<7*10^{-13}$@ 90% C.L. set by the SINDRUM II experiment [4]

The Mu2e detector consist of a low mass straw tracker that provides an accurate track momentum measurement and the electromagnetic calorimeter for powerful μ/e particle identification. The calorimeter will be built from ~1400 CsI scintillation crystals with sizes 3.4x3.4x20cm^3. At the moment, the first probe section, so called Module-0, have been built from 50 crystals, installed and being tested [5], and it is planed to start assembly of the main calorimeter disks in the 2019.

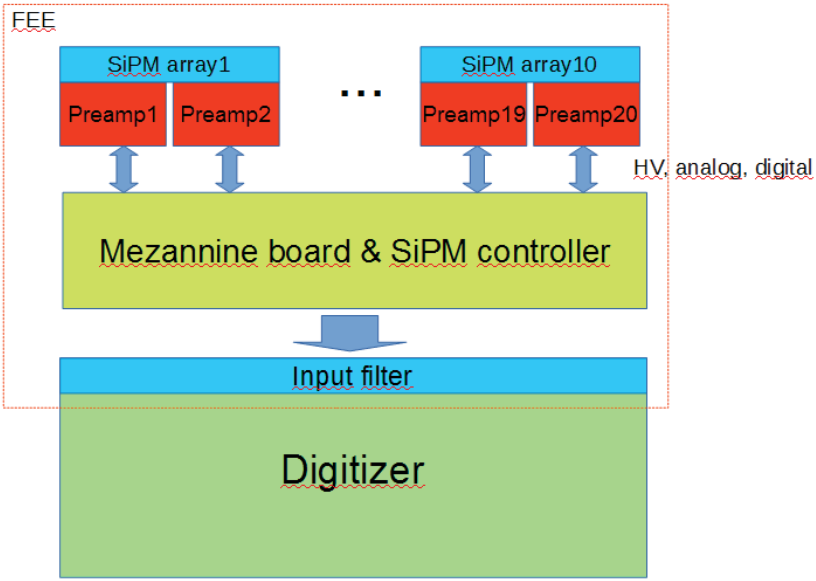

Fig.1 Simplified scheme of electromagnetic calorimeter

The simplified scheme of electromagnetic calorimeter FEE is presented on fig.1. The optical signal from crystal is detected by SiPM array, and to collect one 2 arrays of 6 UV-extended SiPMs are used. Than weak electrical signal is amplified and formed in FEE preamplifier (fig. 2), which is placed at the end of each crystal and each preamplifier is a multi-layer, double-sided, discrete board directly connected to photosensor. Besides amplification function preamplifier provides a regulation of the SiPMs bias voltage with custom digitally controlled low-dropout regulator (LDO).

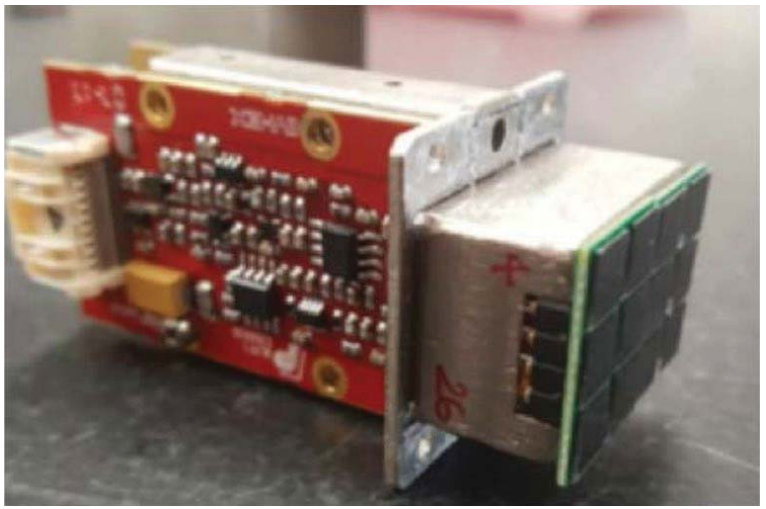

Fig.2. FEE preamplifier with SiPM array connected.

Then preamplifiers are connected to “hub”, so called mezannine board. Each mezzanine board holds 20 preamplifiers, i.e. serves to readout 10 crystals. Another function of mezannine board is a HV distribution and digital control of preamp, in particular LDO, which gives HV to SiPM array.
The design of FEE preamplifier have several constrains and requirements that gives us detector construction. They are:
1)SiPM 6x6 array of photodiodes similar to Hamamatsu capacity has value of 860 pF, that requires special solutions to stabilize preamplifier;
2)radiation hardness, maximum dose ~ 100kRad & strong neutron integrated flux at the level of 10^12 n/cm2 for 3 years;
3)heat efficiency because of a 10-4 Torr vacuum - all detectors are supposed to be placed in vacuum vessel;
4)constant 1T axial magnetic field strength;
5)linearity in wide input current range from 2uA to 2mA, due to variety of particle in background;
6)stable DC/DC conversion in the LDO regulator for all current range.

Preamplifiers that should satisfy this constraints were created in LNF,INFN in collaboration with JINR group. In May 2017 first section made of 40 CsI crystals was built in LNF,INFN, Frascati and the first teastbeam to estimate electromagnetic calorimeter prototype efficiency has been proceed[5]. It demonstrated good results in charge-energy determination, but several changes were necessary to introduce to the preamplifier scheme. Now next version of preamplifier is produced and is subjected to radiation hardness tests.

The structure of FEE preamplifier is presented on fig.3. This is complex device, that consist of next blocks:
1)input transistor cascade;
2)pulse shaper;
3)linear regulator (LDO) for SiPM array;
4)gain switch;
5)current monitor;
6)charge pump for test pulses;
7)temperature sensor.

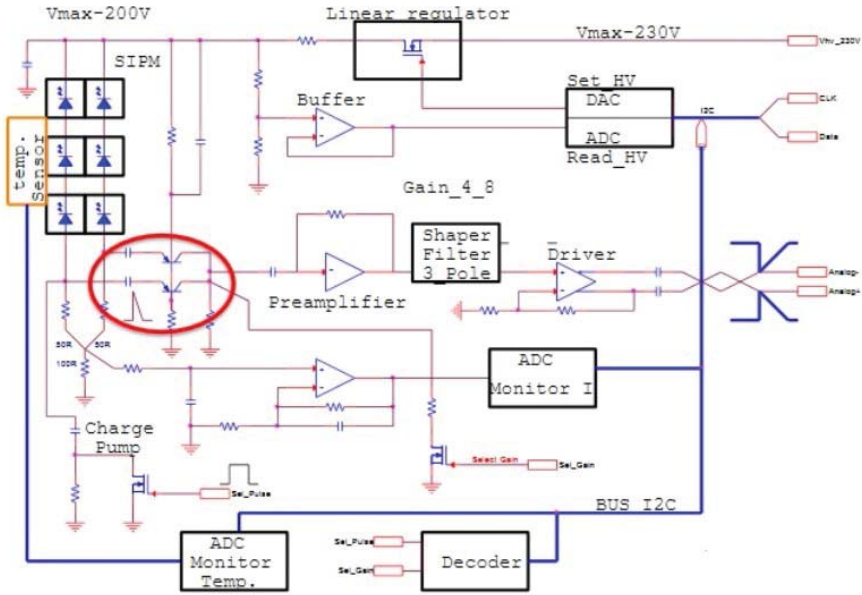

Fig.3. FEE preamplifier simplified scheme.

The the main performance characteristics of preamplifier designed are:

- Input resistance 33 Ohm;
- Output resistance 100 Ohm
- Diff. output range 2V
- Gain for current 4-8
- Bandwidth 40MHz
- Noise 2nV/√Hz
- Power supply +8V
- Power consumption 45mW
- Rise time 25ns
- Fall time <120ns

To provide HV to SiPM array LDO with analog and digital feedback is used. Pass transistor block based on NMOS depletion-mode transistor. It is designed to provide stable DC output for load current from 2uA to 2mA. Analog feedback is formed by divider, buffer and error amplifier. Digital feedback consist of ADC, DAC and it is controlled via I2C interface. LDO performance is presented on fig.4,5: output noise is calculated for DC/DC conversion from Vin=200V to Vout=160 with a constant load current I_load=2mA (maximum) and a total noise level for high current is less then 3 mV peak-to-peak, temperature coefficient is TC=-23ppm/°C.

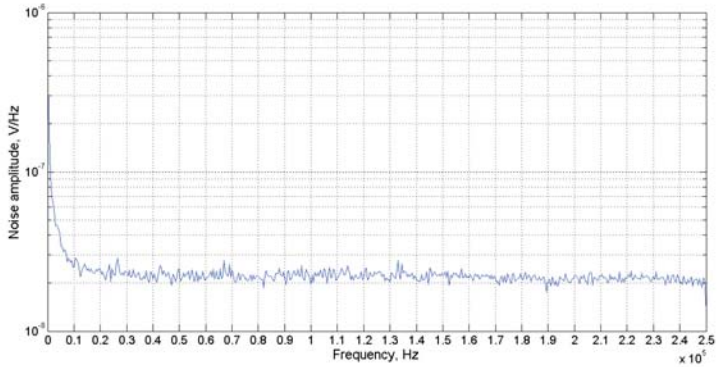

Fig.4. Output noise spectrum, high load current I_load = 2mA, Vin=200V, Vout=160 V

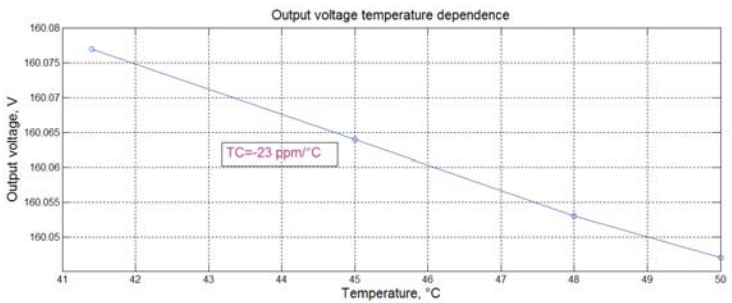

Fig.5. Output LDO voltage temperature dependence

Several more words about heat efficiency. All front-end electronics is placed in vacuum vessel. To avoid overheating only direct connection to rack and radiator is allowed. For this main PCB layer of preamplifier is surrounded with electrically insulated metal layer that is connected to rack. To transfer heat from

electronic components thermal bridge capacitors are placed around the perimeter of PCB (fig.6).

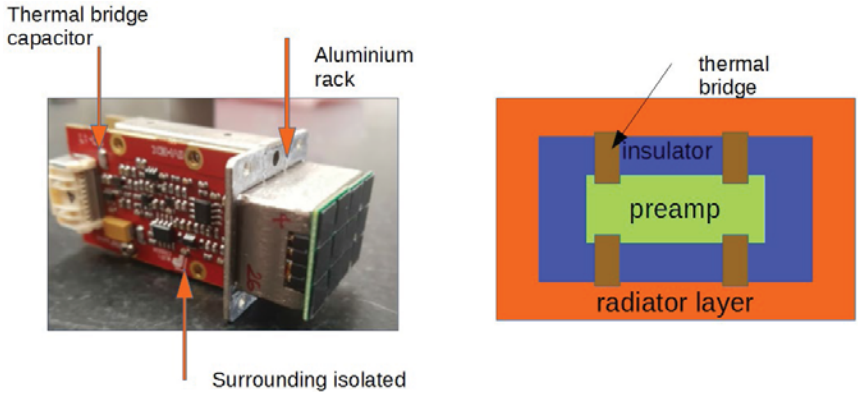

Fig.6. PCB layer of preamplifier is surrounded with electrically insulated metal layer that is connected to rack

Another very useful block in preamplifier is the current monitor. Its main goal is to determine start of a very high current pulse from SiPM. Such signal can be produced by high-energy photons that are born in different ways near the detector. One of the absorption reaction channel in semiconductor layers is massive electron-holes production. By monitoring a start of such waves we can reduce SiPM's supply voltage in time to protect detector from overheating damage.

For QA of preamplifiers for the MU2E electromagnetic calorimeter in DLNP, JINR testbench for preamplifier linearity and LDO settings is created (fig.7). The voltage settings are controlled by digital voltmeter, linearity and noises are estimated by writing and analysis multiple waveforms, that are written with DRS4 digitizer. The source of signal is a pulse signal generator that uses specially designed input probe to emulate SiPM array response. At the moment the first set of preamplifiers is tested (fig.8).

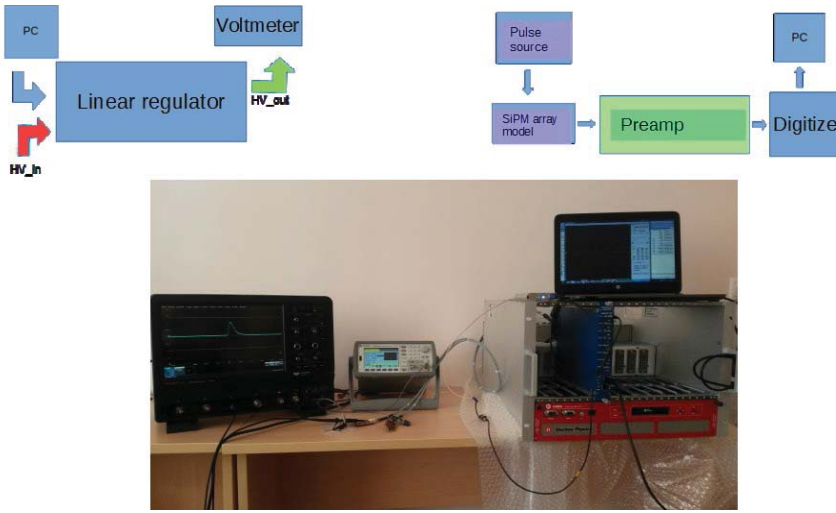

Fig.7. Test-bench for Mu2e FEE preamplifiers QA installed in DLNP, JINR.

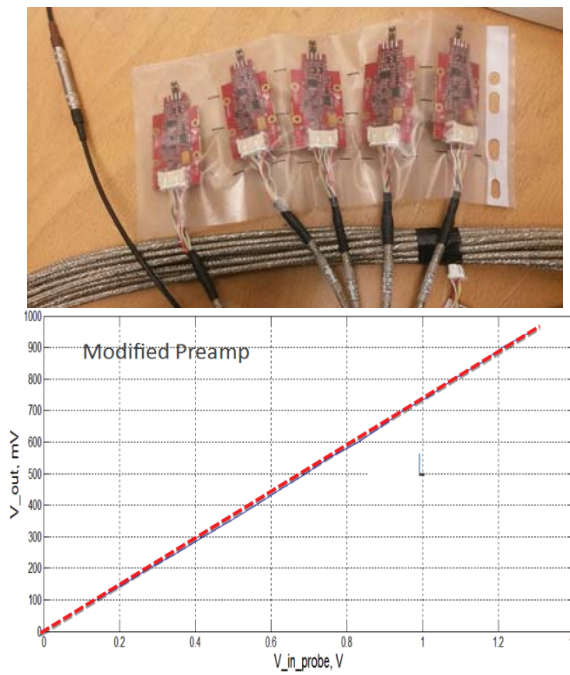

Fig.8. Set of first tested preamplifiers and sample of preamplifier linearity measurement linearity plot.

Conclusion

A FEE electronics to meet MU2E experiment requirements is designed in LNF,INFN in collaboration with JINR group passed, installed in Module0 electromagnetic calorimeter prototype. The test-bench for preamplifiers QA is installed in JINR. To complete design and start mass production dose tests should be passed.

References

[1] L. Bartoszek, et al., Mu2e Technical Design Report, 2014, ⟨arXiv:1501.05241⟩.
[2] A. Czarnecki, X. Garcia i Tormo, W.J. Marciano, Hyperfine Interactions 210 (2012) 19, http://dx.doi.org/10.1007/s10751-011-0540-0 arXiv:1111.4237.
[3] W.J. Marciano, T. Mori, J.M. Roney, The Annual Review of Nuclear and Particle Science 58 (2008) 315,
http://dx.doi.org/10.1146/annurev.nucl.58.110707. 171126.
[4] W.H. Bertl, et al., The European Physical Journal C 47 (2006) 337, http://dx.doi. org/10.1140/epjc/s2006-02582-x.
[5] N. Atanov *et al* 2018 *JINST* **13** C02037

The Hoyle State in ^{12}C Relativistic Dissociation

D. A. Artemenkov, N.K. Kornegrutsa, E. Mitseva, V.V. Rusakova, A.A. Zaitsev, I.G. Zarubina, P.I. Zarubin*

Joint Institute for Nuclear Research (JINR), Dubna, Russia

*zarubin@lhe.jinr.ru

Abstract. Nuclear track emulsion is applied to identify α-particle triples in the Hoyle's state produced in dissociation of 4.5 and 1 *A* GeV/*c* ^{12}C nuclei. The relevant events are identified by invariant mass values calculated on a basis of measurements of α-particle emission angles. An estimate of the Hoyle's state contribution to the dissociation $^{12}C \rightarrow 3\alpha$ is 10-15%.

1.Introduction

Dissociation of relativistic nuclei in a nuclear track emulsion (NTE) is a well-established phenomenon allowing holistic exploration of relativistic ensembles of lightest nuclei. The NTE technique remains the only source of such observations staying unconquerable in sensitivity and angular resolution. Individual features of investigated nuclei manifest themselves in their projectile fragmentation cones. Events of coherent dissociation which does not feature either slow fragments or charged mesons ("white"' stars) are clearly observed in NTE. Since distortions of projectile initial states are minima in them they are especially evident in studies of nuclear structure (example in Fig. 1) (see Table.1).

The cluster structure of light nuclei and the role of the unstable ^{8}Be and ^{9}B nuclei in them is a subject of the BECQUEREL project (reviewed in [1] and [2]). The studies are performed on a basis of NTE layers longitudinally exposed to relativistic Be, B, C and N isotopes, including radioactive ones. To set new limits for NTE technique it is suggested to search for the Hoyle-state (HS) in dissociation relativistic ^{12}C nuclei using the invariant mass approach.

Despite capabilities of the NTE technique its history seemed to be completed in the early 2000s. However, since 2012, the company "Slavich" (Pereslavl Zalessky, Russia) has resumed production of NTE layers of a thickness from 50 to 200 μm on a glass base. NTE samples were tested in state-of-art experiments (reviewed in [3]). On the basis of photography on

microscopes, the experience of computer recognition of short nuclear tracks in NTE was obtained. At the present time, production of baseless 500 μm thick layers of is being mastered. Reproduction of NTE allows one to put forward new proposals grounded on this classical technique.

The status of the experimental and theoretical studies of the second excited state of the ^{12}C nucleus is reviewed in [4]. This excitation is named after the astrophysicist F. Hoyle who postulated its existence to explain the prevalence of the ^{12}C isotope. Following an accurate prediction of the HS energy it was experimentally confirmed that the ^{12}C nucleus has the excited state located at only 378 keV above the mass threshold of the three α particles. Although it is unstable, its width is only 8.5 eV. Such a value indicates that the HS lifetime is comparable with the values for ^{8}Be or π^0-meson. Observation of HS at a contrast of relativistic energy and the minimum possible energy stored by 3α-ensembles can demonstrate HS as a nuclear-molecular object similar to ^{8}Be. First of all it is necessary to establish the very possibility of HS appearance in the relativistic fragmentation cone that is the purpose of the present study.

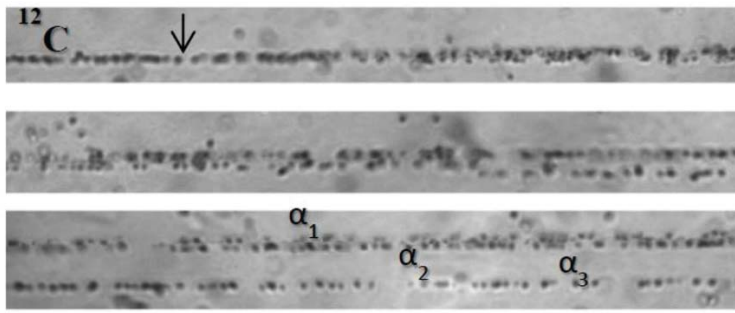

Fig. 1. Consecutive frames of coherent dissociation $^{12}C \rightarrow 3\alpha$ at 1 *A* GeV/*c* ("white" star); arrow indicate interaction vertex; grain sizes are about 0.5 μm.

2. Reconstruction of invariant mass

In general, energy of a few-particle system *Q*, can be defined as difference between the invariant mass of the system M^*, and a primary nucleus mass or a sum of masses of the particles M, that is, $Q = M^* - M$. M is defined as the sum of all products of 4-momenta $P_{i,k}$ fragments $M^{*2} = (\Sigma P_j)^2 = \Sigma\ (P_i P_k)$. Subtraction of M is a matter of convenience and Q is also named an invariant mass. Reconstruction of Q makes possible to identify decays unstable particles and nuclei.

Table 1 The average values of$\langle\Theta_{2\alpha}\rangle$ and $\langle Q_{2\alpha}\rangle$ ($Q2\alpha$ < 300 keV) in the angular regions of ^{8}Be decays.

Nucleus (P_0, A GeV/c)	$\langle\Theta_{2\alpha}\rangle$ (RMS), 10^{-3} rad ($Q_{2\alpha}$ < 300 keV)	$\langle Q_{2\alpha}\rangle$ (RMS), keV
^{12}C (4.5)	2.1 ± 0.1 (0.8)	109 ± 11 (83)
^{14}N (2.9)	2.9 ± 0.2 (1.9)	119.6 ± 9.5 (72)
^{9}Be (2.0)	4.4 ± 0.2 (2.1)	86 ± 4 (48)
^{10}C (2.0)	4.6 ± 0.2 (1.9)	63 ± 7 (83)
^{11}C (2.0)	4.7 ± 0.3 (1.9)	77 ± 7 (40)
^{10}B (1.6)	5.9 ± 0.2 (1.6)	101 ± 6 (46)
^{12}C (1.0)	10.4 ± 0.6 (3.7)	117 ± 12 (75)

For the most part, fragments of a relativistic nucleus are contained in a narrow cone of the polar angle θ, which is estimated as $\theta = 0.2/P_0$, where the factor 0.2 GeV/c is determined by the spectator-nucleon transverse momentum, while P_0 is the momentum of the accelerated projectile nucleon. The fragment 4-momenta $P_{i,k}$ in the cone can be determined in assumption of conservation of momentum per nucleon by fragments of a projectile (or its velocity). This approximation is well grounded when primary energy above 1 A GeV [5]. Then, Q is functionally related with opening angles θ between fragments. In the ^{12}C context the assumption about the correspondence of a doubly charged fragment to the ^{4}He isotope is well justified also.

The unstable ^{8}Be nucleus is an imminent participant of HS decay and its reconstruction is the precondition of HS identification. The ground state ^{8}Be is sufficiently separated from the first excited state 2^+ [6] to be identified in a spectrum over the invariant mass $Q_{2\alpha}$ calculated by α-pair opening angles $\Theta_{2\alpha}$ [1,2]. Like ^{8}Be, HS is well separated from the higher ^{12}C excitations [6]. Therefore, the same approach can be extended to the identification of HS with respect to the invariant mass of α-triples $Q_{3\alpha}$, according to formula

$$Q_{3\alpha} = \sqrt{\sum_{i \neq j} (E_{\alpha_i} E_{\alpha_j} - P_{\alpha_i} P_{\alpha_j} \cos\Theta_{2\alpha})} - 3m_{\alpha}$$

,where E_α and P_α are energy and momentum values of the α-particles i and j, $\Theta_{2\alpha}$ is the angle of separation between them, m_α is the mass of the α-particle; $P_\alpha = 4P_0$, where P_0 is the momentum per nucleon of incident nuclei.

The foundations of required methods of measurements on microscopes in exposure NTE layers were laid at the beginning of studies on the physics of

cosmic rays [7] and, then, used widely beams of relativistic nuclei became available. For these purposes microscopes KSM-1 manufactured by Carl Zeiss (Jena) about half of century and still functioning well are applied in JINR. Each microscope is equipped with apochromatic and achromatic lenses providing an increase of 15x and 50x, two eyepieces 12.5x and a tube lens 2x which together give an image magnification 375 –1250x. The maximum error due to manufacturing tolerances does not exceed 0.05 μm. Further, samples of 99 events $^{10}B \rightarrow 2He + H$ at 1.6 *A* GeV/*c* and 212 events $^{11}C \rightarrow 2He + 2H$ at 2.0 *A* GeV/*c* are used to describe in brief the procedure of coordinate measurements as a key aspect of the ongoing HS search.

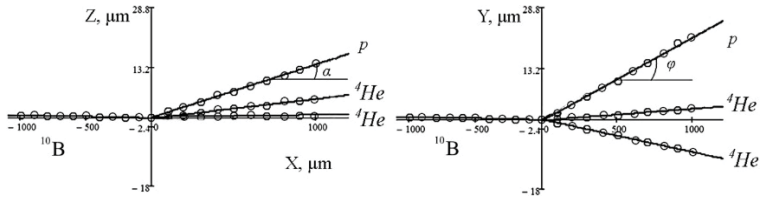

Fig. 2. Example of restored directions in event $^{10}B \rightarrow 2He + H$ over vertical and planar planes.

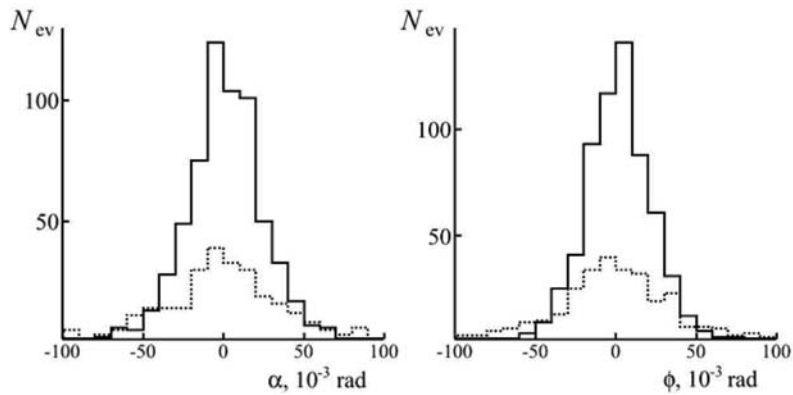

Fig. 3. Distributions of fragments He (solid) and H (dotted) over dip and planar angles α and φ in events $^{10}B \rightarrow 2He + H$.

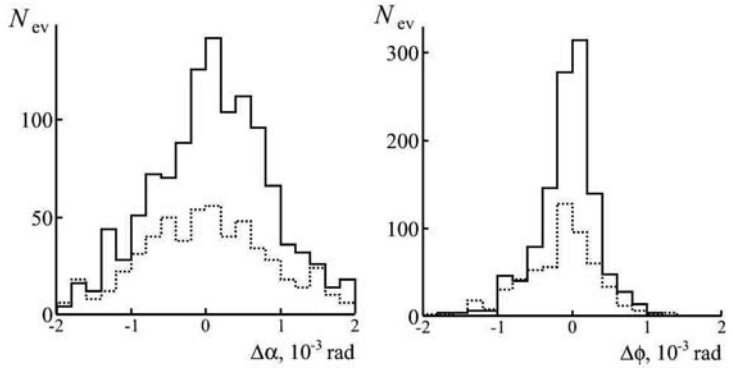

Fig. 4. Distribution of errors in determining dip (α) and planar (φ) angles for fragments He (solid) and H (dotted) in events $^{10}B \rightarrow 2He + H$.

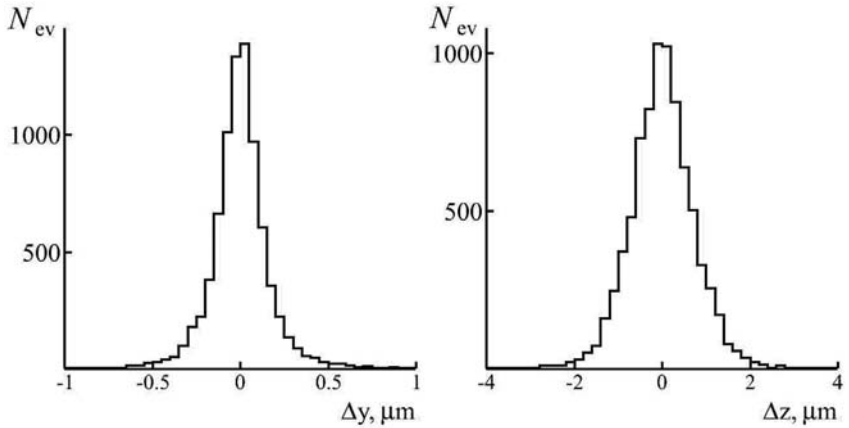

Fig. 5. Distributions of residuals Δ*y* and Δ*z* of fitting of coordinates of H and He tracks in events $^{10}B \rightarrow 2He + H$.

When an event in an emulsion plate is found it is fixed on a microscope stage in such a way that direction of a beam track coincides with direction of lengthwise movement of a microscope stage with an accuracy of 0.1 – 0.2 μm over a 1mm length. All measurements are carried out in 3D-geometry in a Cartesian coordinate system associated with a microscope. Coordinates *x*, *y*, *z* of 10 points at 1mm paths are measured over the primary and fragment tracks. NTE shrinkage due to development has to be taken into account. The found coordinates are linearly approximated to derive the dip and planar angles (α and

φ) for the beam and secondary tracks. The primary track angles are used to transit for the fragment tracks to a coordinate system associated with this track.

Fig.2 shows an outline a reconstructed event $^{10}B \rightarrow 2He + H$. The distributions of the He and H tracks over the angles αand φ are shown in Fig.3. They are characterized by mean values (RMS) $<\alpha_{He}> = -0.7 \pm 0.9$ (24) mrad and $<\varphi_{He}> = 0.2 \pm 0.8$ (21) mrad, for the nuclei H – $<\alpha_H> = -0.1 \pm 2.0$ (37) mrad and $<\varphi_H> = -0.7 \pm 2.1$ (36) mrad. Mean values (RMS) of angular errors are $\Delta\alpha = 0.08 \pm 0.02$ (0.8) mrad and $\Delta\varphi = 0.06 \pm 0.01$ (0.4) mrad (Fig.4). Scattering of the coordinate fitting residuals Δy and Δz (Fig.5) differs about 4 times and doesn't exceed more than 2 – 3 times a track thickness. A dip coordinate accuracy is less than planar one due to noise generated by vertical displacements of a microscope tube, shrinkage coefficient and vertical NTE distortions during development.

Resulting reconstruction of values $Q_{2\alpha p}$ and $Q_{2\alpha}$ for the ^{10}B and ^{11}C fragmentation is presented in Fig.6 in the range which is relevant for ^9B ($Q_{2\alpha p} <$ 400 keV). In these cases the ^9B decays serves as source of ^8Be [2]. Both distributions are similar. Their mean values (at RMS) $<Q_{2\alpha p}> = 265 \pm 14$ (100) keV and $<Q_{2\alpha}> = 91 \pm 7$ (53) keV match the accepted values [6] and expected resolution. Thus, condition $Q_{2\alpha} < 200$ keV is a practical cut-off for ^8Be identification.

3. Angular measurements in ^{12}C exposure

The current material for the HS search is a set 200 μm NTE pellicles on 2 mm glass of size 9 –12 cm which is irradiated longitudinally ^{12}C nuclei at initial momentum $P_0 = 1$ *A* GeV/*c*. This exposure was performed recently in the medical-biological beam of the Institute of High Energy Physics (Protvino). This ^{12}C beam has energy of about 400 *A* MeV and used for medical and biological studies. 2% irradiation homogeneity is provided by application of two rotating electrostatic wobblers. The steps taken in December 2016 and April 2017 resulted in the controllable irradiation with a particle density at the area of irradiation of 2000 – 4500 nuclei/cm^2. Accelerated search for 3α-events the developed pellicles is carried out by scanning along bands that are transverse to the beam direction. By May 2018, 86 events of $^{12}C \rightarrow 3\alpha$ at 1 *A* GeV/*c*, including 36 “white” stars, are founded and measured following the described procedure.

Besides, measurements made in the 90s in NTE layers exposed to ^{12}C beam at momentum $P_0 = 4.5$ *A* GeV/*c* at the JINR Synchrophasotron are available for 72 (G.M. Chernov's group, Tashkent) [8] and 114 “white”' stars $^{12}C \rightarrow 3\alpha$ (A.Sh. Gaitinov's group, Alma-Ata) as a legacy of the emulsion community. At that time, the HS problem was not set. Fig.4 shows jointly

distributions of α-particles at both momentum values over the polar emission angle θ_α. They are described by the Rayleigh distribution with the parameters $\sigma_{\theta\alpha}$ equal to 27 ± 3 (1.0 *A* GeV/*c*) and 6.5 ± 0.6 (4.5 *A* GeV/*c*) corresponding to a simple inverse relationship between P_0 and $\sigma_{\theta\alpha}$. In addition, Fig.7 shows data on He fragments for the 2.0 *A* GeV/*c* ^{11}C dissociation where the ^{4}He isotope dominates.

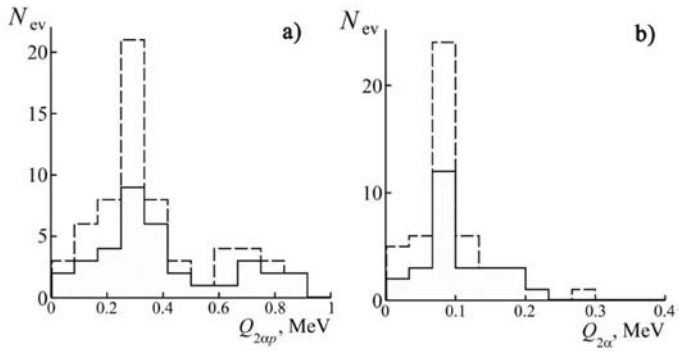

Fig. 6. Distributions of triples 2α*p* over invariant mass $Q_{2\alpha p}$ (a) for fragmentation ^{10}B → 2He + H at 1.6 *A* GeV/*c* (solid) and ^{11}C → 2He + 2H at 2.0 *A* GeV/*c* (added, dashed) and $Q_{2\alpha}$ of α-pairs in ^{9}B decays identified in these events (b).

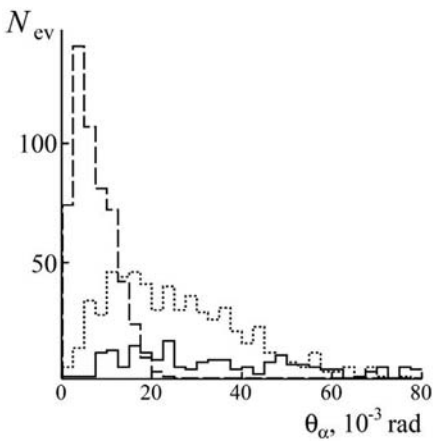

Fig. 7. Distribution over polar angle θ_α of relativistic He fragments in exposures at 4.5 (dashed) and 1 *A* GeV/*c* (solid) ^{12}C and 2.0 *A* GeV/*c* ^{11}C (dotted).

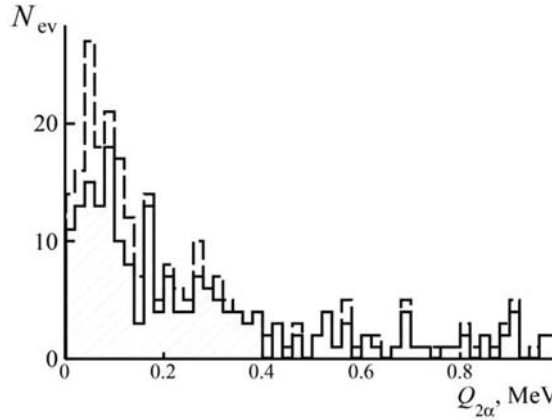

Fig. 8. Distribution of α-pairs over invariant mass $Q_{2\alpha} < 1$ MeV in the dissociation $^{12}C \rightarrow 3\alpha$ at 4.5 (solid) and 1 *A* GeV/*c* (added, dashed).

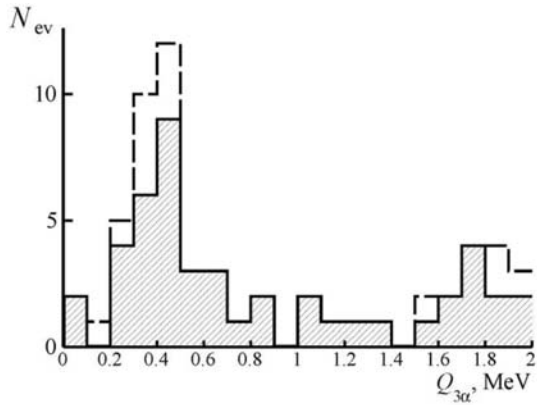

Fig. 9. Distribution of α-triples over invariant mass $Q_{3\alpha} < 2$ MeV in dissociation of $^{12}C \rightarrow 3\alpha$ at 4.5 *A* GeV/*c* (solid) and 1 *A* GeV/*c* (added, dashed).

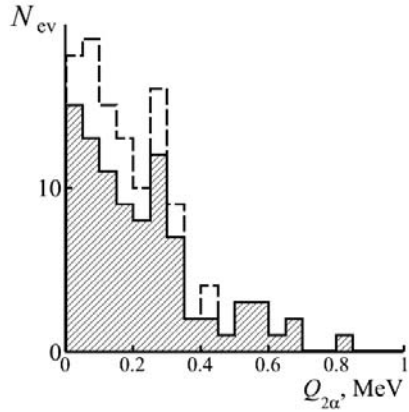

Fig. 10. Distribution of α-pairs over invariant mass $Q_{2\alpha}$ in the HS like decays ($Q_{3\alpha} < 1$ MeV) in dissociation of $^{12}C \rightarrow 3\alpha$ at 4.5 (solid) and 1 *A* GeV/*c* (added, dashed).

The $Q_{2\alpha}$ distributions obtained on a basis of angular measurements of events $^{12}C \rightarrow 3\alpha$ at two values P_0 are presented jointly in Fig.8. Both are distributions do not differ within statistics. The region $Q2\alpha < 200$ keV contains a peak pressed to the origin which corresponds to decays of ^{8}Be. Although the ^{8}Be signal is present the $Q_{2\alpha}$ distribution appears to be significantly wider than in Fig.6(b).

In the $Q_{3\alpha}$ distribution over the invariant mass of the α-triples (Fig.9) there is a peak in the region $Q_{3\alpha} < 1$ MeV where HS decays could be reflected. For events at 4.5 *A* GeV/*c* the mean value for the events at the peak $<Q_{3\alpha}>$ (at RMS) is 441 ± 34 (190) keV, and at 1 *A* GeV/*c*, respectively, 346 ± 28 (85) keV. According to the "soft" condition $Q_{3\alpha} < 1$ MeV in the 4.5 *A* GeV/*c* exposure 30 (of 186) events can be attributed to HS and 9 (of 86) including 5 "white" stars (of 36) in 1 *A* GeV/*c* exposure.

When selecting α-pairs from α-triples that correspond to the HS criterion $Q_{3\alpha} < 1$ MeV the $Q_{2\alpha}$ distribution acquires the form shown in Fig.10. The average value $<Q_{2\alpha}>$ (RMS) is 210 ± 15 (156) keV. The distribution form becomes wider and separation of the ^{8}Be peak in the region $Q_{2\alpha} < 200$ keV is impossible. This change is caused by the increased contribution of non-^{8}Be-resonance α pairs of HS decays masking the ^{8}Be signal. In turn, this circumstance makes unattainable a more detailed analysis of the HS inner structure. It characterizes a limitation of our approach to penetrate in the HS structure. Nevertheless, it is concluded that HS is observed in a relativistic dissociation $^{12}C \rightarrow 3\alpha$ with probability about 10-15%.

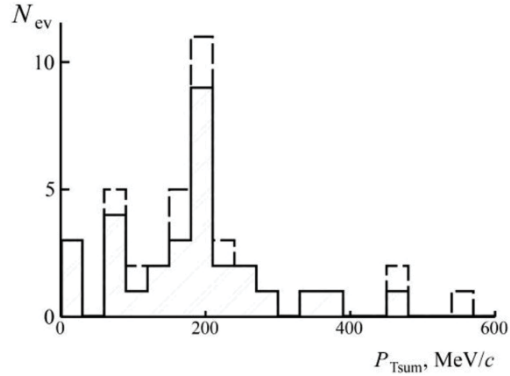

Fig. 11. Distribution of α-triples of HS like decays ($Q_{3\alpha}$ < 1 MeV) over total transverse momentum <P_{Tsum}> in dissociation $^{12}C \rightarrow 3\alpha$ at 4.5 (solid) and 1 *A* GeV/*c* (added, dashed).

The angular measurements make it possible to conclude about the dynamics of the HS appearance according to the distribution of α-particle triples over their total transverse momentum P_{Tsum} (Fig.11). Its average value <P_{Tsum}> (RMS) is equal to 190 ± 19 (118) MeV/*c* corresponding to the nuclear-diffraction mechanism. In the case of electromagnetic dissociation on Ag and Br nuclei composing NTE the limitation is expected to be P_{Tsum} < 100 MeV/*c* [9]. It is surprising that such a "fragile" formation of three α-particles as HS can arise in relativistic collisions as an ensemble which is "bouncing off" with the transverse momentum P_{Tsum} characteristic for strong interactions rather than electromagnetic ones. It can be assumed that increased statistics allow registration of the HS formation outside the angular cone of fragmentation of the parent nucleus. Events of this kind were observed in the cases $^{9}Be \rightarrow {}^{8}Be$ and $^{10}C \rightarrow {}^{9}B$. Such observations would clearly demonstrate HS as a holistic and long-lived nuclear-molecular state.

4. Conclusion

In dissociation $^{12}C \rightarrow 3\alpha$ at 4.5 and 1 *A* GeV/*c* in nuclear track emulsion production of the Hoyle's-state is identified by using approximate invariant mass representation. Contribution of HS is estimated to be about 10-15%. This conclusion is grounded on the basis of the most precise angular measurements performed by three research groups in two exposures at two momentum values that are separated in time by two decades. By itself, this finding demonstrates the thoroughness of the NTE technique.

However, the NTE grounded approach doesn't allow one to address the features of the HS decay. Nevertheless reconstruction of HS in NTE by the invariant mass of relativistic α-triples can be applied to study processes with the HS formation as a wholesome relativistic object at large moment transfers. It is possible that a HS wouldn't be limited only as the ^{12}C excitation but can manifest itself similarly to ^{8}Be as a universal object in fragmentation of heavier nuclei. In this respect, the closest source to verify such a assumption is the ^{14}N nucleus. The ^{13}N and ^{13}C nuclei whose beams can be formed in the ^{14}N fragmentation are even more convenient in this respect.

References

[1] Zarubin, P.I., 2013. “Tomography” of the cluster structure of light nuclei via relativistic dissociation// Lect. Notes in Phys. 875. Clusters in Nuclei 3, 51–93}. Springer Int. Publ; arXiv:1309.4881.

[2] Zarubin, P.I., 2016. Recent application of nuclear track emulsion technique // Phys. Atom. Nucl. 79, 1525–1535;

[3] Artemenkov, D.A., Zaitsev, A.A., Zarubin, P.I., 2017. Unstable nuclei in dissociation of light stable and radioactive nuclei in nuclear track emulsion. // Phys. Part. Nucl. 48, 147–157; arXiv: 1607.08020.

[4] Freer, M., Fynbo, H.O.U., 2014. The Hoyle state in ^{12}C // Prog. Part. Nucl. Phys. 78, 1–23.

[5] Anderson, L., Bruckner, W., Moeller, E., Nagamiya, S., Nilsen-Meyer, S., Schroeder, L., Shapiro, G., Steiner, H., 1983. Inclusive particle production at forward angles from collisions of light relativistic nuclei: nuclear fragments // Phys. Rev. C 28, 1224–1245.

[6] Ajzenberg-Selove, F., 1988. TUNL nuclear data evaluation project // Nucl. Phys. A 490.

[7] Powell, C.F., Fowler, P.H., Perkins, D.H., 1959. Study of Elementary Particles by the Photographic Method. // Pergamon, London.

[8] Belaga, V.V., Benjaza, A.A., Rusakova, V.V., Salomov, D.A., Chernov, G.M., 1995. Coherent dissociation $^{12}C \rightarrow 3\alpha$ in lead-enriched emulsion at 4.5 GeV/*c* per nucleon // Phys. Atom. Nucl. 58, 1905–1910; arXiv:1109.0817.

[9] Peresad’ko, N.G., Fetisov, V.N., Aleksandrov Yu, A., Gerasimov, S.G., Dronov, V.A., Larionova, V.G., Tamm, E.I., Kharlamov, S.P., 2008. Role of the nuclear and electromagnetic interactions in the coherent dissociation of the relativistic ^{7}Li nucleus into the ^{3}H + ^{4}He Channel // JETP Lett. (Engl. Transl.) 88, 75–79.

Научное издание

NEW TRENDS IN HIGH-ENERGY PHYSICS

Proceedings of the Conference

НОВЫЕ ТЕНДЕНЦИИ В ФИЗИКЕ ВЫСОКИХ ЭНЕРГИЙ

Труды конференции

Ответственная за подготовку сборника к печати *И. В. Титкова*.

Сборник отпечатан методом прямого репродуцирования
с оригиналов, предоставленных оргкомитетом.

E1,2-2019-13

Подписано в печать 10.04.2019.
Формат 60×90/16. Бумага офсетная. Печать офсетная.
Усл. печ. л. 17,94. Уч.-изд. л. 28,71. Тираж 100 экз. Заказ 59635.

Издательский отдел Объединенного института ядерных исследований
141980, г. Дубна, Московская обл., ул. Жолио-Кюри, 6.
E-mail: publish@jinr.ru
www.jinr.ru/publish/